

# **Methods in computational cosmology**

by

Mohammadjavad Vakili

A dissertation submitted in partial fulfillment

of the requirements for the degree of

Doctor of Philosophy

Department of Physics

New York University

May 2017

---

Professor David W. Hogg

Copyright © 2017 Mohammadjavad Vakili

This work is licensed under a Creative Commons Attribution 4.0 International License.



## Acknowledgements

# Abstract

State of the inhomogeneous universe and its geometry throughout cosmic history can be studied by measuring the clustering of galaxies and the gravitational lensing of distant faint galaxies. Lensing and clustering measurements from large datasets provided by modern galaxy surveys will forever shape our understanding of the how the universe expands and how the structures grow. Interpretation of these rich datasets requires careful characterization of uncertainties at different stages of data analysis: estimation of the signal, estimation of the signal uncertainties, model predictions, and connecting the model to the signal through probabilistic means. In this thesis, we attempt to address some aspects of these challenges.

The first step in cosmological weak lensing analyses is accurate estimation of the distortion of the light profiles of galaxies by large scale structure. These small distortions, known as the cosmic shear signal, are dominated by extra distortions due to telescope optics and atmosphere (in the case of ground-based imaging). This effect is captured by a kernel known as the Point Spread Function (PSF) that needs to be fully estimated and corrected for. We address two challenges a head of accurate PSF modeling for weak lensing studies. The first challenge is finding the centers of point sources that are used for empirical estimation of the PSF. We show that the approximate methods for centroiding stars in wide surveys are able to optimally saturate the information content that is retrievable from astronomical images in the presence of noise.

The fist step in weak lensing studies is estimating the shear signal by accurately measuring the shapes of galaxies. Galaxy shape measurement involves modeling the light profile of galaxies convolved with the light profile of the PSF. Detectors of many space-based telescopes such as the Hubble Space Telescope (*HST*) sample the the PSF with low resolution. Reliable weak lensing analysis of galaxies observed by the *HST* camera requires knowledge of the PSF at a resolution higher than the pixel resolution of *HST*. This PSF is called the super-

resolution PSF. In particular, we present a forward model of the point sources imaged through filters of the *HST WFC3* IR channel. We show that this forward model can accurately estimate the super-resolution PSF. We also introduce a noise model that permits us to robustly analyze the *HST WFC3* IR observations of the crowded fields.

Then we try to address one of the theoretical uncertainties in modeling of galaxy clustering on small scales. Study of small scale clustering requires assuming a halo model. Clustering of halos has been shown to depend on halo properties beyond mass such as halo concentration, a phenomenon referred to as assembly bias. Standard large-scale structure studies with halo occupation distribution (HOD) assume that halo mass alone is sufficient to characterize the connection between galaxies and halos. However, assembly bias could cause the modeling of galaxy clustering to face systematic effects if the expected number of galaxies in halos is correlated with other halo properties. Using high resolution  $N$ -body simulations and the clustering measurements of Sloan Digital Sky Survey (*SDSS*) DR7 main galaxy sample, we show that modeling of galaxy clustering can *slightly* improve if we allow the HOD model to depend on halo properties beyond mass.

One of the key ingredients in precise parameter inference using galaxy clustering is accurate estimation of the error covariance matrix of clustering measurements. This requires generation of many independent galaxy mock catalogs that accurately describe the statistical distribution of galaxies in a wide range of physical scales. We present a fast and accurate method based on low-resolution  $N$ -body simulations and an empirical bias model for generating mock catalogs. We use fast particle mesh gravity solvers for generation of dark matter density field and we use Markov Chain Monte Carlo (MCMC) to estimate the bias model that connects dark matter to galaxies. We show that this approach enables the fast generation of mock catalogs that recover clustering at a percent-level accuracy down to quasi-nonlinear scales.

Cosmological datasets are interpreted by specifying a likelihood function that is often assumed to be multivariate Gaussian. Likelihood free approaches such as Approximate Bayesian Computation (ABC) can bypass this assumption by introducing a generative forward model of the data and a distance metric for quantifying the closeness of the data and the model. We present the first application of ABC in large scale structure for constraining the connections between galaxies and dark matter halos. We present an implementation of ABC equipped with Population Monte Carlo and a generative forward model of the data that incorporates sample variance and systematic uncertainties. We show that this framework permits us to accurately infer the galaxy/halo connection with the galaxy clustering and galaxy group statistics measurements.

# Contents

Copyright . . . . .	ii
Acknowledgements . . . . .	iv
Abstract . . . . .	v
List of Figures . . . . .	xi
List of Tables . . . . .	xxvi
<b>Introduction</b>	<b>1</b>
<b>1 Fast stellar centroiding and saturation of the Cramer-Rao lower bound</b>	<b>21</b>
1.1 Chapter abstract . . . . .	21
1.2 Introduction . . . . .	22
1.3 The Cramér-Rao lower bound . . . . .	25
1.4 Centroiding methods . . . . .	31
1.5 Tests . . . . .	35
1.6 Results . . . . .	36
1.7 Discussion . . . . .	38
<b>2 Approximate bayesian computation in large scale structure: constraining the galaxy halo connection</b>	<b>51</b>
2.1 Section abstract . . . . .	51

2.2	Introduction . . . . .	52
2.3	Methods . . . . .	56
2.4	ABC at work . . . . .	68
2.5	Summary and Conclusion . . . . .	80
<b>3</b>	<b>How are galaxies assigned to halos? searching for assembly bias in SDSS clustering measurements</b>	<b>89</b>
3.1	chapter abstract . . . . .	89
3.2	Introduction . . . . .	90
3.3	Method . . . . .	96
3.4	Data . . . . .	102
3.5	Analysis . . . . .	104
3.6	Results and Discussion . . . . .	106
3.7	Summary and Conclusion . . . . .	118
<b>4</b>	<b>Accurate galaxy-halo mocks with automatic bias estimation and particle-mesh gravity solvers</b>	<b>130</b>
4.1	abstract . . . . .	130
4.2	Introduction . . . . .	131
4.3	Methodology . . . . .	135
4.4	Demonstration on an accurate $N$ -body based halo catalog . . . . .	143
4.5	Summary and Discussion . . . . .	148
<b>5</b>	<b>Super-resolution PSF model of HST WFC3-IR</b>	<b>156</b>
5.1	Chapter abstract . . . . .	156
5.2	Introduction . . . . .	157
5.3	Data . . . . .	159

5.4	Method	162
5.5	Preliminary Results	168
5.6	Summary and Discussion	171
	<b>Conclusion</b>	<b>185</b>
	<b>Bibliography</b>	<b>187</b>

# List of Figures

1.1	Scatter plots showing the relation between the ratio of error (in x-axis of the centroid positions) to the CRLB and the signal-to-noise ratio of stars. Errors are found from fitting the exact PSF model to the stars, with FWHM of : 2 (upper left), 2.8 (upper right), 4 (lower left), and 5.6 (lower right) pixels. In each scatter plot, the blue solid line represents the ratio of the root-mean-squared-error to the CRLB, and the red line represents the ratio achievable by an optimal estimator. . . . .	43
1.2	Scatter plots showing the relation between the ratio of error (in x-axis of the centroid positions) to the CRLB and the signal-to-noise ratio of stars. Errors are found from applying the matched filter polynomial centroiding to the stars, with FWHM of : 2 (upper left), 2.8 (upper right), 4 (lower left), and 5.6 (lower right) pixels. In each scatter plot, the blue solid line represents the ratio of the root-mean-squared-error to the CRLB, and the red line represents the ratio achievable by an optimal estimator. . . . .	44



1.6 Scatter plots showing the relation between the ratio of error (in x-axis of the centroid poistions) to the CRLB and the FWHM of stars. Errors are found from applying the matched filter polynomial centroiding to the stars, with SNR of : 5 (upper left), 10 (upper right), 20 (lower left), and 40 (lower right). In each scatter plot, the blue solid line represents the ratio of the root-mean-squared-error to the CRLB, and the red line represents the ratio achievable by an optimal estimator. . . . .	48
1.7 Scatter plots showing the relation between the ratio of error (in x-axis of the centroid poistions) to the CRLB and the FWHM of stars. Errors are found from applying the fixed-Gaussian polynomial centroding to the stars, with SNR of : 5 (upper left), 10 (upper right), 20 (lower left), and 40 (lower right). In each scatter plot, the blue solid line represents the ratio of the root-mean-squared-error to the CRLB, and the red line represents the ratio achievable by an optimal estimator. . . . .	49
1.8 Scatter plots showing the relation between the ratio of error (in x-axis of the centroid poistions) to the CRLB and the FWHM of stars. Errors are found from applying the $7 \times 7$ moment method to the stars, with SNR of : 5 (upper left), 10 (upper right), 20 (lower left), and 40 (lower right). In each scatter plot, the blue solid line represents the ratio of the root-mean-squared-error to the CRLB, and the red line represents the ratio achievable by an optimal estimator. . . . .	50

- 2.1 The two-point correlation function  $\xi_{gg}(r)$  (left) and group multiplicity function  $g(N)(N)$  (right) summary statistics of the mock observations generated from the “true” HOD parameters described in Section 2.4.1. The width of the shaded region corresponds to the square root of the covariance matrix diagonal elements (Eq. 2.14). In our ABC analysis, we treat the  $\xi_{gg}(r)$  and  $g(N)(N)$  above as the summary statistics of the observation. . . . .

2.2 We demonstrate the evolution of the ABC particles,  $\vec{\theta}_t$ , over iterations  $t = 1$  to 9 in the  $\log \mathcal{M}_{min}$  and  $\log \mathcal{M}_1$  parameter space.  $\bar{n}$  and  $g(N)(N)$  are used as observables for the above results. For reference, in each panel, we include the “true” HOD parameters (black star) listed in Section 2.4.1. The initial distance threshold,  $\vec{\epsilon}_1 = [\infty, \infty]$  at  $t = 1$  (top left) so the  $\vec{\theta}_1$  spans the entire range of the prior distribution, which is also the range of the panels. We see for  $t < 5$ , the parameter space occupied by the ABC  $\vec{\theta}_t$  shrinks dramatically. Eventually when the algorithm converges,  $t > 7$ , the parameter space occupied by  $\vec{\theta}_t$  no longer shrinks and their distributions represent the posterior distribution of the parameters. At  $t = 9$ , the final iteration, the ABC algorithm has converged and we find that  $\vec{\theta}_{\text{true}}$  lies safely within the 68% confidence region. . . . .

2.3 We illustrate the convergence of the ABC algorithm through the evolution of the ABC particle distribution as a function of iteration for parameters  $\log \mathcal{M}_{min}$  (left),  $\alpha$  (center), and  $\log \mathcal{M}_1$  (right). The top panel corresponds our ABC results using the observables  $(\bar{n}, g(N)(N))$ , while the lower panel plots corresponds to the ABC results using  $(\bar{n}, \xi_{gg}(r))$ . The distributions of parameters show no significant change after  $t > 7$ , which suggests that the ABC algorithm has converged. . . . .

2.4 We present the constraints on the Zheng et al. (2007) HOD model parameters obtained from our ABC-PMC analysis using $\bar{n}$ and $\xi_{gg}(r)$ as observables. The diagonal panels plot the posterior distribution of each HOD parameter with vertical dashed lines marking the 50% quantile and 68% confidence intervals of the distribution. The off-diagonal panels plot the degeneracies between parameter pairs. The range of each panel corresponds to the range of our prior choice. The “true” HOD parameters, listed in Section 2.4.1, are also plotted in each of the panels (black). For $\log \mathcal{M}_0$ , $\alpha$ , and $\sigma_{\log M}$ , the “true” parameter values lie near the center of the 68% confidence interval of the posterior distribution. For $\log \mathcal{M}_1$ and $\log \mathcal{M}_{\min}$ , which have tight constraints, the “true” values lie within the 68% confidence interval. Ultimately, the ABC parameter constraints we obtain in our analysis are consistent with the “true” HOD parameters. . . . .	83
2.5 Same as Figure 2.4 but for our ABC analysis using $\bar{n}$ and $g(N)(N)$ as observables. The ABC parameter constraints we obtain are consistent with the “true” HOD parameters. . . . .	84

- 2.6 We compare the ABC-PMC posterior prediction for the observables  $\xi_{gg}(r)$  (left) and  $g(N)(N)$  (right) (orange; Section 2.4.3) to  $\xi_{gg}(r)$  and  $g(N)(N)$  of the mock observation (black) in the top panels. In the lower panels, we plot the ratio between the ABC-PMC posterior predictions for  $\xi_{gg}$  and  $g(N)$  to the mock observation  $\xi_{gg}^{\text{obvs}}$  and  $g(N)^{\text{obvs}}$ . The darker and lighter shaded regions represent the 68% and 95% confidence regions of the posterior predictions, respectively. The error-bars represent the square root of the diagonal elements of the error covariance matrix (equation 2.14) of the mock observations. Overall, the observables drawn from the ABC-PMC posteriors are in good agreement with  $\xi_{gg}$  and  $g(N)$  of the mock observations. The lower panels demonstrate that for both observables, the error-bars of the mock observations lie within the 68% confidence interval of the ABC-PMC posterior predictions. . . . .

2.7 We compare the  $\log \mathcal{M}_{\min}$ ,  $\alpha$ , and  $\log \mathcal{M}_1$  parameter constraints from ABC-PMC (orange) to constraints from the Gaussian pseudo-likelihood MCMC (blue) using  $\bar{n}_g$  and  $\xi_{gg}(r)$  as observables. The *top* panels compares the two methods' marginalized posterior PDFs over the parameters. In the *bottom* panels, we include box plots marking the confidence intervals of the posterior distributions. The boxes represent the 68% confidence interval while the “whiskers” represent the 95% confidence interval. We mark the “true” HOD parameters with vertical black dashed line. The marginalized posterior PDFs obtained from the two methods are consistent with each other. The ABC-PMC and Gaussian pseudo-likelihood constraints are generally consistent for  $\log \mathcal{M}_{\min}$  and  $\log \mathcal{M}_1$ . The ABC-PMC constraint for  $\alpha$  is slightly less biased and has slightly larger uncertainty than the constraint from Gaussian pseudo-likelihood analysis. . . . .

2.8 Same as Figure 2.7, but both the ABC-PMC analysis and the Gaussian pseudo-likelihood MCMC analysis use $\bar{n}_g$ and $g(N)(N)$ as observables. Both methods derive constraints consistent with the “true” HOD parameters and infer the region of allowed values to similar precision. We note that the MCMC constraint on $\alpha$ is slightly more biased compared to ABC-PMC estimate. This discrepancy may stem from the fact that the use of Gaussian pseudo-likelihood and its associated assumptions is more spurious when modeling the group multiplicity function. . . . .	87
2.9 We compare the ABC-PMC (orange) and the Gaussian pseudo-likelihood MCMC (blue) predictions of the 68% and 95% posterior confidence regions over the HOD parameters ( $\log \mathcal{M}_{\min}$ , $\alpha$ , and $\log \mathcal{M}_1$ ) using $\bar{n}_g$ and $\xi_{gg}(r)$ as observables. In each panel, the black star represents the “true” HOD parameters used to generate the mock observations. Both inference methods derive confidence regions consistent with the “true” HOD parameters. . . . .	88
2.10 Same as Figure 2.9, but using $\bar{n}_g$ and $g(N)(N)$ as observables. Again, the confidence regions derived from both methods are consistent with the “true” HOD parameters used to generate the mock observations. The confidence region of $\alpha$ from the Gaussian pseudo-likelihood method is biased compared to the ABC-PMC contours. This may be due to the fact that the true likelihood function that describes $g(N)(N)$ deviates significantly from the assumed Gaussian functional form. . . . .	88

3.1 Constraints on the central assembly bias $\mathcal{A}_{\text{cen}}$ (Top panel) and the satellite assembly bias $\mathcal{A}_{\text{sat}}$ (Bottom panel) parameters. The $\mathcal{A}_{\text{cen}}$ constraints for the $M_r < -20.5, -20, -19.5$ samples favor positive values of $\mathcal{A}_{\text{cen}}$ with the tightest constraint coming from the $M_r < -20$ sample. The $\mathcal{A}_{\text{cen}}$ constraints for the $M_r < -18$ sample favor negative values of $\mathcal{A}_{\text{cen}}$ . All the $\mathcal{A}_{\text{sat}}$ constraints are consistent with no satellite assembly bias. . . . .	122
3.2 Comparison between the posterior predictions of $w_p(r_p)$ and the SDSS $w_p(r_p)$ measurements. Predictions from the standard HOD model (HOD model with assembly bias) are shown in red (blue). The Dark and light shaded regions mark the 68% and the 95% confidence intervals. The errorbars are from the diagonal elements of the covariance matrix. . . . .	123
3.3 Same as Figure 3.2, but showing the fractional difference between the posterior predictions and the observed projected 2PCF for all the luminosity threshold samples. In all luminosity threshold samples, predictions of the two models for small scale clustering are consistent. In the samples that favor more positive values of the central assembly bias parameter ( $M_r < -19.5, -19, -20, -20.5$ ), modeling of the intermediate and large scale clustering is slightly improved. The large scale clustering modeling of the $M_r < -18$ sample is also improved because of negative constraints on $\mathcal{A}_{\text{cen}}$ which is equivalent to allocation of more central galaxies in low concentration halos at fixed halo mass. . . . .	124

3.4 Demonstration of the relative difference in $w_p$ between randomized and non-randomized catalogs for different luminosity threshold samples: $M_r < -20, -20.5, -21$ . The errorbars are from the diagonal elements of the covariance matrix. The blue lines correspond to the random draws from the posterior probability (summarized in Table 3.6.1) over the parameters of the HOD model with assembly bias. The red line corresponds to the subhalo abundance matching catalog (Hearin & Watson 2013; Hearin et al. 2014). Our constraints favor <i>more moderate</i> levels of the impact of assembly bias on galaxy clustering than the levels seen in the abundance matching mock catalogs. Within both models, the small scale clustering remains unaltered after randomizing the catalogs, signaling the lack of correlation between the satellite occupation and the halo concentration at a fixed mass in the two models. . . . .	125
3.5 Difference in the information criteria between the HOD model with assembly bias and the model without assembly bias. <b>Top:</b> $\Delta\text{BIC} = \text{BIC}(\text{with assembly bias}) - \text{BIC}(\text{without assembly bias})$ . <b>Bottom:</b> $\Delta\text{AIC} = \text{AIC}(\text{with assembly bias}) - \text{AIC}(\text{without assembly bias})$ . According to BIC (AIC), the more complex model with assembly bias is favored once $\Delta\text{BIC} < 0$ ( $\Delta\text{AIC} < 0$ ). Both $\Delta\text{BIC}$ and $\Delta\text{AIC}$ are lower for the samples with tighter constraints over the central assembly bias parameter $\mathcal{A}_{\text{cen}}$ , with $\Delta\text{BIC}$ being (marginally) negative only for $M_r < -20, -18$ samples that yield strongest constraints on $\mathcal{A}_{\text{cen}}$ . . .	126

3.6 Comparison between the constraints on the assembly bias parameters $\mathcal{A}_{\text{cen}}$ (shown in the top panel) and $\mathcal{A}_{\text{sat}}$ (shown in the bottom panel) for different simulations: <b>SMDP</b> (shown with circle), and <b>BolshoiP</b> (shown with cross). The errorbars mark the 68% uncertainty over the parameters. Shaded blue regions show the upper and lower bounds reported by Zentner et al. (2016) that uses the <b>BolshoiP</b> and clustering measurements of Zehavi et al. (2011). For the confidence intervals corresponding to the shaded blue regions, we refer the readers to Table 2 of Zentner et al. (2016). The central assembly bias constraints found from the two simulations are consistent, with the constraints for from the <b>SMDP</b> simulation being tighter for the most luminous samples. The constraints on $\mathcal{A}_{\text{sat}}$ from the two simulations are largely in agreement with the exception of $M_r < -19, -20.5$ samples that favor more positive values of $\mathcal{A}_{\text{sat}}$ when the <b>BolshoiP</b> simulation is used.	127
3.7 Constraints over the satellite assembly bias parameters from luminosity-threshold samples $M_r < -19, -20.5$ , for two different simulations: <b>BolshoiP</b> (yellow), and <b>SMDPL</b> (green). The $\mathcal{A}_{\text{sat}}$ constraints found using the <b>BolshoiP</b> simulation favor more positive values of $\mathcal{A}_{\text{sat}}$ , while the constraints found using the <b>SMDP</b> simulation favor zero satellite assembly bias.	128

3.8 An example of posterior probability distribution over the parameters of the standard HOD model with no assembly bias (shown with yellow), and the HOD model with assembly bias (shown in blue). These constraints are obtained from the clustering measurements of the $M_r < -20.5$ luminosity threshold sample. The dark (light) blue shaded regions show the 68% (95 %) confidence intervals. The constraints on $\mathcal{A}_{\text{cen}}$ and $\mathcal{A}_{\text{sat}}$ show positive correlation between the central occupation and the halo concentration at fixed halo mass, and lack of correlation between the satellite occupation and halo concentration at fixed halo mass. . . . .	129
4.1 Dark matter overdensity $\delta = \rho_m / \rho - 1$ slices of $20 h^{-1} \text{Mpc}$ from the high-resolution BigMultiDark simulation (left panels), the low-resolution FASTPM simulation (central panels) and from the ALPT simulation (right panels), taking a subvolume of $(1250 h^{-1} \text{Mpc})^3$ (top panels), $(625 h^{-1} \text{Mpc})^3$ (middle panels), and $(312.5 h^{-1} \text{Mpc})^3$ (bottom panels). The structures in the high-resolution $N$ -body simulation and the low-resolution FASTPM simulation look very similar inspite of having very different resolutions ( $3840^3$ vs $960^3$ particles). The low-resolution ALPT simulation looks more diffuse. . . . .	152
4.2 Posterior probability distribution of the PATCHY bias parameters $\{\delta_{\text{th}}, \alpha, \beta, \rho_\epsilon, \epsilon\}$ . The contours mark the 68% and the 95% confidence intervals of the posterior probabilities. This plot is made using the open-source software CORNER (Foreman-Mackey 2017). . . . .	153

- 4.3 Top: Demonstration of the halo bivariate probability distribution function of halos (halo counts-in-cells) in the BigMultiDark simulation (shown in black) and in the FASTPM-PATCHY simulation (shown in blue) and in the ALPT-PATCHY simulation (shown in red) on the left. Comparison between the real-space power spectrum of the BDM halos (shown in black) in the reference BigMultiDark simulation and that of the halos in the FASTPM-PATCHY (ALPT-PATCHY) simulation shown in blue (red) on the right. Bottom: Ratio between the halo PDFs of the approximate mocks and halo PDF of the BigMultiDark simulation on the left. Ratio between the halo power spectra of the approximate mocks and the halo power spectrum of the BigMultiDark simulation on the right. . . . . 154
- 4.4 Real-space bispectrum of the BigMD BDM halos and that of the approximate mocks as a function of angle  $\alpha_{12}$  between  $\mathbf{k}_1$  and  $\mathbf{k}_2$  for  $k_1 = k_2 = 0.1 \ h \text{Mpc}^{-1}$  (upper left),  $2k_1 = k_2 = 0.2 \ h \text{Mpc}^{-1}$  (upper right),  $k_1 = k_2 = 0.15 \ h \text{Mpc}^{-1}$  (middle left),  $k_1 = k_2 = 0.2 \ h \text{Mpc}^{-1}$  (middle right),  $2k_1 = k_2 = 0.3 \ h \text{Mpc}^{-1}$  (lower left), and  $2k_1 = k_2 = 0.4 \ h \text{Mpc}^{-1}$  (lower right). The BigMD is represent by the solid black line, while ALPT-PATCHY is represented by the dashed red line, and FASTPM-PATCHY is represented by the dashed blue line. 155

5.1 Left: Demonstration of the initialization of the super-resolution PSF model. The initial PSF was constructed by scaling (background subtraction and flux normalization), shifting (through matched-filter polynomial centroiding), up-sampling (with cubic spline interpolation), and averaging the isolated stars in the observation sample. Right: Super-resolution PSF estimated by optimizing the likelihood function after six iterations. We note that the averaged upsampled initial PSF is smooth and lacks the sharp features visible across the full radian support of the PSF, specially the tails. . . . .	173
5.2 An example of a patch containing a high signal-to-noise ratio star in the training set. Upper-left and upper-right panels show the data and the model respectively. The lower left panel shows $\chi$ . The lower right panel shows the flagged pixels. Pixels with $\text{FLAG} = 0$ are used in PSF-fitting. Pixels with are $\text{FLAG} = 1$ (provided by the MAST data) are masked out prior to the analysis. Finally, pixels with $\text{FLAG} = 2$ correspond to the pixels in a given model realization with $\chi^2_{\text{clip}} > 3$ . . . . .	174
5.3 Same as Figure 5.2 but showing a different high signal-to-noise ratio star in the training set. . . . .	175
5.4 Same as Figure 5.2 but showing a low signal-to-noise ratio star in the training set. . . . .	176
5.5 Same as Figure 5.2 but showing a different low signal-to-noise ratio star in the training set. . . . .	177

5.6 An example of a patch in the validation set containing multiple point sources. Upper-left and upper-right panels show the data and the model respectively. The lower left panel shows the $\chi$ map. The lower right panel shows the flagged pixels. Pixels with <b>FLAG</b> = 0 are used in PSF-fitting. Pixels with <b>FLAG</b> = 1 (provided by the MAST data) are masked out prior to the analysis. Finally, pixels with <b>FLAG</b> = 2 correspond to the pixels in a given model realization with $\chi_{\text{clip}}^2 > 3$ . In the lower left panel, pixels with $\chi_{\text{clip}}^2 > 3$ are masked out from the $\chi$ map. Note that the point sources visible in the lower right and upper right corner of the data are masked out in the $\chi$ map. Here we do not grow the masked regions and therefore a small fraction of the light from the other point sources still contribute to the map. . . . .	178
5.7 Same as Figure 5.6 but showing a different patch of sky. . . . .	179
5.8 Same as Figure 5.6 but showing a different patch of sky. Two nearly overlapping faint point sources are present in this patch. The clipping algorithm masks out the second star. Since we do not grow the masking regions in this example, it is likely that the second faint star could still have slight contribution to the $\chi$ map. . . . .	180
5.9 Same as Figure 5.6 but showing a different patch of the sky and and a PSF diffraction spike from a nearby source whose centroid is not in the patch. The clipping algorithm masks out most of the pixels that are affected by the PSF tail from an external source. Once again, this demonstrates the need to adopt the more conservative masking algorithm that grows the clipped regions in every direction. . . . .	181

5.10 Same as Figure 5.6 but showing a different patch of sky and a more <i>conservative</i> clipping algorithm. Masked regions containing the pixels with $\chi_{\text{clip}}^2 > 3$ are grown in every direction with one pixel. . . . .	182
5.11 Same as Figure 5.10 but showing a different patch of sky. The more <i>conservative</i> clipping algorithm masks out pixels that are ill-fit given the downsampled PSF model given by Eq. 5.2. . . . .	183
5.12 Same as Figure 5.10 but showing a different patch of sky. Note that the pixels along the lower tails of the PSF receive light contribution from other point sources and are masked out in the $\chi$ -map. . . . .	184

# List of Tables

2.1 <b>Prior Specifications:</b> The prior probability distribution and its range for each of the Zheng et al. (2007) HOD parameters. All mass parameters are in unit of $h^{-1}M_{\odot}$ . . . . .	72
3.1 <b>Prior Specifications:</b> The prior probability distribution and its range for each of the parameters. All mass parameters are in unit of $h^{-1}M_{\odot}$ . The parameters marked by * are only used in the Heaviside Assembly bias modeling and by definition are bounded between -1 and 1. . . . .	106
3.2 <b>Constraints:</b> Constraints on the parameters of the HOD models with and without assembly bias. All mass parameters are in unit of $h^{-1}M_{\odot}$ . The best-estimates and the error bars correspond to the 50% quantile and 68% confidence intervals obtained from the marginalized posterior probability pdfs. The last column is $\chi^2$ per degrees of freedom ( <i>dof</i> ), where $dof = N_{data} - N_{par}$ . . . . .	115
5.1 <b>Source Extraction:</b> Source Extractor configuration file for extraction of the point sources from the <i>HST WFC3 IR</i> . . . . .	161

# Introduction

Cosmology is entering a new era. Thanks to the ongoing and the upcoming low redshift galaxy surveys as well as the early universe probes, we are able to put cosmological theories into test with high precision. With the observations of the cosmic microwave background (CMB) radiation and the distant Type Ia supernovae, our understanding of universe was revolutionized in the late 90s. Later datasets advanced our understanding of the universe even further.

The early universe was in a hot and dense state where matter and radiation formed a primordial plasma. Eventually, the plasma cooled down, first atoms formed and photons started streaming freely. Today, we can observe these ancient photons as a microwave background radiation. The temperature of this radiation is approximately  $2.7\text{ K}$  in all directions with fluctuations that are 1 part in 10000.

In a strikingly great agreement with the CMB observations, models of inflation—nearly exponential rapid phase in the expansion of early universe—predict *nearly Gaussian and scale invariant* random fluctuations around a homogeneous background. Microscopic quantum fluctuations generated in an inflationary stage were stretched to cosmic volumes. Evolution of these initial seeds resulted in the formation of structures such as planets, stars, galaxies, clusters of galaxies, filaments, *etc.*

By measuring the brightness of supernovae type Ia, we have also learned that supernovae

Ia are fainter than what we expect them to be in an expanding universe filled with matter. This surprising observation led us to believe that approximately 70 % of the energy budget of the universe is given by a dark energy component which can be considered a liquid with negative pressure.

From a theoretical standpoint, cosmic acceleration can be explained in numerous modified gravity frameworks. Despite the astonishing success of general relativity in certain regimes such as the solar system, binary pulsars, and gravitational waves as a result of merging supermassive blackholes, precision test of GR on large scales remains an active area of research. Current constraints on the accelerated expansion and growth of structure can not rule out with certainty some of the theories of modified gravity.

Detection of the Baryonic Acoustic Oscillation feature in clustering of galaxies further enhanced our understanding of the expansion history. Acoustic oscillations in the early universe plasma result in a sound wave that leaves an imprint with a characteristic scale on the perturbations in late time universe. Therefore the BAO provides a highly accurate estimate of the angular diameter distance and it provides a powerful probe of the geometry and expansion history of the universe.

In galaxy redshift surveys, the distances to galaxies can be estimated by the measured redshifts. The distance information provided by these surveys is distorted by the peculiar velocities of galaxies along the line of sight. These distortions are referred to as redshift space distortions (RSD). Redshift space distortions are highly sensitive probes of the growth of structure and contain additional cosmological information beyond what is provided by the BAO feature. Thus measurements of galaxy clustering with redshift surveys can constrain dark energy and laws of gravity.

The large datasets from galaxy surveys are analyzed by estimating the statistical summaries of the data and then interpreting them with the predictions from cosmological theo-

ries. This is formally done by writing down a likelihood function which is the probability of the observed data given the theoretical model under consideration. Cosmological likelihood functions are often assumed to have a Gaussian functional form. Given this assumption, the likelihood can be fully specified with three ingredients: a data vector which is estimated from observations, a mean model vector which is computed from the predictions of theoretical models, and an inverse covariance matrix.

Therefore, a crucial step in interpreting the data is computing the error covariance matrix. In fact, the quantity that we need to know precisely is the inverse covariance matrix (precision matrix) because it is this matrix that appears in the likelihood function. Modern cosmological analyses rely on computing the covariance matrix analytically, estimating the matrix from a large suite of simulations, or from internal resampling of the data.

Motivated by the pursuit of minimizing the effect of the noise properties of the precision matrix on cosmological parameter estimation, [Dodelson & Schneider \(2013\)](#); [Taylor et al. \(2013\)](#); [Taylor & Joachimi \(2014\)](#) derived a set of requirements on the number of independent mock simulations given the number of data points and the number of parameters in a given cosmological analysis. Assuming that the estimated covariance matrix follows a *Wishart* distribution, ([Sellentin & Heavens, 2016](#)) present a method for marginalizing over the precision matrix. They demonstrate that the resulting likelihood function is no longer Gaussian and instead follows a *t*-distribution.

[Dodelson & Schneider \(2013\)](#); [Sellentin & Heavens \(2017\)](#) demonstrate that a noisy estimate of the precision matrix constructed from insufficient number of simulated mocks can systematically bias the confidence intervals over the cosmological parameters. These findings place strict requirement on the number of mock catalogs for the ongoing and future galaxy surveys. In general, the number of mocks need to be much larger than the number of data points.

Common practices in analysis of deep imaging surveys are tomographic binning of the data and combining probes. In tomographic binning, the dataset is split into multiple redshift slices and the summary statistics of the data are estimated by correlating the data within each redshift slice and cross-correlating the data across multiple redshift slices. The size of the resulting data vector can be as large as a few hundred which makes the task of creating mock catalogs even more challenging.

Combining probes involves joint analysis of different cosmic probes such as galaxy positions and galaxy shears. Multi-probe analyses are more robust against systematic uncertainties (specially systematics that only affect one of the probes) and have more constraining power. Most modern surveys offer this great opportunity. One of the main obstacles a head of these efforts is the large data vector under investigation. Production of the covariance of this data vector requires many simulations which may not be feasible to provide.

Analytical covariance matrices on the other hand, are not as computationally demanding. Their inverse (precision matrix) is noise free. But the model approximations and assumptions used in these methods may not be sufficient for the accuracy requirements of precision cosmology. Analytical covariance matrices are considered to receive Gaussian and a non-Gaussian contributions. Assuming that the density field is a Gaussian random field, the Gaussian part of the covariance matrix is straightforward to compute ([Grieb et al., 2016](#); [Kalus et al., 2016](#); [Slepian et al., 2016b](#)).

Including the non-Gaussian part of the covariance matrix however, is necessary for accurate parameter estimation ([Takahashi et al., 2011](#); [Blot et al., 2016](#); [Chan & Blot, 2016](#)). Significant progress has been made in modeling the non-Gaussian contribution to covariance matrices based on perturbation theory and effective theories of large scale structure ([Mohammed & Seljak, 2014](#); [Mohammed et al., 2017](#)) or by adopting halo (virialized regions of matter overdensity) model ([Takada & Spergel, 2014](#); [Eifler et al., 2014](#)). Regardless of the

applicability of analytical covariance matrices in analyzing the survey data, production of simulated mocks remains an important step in *validation* and *calibration* of these analytical covariance matrices (Slepian et al., 2016b; Hildebrandt et al., 2017).

Considerable progress has been made in developing methods that take into account our prior beliefs about the of covariance matrices. By considering sparsity of the covariance matrix, Paz & Sánchez (2015); Padmanabhan et al. (2016) present methods to estimate the precision matrices with fewer mocks. Shrinkage methods (Pope & Szapudi, 2008; Joachimi, 2016) also require fewer simulations. Friedrich & Eifler (2017) presents a trick for expanding the precision matrix around a part that can be easily computed through analytical means and estimating the leading expansion terms with finite number of simulations.

One of the common tools for estimation of covariance matrices is internal resampling of the data such as jackknife and bootstrap. These estimators have been extensively used in analyses of galaxy clustering and galaxy-galaxy lensing (for example see Reid et al. 2014; Guo et al. 2016a; Shirasaki et al. 2016; Singh et al. 2016; Kwan et al. 2017). In certain cases when no reliable analytical or simulation-based estimate of the covariance is available, one could use these estimators. For instance in Chapter 3, for interpreting the SDSS DR7 galaxy clustering measurements, we make use of covariance estimates based on jackknife resampling of the data. But as Norberg et al. (2009); Friedrich et al. (2016) point out, data resampling methods do not faithfully capture the uncertainties of the data.

Precision estimation of the covariance matrix from mocks requires generation of a large number of mocks for a given analysis. This has led to development of *approximate methods* for mass production of galaxy and halo mock catalogs. Approximate methods rely on approximate gravity solvers for generating dark matter density fields with reasonable accuracy on large scales and statistical prescriptions for populating the dark matter density field with mock galaxies (see for example Manera et al. 2013; White et al. 2014; Chuang et al. 2015a;

Kitaura et al. 2016 and references therein). The state-of-the-art techniques for production of mock catalogs are QPM (White et al., 2014) and PATCHY (Kitaura et al., 2016). These methods were used in cosmological analyses of the SDSS III-BOSS final data release (Alam et al., 2016).

In the PATCHY method the density field is generated with perturbation theory. Then the expected number of galaxies in a cosmic volume given the density field is computed according to a biasing relation whose parameters are unknown. Finally, the number of galaxies is drawn from a negative binomial distribution which is a Poisson distribution with additional stochasticity. Chuang et al. (2015b) demonstrates that this approach is very powerful at reproducing the two-point and three-point statistics of galaxies with high accuracy toward mildly nonlinear regimes.

In Chapter 4, we address two limitations of this method: *bias estimation* and *accuracy on small scales*. We replace the perturbation theory-based gravity solver of the PATCHY code with the fast particle mesh (PM) method of Feng et al. (2016). The main difference between the Particle mesh implementations of Feng et al. (2016) and White et al. (2014) is that FastPM imposes exact large scale growth and thus it does not suffer from the loss of power on large scales as a result of using a limited number of time steps for solving equations of motion. We also introduce an automatic bias estimation method based on MCMC.

In comparison with the previous version of the code based on perturbation theory, our novel approach yields higher accuracy toward nonlinear scales for both two-point and three-point statistics. One of the main advantages of our approach is the following. In order to reach reasonable accuracy, the common approximate  $N$ -body methods (White et al., 2014; Feng et al., 2016; Izard et al., 2016) require a larger grid size than the number of particles. That is, the gravitational forces between the particles need to be calculated on a mesh (at least) twice larger than the number of particles (see also Chuang et al. 2015b; Monaco

2016) in order to resolve halos. We note that our effective bias prescription for populating the dark matter density field with halos bypasses this requirement and as a consequence, it significantly reduces the computational cost of generating mocks. Gravitational lensing of luminous sources (galaxies, CMB) can measure the state of the inhomogeneous matter density and the time-dependence of dark energy. Lensing of the light emitted by background faint galaxies by the intervening large scale structure results in very small but correlated distortions in the shapes of galaxies. This phenomenon is referred to as cosmic shear.

Cosmic shear studies are hurdled by a number of statistical uncertainties (unknown distribution of galaxy intrinsic morphologies) and systematics. The long list of systematic error budget of cosmic shear studies can in general fall into the following categories: uncertain distance (photometric redshift) information, and imperfect knowledge of intrinsic alignments of galaxies and non-linear matter power spectrum models, and image systematics.

Tomographic reconstruction of the distribution of dark matter with imaging surveys requires accurate distance information which is encoded in the redshifts of galaxies. The redshift that are estimated from the imaging surveys are usually uncertain as they are measured with coarse spectra in the form of a few magnitude numbers based on broadband photometry. These redshifts are called photometric redshifts and their accuracy depends on the number of broadband filters and the overlapping spectroscopic sample of galaxies (Bonnett et al., 2016; Choi et al., 2016; Leistedt & Hogg, 2016; Hildebrandt et al., 2017).

Intrinsic alignment of galaxies (IAs) also contaminate the cosmic shear signal. These IAs, if not accounted for, can significantly bias the cosmological parameter inference (Codis et al., 2015; Joachimi et al., 2015; Kirk et al., 2015; Krause et al., 2016). Cosmological interpretation of the cosmic shear signal requires an accurate knowledge of the nonlinear matter power spectrum (Sembolini et al., 2013; Eifler et al., 2015; Schaye, 2015; Joudaki et al., 2016; Kitching et al., 2016; Mead et al., 2016). Modeling the role of Baryonic feedback

and the accuracy of the emulators for nonlinear matter clustering remains an active area of research.

Perhaps the most widely and extensively studied sources of systematics in weak lensing are the image systematics which make the process of inferring the cosmic shear from noisy images of galaxies far from trivial. The light profile of galaxies is distorted with the atmosphere and telescope optics. The amount of distortion is captured in a kernel called the Point Spread Function (PSF). The size and shear of the background galaxies used in weak lensing studies is often smaller than those of the PSF, making the cosmic shear signal dominated by the PSF which is empirically estimated at the positions of stars and then interpolated to the positions of galaxies.

Furthermore, additional systematics arise from unrealistic models of galaxy light profile (Voigt & Bridle, 2010; Zuntz et al., 2013; Kacprzak et al., 2014), detector effects (Kannawadi et al., 2016; Jayaraman et al., 2016; Plazas et al., 2016), nonlinear dependence of galaxy ellipticities on the pixel data in the presence of noise that biases the shear *point estimates* (Melchior & Viola, 2012; Mandelbaum et al., 2015; Conti et al., 2017), and incorrect model of the PSF or inaccurate PSF interpolation (Rowe, 2010; Kuijken et al., 2015; Mandelbaum et al., 2015; Jarvis et al., 2016).

These systematics lead to shear calibration biases in the form of additive and multiplicative shear biases. For instance, an incorrect size or anisotropy in the PSF model can introduce a multiplicative bias shear. This bias gives rise to a spurious correlation function with the same order of magnitude as the cosmological signal.

The shear biases are either calibrated with realistic image simulations (Zuntz et al., 2013; Jee et al., 2016; Conti et al., 2017) or through cross correlation of the cosmic shear signal with other cosmic probes that do not suffer from the same biases (*e.g.* galaxy positions) (Liu et al., 2016; Schaan et al., 2016; Singh et al., 2017).

Simulation based techniques are limited due to difficulty in generation of realistic galaxy image simulations (Mandelbaum et al., 2015; Lanusse et al., 2017) and our limited ability to match the depth and detection limits of the imaging surveys (Hoekstra et al., 2016). The limitation of cross-correlation technique is that it makes strong assumptions about the assigning a single bias parameter to a large population of galaxies under consideration. The shear biases have been shown to be scale-dependent (Jarvis et al., 2016; Jee et al., 2016) and depend on morphological properties of galaxies (Zuntz et al., 2013; Conti et al., 2017).

Novel shear inference models that do not rely on delivering a point-estimate for the shear signal (Schneider et al., 2015; Bernstein et al., 2016; Huff & Mandelbaum, 2017; Sheldon & Huff, 2017) provide promising venues for mitigation of biases but their accuracy is limited to the accuracy in the PSF model. In chapters 1 and 5, we try to address two challenges in accurate PSF modeling that could lead to biases in cosmological weak lensing analysis.

One of the steps of astronomical image processing that could lead to inaccurate model of the PSF is centroiding of stars. An erroneous method for determination of the centroid of stars could lead to both inaccurate estimation of the PSF at the positions of stars and inaccurate PSF interpolation (Anderson & King, 2000; Lupton et al., 2001; Anderson & King, 2003; LSST Dark Energy Science Collaboration, 2012). Large astronomical surveys rely on approximate methods for centroiding the stars (Bertin & Arnouts, 1996; Lupton et al., 2001; Jarvis et al., 2016).

In chapter one we argue that in the presence of noise, there exist a lower bound on the error arising from centroiding methods. We show that this theoretically set lower bound, also known as the Cramér-Rao lower bound (Le Cam, 1953), is *almost* saturated by centroiding methods that rely on correlating the images of stars with the PSF or some approximation to the PSF. These centroiding methods are called matched-filter centroiding methods and in certain limits provide an approximation to the more accurate methods that rely on fitting a

model to the stars. In other words, the Cramér-Rao bound provides the minimum achievable information loss by an estimator and we show that under certain circumstances, matched-filter centroiding methods achieve this goal.

Additionally, weak lensing shear couples the short wavelength and long wavelength modes of the galaxy light profiles. Therefore estimation of the response of galaxy light profile to shear requires knowing the model of galaxy image with a resolution better than the PSF that the image of galaxy is convolved with.

In most space-based telescopes (Laureijs et al., 2011; Spergel et al., 2015), the detectors are designed to be large in order to yield wider field of view. That is, the detectors sample the light profile of the PSF at a low resolution. In such cases, a large fraction of the light of a given point source is captured by the pixel that contains the centroid of the point source. In other words, the PSF is *undersampled*.

Most galaxies of interest for weak lensing studies with these space-based weak lensing experiments are unresolved. As a consequence, estimating the shear from unresolved galaxy images requires knowing the the galaxy light profile model and the PSF at higher resolutions than the native pixel size of these telescopes (Rowe et al., 2011; Ngolè Mboula et al., 2016).

The filters in HST WFC3 IR channel have the most undersampled detectors among all HST filters. As such, HST WFC3 IR channel could benefit a lot from an accurate model of its super resolution PSF. In this chapter 5, we present the first generative forward model of stellar sources as observed by the HST camera. Unlike previous attempts at inferring the PSF model of HST WFC3, our model is data driven in that it makes use of the observed data and it presents a proper treatment of modeling in the presence of damaged pixels and overlapping point sources.

Galaxies are luminous tracers of the large scale structure. Thus study of galaxy clustering o understand the growth of structure is one of the key drivers of low redshift surveys.

Significant progress has been made in linking the observations of galaxies and our theoretical understanding of the nonlinear evolution of dark matter.

On large scales, cosmological perturbation theory equipped with a prescription for galaxy bias permits us to accurately model the clustering of galaxies. However, nonlinear evolution of matter poses a challenge to applicability of perturbative approaches in small scales. In such limits, galaxy clustering must be understood within the context of the halo model which has had much success in describing time evolution of the clustering of matter.

Modeling galaxy clustering with the halo model follows two central assumptions. *First*, galaxies form in virialized regions of dark matter overdensity known as halos. *Second*, clustering of galaxies is governed by clustering of dark matter halos. In order to use galaxy clustering measurements for gaining insight into cosmological structure formation models we need to know how clustering of galaxies can be determined from clustering of halos. That is, we are required to specify how halos are populated with galaxies (Seljak, 2000; Scoccimarro et al., 2001; Berlind & Weinberg, 2002).

One of the successful prescriptions for assignment of galaxies to halos is the halo occupation distribution (HOD). HOD provides a prescription for the expected number of galaxies that reside a halo as well as the positions and velocities of galaxies that are distributed within a halo. It usually assumes that the halo mass alone is sufficient halo property for characterization of this prescription. This simple assumption has been useful in reproducing the observed statistics of galaxies (Tinker, 2007; Zehavi et al., 2011; Zheng & Guo, 2016).

Despite being successful at reproducing a wide range of the spatial statistics of galaxies, the simple *mass-only* HOD remains challenged by a theoretical phenomenon known as assembly bias. Assembly bias, seen in  $N$ –body simulations, states that at a fixed halo mass, clustering of halos depend on halo properties beyond mass such as their formation history, gravitational potential, *etc.* (Wechsler et al., 2006; Gao & White, 2007; Zentner et

al., 2014; Sunayama et al., 2016). This theoretical prediction has not yet been confirmed with observations and there are very mixed results in the literature.

By weak lensing analysis of the galaxy groups in GAMA (GAlaxy and Mass Assembly, see Driver et al. 2011) with the KiDS (Kilo Degree Survey, see Kuijken et al. 2015) imaging data, Dvornik et al. (2017) find no evidence for halo assembly bias. Using the galaxy-galaxy lensing and clustering measurements of SDSS galaxy *redmapper* clusters (Rykoff et al., 2014) with halo masses  $10^{14} M_{\odot}$ , Miyatake et al. (2016) claimed strong difference between the bias of two populations of clusters with different radial distribution of satellite galaxies (a proxy for the formation history of a dark matter halo). Zu et al. (2016) argues that the findings of Miyatake et al. (2016) is most likely due to projection effects (as a result of highly uncertain photometric redshifts) and they cannot be interpreted as detection of assembly bias.

The effect of assembly bias on galaxy clustering can be seen in many subhalo abundance matching (SHAM, see Hearin et al. 2014; Lehmann et al. 2017 and references therein) methods. SHAM assumes a one-to-one relation between halo (including subhalos) properties (*eg.* mass, circular velocity) and some galaxy properties (*eg.* stellar mass, luminosity). In Chapter 3, with the clustering measurements of SDSS DR7 main sample of galaxies (Abazajian et al., 2009) and the Small MultiDark  $N$ -body simulation, we show that the clustering predictions of (Hearin et al., 2016b) HOD model that takes assembly bias into account are consistent with the predictions of the *mass-only* HOD model within  $1-\sigma$  level.

We also note that for the sample of  $L_{\star}$  galaxies, there is *slight* improvements in galaxy clustering predictions of the HOD model with assembly bias on large scales. Furthermore, we note that in terms of information criteria, there is no gain in using a more complex HOD model to fit the clustering measurements. We note that in terms of the impact of halo assembly bias on galaxy clustering, our constraints show qualitatively similar behavior to the predictions of subhalo abundance matching models. Unlike the findings of Zentner et al.

(2016), we do not find any evidence for assembly bias in the satellite population of galaxies.

One of the perplexities faced by contemporary cosmology is the discordance between the constraints on cosmological parameters from some of the low redshift probes and the Planck CMB results (Planck Collaboration et al., 2016a). This includes the cosmological constraints from the cosmic shear analysis of CFHTLenS (Heymans et al., 2013; Kitching et al., 2016) and KiDs (Hildebrandt et al., 2017). The disagreement appears in the constraints over the parameters  $\sigma_8$  (the amplitude of the linear matter power spectrum) and  $\Omega_m$  (the amount of matter). This tension exists at a  $2\sigma$  level.

This *cosmic discordance* persists even when the low redshift probe under consideration is galaxy-galaxy lensing which contains information regarding galaxy-matter cross correlation. Similar to galaxy clustering, modeling the small scale galaxy-galaxy lensing signal requires assuming a halo model. This signal is an estimate of the lensing of the background galaxies from a *deep* imaging survey and the foreground galaxies in a *shallow* spectroscopic survey.

The galaxy-galaxy lensing measurements of SDSS III/BOSS (Miyatake et al., 2015; Leauthaud et al., 2017) are not consistent with the predictions of best-fit Planck cosmology (Planck Collaboration et al., 2016a). The  $\sigma_8$ - $\Omega_m$  constraint from clustering and galaxy-galaxy lensing measurements of BOSS galaxies (More et al., 2015) does not match the Planck constraint. This disagreements also holds for the cosmological constraints—assuming a simple mass only HOD model—from the clustering and galaxy-galaxy lensing measurements of SDSS DR7 main sample (Cacciato et al., 2013). These discrepancies could signal a new physics that we are missing in our picture of cosmology. But it could also be caused by observational systematics or uncertainties arising from the galaxy formation physics, including *assembly bias*.

Combining the early universe probes of cosmology and large scale structure requires accurate characterization of systematics and nuisance parameters in both datasets. In the context

of large scale structure, models governing the galaxy-halo connection serve as nuisance parameters that we marginalize over. A possible source of uncertainty in characterization of galaxy-halo connection is assembly bias. In order to distinguish between scenarios pointing at potentially new physics and systematics, it is important to study the effect of halo assembly bias on low redshift cosmological probes including galaxy clustering and galaxy-galaxy lensing. In Chapter 3, we take a step toward better understanding the impact of this phenomenon.

Cosmological inferences rely on assuming a functional form for the likelihoods. For instance, interpretation of the two-point correlation functions of galaxy shears or galaxy positions is done through assuming a multivariate Gaussian likelihood and interpreting the Cluster number counts is done through a Poisson likelihood. Therefore common practices in cosmology make strong assumptions about the underlying distribution of the *estimated* observables.

This fundamental assumption may not hold in detail and a robust test of this assumption can only be done with a large number of realistic and accurate mock catalogs. One might expect the Gaussian assumption in large scale structure studies to break down in certain regimes. One of the common arguments for the Gaussianity assumption is the central limit theorem. That is, a sufficiently large copies of random variables, Fourier modes of the density field in the cosmological context, are Gaussian distributed. The central limit theorem may not be applicable on the very large scales where there are very few Fourier modes. Nonlinear evolution of the density field on small scales may also break down this assumption.

The presence of systematics such as missing data as a result of fiber collision, selection effects, incompleteness due to color-magnitude cuts, or catastrophic redshift failures (Guo et al., 2012; Ross et al., 2012; Hahn et al., 2017) could affect the distribution of the estimated summary statistics of the data in a nontrivial way that is difficult to model. Unconventional

observables beyond two-point statistics such as the group statistics are not very robust against methodological systematics such as group identification (see [Berlind et al. 2006](#); [Campbell et al. 2015](#)). Modeling such systematics in an explicit likelihood analysis may not be possible. A similar summary statistics in the context of weak lensing are the convergence peak counts. Convergence peak counts can, in principle, deliver competitive cosmological constraints but they suffer from systematic uncertainties ([Lin et al., 2016](#)) that are hard to model.

Furthermore as we have mentioned earlier, parameter estimation with cosmological datasets requires precise estimate of the sample variance in form of the covariance matrix. Estimation of the covariance matrix is computationally demanding ([Chuang et al., 2015b](#); [Harnois-Déraps & van Waerbeke, 2015](#)) and even in the presence of an estimate of it the form of the likelihood function can no longer be characterized by a Multivariate Gaussian distribution ([Sellentin & Heavens, 2016, 2017](#)). These problems can potentially lead to biases in cosmological parameter estimation.

On the other hand, parameter estimation can be done within the framework of Approximate Bayesian Computation (ABC) without explicitly specifying a likelihood function. In ABC, accounting for the likelihood function is implicitly done through a generative simulation-based inference and a distant metric that quantitatively measures the closeness of the observations and simulations ([Filippi et al., 2011](#); [Beaumont et al., 2008](#)). Accounting for systematics in the ABC approach is done by implementing them in the generative forward model of the data. For instance, the systematics associated with identification of galaxy groups can be built into the forward model that suffers from these group mis-identifications. Uncertain photometric redshifts in deep imaging surveys can be incorporated into the forward model of the data.

This approach also bypasses any assumption regarding the functional form of the un-

derlying distribution of the data. Regardless of how the estimated summary statistics are distributed, one could use the ABC method for inferring the parameters of interest. Dependence of the analysis on the precise knowledge of the precision matrix can be circumvented by accounting for the sample variance in the forward model. It is important to note that, the accuracy of this approach relies on the distance metric. Considerable care is needed in order to find and test a reliable distance metric which in general depends on the cosmological probe under consideration (Weyant et al., 2013; Lin & Kilbinger, 2015; Jennings & Madigan, 2016; Jennings et al., 2016).

In Chapter 2, we present the first application of ABC in the context of large scale structure. In particular, we show that this approach can be reliably used in order to constrain the galaxy-halo connection models with small-scale galaxy clustering and group statistics. Using a simulated data with known true HOD parameters, we show that one can use ABC to infer these true parameters. We show that observables beyond conventional two-point statistics such as the abundance of galaxy groups can robustly constrain the galaxy-halo connection parameters with ABC. More importantly, we make comparison between the performance of ABC equipped with Particle Monte Carlo sampling and Gaussian Pseudo-likelihood with MCMC sampling. We show that the constraints obtained from the two approaches are comparable and consistent within  $1-\sigma$  level, with the ABC-PMC results being slightly less biased when the abundance of galaxy groups is used as the summary statistics.

Furthermore, we discuss why the ABC-PMC method is advantageous in terms of implementing the sample variance and observational systematics in the forward model. We also point out the limitations of applying such technique to cosmological parameter estimation with galaxy clustering measurements of the modern galaxy surveys. We argue that the main computational bottleneck is going to be designing a forward model that includes all relevant observational systematics and complex structure formation models.

In this thesis, we try to address different aspects of solving a cosmological problem which is equivalent to specifying the following general form of likelihood:

$$\mathcal{L} = p(\mathbf{d} \mid \boldsymbol{\mu}, \mathbf{C}), \quad (1)$$

where  $\mathbf{d}$  is an estimated data vector,  $\boldsymbol{\mu}$  is a theoretical prediction, and  $\mathbf{C}$  is a covariance matrix that characterizes the uncertainties on the entries of the datavector. In Chapters 1 and 5, we try to address the systematic uncertainties that affect  $\mathbf{d}$  in weak lensing analyses. In Chapter 3 we attempt to address a source of uncertainty, *assembly bias*, that could impact certain cosmological predictions  $\boldsymbol{\mu}$ . In Chapter 4, we present a method for accurately simulating mock datasets needed for precise estimation of the error covariance matrices  $\mathbf{C}$  of galaxy clustering and its inverse. In Chapter 2, we investigate how one can bypass the need for specifying a functional form for the likelihood function  $p(\mathbf{d} \mid \boldsymbol{\mu}, \mathbf{C})$  and the challenges associated with it.

Chapter 1 of this thesis is based on a paper I wrote with David W. Hogg. The underlying ideas and the direction of this project were developed by David W. Hogg and me. All the codes and text for this chapter was written by me with significant edits and modifications received from David W. Hogg. Chapter 2 is based on a paper I wrote with ChangHoon Hahn, Kilian Walsh, Andrew Hearin, David W. Hogg, and Duncan Campbell. ChangHoon Hahn and I contributed equally to development of the bulk of the code and text for this project. Kilian Walsh had significant contributions to both coding and writing. Andrew Hearin and David Hogg contributed to writing of the paper and Duncan Campbell had some contribution to the code.

Chapter 3 is based on the paper I wrote with ChangHoon Hahn. All of the code and the text for Chapter 3 was written by me. ChangHoon Hahn contributed considerably to editing the text. I also received valuable comments from David W. Hogg, Alex I. Malz regarding

the text and from Andrew Hearin and Chia-Hsun Chuang regarding some of the technical details of the work. Chapter 4 is based on a paper I wrote with Francisco-Shu Kitauro, Yu Feng, Gustavo Yepes, Cheng Zhao, Chia-Hsun Chuang, and ChangHoon Hahn. The idea of Chapter 4 was developed through conversations between Francisco-Shu Kitauro, Yu Feng and myself. I wrote all the code and text, with some contribution to the text from Francisco-Shu Kitaura. For the computations related to this work, I received significant help from Francisco-Shu Kitauro, Yu Feng, Gustavo Yepes, Cheng Zhao, Chia-Hsun Chuang, and ChangHoon Hahn.

Chapter 5 has been developed in collaboration with Ross Fadely and David W. Hogg. Development of the code was done by me and under the supervision of Ross Fadely and David W. Hogg. All the text was written by me with edits by David W. Hogg.

All of the code that I have written for the computations in this thesis are publicly available *except* the PATCHY code which is being prepared for a public release. The codes for Chapters 1,2,3, and 5 are available at [github.com/mjvakili/centerer](https://github.com/mjvakili/centerer), [github.com/mjvakili/ccppabc](https://github.com/mjvakili/ccppabc), [github.com/mjvakili/gambly](https://github.com/mjvakili/gambly), and [github.com/mjvakili/supermean](https://github.com/mjvakili/supermean) respectively.

In Chapters 2,3, and 4 we used the suite of MultiDark cosmological  $N$ -body simulations made publicly available in the CosmoSim database <sup>1</sup>. The CosmoSim database used in this paper is a service by the Leibniz-Institute for Astrophysics Potsdam (AIP). The MultiDark database was developed in cooperation with the Spanish MultiDark Consolider Project CSD2009-00064.

In Chapter 3, we used the measurements done with the SDSS DR7 <sup>2</sup> data ([Abazajian et al., 2009](#)). Funding for the SDSS and SDSS-II has been provided by the Alfred P.

---

<sup>1</sup><https://www.cosmosim.org>

<sup>2</sup><http://classic.sdss.org/dr7/>

Sloan Foundation, the Participating Institutions, the National Science Foundation, the U.S. Department of Energy, the National Aeronautics and Space Administration, the Japanese Monbukagakusho, the Max Planck Society, and the Higher Education Funding Council for England. The SDSS Web Site is <http://www.sdss.org/>. The SDSS is managed by the Astrophysical Research Consortium for the Participating Institutions. The Participating Institutions are the American Museum of Natural History, Astrophysical Institute Potsdam, University of Basel, University of Cambridge, Case Western Reserve University, University of Chicago, Drexel University, Fermilab, the Institute for Advanced Study, the Japan Participation Group, Johns Hopkins University, the Joint Institute for Nuclear Astrophysics, the Kavli Institute for Particle Astrophysics and Cosmology, the Korean Scientist Group, the Chinese Academy of Sciences (LAMOST), Los Alamos National Laboratory, the Max-Planck-Institute for Astronomy (MPIA), the Max-Planck-Institute for Astrophysics (MPA), New Mexico State University, Ohio State University, University of Pittsburgh, University of Portsmouth, Princeton University, the United States Naval Observatory, and the University of Washington.

In Chapter 5, all of the HST archival data were obtained from the Mikulski Archive for Space Telescopes (MAST)<sup>3</sup>. STScI is operated by the Association of Universities for Research in Astronomy, Inc., under NASA contract NAS5-26555.

Bulk of the computations in this work were carried out on the Mercer cluster which is part of the New York University High Performance Computing facilities<sup>4</sup>. For a fraction of computations performed for this thesis, I acknowledge the use of machines in Center for Cosmology and Particle Physics<sup>5</sup> and the computing resources provided by MareNostrum

---

<sup>3</sup><https://archive.stsci.edu>

<sup>4</sup><https://wikis.nyu.edu/display/NYUHPC/Clusters---Mercer>

<sup>5</sup><http://ccpp.nyu.edu>

Cosmological Project <sup>6</sup>.

---

<sup>6</sup><http://astro.ft.uam.es/marenostrum/>

# Chapter 1

## Fast stellar centroiding and saturation of the Cramer-Rao lower bound

This Chapter is joint work with David W. Hogg (NYU) and it is submitted to the *Astronomical Journal*.

### 1.1 Chapter abstract

One of the most demanding tasks in astronomical image processing—in terms of precision—is the centroiding of stars. Upcoming large surveys are going to take images of billions of point sources, including many faint stars, with short exposure times. Real-time estimation of the centroids of stars is crucial for real-time PSF estimation, and maximal precision is required for measurements of proper motion.

The fundamental Cramér-Rao lower bound sets a limit on the root-mean-squared-error achievable by optimal estimators. In this work, we aim to compare the performance of various centroiding methods, in terms of saturating the bound, when they are applied to relatively

low signal-to-noise ratio unsaturated stars assuming zero-mean constant Gaussian noise. In order to make this comparison, we present the ratio of the root-mean-squared-errors of these estimators to their corresponding Cramér-Rao bound as a function of the signal-to-noise ratio and the full-width at half-maximum of faint stars.

We discuss two general circumstances in centroiding of faint stars: (i) when we have a good estimate of the PSF, (ii) when we do not know the PSF. In the case that we know the PSF, we show that a fast polynomial centroiding after smoothing the image by the PSF can be as efficient as the maximum-likelihood estimator at saturating the bound. In the case that we do not know the PSF, we demonstrate that although polynomial centroiding is not as optimal as PSF profile fitting, it comes very close to saturating the Cramér-Rao lower bound in a wide range of conditions. We also show that the moment-based method of center-of-light never comes close to saturating the bound, and thus it does not deliver reliable estimates of centroids.

## 1.2 Introduction

Accuarate estimates of the centers of point sources, which are convolved with telescope point spread function (PSF), and atmospheric PSF in case of ground based telescopes, and the pixel response function, are crucial to further steps of astronomical image processing. For instance, proper measurement of the shapes of galaxies requires interpolation of the PSF estimates from the positions of stars across the image to the positions of galaxies. At the position of each star, the PSF is estimated by sub-pixel shifting of the star so that the PSF is centered on its centroid. If the sub-pixel shifts are wrong, then the PSF estimates will be biased. Moreover, measurements of the parallaxes and the proper motions of stars depend on how well we can measure their centroids.

Ideally, we want a centroiding procedure that provides measurements as precise as possible without putting a huge computational burden on the photometric pipeline. Reducing the computational cost becomes even more important in large surveys, where we want to estimate the centroids of thousands of point sources detected on the telescope’s focal plane, for various real-time applications.

The Cramér-Rao lower bound (CRLB) sets a lower limit on the root-mean-squared error of estimators. When the root-mean-squared error arising from an estimator approaches the bound, the bound is saturated by that estimator. In this paper, we study the optimality of various techniques for centroiding faint, unsaturated stars. Our requirement for optimality is saturation of the theoretically-set lower bound, known as the Cramér-Rao lower bound, by the centroiding methods considered in this study.

We apply a number of centroiding methods to a large number of simulated faint stars, assuming uncorrelated Gaussian noise, with different signal-to-noise ratio and size realizations. The Cramér-Rao lower bound has an inverse relation with the signal-to-noise-ratio of stars. In the context of astrometry, the Cramér-Rao lower bound saturation for least-squares estimators has been tested in specific limits in which the centroiding bias is negligible ([Lobos et al. 2015](#)).

Saturating the Cramér-Rao lower bound in estimating the centroids of stars however, is limited by the lack of knowledge about the exact shape of the PSF and presence of noise. There are many sources of noise such as the CCD readout noise, sky noise, errors resulting from incorrect flatfield corrections, and photon noise from the astronomical object itself. In this study, we limit our investigation to the simulated images that contain non-overlapping faint sources that are sky-limited.

We focus the scope of this investigation to sky-limited images for which the sky level has been subtracted. Furthermore, we assume that any instrument gain has been calibrated out

and that the simulated images are free of any contamination by cosmic rays, stray light from neighboring fields, or any other type of defect in real images. We expect these defects to move the centroiding errors further from the fundamental bound. We intend to investigate whether fast centroiding estimates can saturate the bound in a realistic range of low signal-to-noise ratio images that are sky-limited.

Given an analytic expression for the PSF model adopted in this study, we derive an expression for the fundamental lower bound on the centroiding error as a function of the parameters of the PSF model (e.g. PSF size), and signal-to-noise-ratio of stars. We create two sets of simulations for which we can compute the CRLB, one with variable signal-to-noise ratio and constant full width at half maximum (FWHM), and one with variable FWHM and constant signal-to-noise ratio. After applying different centroiding methods to the simulations, we investigate how close these methods can get to saturating the CRLB for various ranges of background Gaussian noise level and PSF FWHM.

In this work, we focus on four centroiding methods. The first method is the maximum-likelihood estimator which involves fitting a PSF profile, assuming that we have a good PSF estimate, to the star. The second method estimates the centroid of a star by fitting a 2d second-order polynomial to the  $3 \times 3$  patch around the brightest pixel of the image after convolution with the PSF. The third method centroids stars by smoothing the image of stars by a Gaussian kernel of a fixed size, and then applying the same  $3 \times 3$  polynomial trick to the smooth image. This method is fast and does not require any knowledge of the PSF. The last method we consider, is a center-of-light centroiding (measurement of a first moment), applied to the  $7 \times 7$  patch around the brightest pixel of the image.

This paper is structured as follows. In Section 1.3, we discuss the Cramér-Rao lower bound and derive an analytic expression for the lower bound on the centroiding error of the simulated data. In Section 1.4 we give a brief overview of centroiding methods used in our

investigation. In Section 1.5 we discuss the Cramér-Rao lower bound saturation tests and their corresponding simulated data. In Section 1.6, we compare the performances of the methods discussed in Section 1.4 with the CRLB derived in Section 1.3. Finally, we discuss and conclude in Section 1.7.

## 1.3 The Cramér-Rao lower bound

The Cramér-Rao lower bound sets a limit, in some sense, on how well a measurement can be made in noisy data. The bound can only be computed in the context of a generative model, or a probabilistic forward model of the data. That is, we can only compute the CRLB in the context of assumptions about the properties of the data. However, it makes sense for us to use centroiding methods that saturate the CRLB under some reasonable assumptions, even if we find that those assumptions are not strictly correct in real situations.

The closer an estimator is to saturating the CRLB, the more information about the quantity that we need to estimate is preserved. The closer the root-mean-squared-error (RMSE) of a given estimator is to the bound, the more optimal—in terms of preserving the information—the estimator is.

The Cramér-Rao inequality (Doob, 1946) sets a lower bound on the root-mean-squared error of unbiased estimators. The CRLB is given by the square-root of the inverse of the Fisher information matrix  $\mathcal{F}$ . Thus, in order to find the CRLB, it is sufficient to compute the Fisher matrix. This computation relies on a set of assumptions:

- Known PSF model. In this work the presumed model is the Moffat PSF profile.
- Known, stationary noise process. In the context of centroiding stars, this is equivalent to having background limited noise from sky background and CCD readout noise.

- Images are calibrated correctly. Flat-field is correctly calibrated.
- Uncorrelated Gaussian noise with no outliers.

Note that in this study, we explicitly focus on sky-limited images. In the sky-limited images, the contribution to the Poisson pixel noise is largely dominated by the sky rather than the objects. In sky-limited images, when the number of photons per pixel is large, the Poisson noise can be approximated by a Gaussian distribution. Therefore, the Gaussian noise assumption is only an approximation to the Poisson noise. This is a good approximation for a large set of astronomical images.

A number of factors can produce correlation between pixels. These include detector imperfection, saturation, and post-processing of images such as smoothing, rotating, and shifting the images. In raw unsaturated images, pixel noise is close to uncorrelated. Instrument gain can introduce heteroscedasticity. In that case, the noise variance varies between pixels. In an upcoming publication on the inference of the HST WFC3-IR channel PSF (Vakili *et al.*, in preparation), we discuss proper treatment of centroiding in the presence of gain. For simplicity, we assume that per-pixel uncertainty remains constant across all pixels.

Let us assume that there are  $M$  observables  $\mathbf{f} = (f_1, \dots, f_M)$ , each related to  $B$  model parameters  $\boldsymbol{\theta} = (\theta_1, \dots, \theta_B)$

$$f_m = f_m(\theta_1, \dots, \theta_B). \quad (1.1)$$

Assuming uncorrelated Gaussian error with variance  $\sigma_m^2$  for each observable  $f_m$ , elements of the  $B \times B$  Fisher matrix  $\mathcal{F}_{ij}$  are given by

$$\mathcal{F}_{ij} = \sum_{m=1}^M \frac{1}{\sigma_m^2} \frac{\partial f_m}{\partial \theta_i} \frac{\partial f_m}{\partial \theta_j} \quad (1.2)$$

Let us assume that we have computed the root-mean-squared error on the parameter  $\theta_i$

arising from applying an estimator to a large number of data. The Cramér-Rao inequality states that this root-mean-squared error is greater than or equal to the  $i$ -th diagonal element of the inverse of the Fisher information matrix:

$$\text{RMSE} \geq \sqrt{[\mathcal{F}^{-1}]_{ii}}, \quad (1.3)$$

where the left hand side of the inequality is called the Cramér-Rao bound on the root-mean-squared error of estimating the parameter  $\theta_i$ . Note that the bound is computed assuming that the model (equation 1.1) generating the data is known, and that uncertainties are given by additive uncorrelated Gaussian noise.

Based on Cramér-Rao inequality (1.3), Doob (1946) defines efficiency of optimal estimators as the ratio of the CRLB and the root-mean-squared-error such that the maximum efficiency achievable by an estimator is unity. The closer the RMSE to the CRLB, the more information about the parameter of interest is preserved, and thus the more efficient the estimator is.

Let us consider the case of a maximum likelihood estimate  $\boldsymbol{\theta}_{\text{ML}}$ , where the likelihood function corresponds to the same generative assumptions that we used to compute the CRLB.

$$\boldsymbol{\theta}_{\text{ML}} = \text{argmax} \mathcal{L}, \quad (1.4)$$

$$-2 \ln \mathcal{L} = \sum_m \frac{1}{\sigma_m^2} (y_m - f_m(\boldsymbol{\theta}))^2, \quad (1.5)$$

$$(1.6)$$

where  $y_m$  is the  $m$ th component of the observed data  $\mathbf{y}$

$$\mathbf{y} = \mathbf{f}(\boldsymbol{\theta}_{\text{true}}) + \mathbf{n}. \quad (1.7)$$

Maximum likelihood estimators can achieve maximum efficiency. That is, when a maximum likelihood estimator is applied to a large number of data and RMSE is computed, the RMSE approaches the CRLB (see [Doob 1946](#); [Le Cam 1953](#) for proof) in which case the CRLB is saturated. Therefore, we want to investigate the conditions under which the RMSE arising from a given fast centroiding method is close to the CRLB, or whether it can saturate the CRLB.

In this investigation, the model observables for the noisy data are the pixel-convolved PSF (PSF profile evaluated at different pixel locations), and the model parameters under consideration are the centroid coordinates. Therefore,  $\mathcal{F}$  is a  $2 \times 2$  matrix whose elements are given by

$$\mathcal{F}_{ij} = \sum_m \frac{1}{\sigma^2} \frac{\partial f_m}{\partial \theta_i} \frac{\partial f_m}{\partial \theta_j}, \quad (1.8)$$

where the summation is over pixels,  $f_m$  is the value of the PSF at pixel location  $m$ ,  $\theta = \{x_c, y_c\}$ , and  $\sigma^2$  is variance of the uncorrelated Gaussian noise map  $n(\mathbf{x}_m)$

$$\mathbb{E}[n(\mathbf{x}_m)] = 0, \quad (1.9)$$

$$\mathbb{E}[n(\mathbf{x}_m)n(\mathbf{x}_{m'})] = \sigma^2 \delta_{m,m'}. \quad (1.10)$$

Derivation of an explicit expression for the Fisher matrix  $\mathcal{F}$  requires specifying a presumed correct PSF model. We use the Moffat profile ([Trujillo et al., 2001](#)) for our PSF simulations. The Moffat profile is an analytic model for stellar PSFs. It has broader wings than a simple Gaussian profile. The surface brightness of the Moffat profile is given by

$$I(r) = \frac{F(\beta - 1)}{\pi \alpha^2} [1 + (r/\alpha)^2]^{-\beta}, \quad (1.11)$$

where  $F$  is the total flux,  $\beta$  is a dimensionless parameter, and  $\alpha$  is the scale radius of the Moffat profile, with FWHM (hereafter denoted by  $\gamma$ ) being  $2\alpha\sqrt{2^{1/\beta}-1}$ . The Moffat PSF profile has been used in the PSF modeling required for weak lensing galaxy shape measurements (see Zuntz et al. 2013, 2014). It has also been used as one of the methods for generation of the PSF in simulation of images needed for weak lensing systematic studies (Rowe et al. 2015). At a fixed  $\gamma$ , Moffat profiles with lower values of  $\beta$  have broader tails. It is also important to note that for sufficiently large values of the parameter  $\beta$ , the Moffat PSF becomes arbitrarily close to a simple Gaussian PSF.

Note that in our data generation, we simulate images (in the pixel space) that are Nyquist-sampled or close to Nyquist-sampled. All pixels in the images are identical, and the stars are simulated by sampling from the pixel-convolved PSF. In well-sampled images, the center of the pixel-convolved PSF must be very close to the center of the optical PSF.

In order to investigate the performance of centroiding methods for different background noise levels and different values of the parameter  $\gamma$ , simulation of a large number of images of stars—for which the exact positions of centroids and their corresponding lower bounds are known—is required.

Given the PSF model (1.11), an expression for the CRLB as a function of the size, and SNR of stars can be derived. For further simplicity, the flux of all stars in our simulations are set to unity and per-pixel uncertainties are assumed to be uncorrelated Gaussian.

Moreover, it is more convenient to work with the signal-to-noise ratio (SNR) instead of the variance of the Gaussian noise. We use the definition of SNR according to which SNR is given by the ratio of the mean and variance of the distribution which the flux estimator is drawn from. Assuming that the total flux from the point source is  $F$ , and that the sub-pixel shifted PSF at the  $i$ -th pixel is given by  $P_i$ . Therefore the brightness of the  $i$ -th pixel  $y_i$  is

drawn from a Gaussian distribution

$$p(y_i) = \mathcal{N}(FP_i, \sigma^2). \quad (1.12)$$

The optimal estimator of flux is the matched-filter flux estimator  $\tilde{F} = \sum_i y_i P_i$ . It can be shown that

$$p(\tilde{F}) = \mathcal{N}\left(F, \frac{\sigma^2}{\sum_i P_i^2}\right), \quad (1.13)$$

which leads us to

$$\text{SNR} = \frac{F\sqrt{\sum_i P_i^2}}{\sigma}. \quad (1.14)$$

In the case of Moffat profiles (1.11) with total flux of stars set to unity, the SNR given in (1.14) can be analytically expressed in terms of the per pixel uncertainty  $\sigma$ , FWHM  $\gamma$ , and also  $\beta$ , the dimensionless parameter of (1.11)

$$\text{SNR} = \frac{2(\beta - 1)(2^{1/\beta} - 1)^{1/2}}{\pi^{1/2}(2\beta - 1)^{1/2}} \frac{1}{\sigma\gamma}. \quad (1.15)$$

Equation (1.15) implies that at a fixed  $\gamma$  and background Gaussian noise with variance  $\sigma^2$ , stars with broader tails (lower  $\beta$ ) have a lower SNR. On the other hand, stars with higher  $\beta$  have higher SNR. For sufficiently large  $\beta$ —where the PSF can be approximated by Gaussian profile—SNR is approximately given by  $0.664/(\sigma\gamma)$ . Furthermore, at a fixed  $\beta$  and variance of the background noise  $\sigma^2$ , observed stars with higher  $\gamma$  have lower SNR.

Throughout this investigation,  $\beta$  is held fixed at the fiducial value of  $\beta = 2.5$ , where SNR is given by the following expression

$$\text{SNR} \simeq \frac{0.478}{\sigma\gamma} \quad \text{for } \beta = 2.5. \quad (1.16)$$

Given the analytic expression for the Moffat PSF model (1.11), and choice of  $\beta = 2.5$ , the inverse of the Fisher matrix is given by

$$\mathcal{F}^{-1} \simeq \left(0.685 \frac{\gamma}{\text{SNR}}\right)^2 \begin{pmatrix} 1 & 0 \\ 0 & 1 \end{pmatrix}. \quad (1.17)$$

Equation (1.17) implies that at given SNR and  $\gamma$ , CRLB for each component of centroid is approximately given by  $0.685\gamma/\text{SNR}$ , and that a good centroiding technique delivers centroids with root-mean-squared-error close to this.

It is worth noting that for any PSF model whose radial light profile is some function of  $r/\gamma$ , CRLB has the same functional form, in that it is proportional to the ratio between  $\gamma$  and the SNR. For PSF profiles with shorter tails (e.g., Gaussian), the prefactor of 0.685 in (1.17) becomes smaller. In the particular case of Gaussian PSF, the prefactor is approximately 0.6.

## 1.4 Centroiding methods

In this section, we briefly discuss the approximate and the non-approximate centroiding methods considered in this study. The first two methods require knowledge of the PSF at the position of star. That is, the shape and the size of the PSF is known and the only unknown variables are the coordinates of the centroids of stars. Note that in practice however, size and shape of the PSF are also estimated along with the centroid. In the following, we assume that the size and shape of the PSF are known. For the last two methods, we do not use any information about the PSF.

### 1.4.1 Centroiding by fitting a correct PSF profile

We examine fitting an exact PSF profile to the stars. That is, in our Cramér-Rao bound saturation tests, we find the best estimates of flux and centroid by maximizing the likelihood using the correct PSF model. In the model, the size of the Moffat PSF is assumed to be correct. We expect this method to perform best in determining the centroids of stars, and deliver RMSE equal to Cramér-Rao bound.

### 1.4.2 Matched-filter polynomial centroiding

Let us consider the case in which we have a good estimate of the pixel-convolved PSF at the position of the faint star under consideration. We can smooth the image of the star, by correlating it with the full PSF  $\mathcal{P}$  at the position of the star.

$$Y^{(s)} = Y \star \mathcal{P}, \quad (1.18)$$

$$Y_{[i,j]}^{(s)} = \sum_{k,l} Y_{[i-k,j-l]} \mathcal{P}_{[k,l]}, \quad (1.19)$$

where  $Y$  is the image of the star, and  $Y^{(s)}$  is sometimes called a matched filter. A matched filter is a method in which the data  $Y$  is correlated (convolved in the case of symmetrical PSF) with the PSF  $\mathcal{P}$ . It is equivalent to optimizing the likelihood and therefore provides an optimal map where the peak of the map is the likely position of the point source (Lang *et al.*, in preparation).

Then, we fit a simple 2d second-order polynomial  $P(x, y) = a + bx + cy + dx^2 + exy + fy^2$  to the  $3 \times 3$  patch centered on the brightest pixel of the matched-filter image  $Y^s$ . Upon

constructing a universal  $9 \times 6$  design matrix

$$\mathbf{A} = \begin{bmatrix} 1 & x_1 & y_1 & x_1^2 & x_1y_1 & y_1^2 \\ \cdot & \cdot & \cdot & \cdot & \cdot & \cdot \\ \cdot & \cdot & \cdot & \cdot & \cdot & \cdot \\ \cdot & \cdot & \cdot & \cdot & \cdot & \cdot \\ 1 & x_9 & y_9 & x_9^2 & x_9y_9 & y_9^2 \end{bmatrix}, \quad (1.20)$$

the free parameters  $\{a, b, c, d, e, f\}$  (hereafter compactly denoted by  $\mathbf{X}$ ) can be determined by

$$\mathbf{X} = (\mathbf{A}^T \mathbf{A})^{-1} \mathbf{A}^T \mathbf{Z}, \quad (1.21)$$

where  $\mathbf{Z}$  is given by  $(z_1, \dots, z_9)^T$ , with  $z_i$ , being the brightness of the  $i$ -th pixel of the  $3 \times 3$  patch centered on the brightest pixel of  $Y^{(s)}$ . Afterwards, the best fit parameters can be used to compute the centroid coordinate

$$\begin{bmatrix} x_c \\ y_c \end{bmatrix} = \begin{bmatrix} 2d & e \\ e & 2f \end{bmatrix}^{-1} \begin{bmatrix} -b \\ -c \end{bmatrix}. \quad (1.22)$$

It is important to note that the algebraic operation in (1.22) involves inverting a  $2 \times 2$  curvature matrix

$$D = \begin{bmatrix} 2d & e \\ e & 2f \end{bmatrix}. \quad (1.23)$$

When the curvature matrix  $D$  has a zero (or very close to zero) determinant, centroid estimates obtained from equation (1.22) can become arbitrarily large, which leads to catastrophic outliers. In order to tackle this issue, we add a soft regularization term proportional to  $\sigma$  to the diagonals of  $D$  prior to inversion.

The procedure of convolving the image of star with the PSF results in a smoother image. Therefore, a simple second-order polynomial will provide a better fit since convolution with the PSF makes the variation of the brightness of the image across the  $3 \times 3$  patch very smooth.

### 1.4.3 Fixed-Gaussian polynomial centroiding

In the case that we do not know the PSF at the position of star, we change the smoothing step in the following way. Instead of smoothing the image by convolving it with the PSF, smoothing is done by convolving the image with a fixed Gaussian kernel with a fixed size

$$k(\mathbf{x}) = \frac{1}{2\pi w^2} \exp(-\mathbf{x}^2/2w^2), \quad (1.24)$$

where throughout this study, the full-width at half-maximum of the Gaussian kernel is held at a fixed value of 2.8 pixels (corresponding to  $w \simeq 1.2$  pixels). The smoothing step is done as follows

$$Y^{(s)} = Y \star \mathcal{K}, \quad (1.25)$$

$$Y_{[i,j]}^{(s)} = \sum_{k,l} Y_{[i-k,j-l]} \mathcal{K}_{[k,l]}, \quad (1.26)$$

where  $Y$  is the image of the star,  $Y^{(s)}$  is the smooth image, and  $\mathcal{K}$  is an array whose elements are given by the Gaussian kernel

$$\mathcal{K}_{[k,l]} = k(x_k, y_l). \quad (1.27)$$

Note that the size of the kernel  $\mathcal{K}$  is equal to the size of the kernel  $\mathcal{P}$  used in the matched-filter polynomial centroiding. Then we apply the same 2d second-order polynomial method (see (1.21), (1.22)) to the  $3 \times 3$  patch centered on the brightest pixel of the smooth image

$Y^{(s)}$ . Therefore, for a given star and a smoothing kernel, the outcome of equation (1.21) can be plugged into equation (1.22) to find the centroid estimate of the star. This is inspired by the  $3 \times 3$  quartic approximation used in the *Sloan Digital Sky Surveys* photometric pipeline (Lupton et al., 2001).

#### 1.4.4 Center-of-light centroiding

In addition to the fitting methods mentioned so far, we examine centroiding stars by computing their first moments in a  $7 \times 7$  patch around the brightest pixel of the image.

$$x_c = \frac{\sum_m x_m Y_m}{\sum_m Y_m}, \quad (1.28)$$

$$y_c = \frac{\sum_m y_m Y_m}{\sum_m Y_m}, \quad (1.29)$$

where the summation is done over all the pixels of the  $7 \times 7$  patch, and  $x_m$ ,  $y_m$ , and  $Y_m$ , are the  $x$  coordinate,  $y$  coordinate, and the brightness of pixel  $m$  respectively.

In terms of saturating the Cramér-Rao lower bound, we expect this simple center-of-light centroiding to perform worse than all other methods mentioned in this section. Hereafter, we call this method  $7 \times 7$  moment centroiding.

## 1.5 Tests

We perform two sets of simulations. In the first set, we choose four values of 2, 2.8, 4, and 5.6 pixels for  $\gamma$ . For each  $\gamma$ , we generate 100,000  $17 \times 17$  postage-stamps of Moffat profiles with centroids randomly drawn within the central pixel of the  $17 \times 17$  postage-stamps. Moreover, zero-mean uncorrelated Gaussian noise is added to each postage-stamp such that

the simulated stars are uniformly distributed in log-SNR between SNR = 5 to SNR = 100.

In the second set, we generate 100,000  $17 \times 17$  postage-stamps of Moffat profile, with values of  $\gamma$  uniformly distributed between 2 and 6 pixels, and with centroids drawn randomly within the central pixel. We choose four values for SNR: 5, 10, 20, and 40. For each SNR, and for each postage-stamp with a given  $\gamma$ , zero-mean uncorrelated Gaussian noise, with standard deviation corresponding to SNR and  $\gamma$  through equation (1.15), is added to each postage-stamp.

In the first experiment, we study how the centroiding error behaves with changing SNR, while  $\gamma$  is held constant. In the second experiment, we study how the centroiding error behaves with changing  $\gamma$  while SNR is held constant.

## 1.6 Results

### 1.6.1 Experiment 1 : variable SNR; constant $\gamma$

In this experiment, after finding the centroiding errors for each method, we compute the RMSE in bins of SNR in order to compare it to the CRLB. Results of the first experiment are shown in Figures 1.1, 1.2, 1.3, 1.4. Note that the centroid errors, the CRLB, and the RMSE values shown in these figures are computed for only one component. As we expected, the RMSE from centroiding by fitting the exact PSF model (Figure 1.1) lies on the CRLB.

Figure 1.2 demonstrates that even the matched filter polynomial centroiding is able deliver centroiding estimates as efficient as the PSF fitting method in terms of saturating the bound for the simulated stars with  $\gamma = 2.8, 4, 5.6$  pixels. For stars with  $\gamma = 2$  pixels, although this method gets very close to saturating the CRLB, the RMSE arising from this method shows slight deviations from the CRLB since the images of stars are not sufficiently smooth even after correlation of these images with the PSF. For simulated images with higher  $\gamma$ ,

convolving the data with the PSF results in images that are smooth around the brightest pixel. This enables the polynomial centroiding to deliver estimates that can saturate the CRLB.

The RMSE from the fixed-Gaussian polynomial centroiding (Figure 1.3), is very close to the CRLB. As we increase  $\gamma$  from 2 pixels to 2.8 pixels, RMSE approaches the CRLB. For stars with  $\gamma = 2$  pixels, the rate at which the RMSE from this method drops eventually becomes smaller than the constant rate at which the CRLB decreases with increasing SNR. The reason for this is that even after smoothing the data with a Gaussian kernel, the images are not smooth enough for a second-order polynomial fitting to deliver estimates with RMSE close to the bound. For stars with  $\gamma = 2.8$  pixels, a significant fraction of information is in the  $3 \times 3$  patch of the smooth image and this method is able to saturate the bound. When we increase  $\gamma$  to 4 and 5.6 pixels, the mismatch between the width of the Gaussian kernel and the PSF increases and the RMSE deviates from the CRLB. The deviation is largest for the simulated stars with  $\gamma = 5.6$  pixels.

On the other hand, Figure 1.4 shows that in case of  $7 \times 7$  moment method, the RMSE becomes quite large as we move toward fainter stars in our simulation. For stars with larger  $\gamma$ , centroid estimates from the naive center-of-light centroiding do not even come close to saturating the CRLB. As  $\gamma$  increases, the RMSE deviates further from the CRLB.

### 1.6.2 Experiment 2 : constant SNR; variable $\gamma$

In this experiment, after finding the centroiding errors for each method, we compute the RMSE in bins of  $\gamma$  in order to compare it to the CRLB. Behavior of error as a function of  $\gamma$  for different values of SNR, is shown in Figures 1.5, 1.6, 1.7, and 1.8. Note that the centroid errors, the CRLB, and the RMSE values shown in these figures are computed for only one component.

Once again, the RMSE from centroiding by fitting the exact PSF model as a function of FWHM lies on the CRLB (see Figure 1.5). Thus, centroid estimates from fitting the exact PSF model always saturate the CRLB. Once again, we observe that the centroid estimates found by the matched filter polynomial centroiding saturate the CRLB with the exception of simulated stars with  $\gamma$  very close to 2 pixels (see Figure 1.6).

Figure 1.7 illustrates that the fixed-Gaussian polynomial method results in RMSE very close to the CRLB. For all four values of SNR, as we increase  $\gamma$  from 2 pixels to 3 pixels, the RMSE gets closer to the CRLB since the method starts to perform slightly better as we move away from undersampled stars and as the FWHM of the smoothing kernel gets closer to that of the simulated images. After approximately 3 pixels, increasing  $\gamma$  results in deviation of the RMSE of the method from the CRLB. This is a characteristic of the fixed-Gaussian polynomial method as we apply it to a smooth image in which some fraction of the available information is lost in the  $3 \times 3$  patch around the brightest pixel. Furthermore, increasing the SNR from 5 to 40 makes the RMSE (as a function of  $\gamma$ ) closer to the CRLB. In the case of extremely faint stars (SNR = 5), the fixed-Gaussian polynomial centroiding fails to saturate the bound.

The centroid estimates obtained from the naive  $7 \times 7$  moment method (see Figure 1.8) result in RMSE much larger than the CRLB in all ranges of FWHM and for all four values of SNR in this experiment.

## 1.7 Discussion

An efficient stellar centroiding algorithm must saturate—or come close to saturating—the fundamental Cramér-Rao lower bound. That is, in all ranges of background noise level, size, radial light profile, and shape, it must preserve information about the centroids of stars.

In practice however, this is only achievable when we have a reasonably good estimate of the PSF. Since we do not always know the exact PSF profile, we must make use of approximate centroiding algorithms. In this work, we studied how close we get to saturating the CRLB with approximate methods acting on relatively low signal-to-noise ratio unsaturated stars.

We focused on examples from two classes of centroiding algorithms. The first class contains fast and approximate methods that do not require any knowledge of the PSF at the positions of stars. Of methods that belong to this class, we consider centroiding stars based on fitting a second-order polynomial to a  $3 \times 3$  patch of star images smoothed by a Gaussian kernel of fixed width, and finding the center of light of a  $7 \times 7$  patch around the brightest pixel of the star.

The second class of centroiding algorithms make use of the PSF (or some good estimate of the PSF) at the positions of stars. In our investigation, it is assumed that the size and the shape of the PSF are known prior to applying these algorithms to the images of stars. We considered two examples from this class. The first example is the matched filter polynomial centroiding, and the second example is the PSF fitting. In the PSF fitting method, we find the maximum likelihood estimates of the flux and centroids of stars by fitting a PSF model that has the correct shape and size.

In terms of saturating the Cramér-Rao bound, we compared the performances of these methods against each other. Our results suggest that in all ranges of FWHM and SNR, the PSF fitting method returns centroid estimates that saturate the CRLB. This confirms our expectation that maximum-likelihood estimators saturate the Cramér-Rao lower bound.

We note that the estimates found by the  $7 \times 7$  moment method, except in the case of very high SNR values and small values of  $\gamma$ , do not come close to saturating the CRLB. In a considerable range of PSF sizes and background noise levels, this method fails to deliver any centroiding estimate close to saturating the bound. When applied to stars with  $\gamma = 2.8, 4$

pixels, we find deviation of RMSE from the CRLB as large as 600% – 800% below signal-to-noise ratio of 10. For the simulated stars with  $\gamma = 5.6$  pixels, we find deviations as large as 500% for SNR below 10 and as large as 200% for  $\text{SNR} \sim 100$ . It can be noted in Figure 1.8 that in the simulations with the lowest SNR ( $\text{SNR} \sim 5$ ), the errors arising from the  $7 \times 7$  moment method are suppressed by the fact that  $17 \times 17$  postage-stamps are used to simulate images. Therefore in the case of  $\text{SNR} \sim 5$ , we expect the deviation of the RMSE from the CRLB to be larger for this method.

On the other hand, the RMSE of centroid estimates of the fixed-Gaussian polynomial centroiding are much closer to saturating the CRLB in all ranges of signal-to-noise ratio even though this method does not require knowledge of the PSF at the positions of stars. We note that when the FWHM of the stars are close to 2.8 pixels (the FWHM of the Gaussian kernel), the fixed-Gaussian polynomial method saturates the CRLB. Deviation of the RMSE of this method from the CRLB is larger for the simulated stars with larger values of FWHM ( $\gamma \simeq 5$  pixels). Presence of noise is another limiting factor. Although this method is able to get very close to saturating the bound in a wide range of signal-to-noise ratios, it is not reliable in the case of centroding extremely faint stars ( $5 < \text{S/N} < 10$ ).

In matched filter polynomial centroding, the fixed-Gaussian polynomial method is modified by convolving the image with the correct PSF. Our results on the simulated stars show that the matched filter estimator saturates the CRLB for all PSF sizes and noise levels. This is due to the fact that once the images of stars are convolved with the correct PSF, they become smooth that fitting a second-order polynomial to the  $3 \times 3$  patch centered on the brightest pixel of the smooth image is sufficient for us to obtain results as accurate as those from fitting a PSF profile.

The Gaussian kernel (see equation 1.24) in the fixed-Gaussian polynomial centroding is separable, and correlation of the kernel with an image of star can be performed *exactly* in

no time. Therefore in terms of computational cost, this method is more efficient than the matched filter method in which the image of star is correlated with a PSF of arbitrary shape.

In the case that we have a good estimate of the PSF, the matched filter polynomial method can be faster than PSF fitting method for *centroiding purposes*. Additionally, this method is able to saturate the CRLB in a wide range of conditions. It is however important to note that in many cases, reliable estimation of the flux requires a technique as accurate as PSF-fitting. However, in cases in which an investigator only needs an empirical estimates of the centroid offsets, fixed-Gaussian polynomial or matched filter polynomial centroding methods can be employed with negligible loss of information. For instance in modeling the stellar light curves in the *K2* mission, [Foreman-Mackey et al. \(2015\)](#) uses a simple polynomial centroding to marginalize out the systematic trends caused by centroid offsets.

Moreover, we note that the PSF fitting method can be made faster by only keeping the term proportional to the dot product of the PSF model and the image in  $\chi^2$ :

$$\chi^2 = (\mathbf{y} \cdot \mathbf{y} - 2F\mathbf{y} \cdot \mathbf{m} + F^2\mathbf{m} \cdot \mathbf{m})/\sigma^2, \quad (1.30)$$

where  $F$  is the flux,  $\sigma$  is the per-pixel uncertainty, the dot product between two vectors is denoted by  $(\cdot)$ , and the image of star and the normalized shifted PSF model are denoted by  $\mathbf{y}$  and  $\mathbf{m}$  respectively. Upon varying only the centroid, the terms  $\mathbf{y} \cdot \mathbf{y}$  and  $\mathbf{m} \cdot \mathbf{m}$  remain approximately constant. However, this only allows us to vary the position of centroid, and not the flux, while fitting the PSF model to the star.

Finding a centroid coordinate that maximizes the dot product of the PSF and the star image is equivalent to finding the peak of the correlation of the PSF and the image. Therefore optimizing the modified  $\chi^2$  is equivalent to finding the location of the peak of the matched filter.

In the initial smoothing step of the fixed-Gaussian polynomial method, the image of the star is correlated with an approximate Gaussian PSF. When there is mismatch between the widths of the smoothing kernel and the that of the PSF, we loose some information by employing a  $3 \times 3$  polynomial fitting. When we have the advantage of knowing the PSF, this issue can be resolved by employing the matched filter polynomial method.

In this investigation we showed that PSF fitting always performs better—in terms of saturating the CRLB—at centroiding stars. Having a reasonable PSF model always helps us obtain more reliable centroid estimates, but over a certain range of low signal-to-noise ratios and PSF sizes, one can achieve sensibly accurate results by employing a simple  $3 \times 3$  method after smoothing the image with a Gaussian kernel of a fixed width, and without making any assumption about the PSF model at the positions of stars.

In this investigation we narrowed our focus on a set of data simulated from a particular PSF profile. Although there are various cases where Moffat profiles provide reasonable representations of the point spread function, these profiles are not generic enough to let us reach a more general conclusion.

This work was partially supported by the NSF (grants IIS-1124794 and AST-1517237), NASA (grant NNX12AI50G), and the Moore-Sloan Data Science Environment at NYU. We thank Jo Bovy and Alex Malz for discussions related to this work. We are also grateful to Dustin Lang and Alex Malz for reading and making comments on draft.

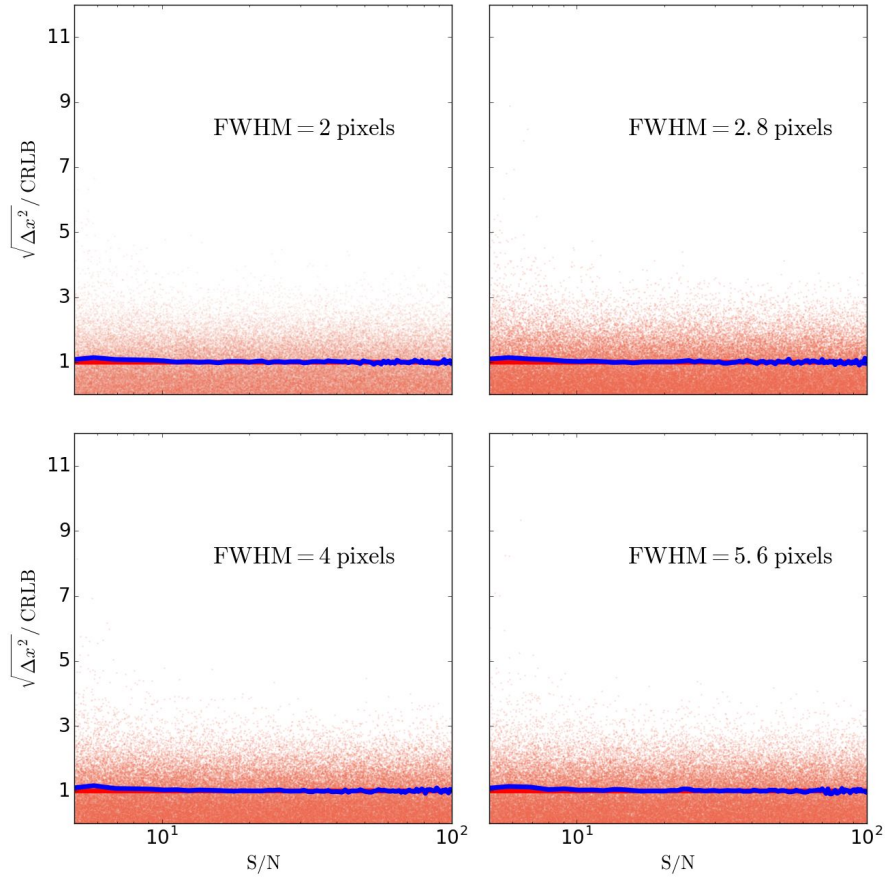


Figure 1.1: Scatter plots showing the relation between the ratio of error (in x-axis of the centroid positions) to the CRLB and the signal-to-noise ratio of stars. Errors are found from fitting the exact PSF model to the stars, with FWHM of : 2 (upper left), 2.8 (upper right), 4 (lower left), and 5.6 (lower right) pixels. In each scatter plot, the blue solid line represents the ratio of the root-mean-squared-error to the CRLB, and the red line represents the ratio achievable by an optimal estimator.

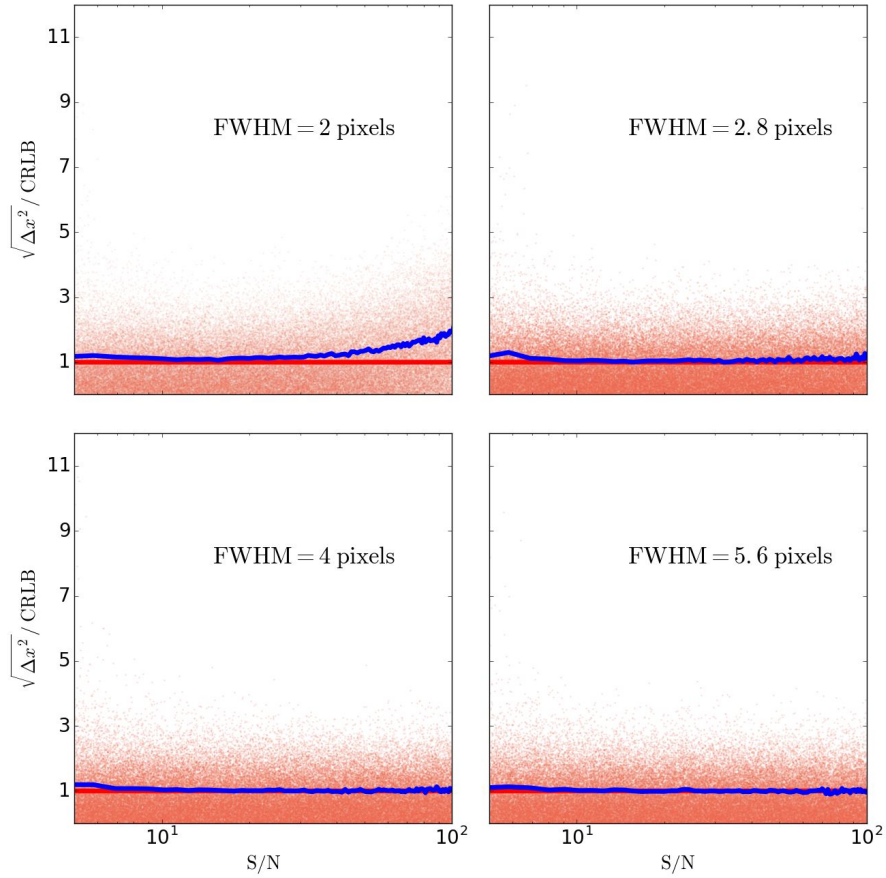


Figure 1.2: Scatter plots showing the relation between the ratio of error (in x-axis of the centroid positions) to the CRLB and the signal-to-noise ratio of stars. Errors are found from applying the matched filter polynomial centroiding to the stars, with FWHM of : 2 (upper left), 2.8 (upper right), 4 (lower left), and 5.6 (lower right) pixels. In each scatter plot, the blue solid line represents the ratio of the root-mean-squared-error to the CRLB, and the red line represents the ratio achievable by an optimal estimator.

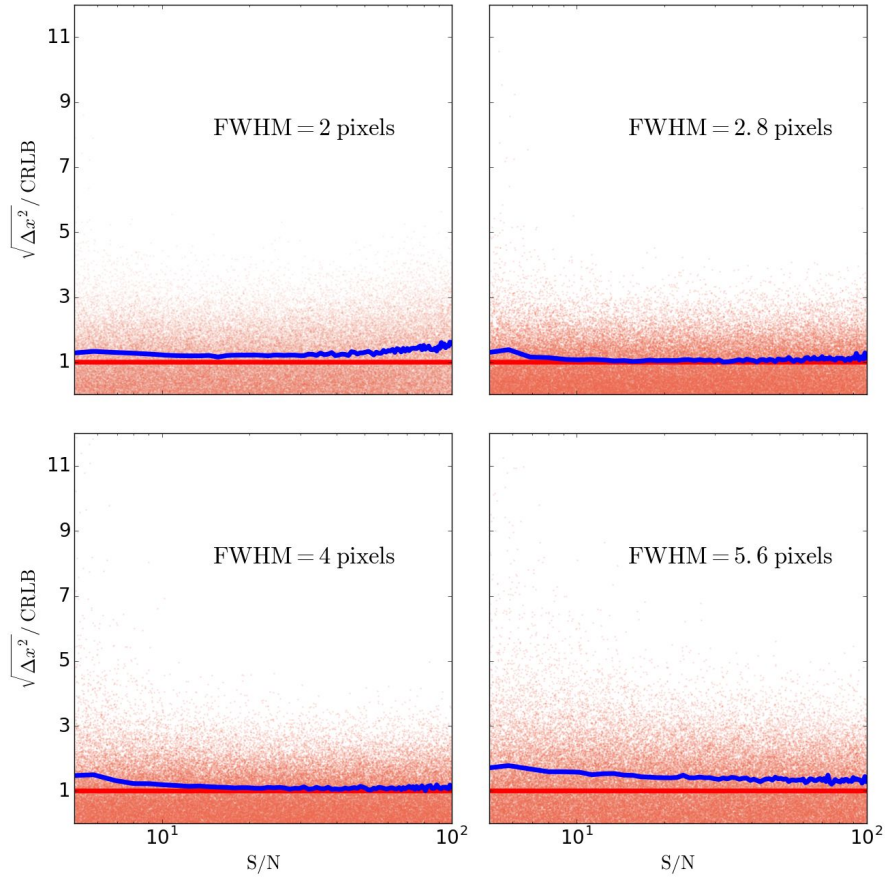


Figure 1.3: Scatter plots showing the relation between the ratio of error (in x-axis of the centroid positions) to the CRLB and the signal-to-noise ratio of stars. Errors are found from applying the fixed-Gaussian polynomial centroiding to the stars, with FWHM of : 2 (upper left), 2.8 (upper right), 4 (lower left), and 5.6 (lower right) pixels. In each scatter plot, the blue solid line represents the ratio of the root-mean-squared-error to the CRLB, and the red line represents the ratio achievable by an optimal estimator.

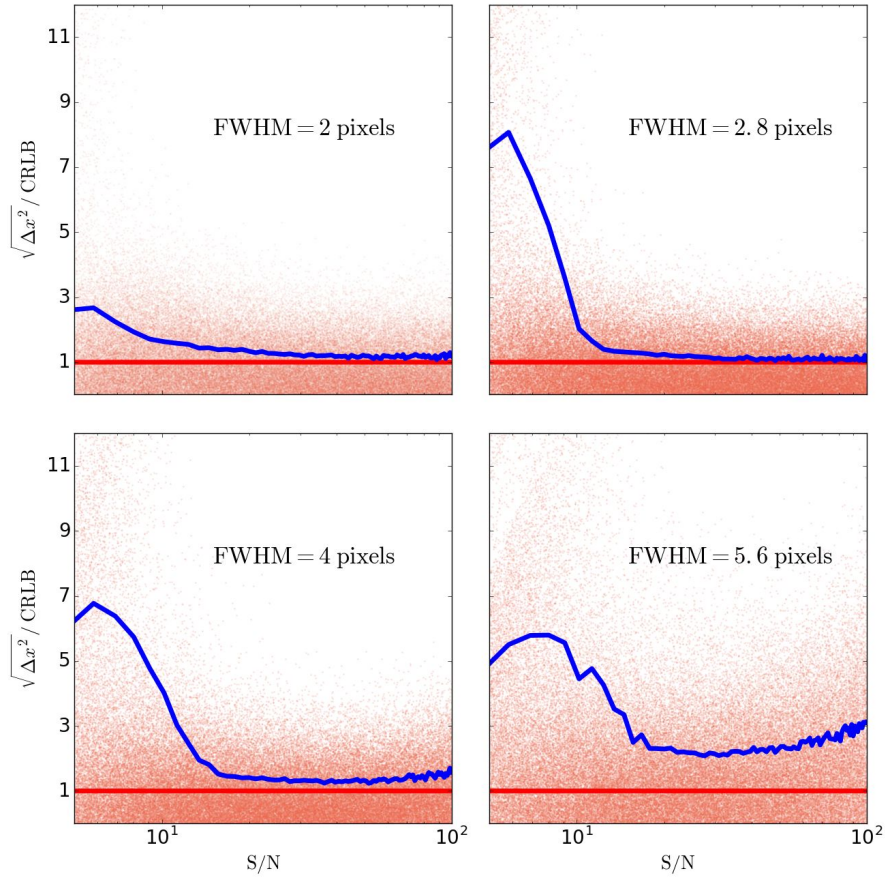


Figure 1.4: Scatter plots showing the relation between the ratio of error (in x-axis of the centroid positions) to the CRLB and the signal-to-noise ratio of stars. Errors are found from applying the  $7 \times 7$  moment method to the stars, with FWHM of : 2 (upper left), 2.8 (upper right), 4 (lower left), and 5.6 (lower right) pixels. In each scatter plot, the blue solid line represents the ratio of the root-mean-squared-error to the CRLB, and the red line represents the ratio achievable by an optimal estimator.

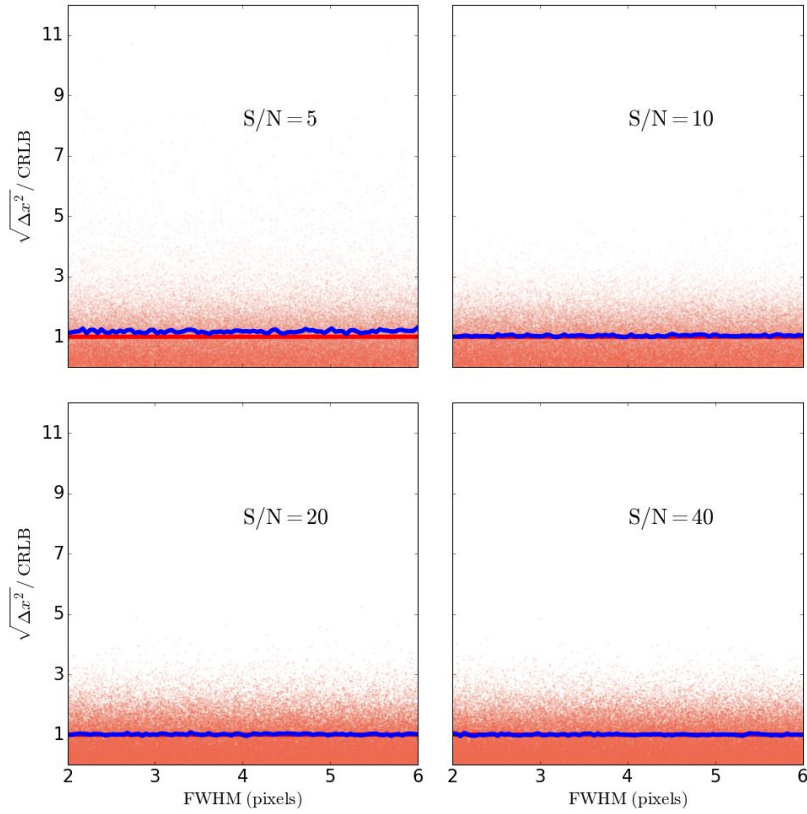


Figure 1.5: Scatter plots showing the relation between the ratio of error (in x-axis of the centroid positions) to the CRLB and the FWHM of stars. Errors are found from fitting the exact PSF model to the stars, with SNR of : 5 (upper left), 10 (upper right), 20 (lower left), and 40 (lower right). In each scatter plot, the blue solid line represents the ratio of the root-mean-squared-error to the CRLB, and the red line represents the ratio achievable by an optimal estimator.

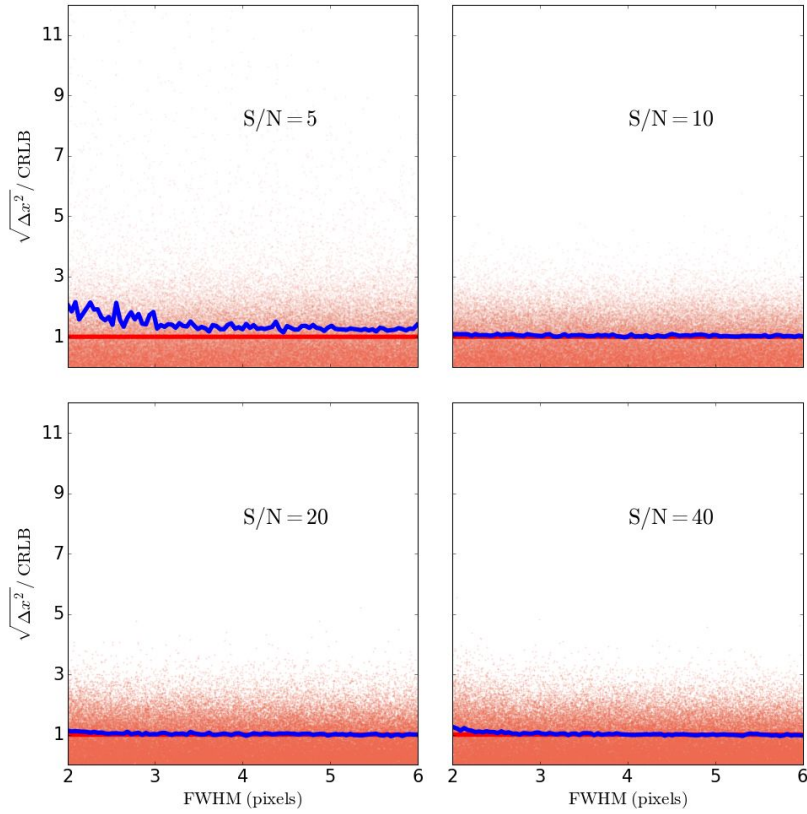


Figure 1.6: Scatter plots showing the relation between the ratio of error (in x-axis of the centroid positions) to the CRLB and the FWHM of stars. Errors are found from applying the matched filter polynomial centroiding to the stars, with SNR of : 5 (upper left), 10 (upper right), 20 (lower left), and 40 (lower right). In each scatter plot, the blue solid line represents the ratio of the root-mean-squared-error to the CRLB, and the red line represents the ratio achievable by an optimal estimator.

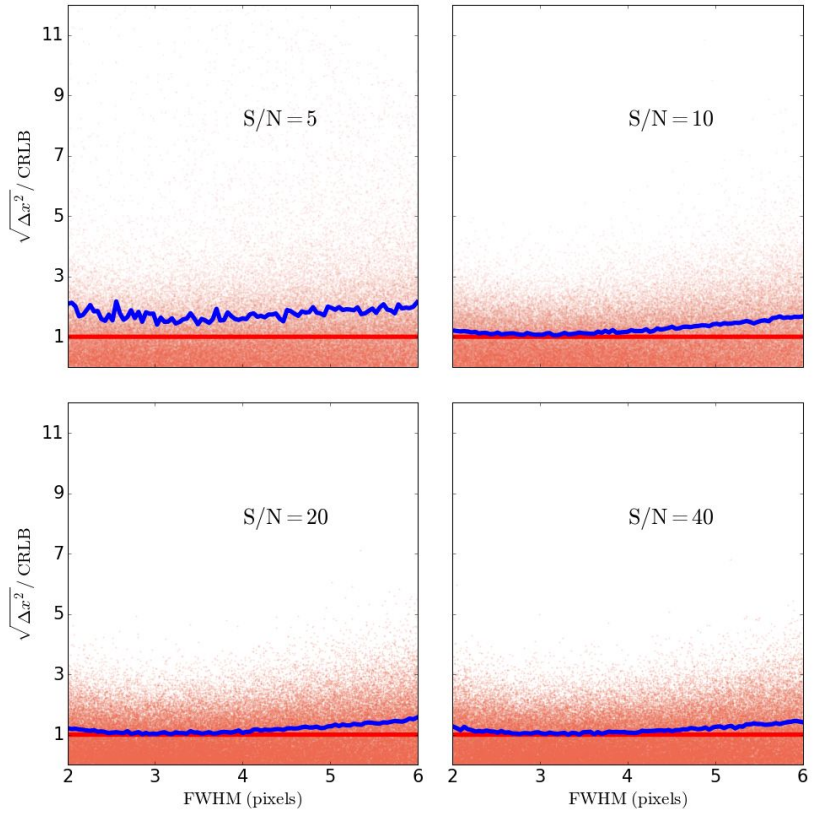


Figure 1.7: Scatter plots showing the relation between the ratio of error (in x-axis of the centroid positions) to the CRLB and the FWHM of stars. Errors are found from applying the fixed-Gaussian polynomial centroiding to the stars, with SNR of : 5 (upper left), 10 (upper right), 20 (lower left), and 40 (lower right). In each scatter plot, the blue solid line represents the ratio of the root-mean-squared-error to the CRLB, and the red line represents the ratio achievable by an optimal estimator.

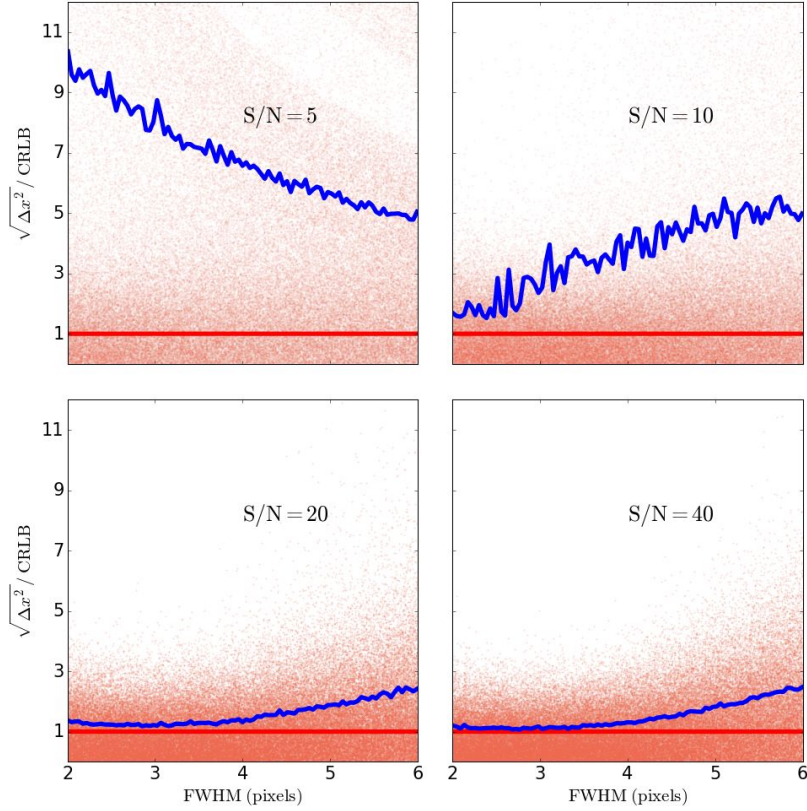


Figure 1.8: Scatter plots showing the relation between the ratio of error (in x-axis of the centroid positions) to the CRLB and the FWHM of stars. Errors are found from applying the  $7 \times 7$  moment method to the stars, with SNR of : 5 (upper left), 10 (upper right), 20 (lower left), and 40 (lower right). In each scatter plot, the blue solid line represents the ratio of the root-mean-squared-error to the CRLB, and the red line represents the ratio achievable by an optimal estimator.

# Chapter 2

## Approximate bayesian computation in large scale structure: constraining the galaxy halo connection

This Chapter is joint work with ChangHoon Hahn (NYU), Kilian W. Walsh (NYU), Andrew Hearin (Yale), David W. Hogg (NYU), and Duncan Campbell (Yale) and it is submitted to the *Monthly Royal Astronomical Society Notice*.

### 2.1 Section abstract

Standard approaches to Bayesian parameter inference in large scale structure assume a Gaussian functional form (chi-squared form) for the likelihood. This assumption, in detail, cannot be correct. Likelihood free inferences such as Approximate Bayesian Computation (ABC) relax these restrictions and make inference possible without making any assumptions on the likelihood. Instead ABC relies on a forward generative model of the data and a metric

for measuring the distance between the model and data. In this work, we demonstrate that ABC is feasible for LSS parameter inference by using it to constrain parameters of the halo occupation distribution (HOD) model for populating dark matter halos with galaxies.

Using specific implementation of ABC supplemented with Population Monte Carlo importance sampling, a generative forward model using HOD, and a distance metric based on galaxy number density, two-point correlation function, and galaxy group multiplicity function, we constrain the HOD parameters of mock observation generated from selected “true” HOD parameters. The parameter constraints we obtain from ABC are consistent with the “true” HOD parameters, demonstrating that ABC can be reliably used for parameter inference in LSS. Furthermore, we compare our ABC constraints to constraints we obtain using a pseudo-likelihood function of Gaussian form with MCMC and find consistent HOD parameter constraints. Ultimately our results suggest that ABC can and should be applied in parameter inference for LSS analyses.

## 2.2 Introduction

Cosmology was revolutionized in the 1990s with the introduction of likelihoods—probabilities for the data given the theoretical model—for combining data from different surveys and performing principled inferences of the cosmological parameters (White & Scott 1996; Riess et al. 1998). Nowhere has this been more true than in cosmic microwave background (CMB) studies, where it is nearly possible to analytically evaluate a likelihood function that involves no (or minimal) approximations (Oh et al. 1999, Wandelt et al. 2004, Eriksen et al. 2004, Planck Collaboration et al. 2014, 2016a).

Fundamentally, the tractability of likelihood functions in cosmology flows from the fact that the initial conditions are exceedingly close to Gaussian in form, and that many sources

of measurement noise are also Gaussian (Knox 1995). Likelihood functions are easier to write down and evaluate when things are closer to Gaussian, so at large scales and in the early universe. Hence likelihood analyses are ideally suitable for CMB data.

In large-scale structure (LSS) with galaxies, quasars, and quasar absorption systems as tracers, formed through nonlinear gravitational evolution and biasing, the likelihood *cannot* be Gaussian. Even if the initial conditions are perfectly Gaussian, the growth of structure creates non-linearities which are non-Gaussian (see Bernardeau et al. 2002 for a comprehensive review). Galaxies form within the density field in some complex manner that is modeled only effectively (Dressler 1980; Kaiser 1984; Santiago & Strauss 1992; Steidel et al. 1998; see Somerville & Davé 2015 for a recent review). Even if the galaxies were a Poisson sampling of the density field, which they are not (Mo & White 1996; Somerville et al. 2001; Casas-Miranda et al. 2002), it would be tremendously difficult to write down even an approximate likelihood function (Ata et al. 2015).

The standard approach makes the strong assumption that the likelihood function for the data can be approximated by a pseudo-likelihood function that is a Gaussian probability density in the space of the two-point correlation function estimate. It is also typically limited to (density and) two-point correlation function (2PCF) measurements, assuming that these measurements constitute sufficient statistics for the cosmological parameters. As Hogg (in preparation) demonstrates, the assumption of a Gaussian pseudo-likelihood function cannot be correct (in detail) at any scale, since a correlation function, being related to the variance of a continuous field, must satisfy non-trivial positive-definiteness requirements. These requirements truncate function space such that the likelihood in that function space could never be Gaussian. The failure of this assumption becomes more relevant as the correlation function becomes better measured, so it is particularly critical on intermediate scales, where neither shot noise nor cosmic variance significantly influence the measurement.

Fortunately, these assumptions are not required for cosmological inferences, because high-precision cosmological simulations can be used to directly calculate LSS observables. Therefore, we can simulate not just the one- or two-point statistics of the galaxies, but also any higher order statistics that might provide additional constraining power on a model. In principle, there is therefore no strict need to rely on these common but specious analysis assumptions as it is possible to calculate a likelihood function directly from simulation outputs.

Of course, any naive approach to sufficiently simulating the data would be ruinously expensive. Fortunately, there are principled, (relatively) efficient methods for minimizing computation and delivering correct posterior inferences, using only a data simulator and some choices about statistics. In the present work, we use Approximate Bayesian Computation—ABC—which provides a *rejection sampling* framework that relaxes the assumptions of the traditional approach.

ABC approximates the posterior probability distribution function (model given the data) by drawing proposals from the prior over the model parameters, simulating the data from the proposals using a forward generative model, and then rejecting the proposals that are beyond a certain threshold “distance” from the data, based on summary statistics of the data. In practice, ABC is used in conjunction with a more efficient sampling operation like Population Monte Carlo (PMC; [Del Moral et al. 2012](#)). PMC initially rejects the proposals from the prior with a relatively large “distance” threshold. In subsequent steps, the threshold is updated adaptively, and samples from the proposals that have passed the previous iteration are subjected to the new, more stringent, threshold criterion ([Beaumont et al. 2008](#)). In principle, the distance metric can be any positive definite function that compares various summary statistics between the data and the simulation.

In the context of astronomy, this approach has been used in a wide range of topics

including image simulation calibration for wide field surveys (Akeret et al. 2015), the study of the morphological properties of galaxies at high redshifts (Cameron & Pettitt 2012), stellar initial mass function modeling (Cisewski et al. in preparation), and cosmological inference with weak-lensing peak counts (Lin & Kilbinger 2015; Lin et al. 2016), Type Ia Supernovae (Weyant et al. 2013), and galaxy cluster number counts (Ishida et al. 2015).

In order to demonstrate that ABC can be tractably applied to parameter estimation in contemporary LSS analyses, we narrow our focus to inferring the parameters of a Halo Occupation Distribution (HOD) model. The foundation of HOD predictions is the halo model of LSS, that is, collapsed dark matter halos are biased tracers of the underlying cosmic density field (Press & Schechter 1974; Bond et al. 1991; Cooray & Sheth 2002). The HOD specifies how the dark matter halos are populated with galaxies by modeling the probability that a given halo hosts  $N$  galaxies subject to some observational selection criteria (Lemson & Kauffmann 1999; Seljak 2000; Scoccimarro et al. 2001; Berlind & Weinberg 2002; Zheng et al. 2005). This statistical prescription for connecting galaxies to halos has been remarkably successful in reproducing the galaxy clustering, galaxy–galaxy lensing, and other observational statistics (Miyatake et al. 2015; Rodríguez-Torres et al. 2016), and is a useful framework for constraining cosmological parameters (van den Bosch et al. 2003; Tinker et al. 2005; Cacciato et al. 2013; More et al. 2013) as well as galaxy evolution models (Conroy & Wechsler 2009; Tinker et al. 2011; Leauthaud et al. 2012; Behroozi et al. 2013; Tinker et al. 2013, Walsh et al. in preparation).

More specifically, we limit our scope to a likelihood analysis of HOD model parameter space, keeping cosmology fixed. We forward model galaxy survey data by populating pre-built dark matter halo catalogs obtained from high resolution N-body simulations (Klypin et al. 2011, 2016) using `Halotoools`<sup>1</sup> (Hearin et al. 2016a), an open-source package for modeling

---

<sup>1</sup><http://halotools.readthedocs.org>

the galaxy-halo connection. Equipped with the forward model, we use summary statistics such as number density, two-point correlation function, galaxy group multiplicity function (GMF) to infer HOD parameters using ABC.

In Section 2.3 we discuss the algorithm of the ABC-PMC prescription we use in our analyses. This includes the sampling method itself, the HOD forward model, and the computation of summary statistics. Then in Section 2.4.1, we discuss the mock galaxy catalog, which we treat as observation. With the specific choices of ABC-PMC ingredients, which we describe in Section 2.4.2, in Section 2.4.3 we present the results of our parameter inference using two sets of summary statistics, number density and 2PCF and number density and GMF. We also include in our results, analogous parameter constraints from the standard MCMC approach, which we compare to ABC results in detail, Section 2.4.4. Finally, we discuss and conclude in Section 2.5.

## 2.3 Methods

### 2.3.1 Approximate Bayesian Computation

ABC is based on rejection sampling, so we begin this section with a brief overview of rejection sampling. Broadly speaking, rejection sampling is a Monte Carlo method used to draw samples from a probability distribution,  $f(\alpha)$ , which is difficult to directly sample. The strategy is to draw samples from an instrumental distribution  $g(\alpha)$  that satisfies the condition  $f(\alpha) < Mg(\alpha)$  for all  $\alpha$ , where  $M > 1$  is some scalar multiplier. The purpose of the instrumental distribution  $g(\alpha)$  is that it is easier to sample than  $f(\alpha)$  (see Bishop & Nasrabadi 2007 and references therein).

In the context of simulation-based inference, the ultimate goal is to sample from the joint probability of a simulation  $X$  and parameters  $\vec{\theta}$  given observed data  $D$ , the posterior

probability distribution. From Bayes rule this posterior distribution can be written as

$$p(\vec{\theta}, X|D) = \frac{p(D|X)p(X|\vec{\theta})\pi(\vec{\theta})}{Z} \quad (2.1)$$

where  $\pi(\vec{\theta})$  is the prior distribution over the parameters of interest and  $Z$  is the evidence,

$$Z = \int d\vec{\theta} dX p(D|X)p(X|\vec{\theta})\pi(\vec{\theta}), \quad (2.2)$$

where the domain of the integral is all possible values of  $X$  and  $\vec{\theta}$ . Since  $p(\vec{\theta}, X|D)$  cannot be directly sampled, we use rejection sampling with instrumental distribution

$$q(\vec{\theta}, X) = p(X|\vec{\theta})\pi(\vec{\theta}) \quad (2.3)$$

and the choice of

$$M = \frac{\max_{\vec{\theta}} p(D|X)}{Z} > 1. \quad (2.4)$$

Note that we do not ever need to know  $Z$ . The choices of  $q(\vec{\theta}, X)$  and  $M$  satisfy the condition

$$p(\vec{\theta}, X|D) < Mq(\vec{\theta}, X) \quad (2.5)$$

so we can sample  $p(\vec{\theta}, X|D)$  by drawing  $\vec{\theta}, X$  from  $q(\vec{\theta}, X)$ . In practice, this is done by first drawing  $\vec{\theta}$  from the prior  $\pi(\vec{\theta})$  and then generating a simulation  $X = f(\vec{\theta})$  via the forward model. Then  $\vec{\theta}, X$  is accepted if

$$\frac{p(\vec{\theta}, X|D)}{Mq(\vec{\theta}, X)} = \frac{p(D|X)}{\max_{\vec{\theta}} p(D|X)} > u \quad (2.6)$$

where  $u$  is drawn from `Uniform[0, 1]`. By repeating this rejection sampling process, we sample

the distribution  $p(\vec{\theta}, X|D)$  with the set of  $\vec{\theta}$  and  $X$  that are accepted.

At this stage, ABC distinguishes itself by postulating that  $p(D|X)$ , the probability of observing data  $D$  given simulation  $X$  (*not* the likelihood), is proportional to the probability of the distance between the data and the simulation  $X$  being less than an arbitrarily small threshold  $\epsilon$

$$p(D|X) \propto p(\rho(D, X) < \epsilon) \quad (2.7)$$

where  $\rho(D, X)$  is the distance between the data  $D$  and simulation  $X$ . Eq. 2.7 along with the rejection sampling acceptance criteria (Eq. 2.6), leads to the acceptance criteria for ABC:  $\vec{\theta}$  is accepted if  $\rho(D, X) < \epsilon$ .

The distance function is a positive definite function that measures the closeness of the data and the simulation. The distance can be a vector with multiple components where each component is a distance between a single summary statistic of the data and that of the simulation. In that case, the threshold  $\epsilon$  in Eq. 2.7 will also be a vector with the same dimensions.  $\vec{\theta}$  is accepted if the distance vector is less than the threshold vector for every component.

The ABC procedure begins, in the same fashion as rejection sampling, by drawing  $\vec{\theta}$  from the prior distribution  $\pi(\vec{\theta})$ . The simulation is generated from  $\vec{\theta}$  using the forward model,  $X = f(\vec{\theta})$ . Then the distance between the data and simulation,  $\rho(D, X)$ , is calculated and compared to  $\vec{\epsilon}$ . If  $\rho(D, X) < \vec{\epsilon}$ ,  $\vec{\theta}$  is accepted. This process is repeated until we are left with a sample of  $\vec{\theta}$  that all satisfy the distance criteria. This final ensemble approximates the posterior probability distribution  $p(\vec{\theta}, X|D)$ .

As it is stated, the ABC method poses some practical challenges. If the threshold  $\epsilon$  is arbitrarily large, the algorithm essentially samples from the prior  $\pi(\vec{\theta})$ . Therefore a sufficiently small threshold is necessary to sample from the posterior probability distribution. However, an appropriate value for the threshold is not known *a priori*. Yet, even if an appropriate

threshold is selected, a small threshold requires the entire process to be repeated for many draws of  $\vec{\theta}$  from  $\pi(\vec{\theta})$  until a sufficient sample is acquired. This often presents computation challenges.

We overcome some of the challenges posed by the above ABC method by using a Population Monte Carlo (PMC) algorithm as our sampling technique. PMC is an iterative method that performs rejection sampling over a sequence of  $\vec{\theta}$  distributions ( $\{p_1(\vec{\theta}), \dots, p_T(\vec{\theta})\}$  for  $T$  iterations), with a distance threshold that decreases at each iteration of the sequence.

---

**Algorithm 1** The procedure for ABC-PMC

---

```

1: if  $t = 1$  : then
2:   for  $i = 1, \dots, N$  do
3:     // This loop can now be done in parallel for all  $i$ 
4:     while  $\rho(X, D) > \epsilon_t$  do
5:        $\vec{\theta}_t^* \leftarrow \pi(\vec{\theta})$ 
6:        $X = f(\vec{\theta}_t^*)$ 
7:     end while
8:      $\vec{\theta}_t^{(i)} \leftarrow \vec{\theta}_t^*$ 
9:      $w_t^{(i)} \leftarrow 1/N$ 
10:   end for
11: end if
12: if  $t = 2, \dots, T$  : then
13:   for  $i = 1, \dots, N$  do
14:     // This loop can now be done in parallel for all  $i$ 
15:     while  $\rho(X, D) > \epsilon_t$  do
16:       Draw  $\vec{\theta}_t^*$  from  $\{\vec{\theta}_{t-1}\}$  with probabilities  $\{w_{t-1}\}$ 
17:        $\vec{\theta}_t^* \leftarrow K(\vec{\theta}_t^*, .)$ 
18:        $X = f(\vec{\theta}_t^*)$ 
19:     end while
20:      $\vec{\theta}_t^{(i)} \leftarrow \vec{\theta}_t^*$ 
21:      $w_t^{(i)} \leftarrow \pi(\vec{\theta}_t^{(i)}) / \left( \sum_{j=1}^N w_{t-1}^{(j)} K(\vec{\theta}_{t-1}^{(j)}, \vec{\theta}_t^{(i)}) \right)$ 
22:   end for
23: end if

```

---

As illustrated in Algorithm 1, for the first iteration  $t = 1$ , we begin with an arbitrarily large distance threshold  $\epsilon_1$ . We draw  $\vec{\theta}$  (hereafter referred to as particles) from the prior dis-

tribution  $\pi(\vec{\theta})$ . We forward model the simulation  $X = f(\vec{\theta})$ , calculate the distance  $\rho(D, X)$ , compare this distance to  $\epsilon_1$ , and then accept or reject the  $\vec{\theta}$  draw. Because we set  $\epsilon_1$  arbitrarily large, the particles essentially sample the prior distribution. This process is repeated until we accept  $N$  particles. We then assign equal weights to the  $N$  particles:  $w_1^i = 1/N$ .

For subsequent iterations ( $t > 1$ ) the distance threshold is set such that  $\epsilon_{i,t} < \epsilon_{i,t-1}$  for all components  $i$ . Although there is no general prescription, the distance threshold  $\epsilon_{i,t}$  can be assigned based on the empirical distribution of the accepted distances of the previous iteration,  $t - 1$ . In [Weyant et al. 2013](#), for instance, the threshold of the second iteration is set to the 25<sup>th</sup> percentile of the distances in the first iterations; afterwards in the subsequent iterations,  $t$ ,  $\epsilon_t$  is set to the 50<sup>th</sup> percentile of the distances in the previous  $t - 1$  iteration. Alternatively, [Lin & Kilbinger 2015](#) set  $\epsilon_t$  to the median of the distances from the previous iteration. In Section 2.4, we describe our prescription for the distance threshold, which follows [Lin & Kilbinger 2015](#).

Once  $\epsilon_t$  is set, we draw a particle from the previous weighted set of particles  $\vec{\theta}_{t-1}$ . This particle is perturbed by a kernel, set to the covariance of  $\vec{\theta}_{t-1}$ . Then once again, we generate a simulation by forward modeling  $X = f(\vec{\theta}^i)$ , calculate the distance  $\rho(X, D)$ , and compare the distance to the new distance threshold ( $\epsilon_t$ ) in order to accept or reject the particle. This process is repeated until we assemble a new set of  $N$  particles  $\vec{\theta}_t$ . We then update the particle weights according to the kernel, the prior distribution, and the previous set of weights, as described in Algorithm 1. The entire procedure is then repeated for the next iteration,  $t + 1$ .

There are a number of ways to specify the perturbation kernel in the ABC-PMC algorithm. A widely used technique is to define the perturbation kernel as a multivariate Gaussian centered on the weighted mean of the particle population with a covariance matrix set to the covariance of the particle population. This perturbation kernel is often called the global multivariate Gaussian kernel. For a thorough discussion of various schemes for

specifying the perturbation kernel, we refer the reader to Filippi et al. 2011.

The iterations continue in the ABC-PMC algorithm until convergence is confirmed. One way to ensure convergence is to impose a threshold for the acceptance ratio, which is measured in each iteration. The acceptance ratio is the ratio of the number of proposals accepted by the distance threshold, to the full number of proposed particles at every step. Once the acceptance ratio for an iteration falls below the imposed threshold, the algorithm has converged and is suspended. Another way to ensure convergence is by monitoring the fractional change in the distance threshold ( $\epsilon_t/\epsilon_{t-1}-1$ ) after each iteration. When the fractional change becomes smaller than some specified tolerance level, the algorithm has reached convergence. Another convergence criteria, is through the derived uncertainties of the inferred parameters measured after each iteration. When the uncertainties stabilize and show negligible variations, convergence is ensured. In Section 2.4.2 we detail the specific convergence criteria used in our analysis.

### 2.3.2 Forward model

#### 2.3.2.1 Halo Occupation Modeling

ABC requires a forward generative model. In large scale structure studies, this implies a model that is able to generate a galaxy catalog. We then calculate and compare summary statistics of the data and model catalog in an identical fashion. In this section, we describe the forward generative model we use within the framework of the halo occupation distribution.

The assumption that galaxies reside in dark matter halos is the bedrock underlying all contemporary theoretical predictions for galaxy clustering. The Halo Occupation Distribution (HOD) is one of the most widely used approaches to characterizing this galaxy-halo connection. The central quantity in the HOD is  $p(n_g|M_h)$ , the probability that a halo of

mass  $M_h$  hosts  $n_g$  galaxies.

The most common technical methods for estimating the theoretical galaxy 2PCF utilize the first two moments of  $P$ , which contain the necessary information to calculate the one- and two-halo terms of the galaxy correlation function:

$$1 + \xi_{\text{gg}}^{1h}(r) \simeq \frac{1}{4\pi r^2 \bar{n}_g^2} \int dM_h \frac{dn}{dM_h} \Xi_{\text{gg}}(r|M_h) \times \langle n_g(n_g - 1)|M_h \rangle, \quad (2.8)$$

and

$$\xi_{\text{gg}}^{2h}(r) \simeq \xi_{\text{mm}}(r) \left[ \frac{1}{\bar{n}_g} \int dM_h \frac{dn}{dM_h} \langle n_g|M_h \rangle b_h(M_h) \right]^2 \quad (2.9)$$

In Eqs. (2.8) and (2.9),  $\bar{n}_g$  is the galaxy number density,  $dn/dM_h$  is the halo mass function, the spatial bias of dark matter halos is  $b_h(M_h)$ , and  $\xi_{\text{mm}}$  is the correlation function of dark matter. If we represent the spherically symmetric intra-halo distribution of galaxies by a unit-normalized  $n_g(r)$ , then the quantity  $\Xi_{\text{gg}}(r)$  appearing in the above two equations is the convolution of  $n_g(r)$  with itself. These fitting functions are calibrated using  $N$ -body simulations.

Fitting function techniques, however, require many simplifying assumptions. For example, Eqs. (2.8) and (2.9) assume that the galaxy distribution within a halo is spherically symmetric. These equations also face well-known difficulties of properly treating halo exclusion and scale-dependent bias, which results in additional inaccuracies commonly exceeding the 10% level (van den Bosch et al. 2013). Direct emulation methods have made significant improvements in precision and accuracy in recent years (Heitmann et al. 2009, 2010); however, a labor- and computation-intensive interpolation exercise must be carried out each time any alternative statistic is explored, which is one of the goals of the present work.

To address these problems, throughout this paper we make no appeal to fitting functions or emulators. Instead, we use the `Halotools` package to populate dark matter halos with mock galaxies and then calculate our summary statistics directly on the resulting galaxy catalog with the same estimators that are used on observational data (Hearin et al. 2016a). Additionally, through our forward modeling approach, we are able to explore observables beyond the 2PCF, such as the group multiplicity function, for which there is no available fitting function. This framework allows us to use group multiplicity function for providing quantitative constraints on the galaxy-halo connection. In the following section, we will show that using this observable, we can obtain constraints on the HOD parameters comparable to those found from the 2PCF measurements.

For the fiducial HOD used throughout this paper, we use the model described in Zheng et al. 2007. The occupation statistics of central galaxies follow a nearest-integer distribution with first moment given by

$$\langle N_{\text{cen}} \rangle = \frac{1}{2} \left[ 1 + \text{erf} \left( \frac{\log M - \log M_{\min}}{\sigma_{\log M}} \right) \right]. \quad (2.10)$$

Satellite occupation is governed by a Poisson distribution with the mean given by

$$\langle N_{\text{sat}} \rangle = \langle N_{\text{cen}} \rangle \left( \frac{M - M_0}{M_1} \right)^\alpha. \quad (2.11)$$

We assume that central galaxies are seated at the exact center of the host dark matter halo and are at rest with respect to the halo velocity, defined according to `Rockstar` halo finder (Behroozi et al. (2013)) as the mean velocity of the inner 10% of particles in the halo. Satellite galaxies are confined to reside within the virial radius following an NFW spatial profile (Navarro et al. 2004) with a concentration parameter given by the  $c(M)$  relation (Dutton & Macciò 2014). The peculiar velocity of satellites with respect to their

host halo is calculated according to the solution of the Jeans equation of an NFW profile (More et al. 2009). We refer the reader to Hearin et al. (2016b), Hearin et al. (2016a), and <http://halotools.readthedocs.io> for further details.

For the halo catalog of our forward model, we use the publicly available `Rockstar` (Behroozi et al. 2013) halo catalogs of the `MultiDark` cosmological  $N$ -body simulation (Klypin et al. 2016).<sup>2</sup> `MultiDark` is a collision-less dark-matter only  $N$ -body simulation. The  $\Lambda$ CDM cosmological parameters of `MultiDark` are  $\Omega_m = 0.27$ ,  $\Omega_\Lambda = 0.73$ ,  $\Omega_b = 0.042$ ,  $n_s = 0.95$ ,  $\sigma_8 = 0.82$ , and  $h = 0.7$ . The gravity solver used in the  $N$ -body simulation is the Adaptive Refinement Tree code (ART; Kravtsov et al. 1997) run on  $2048^3$  particles in a  $1 \ h^{-1}\text{Gpc}$  periodic box. `MultiDark` particles have a mass of  $m_p \simeq 8.72 \times 10^8 \ h^{-1}M_\odot$ ; the force resolution of the simulation is  $\epsilon \simeq 7h^{-1} \ \text{kpc}$ .

One key detail of our forward generative model is that when we populate the `MultiDark` halos with galaxies, we do not populate the entire simulation volume. Rather, we divide the volume into a grid of 125 cubic subvolumes, each with side lengths of  $200 \ h^{-1}\text{Mpc}$ . We refer to these subvolumes as  $\{\text{BOX1}, \dots, \text{BOX125}\}$ . The first subvolume is reserved to generate the mock observations which we describe in Section 2.4.1. When we simulate a galaxy catalog for a given  $\vec{\theta}$  in parameter space, we randomly select one of the subvolumes from  $\{\text{BOX2}, \dots, \text{BOX125}\}$  and then populate the halos within this subvolume with galaxies. We implement this procedure to account for sample variance within our forward generative model.

---

<sup>2</sup>In particular, we use the `halotools_alpha_version2` version of this catalog, made publicly available as part of `Halotools`.

### 2.3.3 Summary Statistics

One of the key ingredients for parameter inference using ABC, is the distance metric between the data and the simulations. In essence, it quantifies how close the simulation is to reproducing the data. The data and simulation in our scenario (the HOD framework) are galaxy populations and their positions. A direct comparison, which would involve comparing the actual galaxy positions of the populations, proves to be difficult. Instead, a set of statistical summaries are used to encapsulate the information of the data and simulations. These quantities should sufficiently describe the information of the data and simulations while providing the convenience for comparison. For the positions of galaxies, sensible summary statistics, which we later use in our analysis, include

- Galaxy number density,  $\bar{n}_g$ : the comoving number density of galaxies computed by dividing the comoving volume of the sample from the total number of galaxies.  $\bar{n}_g$  is measured in units of  $(\text{Mpc}/h)^{-3}$ .
- Galaxy two-point correlation function,  $\xi_{gg}(r)$ : a measurement of the excess probability of finding a galaxy pair with separation  $r$  over a random distribution. To compute  $\xi_{gg}(rr)$  in our analysis, for computational reasons, we use the Natural estimator (Peebles 1980):

$$\xi(r) = \frac{DD}{RR} - 1, \quad (2.12)$$

where  $DD$  and  $RR$  refer to counts of data-data and random-random pairs.

- Galaxy group multiplicity function,  $g(N)(N)$ : the number density of galaxy groups in bins of group richness  $N$  where group richness is the number of galaxies within a galaxy group. We rely on a Friends-of-Friends (hereafter FoF) group-finder algorithm (Davis et al. 1985) to identify galaxy groups in our galaxy samples. That is, if the

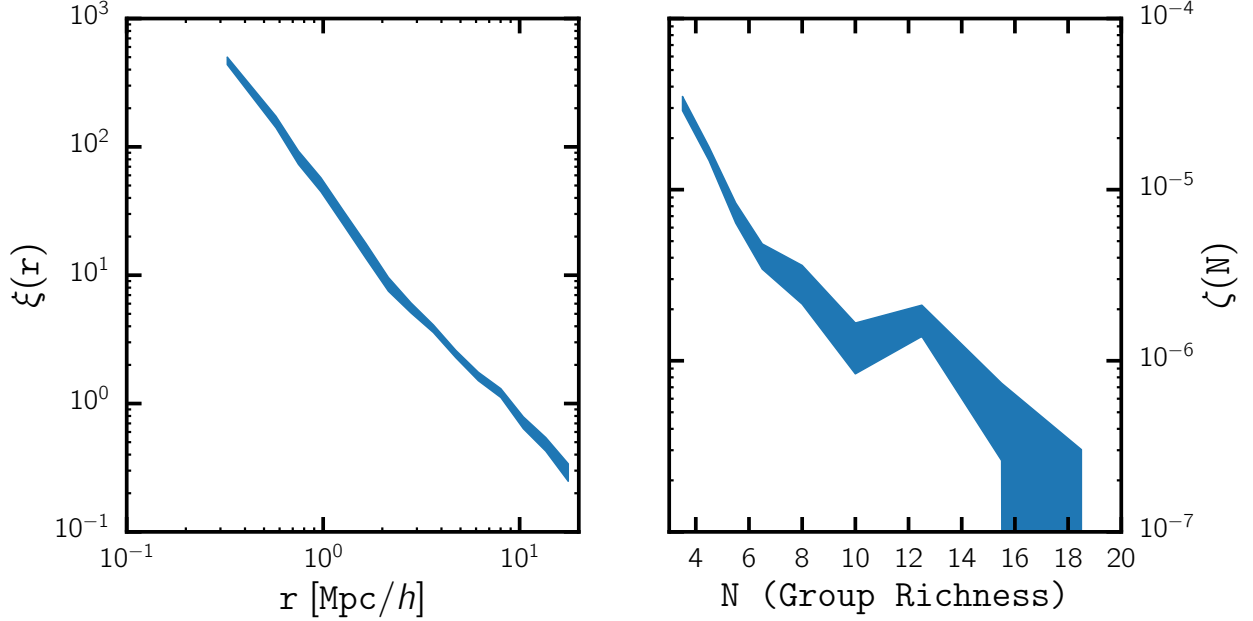


Figure 2.1: The two-point correlation function  $\xi_{\text{gg}}(r)$  (left) and group multiplicity function  $g(N)(N)$  (right) summary statistics of the mock observations generated from the “true” HOD parameters described in Section 2.4.1. The width of the shaded region corresponds to the square root of the covariance matrix diagonal elements (Eq. 2.14). In our ABC analysis, we treat the  $\xi_{\text{gg}}(r)$  and  $g(N)(N)$  above as the summary statistics of the observation.

separation of a galaxy pair is smaller than a specified linking length, the two galaxies are assigned to the same group. The FoF group-finder has been used to identify and analyze the galaxy groups in the SDSS main galaxy sample (Berlind et al. (2006)). For details regarding the group finding algorithm, we refer readers to Davis et al. (1985).

In this study we set the linking length to be 0.25 times the mean separation of galaxies which is given by  $\bar{n}_g^{-1/3}$ . Once the galaxy groups are identified, we bin them into bins of group richness. The total number of groups in each bin is divided by the comoving volume to get  $g(N)(N)$  — in units of  $(\text{Mpc}/h)^{-3}$ .

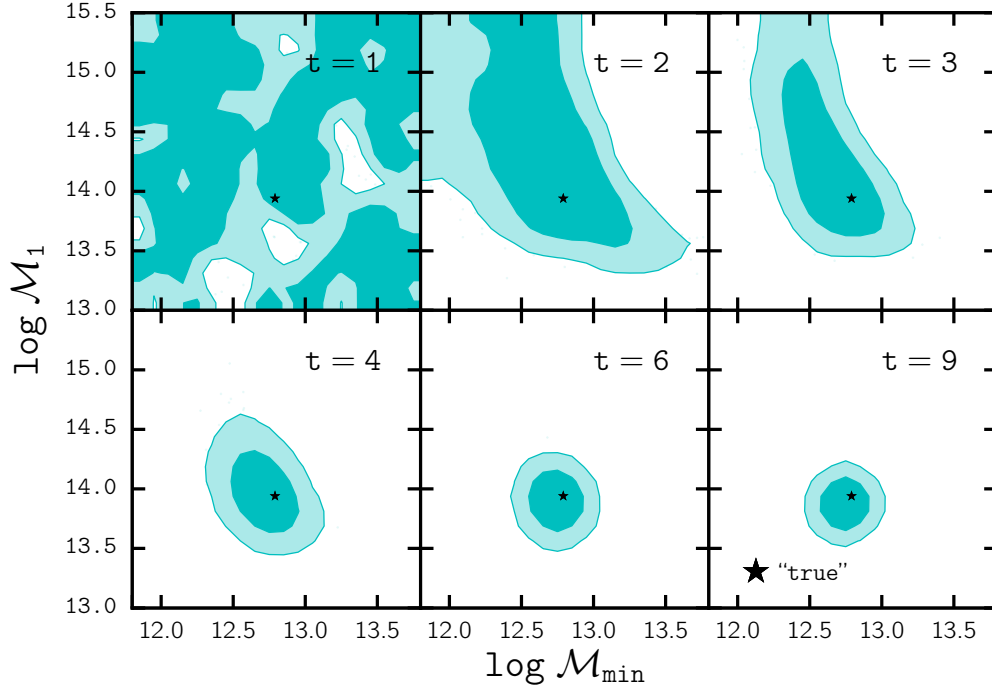


Figure 2.2: We demonstrate the evolution of the ABC particles,  $\vec{\theta}_t$ , over iterations  $t = 1$  to  $9$  in the  $\log \mathcal{M}_{\min}$  and  $\log \mathcal{M}_1$  parameter space.  $\bar{n}$  and  $g(N)(N)$  are used as observables for the above results. For reference, in each panel, we include the “true” HOD parameters (black star) listed in Section 2.4.1. The initial distance threshold,  $\vec{\epsilon}_1 = [\infty, \infty]$  at  $t = 1$  (top left) so the  $\vec{\theta}_1$  spans the entire range of the prior distribution, which is also the range of the panels. We see for  $t < 5$ , the parameter space occupied by the ABC  $\vec{\theta}_t$  shrinks dramatically. Eventually when the algorithm converges,  $t > 7$ , the parameter space occupied by  $\vec{\theta}_t$  no longer shrinks and their distributions represent the posterior distribution of the parameters. At  $t = 9$ , the final iteration, the ABC algorithm has converged and we find that  $\vec{\theta}_{\text{true}}$  lies safely within the 68% confidence region.

## 2.4 ABC at work

With the methodology and the key components of ABC explained above, here we set out to demonstrate how ABC can be used to constrain HOD parameters. We start, in Section 2.4.1 by creating our “observation”. We select a set of HOD parameters which we deem as the “true” parameters and run it through our forward model producing a catalog of galaxy positions which we treat as our observation. Then, in Section 2.4.2, we explain the distance metric and other specific choices we make for the ABC-PMC algorithm. Ultimately, we demonstrate the use of ABC in LSS, in Section 2.4.3, where we present the parameter constraints we get from our ABC analyses. Lastly, in order to both assess the quality of the ABC-PMC parameter inference and also discuss the assumptions of the standard Gaussian likelihood approach, we compare the ABC-PMC results to parameter constraints using the standard approach in Section 2.4.4.

### 2.4.1 Mock Observations

In generating our “observations”, and more generally for our forward model, we adopt the HOD model from [Zheng et al. \(2007\)](#) where the expected number of galaxies populating a dark matter halo is governed by Eqs (2.10) and (2.11). For the parameters of the model used to generate the fiducial mock observations, we choose the [Zheng et al. \(2007\)](#) best-fit HOD parameters for the SDSS main galaxy sample with a luminosity threshold  $M_r = -21$ :

$\log M_{\min}$	$\sigma_{\log M}$	$\log M_0$	$\log M_1$	$\alpha$
12.79	0.39	11.92	13.94	1.15

Since these parameters are used to generate the mock observation, they are the parameters that we ultimately want to recover from our parameter inference. We refer to them as the

true HOD parameters. Plugging them into our forward model (Section 2.3.2), we generate a catalog of galaxy positions.

For our summary statistics of the catalogs we use: the mean number density  $\bar{n}_g$ , the galaxy two-point correlation function  $\xi_{gg}(r)$ , and the group multiplicity function  $g(N)(N)$ . Our mock observation catalog has  $\bar{n}_g = 9.28875 \times 10^{-4} h^{-3}\text{Mpc}^3$  and in Figure 2.1 we plot  $\xi_{gg}(r)$  (left panel) and  $g(N)(N)$  (right panel). The width of the shaded region represent the square root of the diagonal elements of the summary statistic covariance matrix, which is computed as we describe below.

We calculate  $\xi_{gg}$  using the natural estimator (Section 2.3.3) with fifteen radial bins. The edges of the first radial bin are 0.15 and 0.5  $h^{-1}\text{Mpc}$ . The bin edges for the next 14 bins are logarithmically-spaced between 0.5 and 20  $h^{-1}\text{Mpc}$ . We compute the  $g(N)(N)$  as described in Section 2.3.3 with nine richness bins where the bin edges are logarithmically-spaced between 3 and 20. To calculate the covariance matrix, we first run the forward model using the true HOD parameters for all 125 halo catalog subvolumes:  $\{\text{BOX1}, \dots, \text{BOX125}\}$ . We compute the summary statistics of each subvolume galaxy sample  $k$ :

$$\mathbf{x}^{(k)} = [\bar{n}_g, \xi_{gg}, g(N)], \quad (2.13)$$

Then we compute the covariance matrix as

$$C_{i,j}^{\text{sample}} = \frac{1}{N_{\text{mocks}} - 1} \sum_{k=1}^{N_{\text{mocks}}} \left[ \mathbf{x}_i^{(k)} - \bar{\mathbf{x}}_i \right] \left[ \mathbf{x}_j^{(k)} - \bar{\mathbf{x}}_j \right], \quad (2.14)$$

$$\text{where } \bar{\mathbf{x}}_i = \frac{1}{N_{\text{mocks}}} \sum_{k=1}^{N_{\text{mocks}}} \mathbf{x}_i^{(k)}. \quad (2.15)$$

Throughout our ABC-PMC analysis, we treat the  $\bar{n}_g$ ,  $\xi_{gg}(r)$ , and  $g(N)(N)$  we describe in this section as if they were the summary statistics of actual observations. However, we

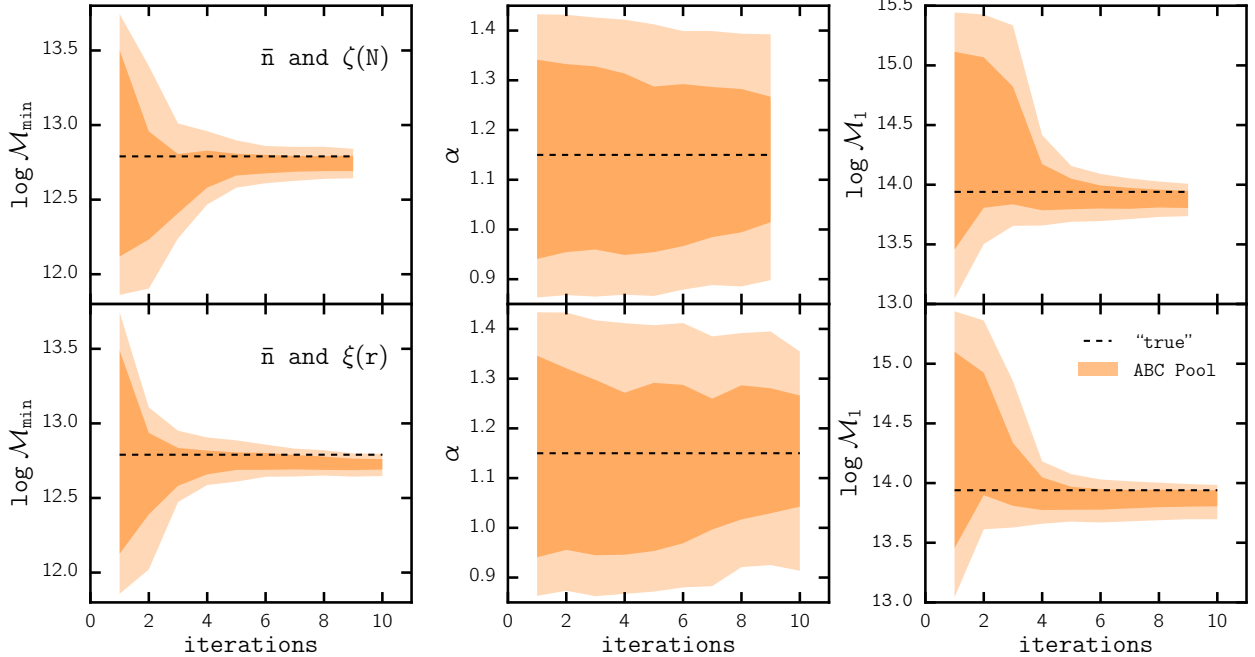


Figure 2.3: We illustrate the convergence of the ABC algorithm through the evolution of the ABC particle distribution as a function of iteration for parameters  $\log \mathcal{M}_{\min}$  (left),  $\alpha$  (center), and  $\log \mathcal{M}_1$  (right). The top panel corresponds our ABC results using the observables  $(\bar{n}, g(N)(N))$ , while the lower panel plots corresponds to the ABC results using  $(\bar{n}, \xi_{gg}(r))$ . The distributions of parameters show no significant change after  $t > 7$ , which suggests that the ABC algorithm has converged.

benefit from the fact that these observables are generated from mock observations using the true HOD parameters of our choice: we can use the true HOD parameters to assess the quality of the parameter constraints we obtain from ABC-PMC.

#### 2.4.2 ABC-PMC Design

In Section 2.3.1, we describe the key components of the ABC algorithm we use in our analysis. Now, we describe the more specific choices we make within the algorithm: the distance metric, the choice of priors, the distance threshold, and the convergence criteria. So far we have described three summary statistics:  $\bar{n}_g$ ,  $\xi_{gg}(r)$ , and  $g(N)(N)$ . In order to

explore the detailed differences in the ABC-PMC parameter constraints based on our choice of summary statistics, we run our analysis for two sets of observables:  $(\bar{n}_g, \xi_{gg})$  and  $(\bar{n}_g, g(N))$ .

For both analyses, we use a multi-component distance (Silk et al. 2012, Cisewsky et al in preparation). Each summary statistic has a distance associated to it:  $\rho_n$ ,  $\rho_\xi$ , and  $\rho_\zeta$ . We calculate each of these distance components as,

$$\rho_n = \frac{(\bar{n}_g^d - \bar{n}_g^m)^2}{\sigma_n^2}, \quad (2.16)$$

$$\rho_\xi = \sum_k \frac{[\xi_{gg}^d(r_k) - \xi_{gg}^m(r_k)]^2}{\sigma_{\xi,k}^2}, \quad (2.17)$$

$$\rho_\zeta = \sum_k \frac{[g(N)^d(N_k) - g(N)^m(N_k)]^2}{\sigma_{\zeta,k}^2}. \quad (2.18)$$

The superscripts d and m denote the data and model respectively. The data, are the observables calculated from the mock observation (Section 2.4.1).  $\sigma_n^2$ ,  $\sigma_{\xi,k}^2$ , and  $\sigma_{\zeta,k}^2$  are not the diagonal elements of the covariance matrix (2.14). Instead, they are diagonal elements of the covariance matrix  $C^{ABC}$ .

We construct  $C^{ABC}$  by populating the entire `MultiDark` halo catalogs 125 times repeatedly, calculating  $\bar{n}_g$ ,  $\xi_{gg}$ , and  $g(N)$  for each realization, and then computing the covariance associated with these observables across all realizations. We highlight that  $C^{ABC}$  differs from Eq. 2.14, in that it does not populate the 125 subvolumes but the entire `MultiDark` simulation and therefore does not incorporate sample variance. The ABC-PMC analysis instead accounts for the sample variance through the forward generative model, which populates the subvolumes in the same manner as the observations. We use  $\sigma_n^2$ ,  $\sigma_{\xi,k}^2$ , and  $\sigma_{\zeta,k}^2$  to ensure that the distance is not biased to variations of observables on specific radial or richness bin.

For our ABC-PMC analysis using the observables  $\bar{n}_g$  and  $\xi_{gg}$ , our distance metric  $\vec{\rho} =$

Table 2.1: **Prior Specifications:** The prior probability distribution and its range for each of the [Zheng et al. \(2007\)](#) HOD parameters. All mass parameters are in unit of  $h^{-1}M_{\odot}$

HOD Parameter	Prior	Range
$\alpha$	Uniform	[0.8, 1.3]
$\sigma_{\log M}$	Log-Uniform	[0.1, 0.7]
$\log M_0$	Uniform	[10.0, 13.0]
$\log M_{min}$	Uniform	[11.02, 13.02]
$\log M_1$	Uniform	[13.0, 14.0]

$[\rho_n, \rho_\xi]$  while the distance metric for the ABC-PMC analysis using the observables  $\bar{n}_g$  and  $g(N)$ , is  $\vec{\rho} = [\rho_n, \rho_\xi]$ . To avoid any complications from the choice for our prior, we select uniform priors over all parameters aside from the scatter parameter  $\sigma_{\log M}$ , for which we choose a log-uniform prior. We list the range of our prior distributions in Table 2.1.

With the distances and priors specified, we now describe the distance thresholds and the convergence criteria we impose in our analyses. For the initial iteration, we set distance thresholds for each distance component to  $\infty$ . This means, that the initial pool  $\vec{\theta}_1$  is simply sampled from the prior distribution we specify above. After the initial iteration, the distance threshold is adaptively lowered in subsequent iterations. More specifically, we follow the choice of [Lin & Kilbinger \(2015\)](#) and set the distance threshold  $\vec{\epsilon}_t$  to the median of  $\vec{\rho}_{t-1}$ , the multi-component distance of the previous iteration of particles ( $\vec{\theta}_{t-1}$ ).

The distance threshold  $\vec{\epsilon}_t$  will progressively decrease. Eventually after a sufficient number of iterations, the region of parameter space occupied by  $\vec{\theta}_t$  will remain unchanged. As this happens, the acceptance ratio begins to fall significantly. When the acceptance ratio drops below 0.001, our acceptance ratio threshold of choice, we deem the ABC-PMC algorithm as converged. In addition to the acceptance ratio threshold we impose, we also ensure that distribution of the parameters converges – another sign that the algorithm has converged. Next, we present the results of our ABC-PMC analyses using the sets of observables ( $\bar{n}_g$ ,  $\xi_{gg}$ ) and ( $\bar{n}_g$ ,  $g(N)$ ).

### 2.4.3 Results: ABC

We describe the ABC algorithm in Section 2.3.1 and list the particular choices we make in the implementation in the previous section. Finally, we demonstrate how the ABC algorithm produces parameter constraints and present the results of our ABC analysis – the parameter constraints for the [Zheng et al. \(2007\)](#) HOD model.

We begin with a qualitative demonstration of the ABC algorithm in Figure 2.2, where we plot the evolution of the ABC  $\vec{\theta}_t$  over the iterations  $t = 1$  to 9, in the parameter space of  $[\log \mathcal{M}_1, \log \mathcal{M}_{min}]$ . The ABC procedure we plot in Figure 2.2 uses  $\bar{n}$  and  $g(N)(N)$  for observables, but the overall evolution is the same when we use  $\bar{n}$  and  $\xi_{gg}(r)$ . The darker and lighter contours represent the 68% and 95% confident regions of the posterior distribution over  $\vec{\theta}_t$ . For reference, we also plot the “true” HOD parameter  $\vec{\theta}_{\text{true}}$  (black star) in each of the panels. The parameter ranges of the panels are equivalent to the ranges of the prior probabilities we specify in Table 2.1.

For  $t = 1$ , the initial pool (top left), the distance threshold  $\vec{\epsilon}_1 = [\infty, \infty]$ , so  $\vec{\theta}_1$  uniformly samples the prior probability over the parameters. At each subsequent iteration, the threshold is lowered (Section 2.4), so for  $t < 6$  panels, we note that the parameter space occupied by  $\vec{\theta}_t$  dramatically shrinks. Eventually when the algorithm begins to converge,  $t > 7$ , the contours enclosing the 68% and 95% confidence interval stabilize. At the final iteration  $t = 9$  (bottom right), the algorithm has converged and we find that  $\vec{\theta}_{\text{true}}$  lies within the 68% confidence interval of the  $\vec{\theta}_{t=9}$  particle distribution. This  $\vec{\theta}_t$  distribution at the final iteration represents the posterior distribution of the parameters.

To better illustrate the criteria for convergence, in Figure 2.3, we plot the evolution of the  $\vec{\theta}_t$  distribution as a function of iteration for parameters  $\log \mathcal{M}_{\min}$  (left),  $\alpha$  (center), and  $\log \mathcal{M}_1$  (right). The darker and lighter shaded regions correspond to the 68% and 95% confidence levels of the  $\vec{\theta}_t$  distributions. The top panels correspond to our ABC results using

$(\bar{n}, g(N))$  as observables and the bottom panels correspond to our results using  $(\bar{n}, \xi_{gg})$ . For each of the parameters in both top and bottom panels, we find that the distribution does not evolve significantly for  $t > 7$ . At this point additional iterations in our ABC algorithm will neither impact the distance threshold  $\vec{\epsilon}_t$  nor the posterior distribution of  $\vec{\theta}_t$ . We also emphasize that the convergence of the parameter distributions coincides with when the acceptance ratio, discussed in Section 2.4.2, crosses the predetermined shut-off value of 0.001. Based on these criteria, our ABC results for both  $(\bar{n}, g(N))$  and  $(\bar{n}, \xi_{gg})$  observables have converged.

We present the parameter constraints from the converged ABC analysis in Figure 2.4 and Figure 2.5. Figure 2.4 shows the parameter constraints using  $\bar{n}$  and  $\xi_{gg}(r)$  while Figure 2.5 plots the constraints using  $\bar{n}$  and  $g(N)(N)$ . For both figures, the diagonal panels plot the posterior distribution of the HOD parameters with vertical dashed lines marking the 50% (median) and 68% confidence intervals. The off-diagonal panels plot the degeneracy between parameter pairs. To determine the accuracy of our ABC parameter constraints, we plot the “true” HOD parameters (black) in each of the panels. For both sets of observables, our ABC constraints are consistent with the “true” HOD parameters. For  $\log M_0$ ,  $\log \sigma_{\log M}$ , and  $\alpha$ , the true parameter values lie near the center of the 68% confidence interval. For the other parameter, which have much tighter constraints, the true parameters lie within the 68% confidence interval.

To further test the ABC results, in Figure 2.6, we compare  $\xi_{gg}(r)$  (left) and  $g(N)(N)$  (right) of the mock observations from Section 2.4.1 to the predictions of the ABC posterior distribution (shaded). The error bars of the mock observations represent the square root of the diagonal elements of the covariance matrix (Eq. 2.14) while the darker and lighter shaded regions represent the 68% and 95% confidence regions of the ABC posterior predictions. In the lower panels, we plot the ratio of the ABC posterior prediction  $\xi_{gg}(r)$  and  $g(N)(N)$  over

the mock observation  $\xi_{\text{gg}}^{\text{obvs}}(r)$  and  $g(N)^{\text{obvs}}(N)$ . Overall, the ratio of the 68% confidence region of ABC posterior predictions is consistent with unity throughout the  $r$  and  $N$  range. We observe slight deviations in the  $\xi_{\text{gg}}$  ratio for  $r > 5 \text{ Mpc}/h$ ; however, any deviation is within the uncertainties of the mock observations. Therefore, the observables drawn from the ABC posterior distributions are in good agreement with the observables of the mock observation.

The ABC results we obtain using the algorithm of Section 2.3.1 with the choices of Section 2.4.2 produce parameter constraints that are consistent with the “true” HOD parameters (Figures 2.4 and 2.5). They also produce observables  $\xi_{\text{gg}}(r)$  and  $g(N)(N)$  that are consistent with  $\xi_{\text{gg}}^{\text{obvs}}$  and  $g(N)^{\text{obvs}}$ . Thus, through ABC we are able to produce consistent parameter constraints. *More importantly, we demonstrate that ABC is feasible for parameter inference in large scale structure.*

#### 2.4.4 Comparison to the Gaussian Pseudo-Likelihood MCMC Analysis

In order to assess the quality of the parameter inference described in the previous section, we compare the ABC-PMC results with the HOD parameter constraints from assuming a Gaussian likelihood function. The model used for the Gaussian likelihood analysis is different than the forward generative model adopted for the ABC-PMC algorithm, to be consistent with the standard approach.

In the ABC analysis, the model accounts for sample variance by randomly sampling a subvolume to be populated with galaxies. Instead, in the Gaussian pseudo-likelihood analysis, the covariance matrix is assumed to capture the uncertainties from sample variance. Hence, in the model for the Gaussian pseudo-likelihood analysis, we populate halos of the *entire MultiDark* simulation rather than a subvolume. We describe the Gaussian pseudo-

likelihood analysis below.

To write down the Gaussian pseudo-likelihood, we first introduce the vector  $\mathbf{x}$ : a combination of the summary statistics (observables) for a galaxy catalog. When we use  $\bar{n}_g$  and  $\xi_{gg}(r)$  as observables in the analysis:  $\mathbf{x} = [\bar{n}_g, \xi_{gg}]$ ; when we use  $\bar{n}_g$  and  $g(N)(N)$  as observables in the analysis:  $\mathbf{x} = [\bar{n}_g, g(N)]$ . Based on this notation, we can write pseudo-likelihood function as

$$-2 \ln \mathcal{L}(\theta|d) = \Delta\mathbf{x}^T \widehat{C^{-1}} \Delta\mathbf{x} + \ln \left[ (2\pi)^d \det(C) \right], \quad (2.19)$$

where

$$\Delta\mathbf{x} = [\mathbf{x}_{obs} - \mathbf{x}_{mod}], \quad (2.20)$$

the difference between  $\mathbf{x}_{obs}$ , measured from the mock observation, and  $\mathbf{x}_{mod}(\theta)$  measured from the mock catalog generated from the model with parameters  $\theta$ .  $d$  here is the dimension of  $\mathbf{x}$  (for  $\mathbf{x} = [\bar{n}_g, \xi_{gg}]$ ,  $d = 13$ ; for  $\mathbf{x} = [\bar{n}_g, g(N)]$ ,  $d = 10$ ).  $\widehat{C^{-1}}$  is the inverse covariance matrix, which we estimate following [Hartlap et al. \(2007\)](#):

$$\widehat{C^{-1}} = \frac{N_{\text{mocks}} - d - 1}{N_{\text{mocks}} - 1} \widehat{C}^{-1}. \quad (2.21)$$

$\widehat{C}$  is the estimated covariance matrix, calculated using the corresponding  $\mathbf{x}$  block of the covariance matrix from Eq. 2.14, and  $N_{\text{mock}}$  is the number of mocks used for the estimation ( $N_{\text{mock}} = 124$ ; see Section 2.4.1). We note that in  $\widehat{C}$  the dependence on the HOD parameters is neglected, so the second term in the expression of Eq. 2.19 can be neglected. Finally, using this pseudo-likelihood, we sample from the posterior distribution given the prior distribution using the MCMC sampler `emcee` ([Foreman-Mackey et al. 2013](#)).

In Figures 2.7 and 2.8, we compare the results from ABC-PMC and Gaussian pseudo-likelihood MCMC analyses using  $[\bar{n}_g, \xi_{gg}]$  and  $[\bar{n}_g, g(N)]$  as observables, respectively. The top panels in each figure compares the marginalized posterior PDFs for three parameters of the HOD model:  $\{\log \mathcal{M}_{\min}, \alpha, \log \mathcal{M}_1\}$ . The lower panels in each figure compares the 68% and 95% confidence intervals of the constraints derived from the two inference methods as a box plot. The “true” HOD parameters are marked by vertical dashed lines in each panel.

In both Figures 2.7 and 2.8, the marginalized posteriors for each of the parameters from both inference methods are comparable and consistent with the “true” HOD parameters. However, we note that there are minor discrepancies between the maringaled posterior distributions. In particular, the distribution for  $\alpha$  derived from ABC-PMC is less biased than the  $\alpha$  constraints from the Gaussian pseudo-likelihood approach.

In Figures 2.9 and 2.10, we plot the contours enclosing the 68% and 95% confidence regions of the posterior probabilities of the two methods using  $[\bar{n}_g, \xi_{gg}]$  and  $[\bar{n}_g, g(N)]$  as observables respectively. In both figures, we mark the “true” HOD parameters (black star). The overall shape of the contours are in agreement with each other. However, we note that the contours for the ABC-PMC method are more extended along  $\alpha$ .

Overall, the HOD parameter constraints from ABC-PMC are consistent with those from the Gaussian pseudo-likelihood MCMC method; however, using ABC-PMC has a number of advantages. For instance, ABC-PMC utilizes a forward generative model. Our forward generative model accounts for sample variance. On the other hand, the Gaussian pseudo-likelihood approach, as mentioned earlier this section, does not account for sample variance in the model and relies on the covariance matrix estimate to capture the sample variance of the data.

Accurate estimation of the covariance matrix in LSS, however, faces a number of challenges. It is both labor and computationally expensive and dependent on the accuracy of

simulated mock catalogs, known to be unreliable on small scales (see Heitmann et al. 2008; Chuang et al. 2015b and references therein). In fact, as Sellentin & Heavens (2016) points out, using estimates of the covariance matrix in the Gaussian psuedo-likelihood approach become further problematic. Even when inferring parameters from a Gaussian-distributed data set, using covariance matrix estimates rather than the *true* covariance matrix leads to a likelihood function that is *no longer* Gaussian. ABC-PMC does not depend on a covariance matrix estimate; hence, it does not face these problems.

In addition to not requiring accurate covariance matrix estimates, forward models of the ABC-PMC method, in principle, also have the advantage that they can account for sources of systematic uncertainties that affect observations. All observations suffer from significant systematic effects which are often difficult to correct. For instance, in SDSS-III BOSS (Dawson et al., 2013), fiber collisions and redshift failures significantly bias measurements and analysis of observables such as  $\xi_{gg}$  or the galaxy powerspectrum (Ross et al., 2012; Guo et al., 2012; Hahn et al., 2017). In parameter inference, these systematics can affect the likelihood, and thus any analysis that requires writing down the likelihood, in unknown ways. With a forward generative model of the ABC-PMC method, the systematics can be simulated and marginalized out to achieve unbiased constraints.

Furthermore, *ABC-PMC – unlike the Gaussian pseudo-likelihood approach – is agnostic about the functional form of the underlying distribution of the summary statistics (e.g.  $\xi_{gg}$  and  $g(N)$ )*. As we explain throughout the paper, the likelihood function in LSS *cannot* be Gaussian. For  $\xi_{gg}$ , the correlation function must satisfy non-trivial positive-definiteness requirements and hence the Gaussian pseudo-likelihood function assumption is not correct in detail. In the case of  $g(N)(N)$ , assuming a Gaussian functional form for the likelihood, which in reality is more likely Poisson, misrepresents the true likelihood function. In fact, this incorrect likelihood, may explain why the constraints on  $\alpha$  are less biased for the ABC-PMC

analysis than the Gaussian-likelihood analysis in 2.10.

Although in our comparison using simple mock observations, we find generally consistent parameter constraints from both the ABC-PMC analysis and the standard Gaussian pseudo-likelihood analysis, more realistic scenarios present many factors that can generate inconsistencies. Consider a typical galaxy catalog from LSS observations. These catalogs consist of objects with different data qualities, signal-to-noise ratios, and systematic effects. For example, catalogs are often incomplete beyond some luminosity/redshift or have some threshold signal-to-noise ratio cut imposed on them.

These selection effects, coupled with the systematic effects earlier this section, make correctly predicting the likelihood intractable. In the standard Gaussian pseudo-likelihood analysis, and other analysis that require writing down a likelihood function, these effects can significantly bias the inferred parameter constraints. In these situations, employing ABC equipped with a generative forward model that incorporates selection and systematic effects may produce less biased parameter constraints.

Despite the advantages of ABC, one obstacle for adopting it to parameter inference has been the computational costs of generative forward models, a key element of ABC. By combining ABC with the PMC sampling method, however, ABC-PMC efficiently converges to give reliable posterior parameter constraints. In fact, in our analysis, the total computational resources required for the ABC-PMC analysis were *comparable* to the computational resources used for the Gaussian pseudo-likelihood analysis with MCMC sampling.

Applying ABC-PMC beyond the analysis in this work, to broader LSS analyses imposes some caveats. In this work, we focus on the galaxy-halo connection, so our generative forward model populates halos with galaxies. LSS analyses for inferring cosmological parameters would require generating halos by running cosmological simulations. The forward models also need to accurately model the observation systematic effects of the latest observations. Hence,

accurate generative forward models in LSS analyses demand improvements in simulations and significant computational resources in order to infer unbiased parameter constraints. Recent cosmology simulations show promising improvements in both accuracy and speed (*e.g.* Feng et al., 2016). Such developments will be crucial for applying ABC-PMC to broader LSS analyses and exploiting the significant advantages that ABC-PMC offers.

## 2.5 Summary and Conclusion

Approximate Bayesian Computation, ABC, is a generative, simulation-based inference that can deliver correct parameter estimation with appropriate choices for its design. It has the advantage over the standard approach in that it does not require explicit knowledge of the likelihood function. It only relies on the ability to simulate the observed data, accounting for the uncertainties associated with observation and on specifying a metric for the distance between the observed data and simulation. When the specification of the likelihood function proves to be challenging or when the true underlying distribution of the observable is unknown, ABC provides a promising alternative for inference.

The standard approach to large scale structure studies relies on the assumption that the likelihood function for the observables – often two-point correlation function – given the model has a Gaussian functional form. In other words, it assumes that the statistical summaries are Gaussian distributed. In principle to rigorously test such an assumption, a large number of realistic simulations would need to be generated in order to examine the actual distribution of the observables. This process, however, is prohibitively—both labor and computationally—expensive. Therefore, our assumption of a Gaussian likelihood function remains largely unconfirmed and so unknown. Fortunately, the framework of ABC permits us to bypass any assumptions regarding the distribution of observables. Through

ABC, we can provide constraints for our models without making the unexamined assumption of Gaussianity.

With the ultimate goal of demonstrating that ABC is feasible for LSS studies, we use it to constrain parameters of the halo occupation distribution, which dictates the galaxy-halo connection. We begin by constructing a mock observation of galaxy distribution with a chosen set of “true” HOD model parameters. Then we attempt to constrain these parameters using ABC. More specifically, in this paper:

- We provide an explanation of the ABC algorithm and present how Population Monte Carlo can be utilized to efficiently reach convergence and estimate the posterior distributions of model parameters. We use this ABC-PMC algorithm with a generative forward model built with `Halotools`, a software package for creating catalogs of galaxy positions based on models of the galaxy-halo connection such as the HOD.
- We choose  $\bar{n}_g$ ,  $\xi_{gg}$  and  $g(N)$  as observables and summary statistics of the galaxy position catalogs. And for our ABC-PMC algorithm, we specify a multi-component distance metric, uniform priors, a median threshold implementation, and an acceptance rate-based convergence criterion.
- From our specific ABC-PMC method, we obtain parameter constraints that are consistent with the “true” HOD parameters of our mock observations. Hence we demonstrate that ABC-PMC can be used for parameter inference in LSS studies.
- We compare our ABC-PMC parameter constraints to constraints using the standard Gaussian-likelihood MCMC analysis. The constraints we get from both methods are comparable in accuracy and precision. However, for our analysis using  $\bar{n}_g$  and  $g(N)$  in particular, we obtain less biased posterior distributions when comparing to the “true” HOD parameters.

Based on our results, we conclude that ABC-PMC is able to consistently infer parameters in the context of LSS. We also find that the computation required for our ABC-PMC and standard Gaussian-likelihood analyses are comparable. Therefore, with the statistical advantages that ABC offers, we present ABC-PMC as an improved alternative for parameter inference.

## Acknowledgements

We thank Jessie Cisewsky for reading and making valuable comments on the draft. We would also like to thank Michael R. Blanton, Jeremy R. Tinker, Uros Seljak, Layne Price, Boris Leidstadt, Alex Malz, Patrick McDonald, and Dan Foreman-Mackey for productive and insightful discussions. MV was supported by NSF grant AST-1517237. DWH was supported by NSF (grants IIS-1124794 and AST-1517237), NASA (grant NNX12AI50G), and the Moore-Sloan Data Science Environment at NYU. KW was supported by NSF grant AST-1211889. Computations were performed using computational resources at NYU-HPC. We thank Shenglong Wang, the administrator of NYU-HPC computational facility, for his consistent and continuous support throughout the development of this project. We would like to thank the organizers of the AstroHackWeek 2015 workshop (<http://astrohackweek.org/2015/>), since the direction and the scope of this investigation was—to some degree—initiated through discussions in this workshop. Throughout this investigation, we have made use of publicly available software packages `emcee` and `abcpmc`. We have also used the publicly available python implementation of the FoF algorithm `pyfof` (<https://github.com/simongibbons/pyfof>).

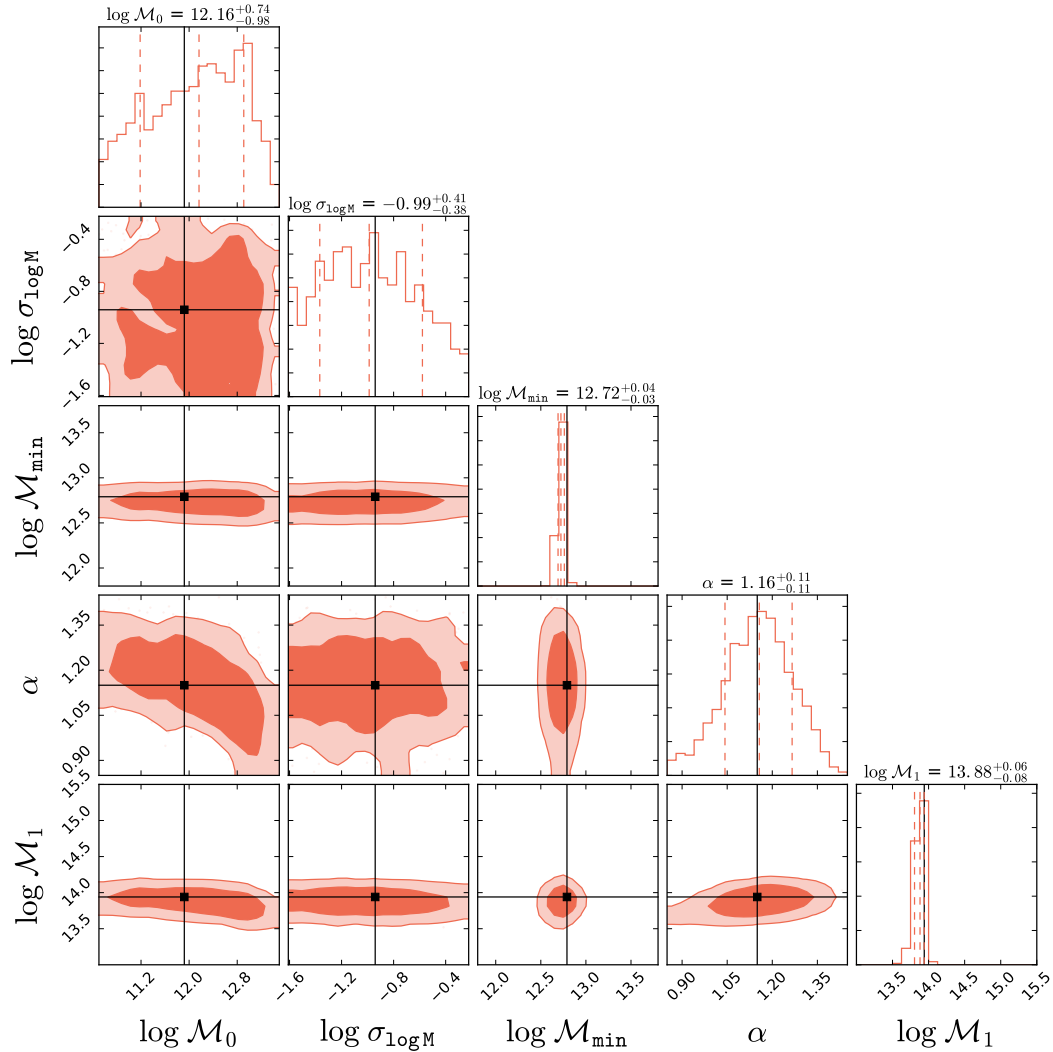


Figure 2.4: We present the constraints on the Zheng et al. (2007) HOD model parameters obtained from our ABC-PMC analysis using  $\bar{n}$  and  $\xi_{gg}(r)$  as observables. The diagonal panels plot the posterior distribution of each HOD parameter with vertical dashed lines marking the 50% quantile and 68% confidence intervals of the distribution. The off-diagonal panels plot the degeneracies between parameter pairs. The range of each panel corresponds to the range of our prior choice. The “true” HOD parameters, listed in Section 2.4.1, are also plotted in each of the panels (black). For  $\log \mathcal{M}_0$ ,  $\alpha$ , and  $\sigma_{\log M}$ , the “true” parameter values lie near the center of the 68% confidence interval of the posterior distribution. For  $\log \mathcal{M}_1$  and  $\log \mathcal{M}_{\min}$ , which have tight constraints, the “true” values lie within the 68% confidence interval. Ultimately, the ABC parameter constraints we obtain in our analysis are consistent with the “true” HOD parameters.

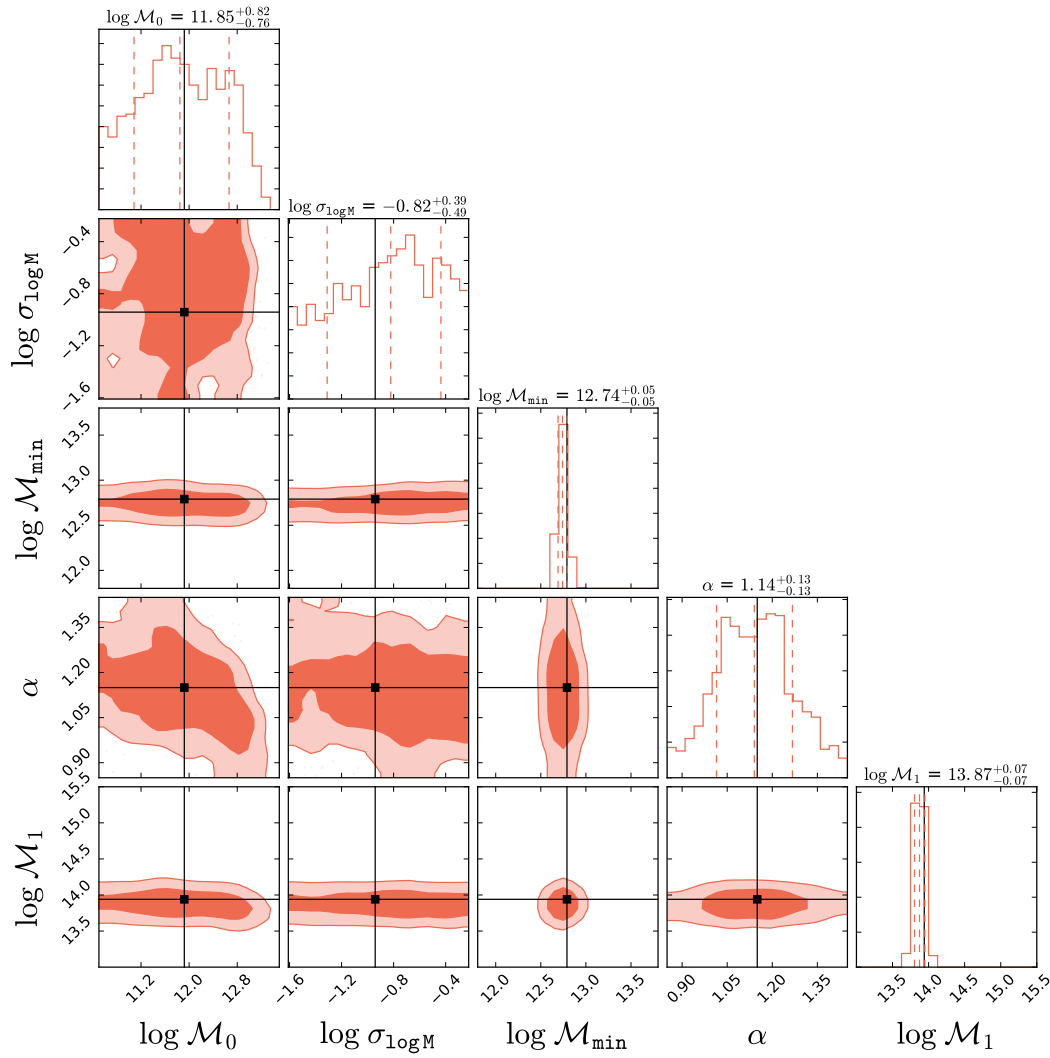


Figure 2.5: Same as Figure 2.4 but for our ABC analysis using  $\bar{n}$  and  $g(N)(N)$  as observables. The ABC parameter constraints we obtain are consistent with the “true” HOD parameters.

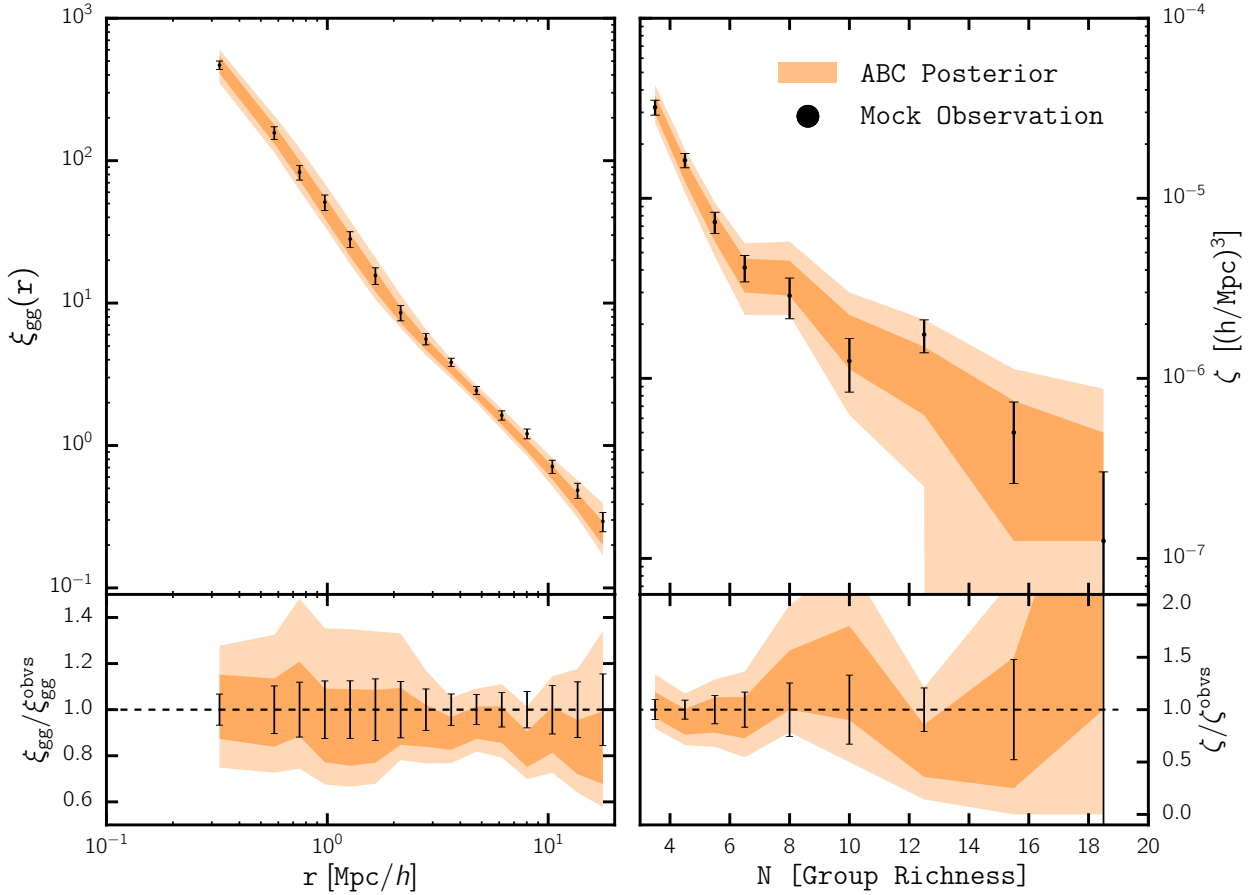


Figure 2.6: We compare the ABC-PMC posterior prediction for the observables  $\xi_{gg}(r)$  (left) and  $g(N)(N)$  (right; Section 2.4.3) to  $\xi_{gg}(r)$  and  $g(N)(N)$  of the mock observation (black) in the top panels. In the lower panels, we plot the ratio between the ABC-PMC posterior predictions for  $\xi_{gg}$  and  $g(N)$  to the mock observation  $\xi_{gg}^{obvs}$  and  $g(N)^{obvs}$ . The darker and lighter shaded regions represent the 68% and 95% confidence regions of the posterior predictions, respectively. The error-bars represent the square root of the diagonal elements of the error covariance matrix (equation 2.14) of the mock observations. Overall, the observables drawn from the ABC-PMC posteriors are in good agreement with  $\xi_{gg}$  and  $g(N)$  of the mock observations. The lower panels demonstrate that for both observables, the error-bars of the mock observations lie within the 68% confidence interval of the ABC-PMC posterior predictions.

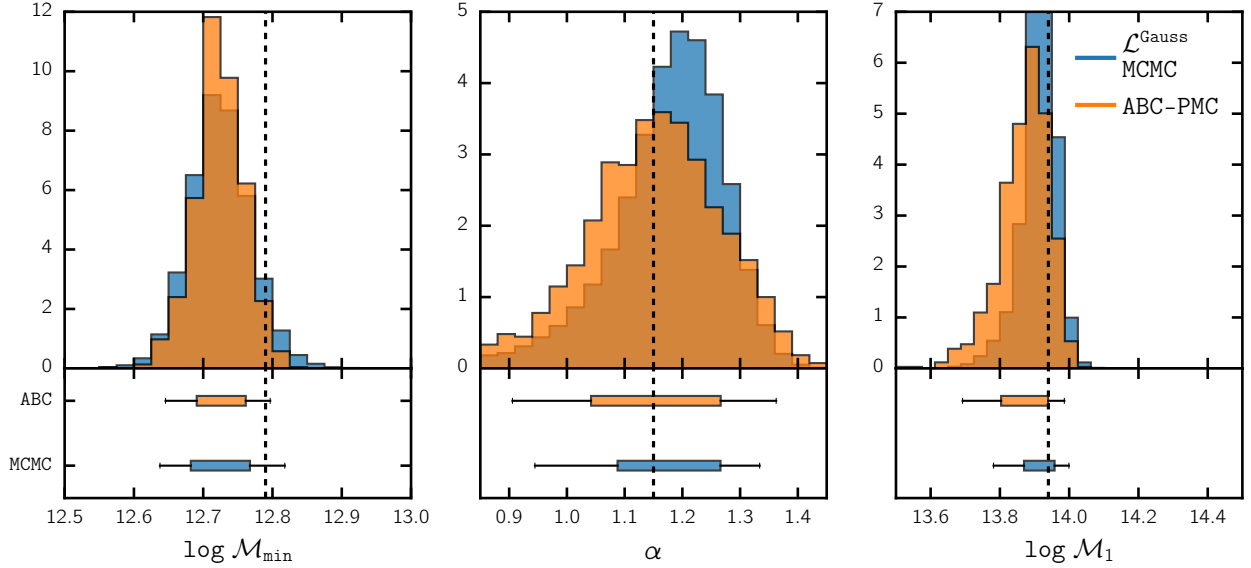


Figure 2.7: We compare the  $\log \mathcal{M}_{\min}$ ,  $\alpha$ , and  $\log \mathcal{M}_1$  parameter constraints from ABC-PMC (orange) to constraints from the Gaussian pseudo-likelihood MCMC (blue) using  $\bar{n}_g$  and  $\xi_{gg}(r)$  as observables. The *top* panels compares the two methods’ marginalized posterior PDFs over the parameters. In the *bottom* panels, we include box plots marking the confidence intervals of the posterior distributions. The boxes represent the 68% confidence interval while the “whiskers” represent the 95% confidence interval. We mark the “true” HOD parameters with vertical black dashed line. The marginalized posterior PDFs obtained from the two methods are consistent with each other. The ABC-PMC and Gaussian pseudo-likelihood constraints are generally consistent for  $\log \mathcal{M}_{\min}$  and  $\log \mathcal{M}_1$ . The ABC-PMC constraint for  $\alpha$  is slightly less biased and has slightly larger uncertainty than the constraint from Gaussian pseudo-likelihood analysis.

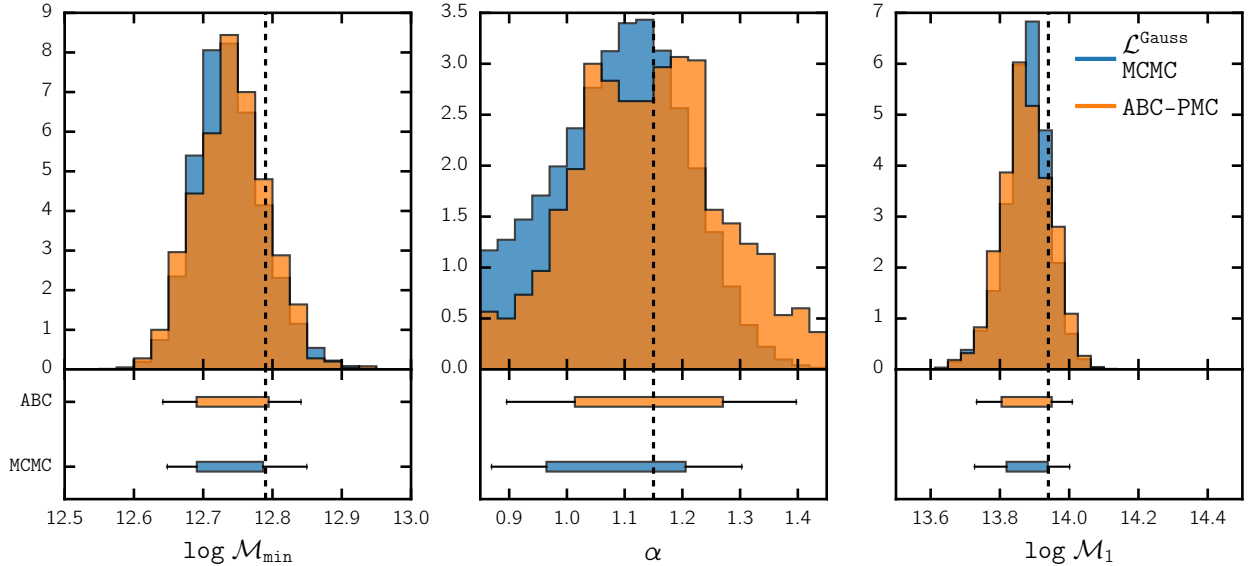


Figure 2.8: Same as Figure 2.7, but both the ABC-PMC analysis and the Gaussian pseudo-likelihood MCMC analysis use  $\bar{n}_g$  and  $g(N)(N)$  as observables. Both methods derive constraints consistent with the “true” HOD parameters and infer the region of allowed values to similar precision. We note that the MCMC constraint on  $\alpha$  is slightly more biased compared to ABC-PMC estimate. This discrepancy may stem from the fact that the use of Gaussian pseudo-likelihood and its associated assumptions is more spurious when modeling the group multiplicity function.

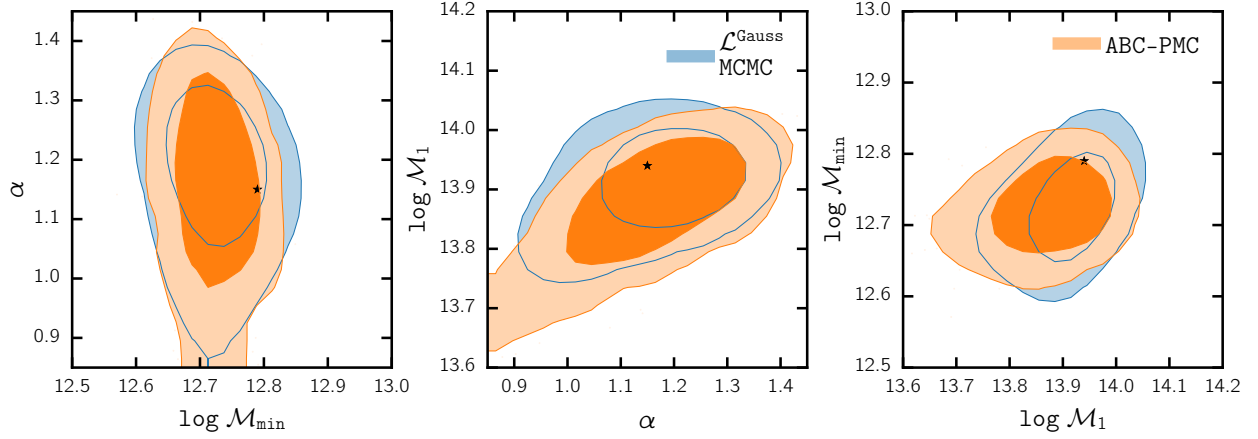


Figure 2.9: We compare the ABC-PMC (orange) and the Gaussian pseudo-likelihood MCMC (blue) predictions of the 68% and 95% posterior confidence regions over the HOD parameters ( $\log \mathcal{M}_{\min}$ ,  $\alpha$ , and  $\log \mathcal{M}_1$ ) using  $\bar{n}_g$  and  $\xi_{gg}(r)$  as observables. In each panel, the black star represents the “true” HOD parameters used to generate the mock observations. Both inference methods derive confidence regions consistent with the “true” HOD parameters.

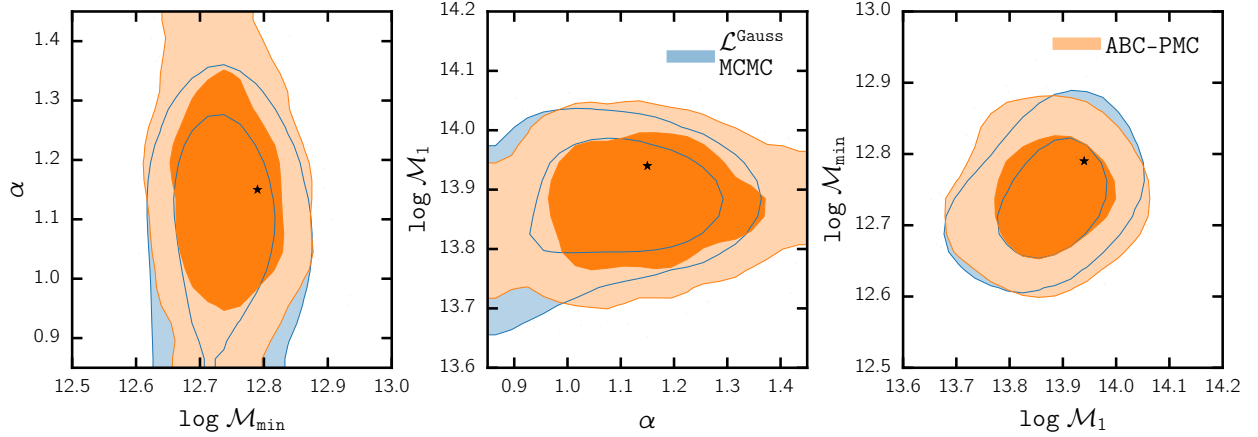


Figure 2.10: Same as Figure 2.9, but using  $\bar{n}_g$  and  $g(N)(N)$  as observables. Again, the confidence regions derived from both methods are consistent with the “true” HOD parameters used to generate the mock observations. The confidence region of  $\alpha$  from the Gaussian pseudo-likelihood method is biased compared to the ABC-PMC contours. This may be due to the fact that the true likelihood function that describes  $g(N)(N)$  deviates significantly from the assumed Gaussian functional form.

# Chapter 3

## How are galaxies assigned to halos? searching for assembly bias in SDSS clustering measurements

This Chapter is joint work with ChangHoon Hahn (NYU) and it is submitted to the *Astrophysical Journal*.

### 3.1 chapter abstract

Clustering of dark matter halos has been shown to depend on halo properties beyond mass such as halo concentration, a phenomenon referred to as halo assembly bias. Standard halo occupation models (HOD) in large scale structure studies assume that halo mass alone is sufficient in characterizing the connection between galaxies and halos.

Modeling of galaxy clustering can face systematic effects if the number of galaxies are correlated with other halo properties. Using the Small MultiDark-Planck high resolution

*N*-body simulation and the measurements of the projected two-point correlation function and the number density of Sloan Digital Sky Survey (SDSS) DR7 main galaxy sample, we investigate the extent to which the dependence of halo occupation on halo concentration can be constrained, and to what extent allowing for this dependence can improve our modeling of galaxy clustering.

From our constraints on HOD with assembly bias, suggests that satellite population is not correlated with halo concentration at fixed halo mass. Furthermore, in terms of the occupation of centrals at fixed halo mass, our results favor lack of correlation with halo concentration in the most luminous samples ( $M_r < -21.5, -21$ ), modest levels of correlation for  $M_r < -20.5, -20, -19.5$  samples, lack of correlation for  $M_r < -19, -18.5$  samples, and anti-correlation for the faintest sample  $M_r < -18$ .

We show that in comparison with abundance-matching mock catalogs, our findings suggest qualitatively similar but modest levels of the impact of halo assembly bias on galaxy clustering. The effect is only present in the central occupation and becomes less significant in brighter galaxy samples. Furthermore, by performing model comparison based on information criteria, we find that in most cases, the standard mass-only HOD model is still favored by the observations.

## 3.2 Introduction

Most theories of cosmology and large-scale structure formation under consideration today rely on the central assumption that galaxies reside in dark matter halos. Detailed study of the galaxy–halo connection is therefore critical in constraining cosmological models (by modeling galaxy clustering at non-linear scales) as well as providing a window into galaxy formation physics. One of the most powerful methods for describing the galaxy–halo connection is the

halo occupation distribution (HOD, see Seljak 2000; Berlind & Weinberg 2002; Scoccimarro et al. 2001; Zheng et al. 2005, 2007; Leauthaud et al. 2012; Tinker et al. 2013; Hearin et al. 2016b; Hahn et al. 2016).

HOD is an empirical framework that provides an analytic prescription for the expected number of galaxies  $N$  that reside in halos by specifying a probability distribution function  $P(N|x)$  where  $x$  is a property of the halo. The standard HOD model assumes that halo mass  $M$  alone is sufficient in determining the galaxy population of a halo. In the standard model, the statistical properties of galaxies is governed by the halo mass. Mathematically, this assumption can be written as  $P(N|M, \{x\}) = P(N|M)$  where  $\{x\}$  is the set of all possible halo properties beyond halo mass  $M$ .

Despite this simplifying assumption, the models of galaxy–halo connection based on HOD have been successfully used in fitting the measurements of a wide range of statistics such as the projected two-point correlation function of galaxies, small scale redshift space distortion, three-point function, and galaxy–galaxy lensing with remarkable success (e.g. Zheng et al. 2007; Tinker 2007; Zehavi et al. 2011; Leauthaud et al. 2012; Parejko et al. 2013; Coupon et al. 2015; Guo et al. 2015; Miyatake et al. 2015; Zu & Mandelbaum 2015; Guo et al. 2016a). HOD has been used in constraining the cosmological parameters through modeling the galaxy two-point correlation function (hereafter 2PCF) (Abazajian et al. 2005), combination of 2PCF with mass-to-light ratio of galaxies (Tinker et al. 2005), redshift space distortions (Tinker 2007), mass-to-number ratio of galaxy clusters (Tinker et al. 2012) galaxy-galaxy weak lensing (van den Bosch et al. 2003; Cacciato et al. 2013; More et al. 2013; van den Bosch et al. 2013) in the main sample of galaxies of the Sloan Digital Sky Survey (hereafter SDSS, York et al. 2000), and also the combination of galaxy clustering and galaxy-galaxy lensing (More et al. 2015) in SDSS III Baryon Oscillation Spectroscopic Survey (BOSS, Dawson et al. 2013). Furthermore, HOD is implemented in producing mock galaxy catalogs

in the BOSS survey (Manera et al. 2013; White et al. 2014). It has also been used in galaxy evolution studies (Conroy & Wechsler 2009; Leauthaud et al. 2012; Behroozi et al. 2013; Hudson et al. 2015; Zu & Mandelbaum 2015, 2016).

The complexity of structure formation however, is not sufficiently modeled under the standard HOD framework. Numerous  $N$ -body simulations that examine the clustering of dark matter halos have demonstrated that halo clustering is correlated with the formation history of halos. That is, at a fixed halo mass, the halo bias is correlated with properties of halos beyond mass, such as the concentration, formation time, or etc. This phenomenon is known as halo assembly bias (see Sheth & Tormen 2004; Gao et al. 2005; Harker et al. 2006; Wechsler et al. 2006; Gao & White 2007; Croton et al. 2007; Wang et al. 2007; Angulo et al. 2008; Dalal et al. 2008; Li et al. 2008; Sunayama et al. 2016). It has been claimed that there is support for halo assembly bias in observations of SDSS redMaPPer galaxy clusters (Miyatake et al. 2016).

Furthermore, the halo occupation may also depend on the formation history of halos. Then we may expect the spatial statistics of galaxies to be tied to the halo properties beyond mass such as the concentration of halos. There have been many attempts in the literature at examining the dependence of halo occupation on environment of the halos. But the results are mixed, and there is very little consensus. Tinker & Conroy (2009) show that the properties of the galaxies that reside in voids can be explained by the halo mass in which they live, and their properties are independent of their large scale environment of the halos. Tinker et al. (2006) proposes an extension of the standard HOD model  $P(N|M)$  such that the number of galaxies residing in a halo not only depends on the mass of the halo, but also on the large scale density contrast  $P(N|M, \delta)$ . Based on modeling the clustering and void statistics of the SDSS galaxies, Tinker et al. (2008) shows that the dependence of the expected number of central galaxies on large scale density is not very strong. By randomly

shuffling the galaxies among host halos of similar mass in the Millenium simulation, Croton et al. (2007) shows that assembly bias significantly impacts the galaxy two-point correlation functions. They also show that the effect is different for the faint and the bright samples.

Another family of empirical galaxy–halo connection models is *Abundance Matching*. In Abundance Matching models, galaxies are assumed to live in halos and are assigned luminosities or stellar masses by assuming a monotonic mapping. In this monotonic mapping, the abundance of the halos are matched to the abundance of some property of galaxies (Kravtsov et al. 2004; Vale & Ostriker 2004; Tasitsiomi et al. 2004; Conroy & Wechsler 2009; Guo et al. 2010; Wetzel & White 2010; Neistein et al. 2011; Watson et al. 2012; Rodríguez-Puebla et al. 2012; Kravtsov 2013; Mao et al. 2015; Chaves-Montero et al. 2016). One of the most commonly used host halo properties in abundance matching is the maximum circular velocity of the host halo  $V_{\max}$  that traces the depth of the gravitational potential well of the halo. Furthermore, a scatter is assumed in this mapping. Within this galaxy–halo connection framework, abundance matching models have been successfully used in modeling a wide range of the statistical properties of galaxies such as two-point correlation function (Reddick et al. 2013; Lehmann et al. 2017; Guo et al. 2016a) as well as the group statistics of galaxies (Hearin et al. 2013).

It has been shown that the abundance matching mock catalogs that use  $V_{\max}$  (see Hearin & Watson 2013; Zentner et al. 2014), or the ones that use some combination of  $V_{\max}$  and host halo virial mass  $M_{\text{vir}}$  (see Lehmann et al. 2017) exhibit significant levels of assembly bias. That is, halo occupation in these models depends not only on halo mass, but also on other halo properties. This has been demonstrated by randomizing the galaxies among host halos in bins of halo mass, such that the HOD remains constant, and then comparing the difference in the 2PCF of the randomized catalog and that of the original mock catalog.

Based on the projected 2PCF measurements of (Hearin & Watson 2013) galaxy catalogs,

Zentner et al. (2014) showed that after fitting the 2PCF measurements of these catalogs with the standard *mass-only* HOD modeling, the inferred HOD does not match the *true* halo occupation of these catalogs. That is, in the presence of assembly bias in a galaxy sample, one can fit the clustering of this sample with the standard *mass-only* HOD, but that does not guarantee recovery of the true HOD parameters.

In this work, we aim to investigate the dependence of halo occupation on halo concentration and how this dependence can be constrained in the low-redshift universe by 2PCF measurements of galaxies in a wide range of luminosities in the SDSS DR7 main galaxy sample.

In order to achieve this goal, we need to adopt a HOD model that takes into account a dependence on halo properties beyond mass. A number of frameworks in the literature (Tinker et al., 2008; Gil-Marín et al., 2011; McEwen & Weinberg, 2016) have proposed environment-dependent HOD models that take into account the large-scale density contrast. In this investigation, we use the following case of the decorated HOD framework (Hearin et al., 2016b). In our decorated HOD framework, at fixed halo mass, halos are populated with galaxies according to the standard HOD model. Then using a secondary halo property, halos are split into two populations in halo mass bins: halos with the highest and lowest secondary property values. Afterwards, based on the assembly bias amplitude parameter, the number of galaxies in the two populations are enhanced or reduced. In this model, the assembly bias parameter is not be degenerate with the rest of the HOD parameters.

The advantage of this framework is that the more complex HOD model is identical to the underlying *mass-only* HOD model in every respect, except that at a fixed halo mass, halos receive enhancement (decrements) in the number of galaxies they host according to the value of their secondary property. In order to constrain assembly bias along with the rest of the HOD parameters, we make use of the publicly available measurements of the projected

2PCF and number density measurements made by (Guo et al. 2015). These measurements made use of the NYU Value-Added Galaxy Catalog (Blanton et al. 2005).

Furthermore, we discuss how taking assembly bias into account in a more complex HOD model can improve our modeling of galaxy clustering in certain brightness limits. Then, we make a qualitative comparison between the levels of the impact of assembly bias in our best-fit decorated HOD model on galaxy clustering, and the impact of assembly bias present in (Hearin & Watson 2013) catalogs on galaxy clustering. Our comparison shows the levels of the impact of assembly bias on galaxy clustering seen in the predictions of both models follow the same trend. That is assembly bias is more prominent in lower luminosity-threshold samples and its impact on galaxy clustering is only significant on large scales (more than a few Mpc).

In order to investigate whether the additional complexity of the decorated HOD model is demanded by the galaxy clustering data, we perform a model comparison between the standard HOD model and the HOD model with assembly bias. We also discuss the effect of our choice of  $N$ -body simulation on our constraints, and previous works in the literature (Zentner et al. 2016) based on smaller  $N$ -body simulations. In addition to analysis of the luminosity-threshold samples presented in Zentner et al. (2016), we consider the faintest ( $M_r < -18, -18.5$ ) and the brightest ( $M_r < -20.5$ ) galaxy samples. For the samples considered in both Zentner et al. (2016) and this investigation, we compare the constraints on the expected levels of assembly bias.

This Chapter is structured as follows: In Section 3.3 we discuss the  $N$ -body simulation, the two halo occupation modeling methods, and the details of the computation of model observables used in this investigation. Then in Section 3.4, we discuss the data used in this study. In Section 3.5 we discuss the details of our inference analysis as well as the results. This includes description of the details of our inference setup. In Section 3.6 we

discuss the constraints and their implications. This includes presentation of the constraints on the parameters of the two models, interpretation of the predictions of our constraints and their possible physical ramifications, assessment of the levels of assembly bias as predicted by our model constraints and its comparison with abundance matching mock catalogs, and finally model comparison. Finally, we discuss and conclude in Section 3.7. Throughout this paper, unless stated otherwise, all radii and densities are stated in comoving units. Standard flat  $\Lambda$ CDM is assumed, and all cosmological parameters are set to the Planck 2015 best-fit estimates.

### 3.3 Method

In this section, we discuss the ingredients of our modeling one-by-one. First, we discuss the simulation used in this study. Afterwards, we talk about the forward modeling of galaxy catalogs in the standard HOD modeling framework as well as the decorated HOD framework. Then, we provide an overview of the two summary statistics of the galaxy catalogs that we used in our inference.

#### 3.3.1 Simulation

For the simulations used in this work, we make use of the Rockstar (Behroozi et al. 2013) halo catalogs in the  $z = 0$  snapshot of the Small MultiDark of Planck cosmology (referred to as SMDP) (Klypin et al. 2016). This high resolution  $N$ -body simulation (publicly available at <https://www.cosmosim.org>) was carried out using the GADGET-2 (see Klypin et al. 2016 and references therein) code, following the Planck  $\Lambda$ CDM cosmological parameters  $\Omega_m = 0.307$ ,  $\Omega_b = 0.048$ ,  $\Omega_\Lambda = 0.693$ ,  $\sigma_8 = 0.823$ ,  $n_s = 0.96$ ,  $h = 0.678$ . The Box size for this  $N$ -body simulation is  $0.4 h^{-1}\text{Gpc}$ , the number of simulation particles is  $3840^3$ , the mass

per simulation particle  $m_p$  is  $9.6 \times 10^7 h^{-1} M_\odot$ , and the gravitational softening length  $\epsilon$  is  $1.5 h^{-1} \text{kpc}$ .

In the **SMDP** simulation, as discussed in Rodríguez-Puebla et al. (2016), the Rockstar algorithm can reliably resolve halos with  $\geq 100$  particles, which corresponds to  $M_{\text{vir}} \geq 9.6 \times 10^9 h^{-1} M_\odot$ .

The **SMDP** simulation provides a number of advantages by satisfying both the size and resolution requirements of studying the galaxy–halo connection in a wide range of luminosity thresholds. For fainter galaxy samples, the faintest galaxies reside in lower mass halos, which requires high resolution. Meanwhile for luminous galaxy samples, their lower number densities requires a large comoving volume.

Furthermore, since we are studying the higher order halo occupation statistics, the concentration-dependence in particular, it is important to use a simulation that can resolve the internal structure of halos.

In the context of Subhalo-Abundance Matching models, which requires subhalo completeness in the low mass limit, the **SMDP** simulation has been used to model the faintest galaxy samples in the SDSS data (see Guo et al., 2016a).

The added advantage of using the **SMDP** simulation over some of the other industrial simulation boxes commonly used in the literature such as **Bolshoi** (Klypin et al. 2011, 2016) simulation is its larger comoving volume. Larger volume makes this simulation more suitable for performing inference with  $L_*$  (corresponding to  $M_r \sim -20.44$ , see Blanton et al. 2003) and more luminous than  $L_*$  galaxy samples that occupy larger comoving volumes.

### 3.3.2 Halo occupation modeling

#### 3.3.2.1 standard model without assembly bias

For our standard HOD model, we assume the HOD parameterization from [Zheng et al. \(2007\)](#). According to this model, a dark matter halo can host a central galaxy and some number of satellite galaxies. The occupation of the central galaxies follows a nearest-integer distribution, and the occupation of the satellite galaxies follows a Poisson distribution. The expected number of centrals and satellites as a function of the host halo mass of  $M_h$  are given by the following equations

$$\langle N_c | M_h \rangle = \frac{1}{2} \left[ 1 + \left( \frac{\log M_h - \log M_{\min}}{\sigma_{\log M}} \right) \right], \quad (3.1)$$

$$\langle N_s | M_h \rangle = \left( \frac{M_h - M_0}{M_1} \right)^\alpha. \quad (3.2)$$

For populating the halos with galaxies, we follow the procedure described in [Hahn et al. \(2016\)](#), and [Hearin et al. \(2016b\)](#). The central galaxies are assumed to be at the center of the host dark matter halos. We assume that the central galaxies are at rest with respect to the bulk motion of the halos and their velocities are given by the velocity of the center of mass of their host halo. Note that this assumption is shown to be violated in brighter than  $L_*$  galaxy samples (see [Guo et al. 2015](#)). But since we are not considering the redshift space 2PCF multipoles in our study, we do not expect this velocity bias to impact our inference. We place the satellite galaxies within the virial radius of the halo following a Navarro-Frenk-White profile (hereafter NFW; [Navarro et al. 2004](#)). This approach is different from other simulation-based halo occupation modeling techniques (see [Guo et al. 2016a; Zheng & Guo 2016](#)) in that the positions of the satellites are not assigned to the dark matter particles in the  $N$ -body simulation.

The concentration of the NFW profile is given by the empirical mass-concentration relation provided by [Dutton & Macciò \(2014\)](#).

The velocities of the satellite galaxies are given by two components. The first component is the velocity of the host halo. The second component is the velocity of the satellite galaxy with respect to the host halo which is computed following the solution to the NFW profile Jeans equations ([More et al. 2009](#)). We refer the readers to [Hearin et al. \(2016b\)](#) for a more comprehensive and detailed discussion of the forward modeling of the galaxy mock catalogs.

### 3.3.2.2 Model with Assembly bias

Now let us provide a brief overview of HOD modeling with `Heaviside Assemblybias` (referred to as the decorated HOD) introduced in [Hearin et al. \(2016b\)](#). At a fixed halo mass  $M_h$ , halos are split into two populations: population of halos with the 0.5-percentile of highest concentration, and population of halos with 0.5 percentile of lowest concentration. For simplicity, we call the first population “type-1” halos, and the second population “type-2” halos. In the decorated HOD model, the expected number of central and satellite galaxies at a fixed halo mass  $M_h$  in the two populations are given by

$$\langle N_{c,i}|M_h, c \rangle = \langle N_c|M_h \rangle + \Delta N_{c,i}, \quad i = 1, 2 \quad (3.3)$$

$$\langle N_{s,i}|M_h, c \rangle = \langle N_s|M_h \rangle + \Delta N_{s,i}, \quad i = 1, 2 \quad (3.4)$$

where  $\langle N_c|M_h \rangle$  and  $\langle N_s|M_h \rangle$  are given by Eqs [3.1](#) and [3.2](#) respectively, and we have  $\Delta N_{s,1} + \Delta N_{s,2} = 0$ , and  $\Delta N_{c,1} + \Delta N_{c,2} = 0$ . These two conditions ensure the conservation of HOD. At a given host halo mass  $M_h$ , the central occupation of the the two populations follows a nearest-integer distribution with the first moment given by [3.3](#); and the satellite occupation

of the two populations follows a Poisson distribution with the first moment given by 3.4.

In this occupation model, the allowable ranges that quantities  $\Delta N_{c,1}$  and  $\Delta N_{s,1}$  can take are given by

$$\max\{-\langle N_c|M_h\rangle, \langle N_c|M_h\rangle - 1\} \leq \Delta N_{c,i} \leq \min\{\langle N_c|M_h\rangle, 1 - \langle N_c|M_h\rangle\}, \quad (3.5)$$

$$-\langle N_s|M_h\rangle \leq \Delta N_{s,i} \leq \langle N_s|M_h\rangle. \quad (3.6)$$

Afterwards, the assembly bias parameter  $\mathcal{A}$  is defined in the following way:

$$\Delta N_{\alpha,1}(M_h) = |\mathcal{A}_\alpha| \Delta N_{\alpha,1}^{\max}(M_h) \text{ if } \mathcal{A}_\alpha > 0, \quad (3.7)$$

$$\Delta N_{\alpha,1}(M_h) = |\mathcal{A}_\alpha| \Delta N_{\alpha,1}^{\min}(M_h) \text{ if } \mathcal{A}_\alpha < 0, \quad (3.8)$$

where the subscript  $\alpha = c, s$  stands for the centrals and satellites respectively, and  $\Delta N_{\alpha,1}^{\max}(M_h), \Delta N_{\alpha,1}^{\min}(M_h)$  are given by Eqs. 3.5 and 3.6.

For a given  $\mathcal{A}_\alpha$ , once  $\Delta N_{\alpha,1}$  is computed using equation (3.7)—if  $\mathcal{A}_\alpha > 0$ —or equation (3.8)—if  $\mathcal{A}_\alpha < 0$ —,  $\Delta N_{\alpha,2} = 1 - \Delta N_{\alpha,1}$  is computed. At a fixed halo mass  $M_h$ , once the first moments of occupation statistics for the *type-1* and *type-2* halos are determined, we perform the same procedure described in 3.3.2.1 to populate the halos with mock galaxies.

### 3.3.2.3 Redshift-space distortion

Once the halo catalogs are populated with galaxies, the real-space positions and velocities of all mock galaxies are obtained. The next step is applying a redshift-space distortion transformation by assuming plane-parallel approximation. Our use of plane parallel approximation is justified because of the narrow redshift range of the SDSS main galaxy sample

considered in this study. If we assume that the  $\hat{z}$  axis is the line-of-sight direction, then with the transformation  $(X, Y, Z) \rightarrow (S_x, S_y, S_z) = (X, Y, Z + v_z(1+z)/H(z))$  for each galaxy with the real space coordinates  $(X, Y, Z)$ , velocities  $(v_x, v_y, v_z)$ , and redshift  $z$ , we obtain the redshift-space coordinate of the produced mock galaxies. Here we assume  $z \simeq 0$ , and therefore transformation is given by  $(X, Y, Z) \rightarrow (X, Y, Z + v_z/H_0)$ .

### 3.3.3 Model Observables

As described in [Hearin et al. \(2016b\)](#) and [Hahn et al. \(2016\)](#), this approach makes no appeal to the fitting functions used in the analytical calculation of the 2PCF. The accuracy of these fitting functions is limited ([Tinker et al. 2008, 2010; Watson et al. 2013](#)). Our approach also does not face the known issues of the treatment of halo exclusion and scale-dependent bias that can lead to potential inaccuracies in halo occupation modeling (see [van den Bosch et al. 2013](#)).

The projected 2PCF  $w_p(r_p)$  can be computed by integrating the 3D redshift space 2PCF  $\xi(r_p, \pi)$  along the line-of-sight (where  $r_p$  and  $\pi$  denote the projected and line-of-sight separation of galaxy pairs respectively):

$$w_p(r_p) = 2 \int_0^{\pi_{max}} \xi(r_p, \pi) d\pi \quad (3.9)$$

For our 2PCF calculations, we use the  $w_p$  measurement functionality of the fast and publicly available pair-counter code `CorrFunc` ([Sinha 2016](#), available at <https://github.com/manodeep/Corrfunc>). To be consistent with the SDSS measurements described in Section 3.4,  $w_p(r_p)$  is obtained by the line-of-sight integration to  $\pi_{max} = 40 h^{-1}\text{Mpc}$ . Note that  $w_p(r_p)$  is measured in units of  $h^{-1}\text{Mpc}$ . To be consistent with [Guo et al. \(2015\)](#), we use the same binning (as specified in Section 3.4) to measure  $w_p$ . In addition to the projected 2PCF,

we use the number density given by the number of mock galaxies divided by the comoving volume of the SMDP simulation.

Note that a full forward model of the data requires running the simulation at different redshifts, generation of light cones, accounting for the complex survey geometry and systematic errors such as fiber collisions. Using the  $z = 0$  output of the SMDP simulation in our forward model of the spatial distribution of galaxies is only an approximation. This approximation can be justified by the small redshift range of the SDSS DR7 main galaxy sample. As described in [Zehavi et al. 2011](#), using random catalogs with angular window function of the data in measurements of galaxy clustering accounts for the geometry of the data. As described in Section 3.4, the fiber collision correction method of [Guo et al. 2012](#) is applied to the SDSS clustering measurements used in this study. Therefore we do not account for that effect in our forward model.

## 3.4 Data

We focus on the measurements made on the volume-limited luminosity-threshold main sample of galaxies in the SDSS spectroscopic survey. In this section, we briefly describe the measurements used in our study for finding constraints on the assembly bias as well as the HOD parameters.

The measurements consist of the number density  $n_g$  and the projected 2PCF  $w_p(r_p)$  made by [Guo et al. \(2015\)](#) for the volume-limited sample of galaxies in NYU Value Added Galaxy Catalog ([Blanton et al. 2005](#)) constructed from the SDSS DR7 main galaxy sample ([Abazajian et al. 2009](#)). In particular, eight volume-limited luminosity-threshold samples are constructed with maximum absolute luminosity in  $r$ -band of -18, 18.5, -19, -19.5, -20, -20.5, -21, and -21.5. Qualitatively, these samples are constructed in a similar way to those

constructed in [Zehavi et al. \(2011\)](#). For detailed differences between the samples in [Guo et al. \(2015\)](#) and [Zehavi et al. \(2011\)](#), we refer the reader to the Table 1 and Table 2 in those papers respectively.

The projected 2PCFs are measured in 12 logarithmic  $r_p$  bins (in units of  $h^{-1}\text{Mpc}$ ) of width  $\Delta \log(r_p) = 0.2$ , starting from  $r_p = 0.1 h^{-1}\text{Mpc}$ . For all luminosity threshold samples, the integration along the line-of-sight (3.9) are performed to  $\pi_{max} = 40 h^{-1}\text{Mpc}$ .

The 2PCF measurement of each luminosity-threshold sample is accompanied by a covariance matrix constructed using 400 jackknife sub-samples of the data. The number density measurements are also accompanied by uncertainties measured using the jackknife method. Furthermore, the covariance between the number denisty and the projected 2PCF measurements are neglected. As [Norberg et al. \(2009\)](#) shows, parameter estimation using jackknife covariance matrices is conservative as the jackknife method overestimates the errors in the observations.

The advantage of using these measurements is that the effects of fiber collision systematic errors on the two-point statistics are corrected for (with the method described in [Guo et al. 2012](#)), and therefore, these measurements provide accurate small scale clustering measurements. The assembly bias parameters introduced in section 3.3 can have a 10-percent level impacts on galaxy clustering ([Hearin et al. 2016b](#)). Presence of assembly bias in the satellite population impacts the very small-scale clustering ([Hearin et al. 2016b](#)). Moreover as [Sunayama et al. \(2016\)](#) demonstrates, the scale-dependence of the halo assembly bias has a pronounced bump in the 1-halo to 2-halo transition regime ( $1\sim2 h^{-1}\text{Mpc}$ ). This scale can be impacted by fiber collision systematics. Precise investigation of the possible impact of this signal on the galaxy clustering modeling requires accurate measurements of 2PCF on small scales. The method of [Guo et al. \(2012\)](#) is able to recover the true  $w_p$  with  $\sim 6\%$  accuracy in small scales ( $r_p = 0.1 h^{-1}\text{Mpc}$ ) and with  $\sim 2.5\%$  at relatively large scales  $r_p \sim 30 h^{-1}\text{Mpc}$ .

Note that the comoving volume of the  $N$ -body simulation used in this investigation is  $64 \times 10^6 h^{-3} \text{Mpc}^3$  which is larger than the comoving volume of all the luminosity-threshold samples in the SDSS data considered in this study except the two most luminous samples. The comoving volumes of the  $M_r < -21, 21.5$  samples are 71.74 and 134.65 (in units of  $10^6 h^{-3} \text{Mpc}^3$ ) respectively. Since we are not studying very large scale clustering ( $r_{p, \max} \leq 25 h^{-1} \text{Mpc}$ ), using a slightly smaller box for those samples is justified.

## 3.5 Analysis

### 3.5.1 Inference setup

Given the SDSS measurements described in Section 3.4, we aim to constrain the HOD model without assembly bias (described in 3.3.2.1), and the HOD model with assembly bias (described in 3.3.2.2) for each luminosity-threshold sample, by sampling from the posterior probability distribution  $p(\theta|d) \propto p(d|\theta)\pi(\theta)$  where  $\theta$  denotes the parameter vector and  $d$  denotes the data vector. In the standard HOD modeling  $\theta$  is given by

$$\theta = \{\log M_{\min}, \sigma_{\log M}, \log M_0, \alpha, \log M_1\}, \quad (3.10)$$

and in the HOD modeling with assembly bias we have

$$\theta = \{\log M_{\min}, \sigma_{\log M}, \log M_0, \alpha, \log M_1, A_{\text{cen}}, A_{\text{sat}}\}, \quad (3.11)$$

Furthermore, data (denoted by  $d$ ) is the combination of  $[n_g, w_p(r_p)]$ . The negative log-likelihood (assuming negligible covariance between  $n_g$  and  $w_p(r_p)$ ) is given by

$$-2 \ln p(d|\theta) = \frac{[n_g^{\text{data}} - n_g^{\text{model}}]^2}{\sigma_n^2} + \Delta w_p^T \widehat{C^{-1}} \Delta w_p + \text{const.}, \quad (3.12)$$

where  $\Delta w_p$  is a 12 dimensional vector,  $\Delta w_p(r_p) = w_p^{\text{data}}(r_p) - w_p^{\text{model}}(r_p)$ , and  $\widehat{C^{-1}}$  is the estimate of the inverse covariance matrix that is related to the inverse of the jackknife covariance matrix (provided by Guo et al. 2015)  $\widehat{C}^{-1}$ , following Hartlap et al. (2007):

$$\widehat{C^{-1}} = \frac{N - d - 2}{N - 1} \widehat{C}^{-1}, \quad (3.13)$$

where  $N = 400$  is the number of the jackknife samples, and  $d = 12$  is the length of the data vector  $w_p$ . Another important ingredient of our analysis is specification of the prior probabilities  $\pi(\theta)$  over the parameters of the halo occupation models considered in this study. For both models, we use uniform flat priors for all the parameters. The prior ranges are specified in the Table 3.5.1. Note that a uniform prior between -1 and 1 is chosen for assembly bias parameters since these parameters are, by definition, bounded between -1 and 1.

For sampling from the posterior probability, given the likelihood function (see equation 3.12) and the prior probability distributions (see Table 3.5.1), we use the affine-invariant ensemble MCMC sampler (Goodman & Weare 2010) and its implementation `emcee` (Foreman-Mackey et al. 2013). In particular, we run the `emcee` code with 20 walkers and we run the chains for at least 10000 iterations. We discard the first one-third part of the chains as burn-in samples and use the remainder of the chains as production MCMC chains. Furthermore, we perform Gelman-Rubin convergence test (Gelman & Rubin 1992) to ensure that the MCMC chains have reached convergence.

Table 3.1: **Prior Specifications:** The prior probability distribution and its range for each of the parameters. All mass parameters are in unit of  $h^{-1}M_{\odot}$ . The parameters marked by \* are only used in the Heaviside Assembly bias modeling and by definition are bounded between -1 and 1.

Parameter	Prior	Range
$\alpha$	Uniform	[0.85, 1.45]
$\sigma_{\log M}$	Uniform	[0.05, 1.5]
$\log M_0$	Uniform	[10.0, 14.5]
$\log M_{\min}$	Uniform	[10.0, 14.0]
$\log M_1$	Uniform	[11.5, 15.0]
$\mathcal{A}_{\text{cen}}^*$	Uniform	[-1.0, 1.0]
$\mathcal{A}_{\text{sat}}^*$	Uniform	[-1.0, 1.0]

## 3.6 Results and Discussion

### 3.6.1 Constraints and Interpretations

In this section, we present the constraints derived for the two assembly bias parameters: the satellite assembly bias parameter ( $\mathcal{A}_{\text{sat}}$ ) and the central assembly bias parameter  $\mathcal{A}_{\text{cen}}$ . As shown in Figure 3.1, for all the eight luminosity-threshold samples in the SDSS DR7 data, our constraints on the parameter  $\mathcal{A}_{\text{sat}}$  are consistent with zero. On the other hand, our constraints on the parameter  $\mathcal{A}_{\text{cen}}$ — albeit not tightly constrained— show a trend which can be summarized as the following. In the most luminous galaxy samples, i.e.  $M_r < -21.5$  and  $M_r < -21$ ,  $\mathcal{A}_{\text{cen}}$  is poorly constrained and the constraints are equivalent to zero. As we investigate less luminous samples,  $M_r < -20.5, -20, -19.5$ , our constraints on  $\mathcal{A}_{\text{cen}}$  shift toward positive values, with the  $M_r < -20$  sample favoring the highest values for  $\mathcal{A}_{\text{cen}}$ . Furthermore, the posterior constraints on the assembly bias parameters in the slightly fainter samples, i.e.  $M_r < -19$  and i.e.  $M_r < -18.5$ , are consistent with zero. In the faintest galaxy sample, i.e.  $M_r < -18$ , our constraints favor negative values of  $\mathcal{A}_{\text{cen}}$ .

The underlying theoretical consideration for explaining the assembly bias of the central and satellite galaxies are different. The large scale clustering—or the two halo term in the galaxy clustering—is mainly governed by the clustering of the central galaxies. The central galaxy clustering can be thought as the weighted average over the halo clustering. The large scale bias of the dark matter halo clustering depends not only on mass, but also on the other properties of halos beyond mass, such as concentration (Wechsler et al. 2006; Gao & White 2007; Miyatake et al. 2016), spin (Gao & White 2007), formation time (Gao & White 2007; Li et al. 2008), and maximum circular velocity of the halo  $V_{\max}$  (Sunayama et al. 2016).

In particular, findings of Wechsler et al. (2006) and Sunayama et al. (2016) have demonstrated that for halos with mass below the collapse mass ( $M \leq M_{\text{col}} \simeq 10^{12.5} M_{\odot}$ ) the large scale bias of high- $V_{\max}$  (or equivalently high- $c$  halos at a fixed halo mass) is larger than that of the low- $V_{\max}$  (low- $c$  halos). This signal reverses and weakens for the high mass halos ( $M \geq M_{\text{col}}$ ). Note that the halo concentration traces the maximum circular velocity  $V_{\max}$  such that halos with higher  $V_{\max}$  have higher concentration and vice versa (see Prada et al. 2012). For halos described by NFW profile, at a fixed halo mass, halos with higher values of concentration have higher values of  $V_{\max}$ .

Furthermore, investigation of the scale dependence of halo assembly bias has shown that the ratio of the bias of high- $V_{\max}$  halos and the low- $V_{\max}$  halos has a bump-like feature in the quasi-linear scales  $\sim 0.5 \text{ Mpc}h^{-1} - 5 \text{ Mpc}h^{-1}$ . From the theoretical standpoint, this phenomenon has been attributed to a population of distinct halos with  $M \sim 10^{11.7} h^{-1} M_{\odot}$  at the present time that are close to the most massive groups and clusters (Sunayama et al. 2016).

Consequently, at a fixed halo mass less than  $M_{\text{col}}$ , assignment of more central galaxies to the high- $c$  halos (higher expected number of central galaxies in the high- $c$  halos) gives rise to a boost in the galaxy clustering in the linear scales as well as in regimes corresponding to

the one-halo to two-halo transition. For the more massive halos ( $M \geq M_{\text{col}}$ ), we expect the large-scale clustering boost to reverse sign, and the quasi-linear bump feature to vanish.

Figure 3.2 demonstrates the 68% and 95% posterior predictions for the projected 2PCF  $w_p$  from the occupation model without assembly bias (shown in red) and the occupation model with assembly bias (shown in blue) for all eight luminosity-threshold samples. For the brightest galaxies,  $M_r < -21.5$  and  $M_r < -21.0$ , the posterior prediction of  $w_p$  from the two models are consistent with one another. Note that these galaxies reside in the most massive halos ( $M > M_{\text{col}}$ ) for which the scale-dependence of the halo assembly bias and the difference between the large-scale bias of the high- $c$  and low- $c$  halos become negligible.

Figure 3.3 shows the fractional difference between the 68% and 95% posterior predictions of  $w_p$  and the SDSS data. It is evident from Figure 3.3 that some improvement on modeling the clustering of the samples of  $L_\star$  and slightly less brighter than  $L_\star$  galaxies can be achieved by employing the more complex halo occupation model with assembly bias. As a result of apportioning more central galaxies to the high- $c$  halos relative to the low- $c$  halos, in the samples with luminosity thresholds of  $M_r < -20.5, -20, -19.5$ , the posterior predictions for  $w_p$  are slightly improved in the intermediate scales ( $1 \sim 2 \text{ Mpc}h^{-1}$ ) and large scales. This can be also noted in significantly lower  $\chi^2$  values—at the cost more model flexibility and higher degrees of freedom—achieved by the assembly bias model in these luminosity-threshold samples (see Table 3.6.1).

In the sample of galaxies with the luminosity threshold  $M_r < -19, -18.5$ , the constraints on  $\mathcal{A}_{\text{cen}}$  become consistent with zero with the tendency towards positive values for the  $M_r < -19$  sample and towards more negative values for the  $M_r < -18.5$  sample. As shown in Figures 3.2 and 3.3, for the  $M_r < -19$  ( $M_r < -18.5$ ) sample this results in slightly higher (lower) posterior predictions for  $w_p$  in the intermediate toward large scales. Overall, for these two samples, the assembly bias parameters remain largely unconstrained and the decorated

HOD model does not yield better  $\chi^2$  values.

Finally, In the faintest sample ( $M_r < -18$ ), negative constraints on the parameter  $\mathcal{A}_{\text{cen}}$  results in higher expected number of centrals in the low- $c$  halos, which at a fixed halo mass, cluster less strongly. This affects both the large scale bias and the intermediate regimes as a result of the scale-dependent bump feature (see Figures 3.2 and 3.3). Furthermore, the model with assembly bias provides better fit to the SDSS data in this luminosity-threshold sample.

The luminosity dependent trend in the constraints on the central assembly bias for the six dimmest samples can be attributed to the fact that the halo concentration is highly correlated with the maximum circular velocity  $V_{\max}$  which is a tracer of the potential well of dark matter halos (Prada et al. 2012). In a dark matter halo described by an NFW profile, the depth of the gravitational potential well of dark matter halos can be directly measured by the maximum circular velocity  $V_{\max}$  (van den Bosch et al. 2014). In particular, the magnitude of the potential well at the center of an NFW halo—where the central galaxy is assumed to reside—scales as  $V_{\max}^2$ . More specifically, we have:

$$\Phi(r = 0) = - \left( \frac{V_{\max}}{0.465} \right)^2, \quad (3.14)$$

where  $\Phi(r = 0)$  is the central potential of an NFW profile. Note that  $V_{\max}$  is also the quantity often used in the abundance matching technique in which the luminosity of galaxies is monotonically matched to  $V_{\max}$  (see for example Reddick et al. 2013; Lehmann et al. 2017; Guo et al. 2016a; Rodríguez-Puebla et al. 2016). The trend between the constraint on  $\mathcal{A}_{\text{cen}}$  and the luminosity threshold of the samples may suggest that at a *fixed halo mass*, the central galaxies in the dimmest samples ( $M_r < -18$ ,  $-18.5$ ) tend to reside in dark matter halos with shallower gravitational well. In brighter galaxy samples ( $M_{\max} < -19$ ,  $-19.5$ ,  $-20$ ,

-20.5), at a *fixed halo mass*, the central galaxies have a tendency to reside in dark matter halos with deeper gravitational potential well.

The satellite assembly bias can only significantly alter the galaxy clustering at small-to-intermediate scales. Assigning more satellite galaxies to lower (or higher) concentration halos affects the one-halo term through increasing the satellite-satellite pair counts  $\langle N_s N_s \rangle$ . This results in boosting the small-scale clustering. But as pointed out by Hearin et al. (2016b), the amount by which small-scale clustering increases also depends on the sign of the central assembly bias parameter  $\mathcal{A}_{\text{cen}}$ . Formation history of the halos can lead to the dependence of the abundance of subhalos on halo concentration (Zentner et al. 2005; Mao et al. 2015) at fixed halo mass, and since the occupation of the satellite galaxies is related to the abundance of subhalos, the satellite occupation may depend on halo concentration.

However, our results suggest that for all the luminosity-threshold samples considered in this study, the satellite assembly bias parameter is largely unconstrained and consistent with zero. We do not expect the galaxy clustering data to be a sufficient statistics for obtaining constraints on the satellite assembly bias. Group statistics probes the high mass end of the galaxy–halo connection and is sensitive to the parameters governing the satellite population (see Hearin et al. 2013; Hahn et al. 2016). Therefore these measurements may shed some light on potential presence of assembly bias in satellite population.

It is important to note that the halo mass range in which the central assembly bias  $\mathcal{A}_{\text{cen}}$  affects the central galaxy population is the mass range in which the condition  $0 < \langle N_c | M \rangle < 1$  is met. Consequently, larger scatter parameter  $\sigma_{\log M}$  increases the dynamical mass range in which assembly bias affects the galaxy clustering. Note that in the luminosity regimes for which we obtain tighter constraints on  $\mathcal{A}_{\text{cen}}$ , the best-estimate values of the scatter parameter  $\sigma_{\log M}$  appear to be higher in the model with assembly bias. This is evident in Figure 3.8. The model with assembly bias tends to push  $\sigma_{\log M}$  to higher values. This can be attributed to the

tendency of this model to increase the effective dynamical mass range of central assembly bias.

As shown in Table 3.6.1, in the HOD model with assembly bias, the constraints found on the scatter parameter are not tight. This is in keeping with the results of Guo et al. (2015) which uses the same SDSS measurements and finds that the scatter parameter remains largely unconstrained when only  $n_g$  and  $w_p$  are used as observables. Note that scatter is better constrained for the most luminous galaxy samples (this is attributed to the steep dependence of the halo bias and halo mass function on halo mass in the high mass end). But since these samples live in the most massive halos, we do not expect the tighter constraints on scatter to help us constrain the central assembly bias parameter. Guo et al. (2015) shows that by employing additional measurements such as the monopole ( $\xi_0$ ), quadrupole ( $\xi_2$ ), and hexadecapole ( $\xi_4$ ), one can obtain tighter constraints on the scatter parameter. Tightening the constraints on the scatter parameter can lead to more precise inference of the central assembly bias parameter.

As shown in Table 3.6.1, our constraints on the underlying standard HOD model obtained from the model with assembly bias and the model without assembly bias are in good agreement. The only cases in which there are mild tensions between the constraints found from the two models on the underlying HOD parameters, are the  $M_r < -20$  and the  $M_r < -20.5$  samples. However, these tensions are still within one-sigma level. For instance, Figure 3.8 shows that in the  $M_r < -20.5$  sample, the constraint on the parameter  $\alpha$  found from the model without assembly bias favor slightly higher values than the constraint found from the model with assembly bias. Also the scatter parameter  $\sigma_{\log M}$  is more tightly constrained in the standard HOD model. However, it is important to emphasize that these constraints are still in agreement with each other within a one-sigma level.

Zentner et al. (2014) shows that in the mock catalogs that exhibit significant levels of

assembly bias, using a simple mass-only occupation model can lead to considerable biases in inference of the galaxy–halo connection parameters. Although we cannot rule out moderate levels of assembly bias in our findings, we do not find any considerable discrepancy between the two models in terms of estimating the underlying HOD parameters.

A few galaxy–halo connection methods have been proposed in the literature that give rise to assembly bias in the galaxy population. Zentner et al. (2014) demonstrates that the abundance matching techniques based on  $V_{\max}$  (Conroy et al., 2006; Hearin & Watson, 2013; Reddick et al., 2013) exhibit some levels of assembly bias.

We aim to provide a comparison between the impact of assembly bias on clustering in these mock catalogs and the mock catalogs predicted from our constraints on the decorated HOD model for  $L_*$ -type galaxies. In particular, we consider the abundance matching catalogs produced by Hearin & Watson (2013). These catalogs have been extensively studied for examining potential systematic effects of galaxy assembly bias on cosmological (McEwen & Weinberg 2016) and halo occupation (Zentner et al. 2014) parameter inferences.

This abundance matching catalog was built based on the *Bolshoi*  $N$ -body simulation (Klypin et al. 2011) using the adaptive refinement tree code (ART Kravtsov et al. 1997). The Box size for this simulation is  $250 h^{-1}\text{Mpc}$ , the number of simulation particles is  $2048^3$ , the mass per simulation particle  $m_p$  is  $1.35 \times 10^8 h^{-1} M_\odot$ , and the gravitational softening length  $\epsilon$  is  $1 h^{-1}\text{kpc}$ . The halos and subhalos in this simulation are identified using the ROCKSTAR algorithm (Behroozi et al. 2013). The Hearin & Watson 2013 catalogs make use of  $V_{\text{peak}}$  (maximum  $V_{\max}$  throughout the assembly history of halo) as the subhalo property to be matched to galaxy luminosity.

As noted by Zentner et al. (2014) and McEwen & Weinberg (2016), these galaxy mock catalogs show significant levels of assembly bias in the central galaxy population. This has been demonstrated by investigating the difference in  $w_p$  between the randomized mock cata-

logs and the original mock catalogs. Randomization is performed in a procedure described in [Zentner et al. \(2014\)](#) which we briefly summarize here: First, halos are divided into different bins of halo mass with width of 0.1 dex. Then all central galaxies are shuffled among all halos within each bin. Once the centrals have been shuffled, within each bin, the satellite systems are shuffled among all halos in that mass bin, preserving their relative distance to the center of halo. This procedure preserves the HOD, but erases any dependence of the galaxy population on the assembly history of halos. Therefore, assembly bias is erased in the randomized galaxy catalog.

For  $L_*$  galaxies, the difference in  $w_p$  between the randomized and the original catalogs of [Hearin & Watson \(2013\)](#) is shown in Figure 3.4 with the red curves. As demonstrated in Figure 3.4 (and as previously noted by [Zentner et al. 2014; McEwen & Weinberg 2016](#)), the relative difference in  $w_p$  is only significant in relatively large scales ( $r_p > 1\text{Mpc } h^{-1}$ ). This implies that in these catalogs, only the central occupation is affected by assembly bias. This is in agreement with our findings.

Furthermore, we investigate whether the impact of assembly bias on galaxy clustering predicted by our findings are in agreement with the abundance matching catalogs of [Hearin & Watson \(2013\)](#). First, we make random draws from the posterior probability distribution function over the parameters of the model with assembly bias. Then, we create mock catalogs with these random draws, and then we compute the difference in  $w_p$  between the randomized catalogs and the original catalogs. The relative difference in  $w_p$  predicted from our constraints are shown with blue curves in Figure 3.4.

We note that our findings follow the same trend. That is, we see negligible difference in the small scale clustering and more considerable differences in  $w_p$  on larger scales ( $r_p > 1 \text{ Mpc} h^{-1}$ ). Similar to findings of [Zentner et al. \(2014\)](#), [Lehmann et al. \(2017\)](#), and [McEwen & Weinberg \(2016\)](#), we see that the impact of assembly bias on galaxy clustering becomes

less significant in brighter galaxy samples. Furthermore, we notice that our mock catalogs favor more moderate changes in galaxy clustering as a result of assembly bias.

### 3.6.2 model comparison

We want to address this question that whether the constraints on the model with assembly bias and the model without assembly bias given the galaxy clustering data lead us to claim that assembly bias is strongly supported by the observations or not. Within the standard HOD framework, the distribution of the galaxies is modeled using a simple description based on the *mass-only* ansatz:  $P(N|M)$ . The decorated HOD model however, provides a more complex description of the data by adding a secondary halo property (halo concentration in this study) and a more flexible occupation model:  $P(N|M, c)$ .

In order to investigate whether the higher level of model complexity is demanded by the observations or not, we present model comparison between the models with and without assembly bias. In particular, we make use of two simple methods for model comparison: *Akaike Information Criterion* (AIC, [Akaike 1974](#), see [Gelman et al. 2013](#) for detailed discussion on AIC), and *Bayesian Information Criteria* (BIC, [Schwarz 1978](#)). BIC and AIC are more computationally tractable than alternatives approaches such as computing the fully marginalized likelihood. The underlying assumption of these information criteria is that models that yield higher likelihoods are more preferable, but at the same time, models with more flexibility are penalized.

Suppose that  $\mathcal{L}^*$  is the maximum likelihood achieved by the model,  $N_{\text{par}}$  is the number of free parameters in the model, and  $N_{\text{data}}$  is the number of data points in the data set. Then we have

Table 3.2: **Constraints**: Constraints on the parameters of the HOD models with and without assembly bias. All mass parameters are in unit of  $h^{-1}M_{\odot}$ . The best-estimates and the error bars correspond to the 50% quantile and 68% confidence intervals obtained from the marginalized posterior probability pdfs. The last column is  $\chi^2$  per degrees of freedom ( $dof$ ), where  $dof = N_{data} - N_{par}$

$M_{r,\text{lim}}$	$\log M_{\text{min}}$	$\sigma_{\log M}$	$\log M_0$	$\alpha$	$\log M_1$	$\mathcal{A}_{\text{cen}}$	$\mathcal{A}_{\text{sat}}$	$\chi^2/\text{dof}$
-18	$11.56^{+0.21}_{-0.25}$	$1.05^{+0.31}_{-0.52}$	$10.84^{+0.77}_{-0.59}$	$0.98^{+0.05}_{-0.05}$	$12.50^{+0.10}_{-0.10}$	—	—	14.51/8
-18	$11.53^{+0.23}_{-0.21}$	$1.08^{+0.28}_{-0.51}$	$10.86^{+0.81}_{-0.62}$	$0.97^{+0.05}_{-0.04}$	$12.56^{+0.09}_{-0.10}$	$-0.67^{+0.55}_{-0.25}$	$-0.30^{+1.09}_{-0.54}$	7.52/6
-18.5	$11.67^{+0.29}_{-0.25}$	$0.83^{+0.45}_{-0.53}$	$10.85^{+0.64}_{-0.60}$	$1.02^{+0.04}_{-0.04}$	$12.69^{+0.08}_{-0.08}$	—	—	6.17/8
-18.5	$11.60^{+0.31}_{-0.20}$	$0.74^{+0.49}_{-0.46}$	$10.73^{+0.69}_{-0.51}$	$1.01^{+0.05}_{-0.05}$	$12.72^{+0.09}_{-0.10}$	$0.02^{+0.67}_{-0.62}$	$0.07^{+0.53}_{-0.59}$	6.23/6
-19	$11.74^{+0.37}_{-0.18}$	$0.62^{+0.52}_{-0.39}$	$10.82^{+0.62}_{-0.56}$	$1.04^{+0.04}_{-0.04}$	$12.87^{+0.09}_{-0.09}$	—	—	8.69/8
-19	$11.71^{+0.37}_{-0.16}$	$0.58^{+0.53}_{-0.38}$	$10.75^{+0.66}_{-0.52}$	$1.03^{+0.04}_{-0.05}$	$12.90^{+0.10}_{-0.09}$	$0.36^{+0.44}_{-0.62}$	$-0.01^{+0.56}_{-0.54}$	8.87/6
-19.5	$11.78^{+0.37}_{-0.13}$	$0.51^{+0.53}_{-0.31}$	$11.09^{+0.69}_{-0.73}$	$1.06^{+0.03}_{-0.04}$	$13.03^{+0.08}_{-0.07}$	—	—	6.80/8
-19.5	$11.82^{+0.41}_{-0.17}$	$0.62^{+0.54}_{-0.44}$	$11.11^{+0.68}_{-0.77}$	$1.03^{+0.04}_{-0.06}$	$13.03^{+0.10}_{-0.08}$	$0.52^{+0.32}_{-0.47}$	$-0.01^{+0.66}_{-0.49}$	5.56/6
-20	$12.01^{+0.17}_{-0.08}$	$0.32^{+0.32}_{-0.19}$	$11.69^{+0.54}_{-0.99}$	$1.08^{+0.03}_{-0.05}$	$13.32^{+0.08}_{-0.07}$	—	—	13.45/8
-20	$12.23^{+0.39}_{-0.24}$	$0.76^{+0.41}_{-0.43}$	$11.66^{+0.62}_{-0.94}$	$1.00^{+0.08}_{-0.05}$	$13.26^{+0.08}_{-0.09}$	$0.81^{+0.12}_{-0.26}$	$-0.15^{+0.33}_{-0.31}$	8.12/6
-20.5	$12.31^{+0.06}_{-0.06}$	$0.21^{+0.14}_{-0.11}$	$12.36^{+0.27}_{-0.77}$	$1.11^{+0.08}_{-0.08}$	$13.56^{+0.09}_{-0.09}$	—	—	11.40/8
-20.5	$12.37^{+0.16}_{-0.09}$	$0.44^{+0.28}_{-0.26}$	$12.38^{+0.27}_{-0.54}$	$1.05^{+0.08}_{-0.07}$	$13.60^{+0.10}_{-0.08}$	$0.81^{+0.15}_{-0.43}$	$-0.11^{+0.26}_{-0.27}$	6.82/6
-21	$12.73^{+0.14}_{-0.07}$	$0.32^{+0.22}_{-0.17}$	$12.62^{+0.48}_{-1.36}$	$1.17^{+0.10}_{-0.16}$	$14.01^{+0.08}_{-0.10}$	—	—	7.34/8
-21	$12.81^{+0.28}_{-0.11}$	$0.47^{+0.41}_{-0.25}$	$12.51^{+0.61}_{-1.17}$	$1.08^{+0.17}_{-0.13}$	$14.02^{+0.08}_{-0.10}$	$0.33^{+0.51}_{-0.64}$	$-0.18^{+0.41}_{-0.35}$	7.21/6
-21.5	$13.44^{+0.11}_{-0.09}$	$0.60^{+0.09}_{-0.11}$	$12.57^{+0.77}_{-1.27}$	$1.33^{+0.07}_{-0.21}$	$14.53^{+0.05}_{-0.07}$	—	—	3.29/8
-21.5	$13.43^{+0.12}_{-0.06}$	$0.60^{+0.12}_{-0.08}$	$12.59^{+0.64}_{-1.25}$	$1.27^{+0.11}_{-0.19}$	$14.54^{+0.05}_{-0.05}$	$-0.24^{+0.50}_{-0.40}$	$-0.30^{+0.86}_{-0.49}$	3.37/6

$$\text{BIC} = -2 \ln \mathcal{L}^* + N_{\text{par}} \ln N_{\text{data}}, \quad (3.15)$$

$$\text{AIC} = -2 \ln \mathcal{L}^* + 2N_{\text{par}}. \quad (3.16)$$

Given a data set, models with lower value of AIC and BIC are more desired. That is, in order for the higher model complexity (given by  $N_{\text{par}}$ ) to be justified,  $\mathcal{L}^*$  must be sufficiently higher. Therefore in this formulation, models that deliver lower information criteria scores are more preferable.

Figure 3.5 shows the comparison between the BIC and AIC scores for the model with assembly bias and the model without assembly bias. We note that the model without assembly bias is still preferable by the galaxy clustering observations. That is, although some improvements to fitting the clustering data can be achieved as a result of using a more complicated occupation model, these improvements are not significant enough to justify the use of a more complicated model that takes assembly bias into account.

We note that both AIC and BIC scores improve in the luminosity-threshold samples for which, we have tighter constraints over the central assembly bias parameter. In particular, the model with assembly bias deliver *only slightly* lower AIC scores for the  $M_r < -18, -20$  samples. This supports our intuition that AIC and BIC penalize unconstrained parameters. Also note that, the difference between both BIC and AIC scores are marginal.

### 3.6.3 choice of simulation

Given the SDSS clustering measurements described in Section 3.4, We repeat the inference of the assembly bias parameters  $\mathcal{A}_{\text{sat}}$  and  $\mathcal{A}_{\text{cen}}$  with the `BolshoiP` simulation (Klypin et al. 2016). This  $N$ -body simulation is carried out with similar setting as the `Bolshoi` sim-

ulation with the exception that in the `BolshoiP` simulation, Planck cosmology is adapted and the mass per simulation particle is  $1.49 \times 10^8 h^{-1} M_\odot$ .

The summary of constraints are shown in Figure 3.6. In Figure 3.6, the constraints from the `SMDP` and the `BolshoiP` simulations are shown with circles and crosses respectively. Additionally, the upper and lower bounds on the inferred parameters reported by Zentner et al. (2016) are shown in shaded blue regions. In the case of central assembly bias, all three constraints are consistent. For the luminosity-threshold samples  $M_r < -20.5, -20, -19.5$ , where the central assembly bias parameters are strongly positive, the constraints obtained from the `SMDP` simulation are tighter.

In the case of the satellite assembly bias parameters however, constraints from the `BolshoiP` simulation for the luminosity threshold samples  $M_r < -20.5, -19$  favor more positive values of the parameter, while our constraints from the `SMDP` simulation for these two luminosity thresholds favor zero satellite assembly bias. As it is shown in the lower panel of Figure 3.6, our constraints from the `BolshoiP` simulations for the  $M_r < -21, -20.5, -20, -19.5, -19$  samples are consistent with the lower and upper bounds (shown with the shaded blue region) reported by Zentner et al. (2016) that uses the same simulation but different  $w_p$  measurements (Zehavi et al. 2011). Therefore, there is some discrepancy between our  $\mathcal{A}_{\text{sat}}$  constraints using the `SMDP` simulation and the `BolshoiP` simulations.

For the  $M_r < -19, -20.5$  samples, the marginalized posterior PDFs over  $\mathcal{A}_{\text{sat}}$  from the two simulations are shown in Figure 3.7. Note that  $\mathcal{A}_{\text{sat}}$  is poorly constrained in both simulations and for both luminosity-threshold samples. For the  $M_r < -19$  sample, considering how poorly constrained the parameters are, the discrepancy between the constraints is not very stark. Note that the tension is still at a one-sigma level. The discrepancy however, becomes more pronounced in the  $M_r < -20.5$  sample.

In terms of the effect of assembly bias on galaxy clustering, note that mocks created using the inferred parameters with the `SMDP` simulation show the same behavior as we observe in the abundance matching catalogs presented in [Zentner et al. \(2014\)](#) and [Lehmann et al. \(2017\)](#). That is, the difference in  $w_p$  between the mock catalogs and the randomized catalogs is mostly on large scales where the clustering is governed by the central galaxies. That is, the impact of assembly bias on the satellite occupation is negligible and only the central occupation is affected.

## 3.7 Summary and Conclusion

In this investigation, we provide constraints on the concentration-dependence of halo occupation for a wide range of galaxy luminosities in the SDSS data. In particular, the modeling is done in the context of the decorated HOD model [Hearin et al. \(2016b\)](#), and the data used in this investigation is the projected 2PCF measurements published by [Guo et al. \(2015\)](#). We make use of `SMDP` high resolution  $N$ -body simulation that enables us to reliably perform inference for the faintest galaxy samples in the SDSS DR7 catalog that live in low mass halos, and the brightest galaxy samples that occupy large comoving volumes.

Our findings suggest that the satellite assembly bias remains consistent with zero. However, our constraints on the central assembly bias parameter exhibit a trend with the luminosity limits of the galaxy samples. For the brightest samples, central assembly bias is consistent with zero, which is in agreement with this picture that the halo assembly bias becomes negligible for the most massive halos.

For the  $M_r < -20.5, -20, -19.5$  samples, at a fixed halo mass, we find positive correlation between the central population and halo concentration at fixed halo mass. For  $M_r < -19, -18.5$  we find no correlation, and for the faintest sample, we find negative corre-

lation. Given the large scale halo assembly bias and the scale-dependent feature of assembly bias in the quasi-linear scales, our constraints on the more flexible HOD model lead to improvement in modeling the galaxy clustering. However, we do not find these improvements to be sufficient to lower the information criteria scores associated with the more complex model. The exceptions are the  $M_r < -20, -18$  luminosity-threshold samples for which we find the strongest constraints on the central assembly bias. For these two samples, the HOD model with assembly bias yields lower BIC score than the model without assembly bias.

We compare the impact of assembly bias on galaxy clustering between the catalogs constructed from our results and the abundance matching catalogs presented in [Hearin & Watson \(2013\)](#); [Zentner et al. \(2014\)](#). We demonstrate that the effect of assembly bias on galaxy clustering predicted from our results is similar to (but more moderate than) the effects seen in the abundance matching catalogs of [Hearin & Watson \(2013\)](#). That is, assembly bias mostly affects the large scales and the quasi-linear clustering and the small scale clustering remains unaltered. In addition, the effect of assembly bias on galaxy clustering vanishes in the brightest galaxy samples.

Moreover, we repeat our inference using the `BolshoiP` simulation. We find that our findings based on the `BolshoiP` simulation are consistent with constraints reported by [Zentner et al. \(2016\)](#) (in the  $M_r < -21, -20.5, -20, -19.5, -19$  luminosity-threshold samples) that predicts positive satellite assembly bias (correlation between the expected number of satellites and  $V_{\max}$  at fixed host halo mass) for the  $M_r < -19, -20.5$  samples. However, we note that the results based on the `SMDP` simulation are more consistent with the picture provided by the previous models based on the abundance matching technique (e.g. [Zentner et al. 2014](#); [Lehmann et al. 2017](#)). That is, only the large-scale clustering, governed by the centrals, is affected by assembly bias.

## Acknowledgments

We are grateful to David W. Hogg, Alex I. Malz, Andrew Hearin, Andrew Zentner, Chia-Hsun Chuang, Michael R. Blanton, and Kilian Walsh for discussions related to this work. This work was supported by the NSF grant AST-1517237. All the computations in this work were carried out in the New York University High Performance Computing Mercer facility. We thank Shenglong Wang, the administrator of the NYU HPC center for his continuous and consistent support throughout the completion of this study.

The CosmoSim database used in this paper is a service by the Leibniz-Institute for Astrophysics Potsdam (AIP). The MultiDark database was developed in cooperation with the Spanish MultiDark Consolider Project CSD2009-00064. The authors gratefully acknowledge the Gauss Centre for Supercomputing e.V. ([www.gauss-centre.eu](http://www.gauss-centre.eu)) and the Partnership for Advanced Supercomputing in Europe (PRACE, [www.prace-ri.eu](http://www.prace-ri.eu)) for funding the MultiDark simulation project by providing computing time on the GCS Supercomputer SuperMUC at Leibniz Supercomputing Centre (LRZ, [www.lrz.de](http://www.lrz.de)).

All of the code written for this project is available in an open-source code repository at <https://github.com/mjvakili/gambly>. The SDSS clustering measurements and the covariance matrices used in this work are available at [http://sdss4.shao.ac.cn/guoh/files/wpxi\\_measurements\\_Guo15.tar.gz](http://sdss4.shao.ac.cn/guoh/files/wpxi_measurements_Guo15.tar.gz). Description of the SMDP and the BolshoiP halo catalogs used in this investigation can be found at <https://www.cosmosim.org/cms/simulations>. The RockStar halo catalogs of the SMDP and the BolshoiP simulations are publicly available at <http://yun.ucsc.edu/sims/SMDPL/hlists/index.html> and [http://yun.ucsc.edu/sims/Bolshoi\\_Planck/hlists/index.html](http://yun.ucsc.edu/sims/Bolshoi_Planck/hlists/index.html) respectively. We thank Peter Behroozi for making the halo catalogs publicly available. In this work we have made use of the publicly available codes: corner (Foreman-Mackey 2017), emcee (Foreman-Mackey et al. 2013), halotools (Hearin et al. 2016a), Corrfunc (Sinha 2016), and changtools

(<https://github.com/changhoonhahn/ChangTools>). The abundance matching mock catalogs used in this study are available at (<http://logrus.uchicago.edu/~aphearin/>).

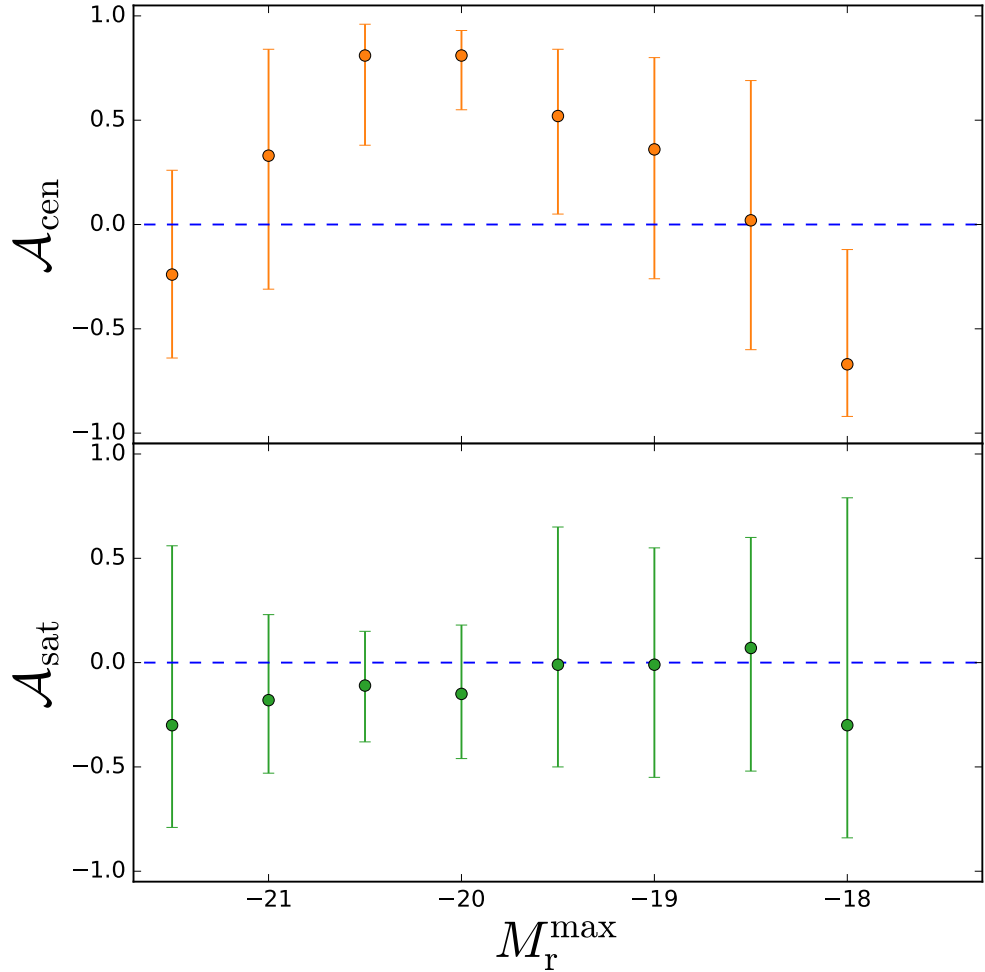


Figure 3.1: Constraints on the central assembly bias  $\mathcal{A}_{\text{cen}}$  (Top panel) and the satellite assembly bias  $\mathcal{A}_{\text{sat}}$  (Bottom panel) parameters. The  $\mathcal{A}_{\text{cen}}$  constraints for the  $M_r < -20.5, -20, -19.5$  samples favor positive values of  $\mathcal{A}_{\text{cen}}$  with the tightest constraint coming from the  $M_r < -20$  sample. The  $\mathcal{A}_{\text{cen}}$  constraints for the  $M_r < -18$  sample favor negative values of  $\mathcal{A}_{\text{cen}}$ . All the  $\mathcal{A}_{\text{sat}}$  constraints are consistent with no satellite assembly bias.

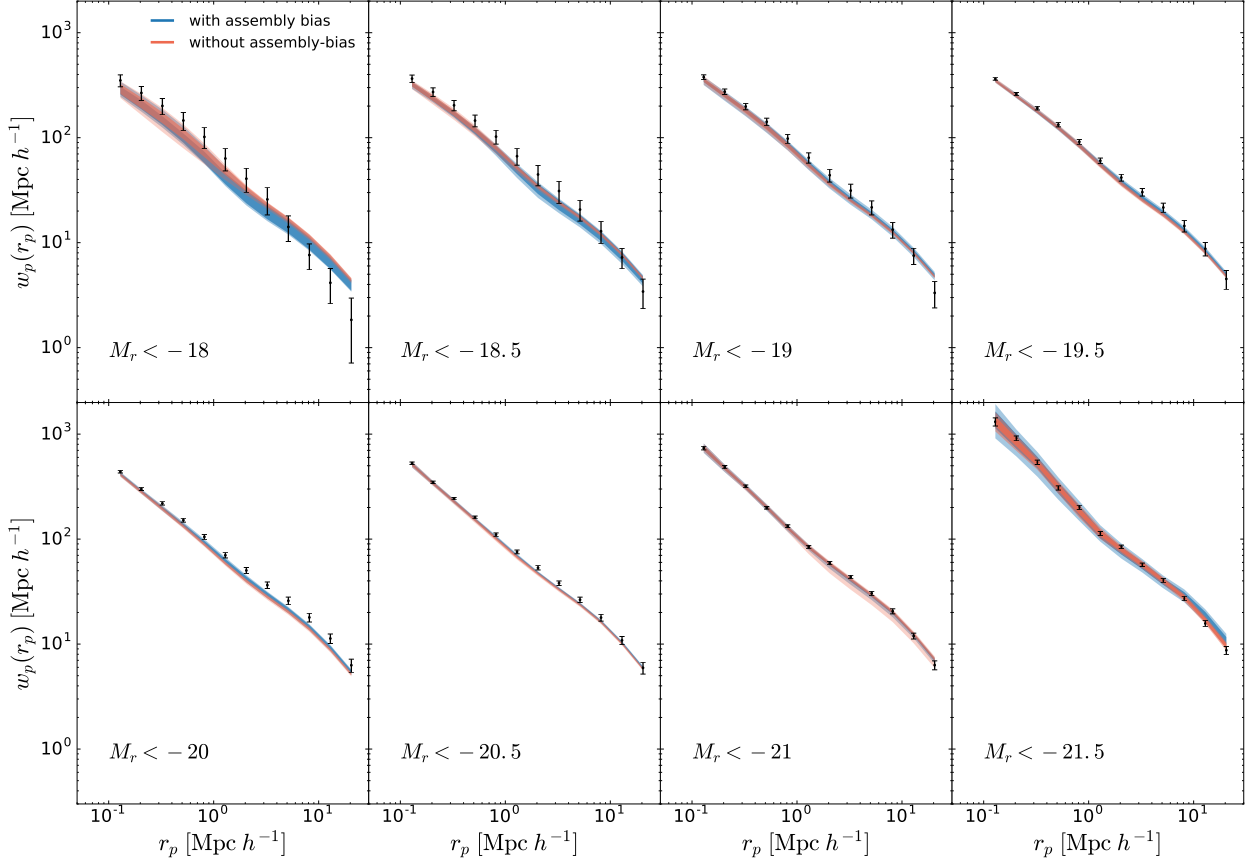


Figure 3.2: Comparison between the posterior predictions of  $w_p(r_p)$  and the SDSS  $w_p(r_p)$  measurements. Predictions from the standard HOD model (HOD model with assembly bias) are shown in red (blue). The Dark and light shaded regions mark the 68% and the 95% confidence intervals. The errorbars are from the diagonal elements of the covariance matrix.

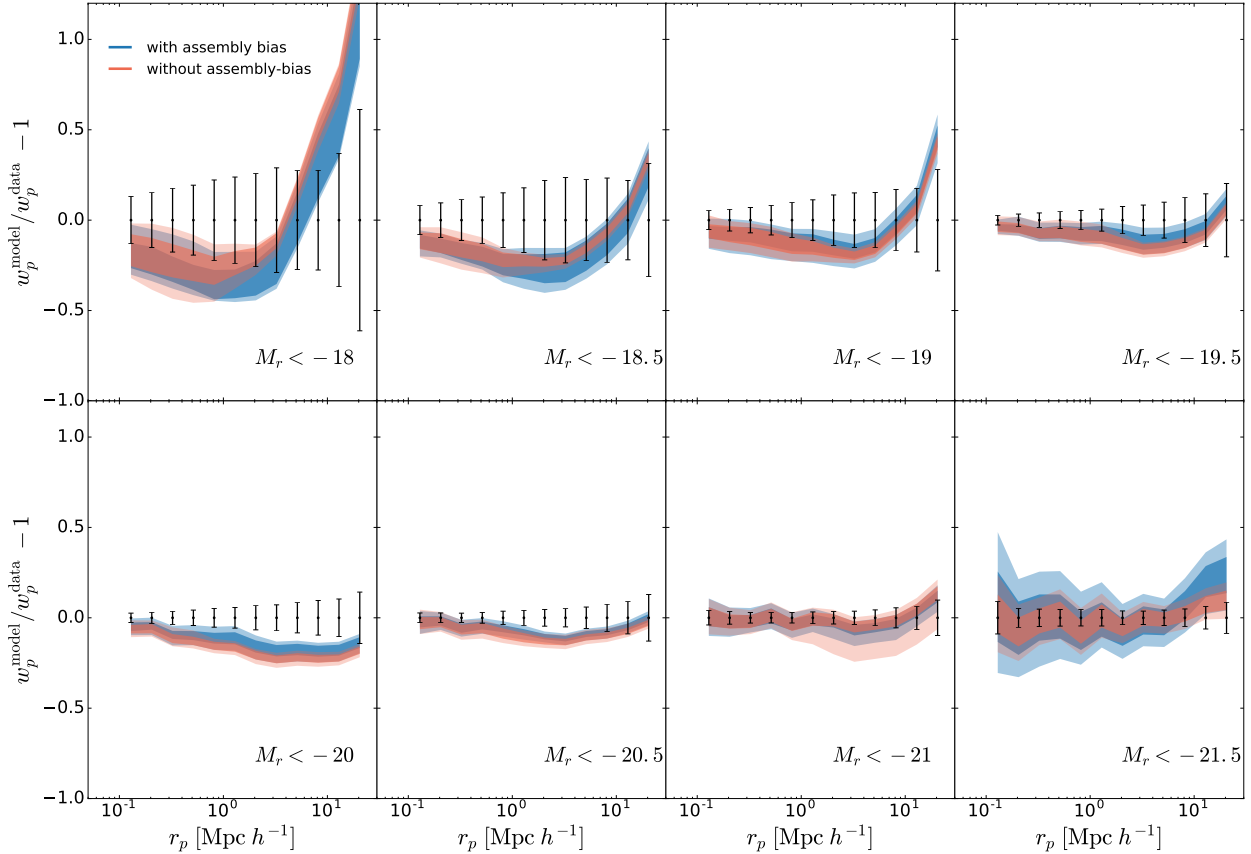


Figure 3.3: Same as Figure 3.2, but showing the fractional difference between the posterior predictions and the observed projected 2PCF for all the luminosity threshold samples. In all luminosity threshold samples, predictions of the two models for small scale clustering are consistent. In the samples that favor more positive values of the central assembly bias parameter ( $M_r < -19.5, -19, -20, -20.5$ ), modeling of the intermediate and large scale clustering is slightly improved. The large scale clustering modeling of the  $M_r < -18$  sample is also improved because of negative constraints on  $\mathcal{A}_{\text{cen}}$  which is equivalent to allocation of more central galaxies in low concentration halos at fixed halo mass.

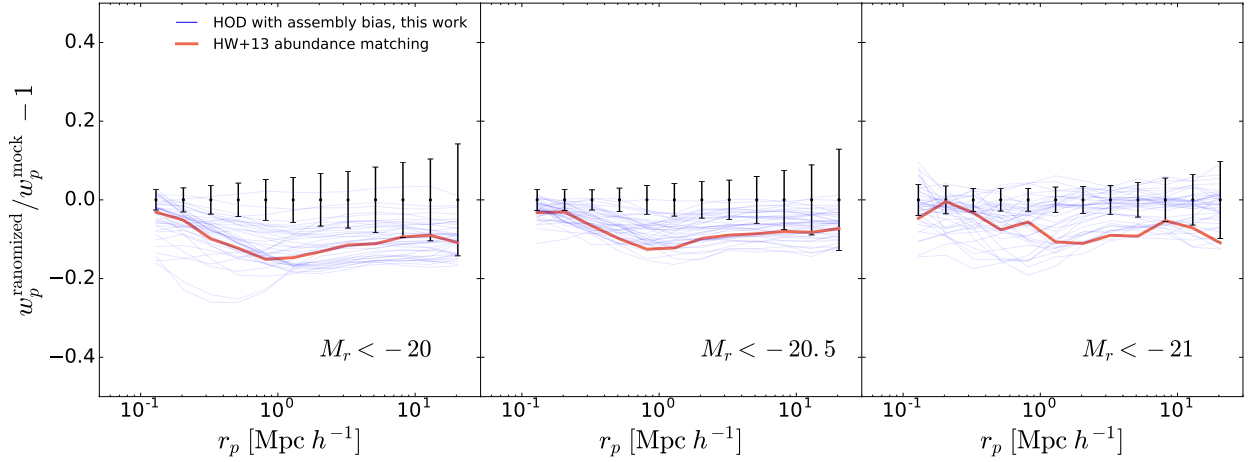


Figure 3.4: Demonstration of the relative difference in  $w_p$  between randomized and non-randomized catalogs for different luminosity threshold samples:  $M_r < -20, -20.5, -21$ . The errorbars are from the diagonal elements of the covariance matrix. The blue lines correspond to the random draws from the posterior probability (summarized in Table 3.6.1) over the parameters of the HOD model with assembly bias. The red line corresponds to the subhalo abundance matching catalog (Hearin & Watson 2013; Hearin et al. 2014). Our constraints favor *more moderate* levels of the impact of assembly bias on galaxy clustering than the levels seen in the abundance matching mock catalogs. Within both models, the small scale clustering remains unaltered after randomizing the catalogs, signaling the lack of correlation between the satellite occupation and the halo concentration at a fixed mass in the two models.

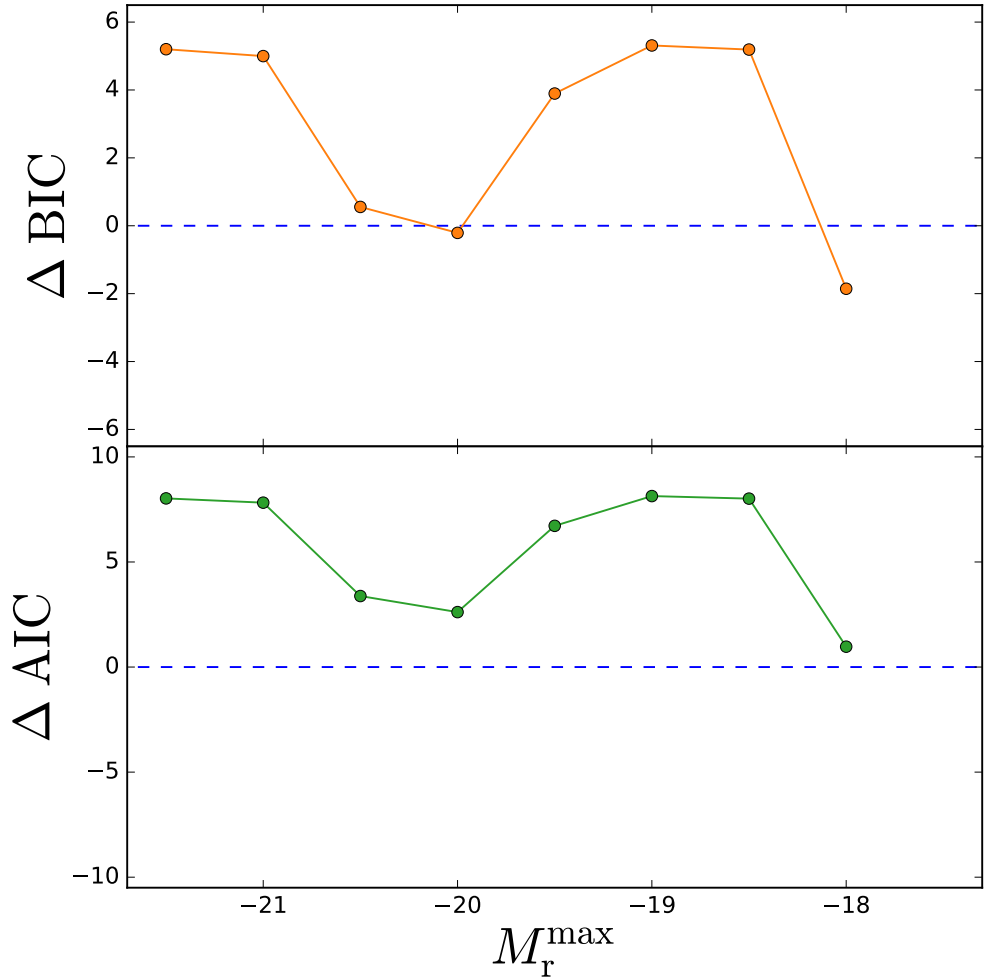


Figure 3.5: Difference in the information criteria between the HOD model with assembly bias and the model without assembly bias. **Top:**  $\Delta\text{BIC} = \text{BIC}(\text{with assembly bias}) - \text{BIC}(\text{without assembly bias})$ . **Bottom:**  $\Delta\text{AIC} = \text{AIC}(\text{with assembly bias}) - \text{AIC}(\text{without assembly bias})$ . According to BIC (AIC), the more complex model with assembly bias is favored once  $\Delta\text{BIC} < 0$  ( $\Delta\text{AIC} < 0$ ). Both  $\Delta\text{BIC}$  and  $\Delta\text{AIC}$  are lower for the samples with tighter constraints over the central assembly bias parameter  $\mathcal{A}_{\text{cen}}$ , with  $\Delta\text{BIC}$  being (marginally) negative only for  $M_r < -20, -18$  samples that yield strongest constraints on  $\mathcal{A}_{\text{cen}}$ .

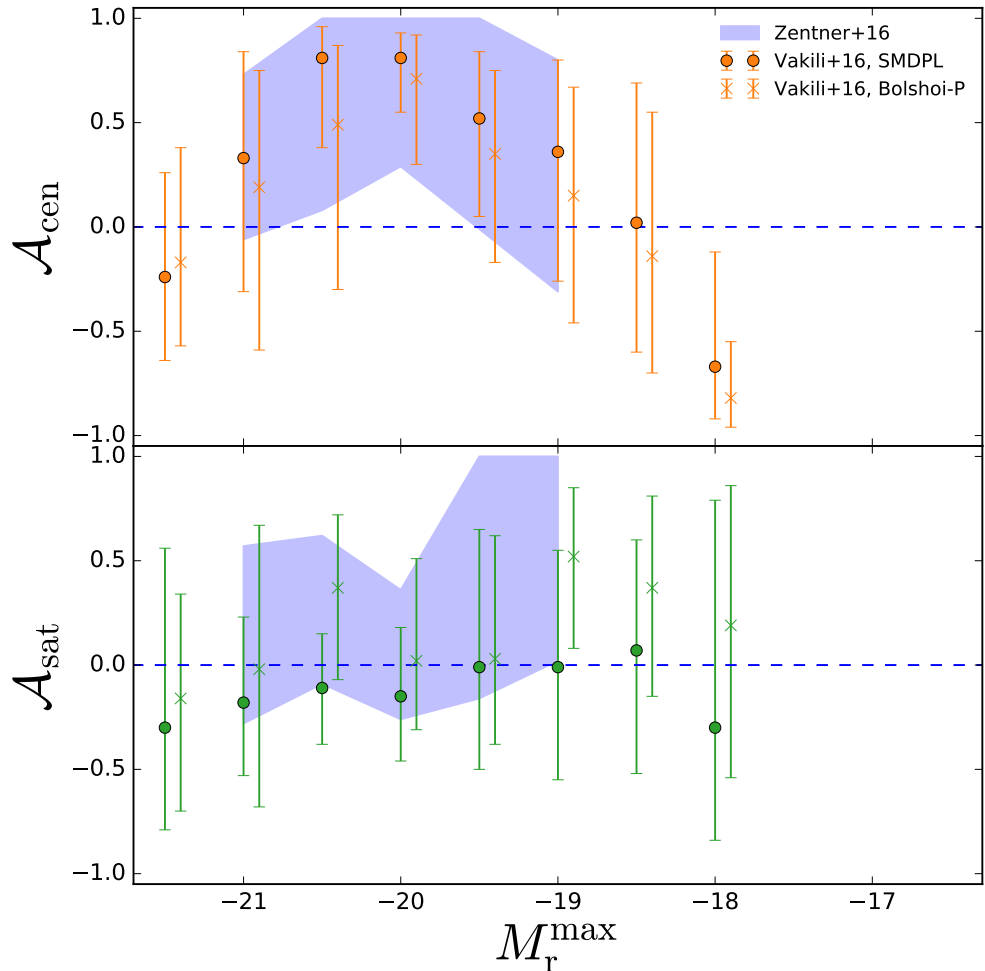


Figure 3.6: Comparison between the constraints on the assembly bias parameters  $\mathcal{A}_{\text{cen}}$  (shown in the top panel) and  $\mathcal{A}_{\text{sat}}$  (shown in the bottom panel) for different simulations: **SMDP** (shown with circle), and **BolshoiP** (shown with cross). The errorbars mark the 68% uncertainty over the parameters. Shaded blue regions show the upper and lower bounds reported by [Zentner et al. \(2016\)](#) that uses the **BolshoiP** and clustering measurements of [Zehavi et al. \(2011\)](#). For the confidence intervals corresponding to the shaded blue regions, we refer the readers to Table 2 of [Zentner et al. \(2016\)](#). The central assembly bias constraints found from the two simulations are consistent, with the constraints for from the **SMDP** simulation being tighter for the most luminous samples. The constraints on  $\mathcal{A}_{\text{sat}}$  from the two simulations are largely in agreement with the exception of  $M_{\text{r}} < -19, -20.5$  samples that favor more positive values of  $\mathcal{A}_{\text{sat}}$  when the **BolshoiP** simulation is used.

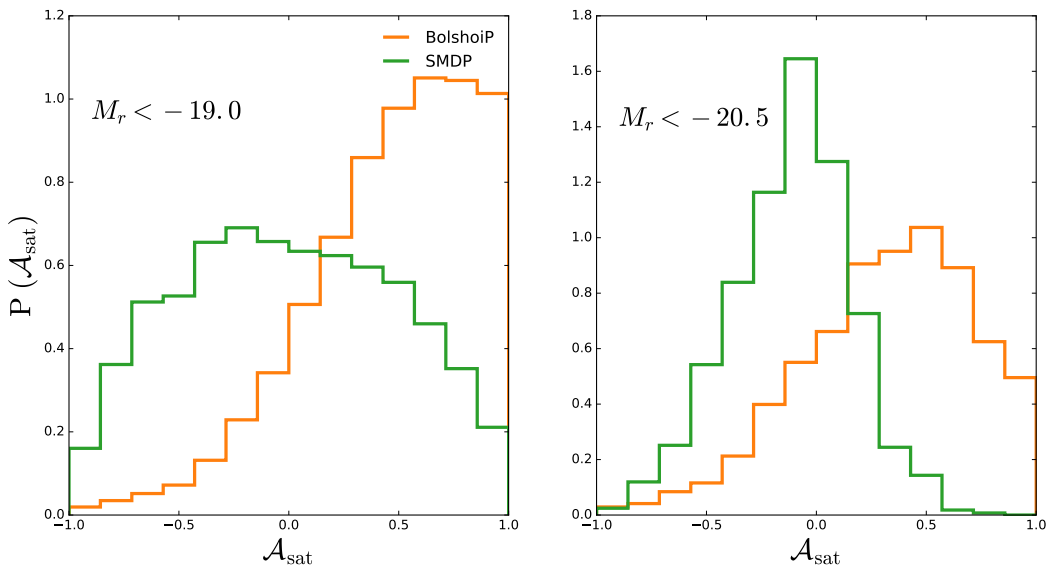


Figure 3.7: Constraints over the satellite assembly bias parameters from luminosity-threshold samples  $M_r < -19$ ,  $-20.5$ , for two different simulations: **BolshoiP** (yellow), and **SMDPL** (green). The  $\mathcal{A}_{\text{sat}}$  constraints found using the **BolshoiP** simulation favor more positive values of  $\mathcal{A}_{\text{sat}}$ , while the constraints found using the **SMDPL** simulation favor zero satellite assembly bias.

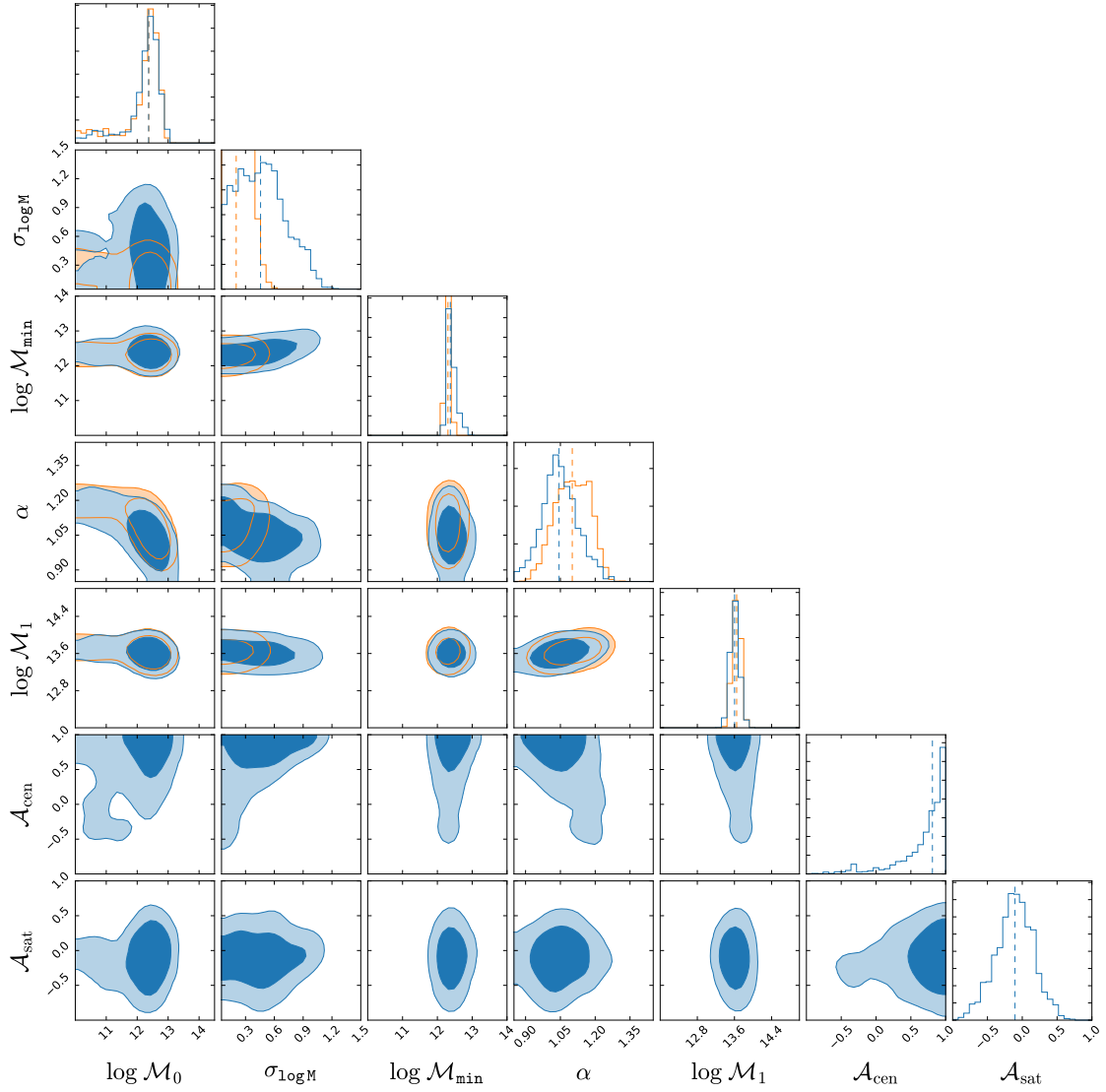


Figure 3.8: An example of posterior probability distribution over the parameters of the standard HOD model with no assembly bias (shown with yellow), and the HOD model with assembly bias (shown in blue). These constraints are obtained from the clustering measurements of the  $M_r < -20.5$  luminosity threshold sample. The dark (light) blue shaded regions show the 68% (95 %) confidence intervals. The constraints on  $\mathcal{A}_{\text{cen}}$  and  $\mathcal{A}_{\text{sat}}$  show positive correlation between the central occupation and the halo concentration at fixed halo mass, and lack of correlation between the satellite occupation and halo concentration at fixed halo mass.

# Chapter 4

## Accurate galaxy-halo mocks with automatic bias estimation and particle-mesh gravity solvers

This Chapter is joint work with Francisco-Shu Kitaura (IAC), Yu Feng (Berkeley), Gustavo Yepes (UAM), Cheng Zhao (Tsinghua), Chia-Hsun Chuang (Leibniz), ChangHoon Hahn (NYU) and it is submitted to the *Monthly Royal Astronomical Society Notice*.

### 4.1 abstract

Reliable extraction of cosmological information from clustering measurements of galaxy surveys requires estimation of the error covariance matrices of observables. The accuracy of covariance matrices is limited by our ability to generate sufficiently large number of independent mock catalogs that can describe the physics of galaxy clustering across a wide range of scales. Furthermore, galaxy mock catalogs are required to study systematics in galaxy

surveys and to test analysis tools. In this investigation, we present a fast and accurate approach for generation of mock catalogs for the upcoming galaxy surveys. Our method relies on low-resolution approximate gravity solvers to simulate the large scale dark matter field, which we then populate with halos according to a flexible nonlinear and stochastic bias model. In particular, we extend the PATCHY code with an efficient particle mesh algorithm to simulate the dark matter field (the FASTPM code), and with an efficient and robust MCMC method relying on the EMCEE code for constraining the parameters of the bias model. Using the halos in the BigMultiDark high-resolution  $N$ -body simulation as a reference catalog, we demonstrate that our technique can model the bivariate probability distribution function, power spectrum, and bispectrum of halos in the reference catalog. Specifically, we show that the new ingredients permit us to reach percentage accuracy in the power spectrum up to  $k \sim 0.4 \ h \text{Mpc}^{-1}$  (within 5% up to  $k \sim 0.6 \ h \text{Mpc}^{-1}$ ) with accurate bispectra improving previous results based on Lagrangian perturbation theory.

## 4.2 Introduction

The current and the next generation of galaxy surveys such as EBOSS<sup>1</sup> (Extended Baryon Oscillation Spectroscopic Survey, Dawson et al. 2016), DESI<sup>2</sup> (Dark Energy Spectroscopic Instrument, Levi et al. 2013), EUCLID<sup>3</sup> (Laureijs et al. 2011), LSST<sup>4</sup> (LSST Science Collaboration et al. 2009), and WFIRST<sup>5</sup> (Spergel et al. 2015) are expected to achieve unprecedented constraints on the cosmological parameters, growth of structure, expansion history of the universe, and modified theories of gravity. Accurate cosmological inferences with these

---

<sup>1</sup><http://www.sdss.org/surveys/eboss/>

<sup>2</sup><http://desi.lbl.gov/>

<sup>3</sup><http://www.euclid-ec.org/>

<sup>4</sup><http://www.lsst.org/>

<sup>5</sup><https://www.nasa.gov/wfirst>

surveys requires accurate computation of the likelihood function of the observed data given a cosmological model. This goal can be achieved provided that the uncertainties, in the form of error covariance matrices in the likelihood functions, are reliably estimated. Therefore, covariance matrices are essential ingredients in extraction of cosmological information from the data.

The most commonly used technique in estimation of the covariance matrix for galaxy clustering observables requires generation of a large number of simulated galaxy mock catalogs. These mock catalogs need to reproduce the cosmic volume probed by the galaxy surveys. They also need to describe the clustering observables with high accuracy in a wide range of scales. It has been demonstrated that both the precision and the accuracy of constraints on the cosmological parameters, regardless of the details of a given galaxy survey, depend on the number of realizations of the survey (Dodelson & Schneider 2013; Taylor & Joachimi 2014). The requirement on the number of independent realizations of the survey becomes more stringent as the number of data points in a given analysis grows (Taylor et al. 2013). The most pressing challenges ahead of simulating a large number of catalogs are: simulation of large volumes for sampling the Baryonic Acoustic feature in the galaxy clustering, accurate description of the clustering signal at small scales, accurate clustering not only at the level of two-point statistics but also at the level of higher order statistics. and resolving low mass halos that host fainter galaxy samples.

High-resolution  $N$ -body simulations are ideal venues for reproducing the dark matter clustering accurately. But production of a large number of density field realizations with  $N$ -body simulations is not computationally feasible. In order to alleviate the computational cost of  $N$ -body simulations, several methods based on approximate gravity solvers have been introduced. Methods based on higher order Lagrangian perturbation theory (Buchert & Ehlers 1993; Bouchet et al. 1995; Catelan 1995; Monaco et al. 2002; Scoccimarro & Sheth

2002; Kitaura & Heß 2013), Zeldovich approximation (Chuang et al. 2015a), and approximate  $N$ -body simulations (Tassev et al. 2013; White et al. 2014; Howlett et al. 2015; Tassev et al. 2015; Feng et al. 2016; Izard et al. 2016; Koda et al. 2016) have been demonstrated to be promising for fast generation of dark matter density field. Sampling the structures such as galaxies and halos from the dark matter density field requires an additional step. Identification of virialized regions of matter overdensity is either done through a biasing scheme (Kitaura et al. 2014; White et al. 2014) or is done through application of friends-of-friend algorithm (Manera et al. 2013; Koda et al. 2016; Feng et al. 2016). Methods that employ a biasing scheme need to be calibrated such that they are statistically consistent with accurate  $N$ -body simulations or observations.

The PATCHY method (Kitaura et al. 2014, 2015) produces mock catalogs by first generating dark matter field with Lagrangian Perturbation Theory modified with spherical collapse model on small scales ( $r \leq 2 h^{-1} \text{ Mpc}$ ) and then sampling galaxies (halos) from the density field using nonlinear stochastic biasing introduced in Kitaura et al. (2014). This method has been shown to reproduce the two-point clustering down to  $k \sim 0.3 h \text{ Mpc}^{-1}$  and the counts-in-cell of the massive halos in an accurate  $N$ -body simulation. Kitaura et al. (2015) demonstrate that the mock catalogs generated using this technique are capable of accurately describing the halo bispectrum in the reference  $N$ -body simulations. Furthermore, Kitaura et al. (2016) used this method for massive production of mock catalogs for the cosmological analysis of the completed SDSS III Baryon Oscillation Spectroscopic Survey DR12 galaxy sample.

Alternatively, computation of error covariance matrices can be delivered with analytical models (Feldman et al. 1994; Smith et al. 2008; Crocce et al. 2011; Sun et al. 2013; Grieb et al. 2016; Kalus et al. 2016). These methods are promising, though still need further investigation especially including systematic effects, such as the survey geometry. They

will potentially permit us to use a smaller number of mock catalogs to obtain accurate covariance matrices.

In recent years, development of the shrinkage methods (Ledoit & Wolf 2004; Pope & Szapudi 2008; Ledoit & Wolf 2012; Joachimi 2016; Simpson et al. 2016) have been shown to be promising for alleviating the requirement on the number of mocks. In principle, one could use a combination of the shrinkage methods and a smaller number of mock catalogs to reach the same level of accuracy needed for large scale structure inferences.

Moreover, production of mocks will be a useful tool for investigation of possible sources of systematic errors as well as verification of covariance matrices derived from analytical methods.

In this investigation, we introduce an MCMC method for calibration of the bias model of the PATCHY code. This method constrains the bias parameters by the halo power spectrum and the halo counts-in-cells (hereafter halo PDF) of a reference halo catalog constructed from an accurate  $N$ -body simulation.

Furthermore, we replace the dark matter gravity solver of the code with the fast particle-mesh approximate  $N$ -body solver implemented in the FASTPM code (Feng et al. 2016). The advantage of the FASTPM algorithm over other methods based on particle-mesh is its low memory requirements as well as accurate large scale growth. In addition, the dark matter density field produced by the FASTPM code yields better nonlinear clustering than that of the perturbation theory.

As a proof of concept, we make use of the halos in the BigMultiDark Planck high-resolution  $N$ -body simulation (Klypin et al. 2016). This catalog has been extensively used for validation, comparison and production of galaxy mock catalogs (Chuang et al. 2015b; Zhao et al. 2015; Kitaura et al. 2016; Rodríguez-Torres et al. 2016). In addition, we will make a statistical comparison between our PATCHY mocks and the reference catalog. We present

the number density, halo PDF, and halo two-point statistics. We also present our results in terms of the three-point statistics since it is rising as a major complementary approach in various large-scale structure analyses (Slepian et al., 2015; Gil-Marín et al., 2015a,b; Guo et al., 2016b; Slepian et al., 2016a,b; Gil-Marín et al., 2017).

The remainder of this paper is structured as follows: In section §4.3, we present our method for generating and calibrating mock catalogs. This includes description of the structure formation model, nonlinear stochastic bias model of the PATCHY code, and our MCMC method for constraining the bias parameters. We illustrate the performances using a reference halo catalog constructed from an accurate  $N$ -body simulation in section §4.4, and we discuss the main results and present our conclusions in section §4.5.

### 4.3 Methodology

Our method consists of producing the large scale dark matter field on a mesh and then populating it with halos (or galaxies) with a given bias model. The parameters of that bias model are constrained with a reference catalog in an automatic statistical way. Our approach is agnostic about the method used for identification of halos in the reference catalog. The PATCHY code permits us to sample galaxies directly from the density field. For instance Kitaura et al. (2016) samples mock galaxy catalogs based on an accurate reference mock galaxy catalog (Rodríguez-Torres et al., 2016). Let us first describe in §4.3.1 the new implementation of the structure formation in PATCHY, followed in §4.3.2 by the bias model, and finally in §4.3.3 our novel MCMC sampling procedure to obtain the bias parameters.

### 4.3.1 Structure formation model

Originally, the PATCHY code used Augmented Lagrangian Perturbation Theory (ALPT, Kitaura & Heß 2013) as a structure formation model. In this model the second order Lagrangian perturbation theory is modified by employing a spherical collapse model on small comoving scales ( $r \leq 2 h^{-1} \text{ Mpc}$ ). Any LPT based approximation will lack the one halo term in the clustering. This can be partially compensated within the bias model, however, at the price of obtaining a less accurate description of the biasing relation. Therefore we introduce in this work within the PATCHY code the fast particle mesh code FASTPM (Feng et al., 2016). In FASTPM, the kick and drift steps of the PM codes are modified such that the linear growth of structure is exact. Feng et al. (2016) demonstrate that the memory requirements of this algorithm are much lower than those of the COmoving Lagrangian Acceleration  $N$ -body solver (COLA, Tassev et al., 2013).

Moreover, Feng et al. (2016) shows that running the code with relatively few time steps, and applying a friends-of-friend (hereafter fof) halo finder (Davis et al. 1985) to the density field, one can accurately recover the redshift space power spectrum of the fof halos of TreePM accurate  $N$ -body solver (Bagla 2002) down to  $k \sim 0.5 h \text{ Mpc}^{-1}$ . The linking length of 0.2 was chosen to be consistent with other works in the literature (Tassev et al. 2013). In this work, we run the FASTPM code with 10 time steps.

In this work we will use as a reference the high-resolution  $N$ -body BigMultiDark simulation described in more detail in section §4.4.1. A comparison of the dark matter density fields obtained with the different methods is shown in Fig. 4.1. While the structures in the high-resolution  $N$ -body simulation and the low-resolution FASTPM simulation look very similar inspite of having very different resolutions ( $3840^3$  vs  $960^3$  particles), the low-resolution ALPT simulation looks more diffuse due to the exaggerated shell crossing inherent to LPT based methods. We will study the impact of this inaccuracy in more detail in section §4.4.3.

### 4.3.2 Sampling halos from the density field

In this section, we describe the statistical bias model of the PATCHY code. This model generates halos/galaxies from a given dark matter density field and consists of: deterministic bias, stochastic bias, and an additional step for applying redshift space distortions (RSDs) to the catalogs. We describe the bias steps below and leave RSDs for a later work.

#### 4.3.2.1 Deterministic bias

The expected number of halos  $\langle \rho_h \rangle$  in a given volume element  $dV$  (cosmic cell) can be described in general by a deterministic bias relation  $B(\rho_h | \rho_m)$ :

$$\langle \rho_h \rangle_{dV} = f_h B(\rho_h | \rho_m), \quad (4.1)$$

where  $\rho_m$  is the matter density field. The prefactor  $f_h$  is an overall normalization factor which can be determined by requiring the halo density field to have the number density of the reference sample  $n_h$ , i.e.,  $n_h = \langle \langle \rho_h \rangle_{dV} \rangle_V$ . Formally, this can be written as

$$f_h = \frac{n_h}{\langle B(\rho_h | \rho_m) \rangle_V}, \quad (4.2)$$

where  $\langle \cdot \rangle_V$  is an ensemble volume average. In particular, we will adopt the following compact deterministic bias model:

$$\begin{aligned} B(\rho_h | \rho_m) &= \underbrace{\rho_m^\alpha}_{\text{nonlinear bias}} \\ &\times \underbrace{\theta(\rho_m - \rho_{th})}_{\text{threshold bias}} \times \underbrace{\exp(-(\rho_m / \rho_\epsilon)^\epsilon)}_{\text{exponential cutoff}}, \end{aligned} \quad (4.3)$$

where  $\rho_{\text{th}}$  is the density threshold which suppresses halo formation in under-dense regions, and  $\alpha$  is a nonlinear bias parameter. The threshold bias (Kaiser 1984; Bardeen et al. 1986; Sheth et al. 2001; Mo & White 2002) is modeled by a step function  $\theta(\rho_m - \rho_{\text{th}})$  (Kitaura et al. 2014) and an exponential cutoff  $\exp(-(\rho/\rho_\epsilon)^\epsilon)$  (Neyrinck et al. 2014). Therefore, for this particular bias model we have a normalisation of

$$f_h = \frac{n_h}{\langle \theta(\rho_m - \rho_{\text{th}}) \rho_m^\alpha \exp(-(\rho_m/\rho_\epsilon)^\epsilon) \rangle_V}. \quad (4.4)$$

The advantage of this kind of bias model is that it is flexible, it is able to incorporate additional terms, and each of the terms have a physical interpretation. The power law bias stands for one of the simplest possible nonlinear bias models: a linear Lagrangian bias in a comoving framework, which can be derived from the lognormal approximation (see Kitaura et al., 2015), and it resumes in one single bias parameter an infinite Taylor expansion of the dark matter density field (Cen & Ostriker, 1993; Fry & Gaztanaga, 1993; de la Torre & Peacock, 2013).

The threshold bias and the exponential cut-off describe the fact that halos (or galaxies) can only reside in regions which contain a minimum mass. They also represent the loss of information with respect to the full cosmic density field from selecting only gravitationally collapsed objects.

#### 4.3.2.2 Stochastic bias

The number of halos in each cell is drawn from a Negative Binomial (NB) distribution which can be characterized by the expected number of halos in the cell  $\lambda_h = \langle \rho_h \rangle_{dV} \times dV$ , and a parameter  $\beta$  which quantifies the stochasticity (deviation of the distribution from Poissonity) in the halo distribution. According to this model, the probability of having  $N_h$

objects in a volume element is given by

$$\begin{aligned}
P(N_h|\lambda_h, \beta) &= \underbrace{\frac{\lambda_h^{N_h}}{N_h!} e^{-\lambda_h}}_{\text{Poisson distribution}} \\
&\times \underbrace{\frac{\Gamma(\beta + N_h)}{\Gamma(\beta)(\beta + \lambda_h)^{N_h}} \times \frac{e^{\lambda_h}}{(1 + \lambda_h/\beta)^\beta}}_{\text{Deviation from Poissonity}}.
\end{aligned} \tag{4.5}$$

For  $\beta \rightarrow \infty$  we can show that the second raw in the above equation goes to one. Since  $\Gamma(\beta) = \frac{\Gamma(\beta+1)}{\beta} = \frac{\Gamma(\beta+N_h)}{\beta(\beta+1)\cdots(\beta+N_h-1)}$ , the first factor can be written as  $\frac{\Gamma(\beta+N_h)}{\Gamma(\beta)(\beta+\lambda_h)^{N_h}} = \frac{\beta(\beta+1)\cdots(\beta+N_h-1)}{(\beta+\lambda_h)^{N_h}} = \frac{(1+\beta)\cdots(1+(N_h-1)/\beta)}{(1+\lambda_h/\beta)^{N_h}}$ . It is now straightforward to see that this goes to one for  $\beta \rightarrow \infty$ . The same happens for the second factor  $\frac{e^{\lambda_h}}{(1+\lambda_h/\beta)^\beta} \rightarrow 1$ , since  $(1 + \lambda_h/\beta)^\beta \rightarrow e^{\lambda_h}$  in that limit.

Given a dark matter density field  $\rho_m$ , the halo density field can be constructed by drawing samples from the expected halo density field  $\rho_h$  with the Negative-Binomial (hereafter NB) distribution (Eq. 4.5). This is inspired by the fact that the excess probability of finding halos in high density regions generates over-dispersion (Somerville et al., 2001; Casas-Miranda et al., 2002). This over-dispersion is modeled by a NB distribution (Kitaura et al. 2014; Neyrinck et al. 2014).

The stochastic bias stands for the shot noise from the transition of the continuous dark matter field to the discrete halo (or galaxy) distribution. As predicted by Peebles (1980), it produces a dispersion larger than Poisson, as long as the two-point correlation function remains positive below the scale of the cell size. This is captured by the negative binomial PDF (Eq. 4.5).

### 4.3.3 Constraining the bias model

Production of approximate mock catalogs with PATCHY requires a reference catalog constructed from the observations or based on an accurate  $N$ -body simulation. We aim at constraining the parameters describing the deterministic bias  $\{\delta_{\text{th}}, \alpha, \rho_\epsilon, \epsilon\}$ , and the parameter that governs the stochasticity of the halo population  $\{\beta\}$ .

The bias parameters are estimated such that the statistical summaries of the halos (galaxies) in the PATCHY mocks match the statistical summaries of the halos (galaxies) in the reference catalog. The set of statistical summaries of the catalog can in principle include number density, bivariate probability distribution function or number of counts-in-cells  $\rho$  (hereafter halo PDF), two-point statistics  $\xi_2$ , and higher-order statistics such as the three-point statistics  $\xi_3$ .

By construction, the PATCHY mocks reproduce the exact number density of objects in the reference catalog. This comes from the particular choice of normalization in the deterministic bias relation (see Eqs. 4.3,4.4). In this work, we follow Kitaura et al. (2015) and constrain the bias parameters with the halo PDF and the two-point statistics  $\xi_2$ . These two quantities can be computed very fast and the skewness of the halo PDF determines the three point statistics. Given the bias parameters found fitting the PDF and the two-point statistics, we will demonstrate a comparison between the approximate mocks and the reference catalog in terms of the two- and three-point statistics.

We simultaneously fit the real-space power spectrum  $P(k)$  and the PDF  $\rho(n)$  of the PATCHY halo density field to  $P(k)$  and  $\rho(n)$  measured for the BigMultiDark halo catalog. Specifically, constraints on  $\theta = \{\delta_{\text{th}}, \alpha, \rho_\epsilon, \epsilon, \beta\}$  are found by sampling from the posterior probability  $p(\theta|\text{data}) \propto p(\text{ref}|\theta)p(\theta)$ , where ref denotes the combination  $\{P_{\text{ref}}(k), \rho_{\text{ref}}(n)\}$ ,

and the likelihood  $p(\text{ref}|\theta)$  is given by

$$\begin{aligned} -2 \ln p(\text{ref}|\theta) &= \sum_k \frac{(P_{\text{ref}}(k) - P_{\text{mock}}(k))^2}{\sigma_k^2} \\ &+ \sum_n \frac{(\rho_{\text{ref}}(n) - \rho_{\text{mock}}(n))^2}{\sigma_n^2}. \end{aligned} \quad (4.6)$$

For the purpose of estimating the bias parameters, we find it sufficient to assume simple uncorrelated noise terms  $\{\sigma_k, \sigma_n\}$  in the above likelihood (4.6). We assume  $\sigma_k^2$  to be  $4\pi^2 P_{\text{ref}}^2(k)/(V_{\text{box}} k^2 \Delta k)$ , and  $\sigma_n^2$  to be  $N_n$  where  $N_n$  is the number of cells containing  $n$  number of halos (including parent halos and subhalos). Furthermore, we choose a flat prior for all parameters of the bias model with the following lower and upper bounds:  $-1 < \delta_{\text{th}} < 2$ ,  $0 < \alpha < 1$ ,  $0 < \beta < 1$ ,  $0 < \rho_\epsilon < 1$ , and  $0 < \epsilon < 1$ .

For sampling from the posterior probability, given the likelihood function (Eq. 4.6) and the prior, we use the affine-invariant ensemble MCMC sampler (Goodman & Weare 2010) and its implementation EMCEE (Foreman-Mackey et al. 2013). In particular, we run the EMCEE code with 10 walkers and we run the chains for at least 2000 iterations. We discard the first 500 chains as burn-in samples and use the remainder of the chains as production MCMC chains. Furthermore, we perform Gelman-Rubin convergence test (Gelman & Rubin 1992) to ensure that the MCMC chains have reached convergence.

#### 4.3.4 Comparison with other approximate methods

Pioneering fast halo/galaxy generating methods have relied on approximate gravity solvers based on Lagrangian perturbation theory (LPT) to compute the position and mass of the objects, such as PINOCCHIO (Zeldovich: Monaco et al. 2002, 2013, 3LPT: Monaco 2016) and PTHALOS (2LPT: Buchert & Ehlers 1993; Bouchet et al. 1995; Catelan 1995; Scoccimarro & Sheth 2002; Manera et al. 2013, 2015). This has the disadvantage of be-

ing affected by an inaccurate description of the small scale clustering, and, in particular, of missing the one halo term contribution. As a consequence, the power spectra of such catalogs have systematic deviations towards high values of  $k$ , already deviating about 10% at  $k \sim 0.2 h \text{ Mpc}^{-1}$  (Monaco et al., 2013).

While fast particle mesh solvers, such as COLA or FASTPM, are much more precise than LPT based approaches, they are still computationally too expensive to be suitable for massive production, if one is trying to resolve all the necessary structures required to interpret the next generation of galaxy surveys. Therefore three methods were recently proposed: PATCHY (Kitaura et al., 2014), QPM (White et al., 2014), and EZMOCKS (Chuang et al., 2015a), which do not try to resolve halos (nor galaxies) with the approximate gravity solvers, but just get a reliable large scale dark matter field, which can then be populated with some bias prescription. The gravity solver thus only needs to be accurate on a certain scale, then the halo/galaxy-dark matter connection is exploited to reach a high accuracy, as described above. These methods use both different gravity solvers and different bias models. While PATCHY originally relies on ALPT, QPM uses a quick particle mesh solver, and EZMOCKS uses the Zeldovich linear LPT. But more importantly the bias prescription follows very different philosophies. QPM uses a rank ordering scheme relating the halo mass to density peaks. However, a recent study demonstrated that the dependence of the halo mass to its environment is not trivial (see Zhao et al., 2015). EZMOCKS, on the other hand, first modifies the initial power spectrum introducing a tilt to adjust the final two point statistics, correcting hereby the missing one halo term of the approximate gravity solver. Second it imposes the halo PDF, which was shown to determine the 3pt statistics (Kitaura et al., 2015). PATCHY on the other hand follows a more physical approach, relying on an effective analytical stochastic bias model. In this sense the statistics is not directly imposed as in EZMOCKS, but fitted through the bias parameters. In fact PATCHY was shown to be considerably more

accurate than EZMOCKS when assigning halo masses (Zhao et al., 2015), and than QPM when fitting the two and three point statistics of the luminous red galaxies (LRGs) in the Baryon Oscillation Spectroscopic Survey (BOSS) (Kitaura et al., 2016).

Moreover, the approach we follow in PATCHY tests the validity range of effective bias prescriptions commonly used in large scale structure analysis methods (see e.g. Ata et al., 2015).

Now for the first time we include a robust MCMC sampling scheme to determine the bias parameters, and have improved the gravity solver with FASTPM.

## 4.4 Demonstration on an accurate $N$ -body based halo catalog

In this section we present the application of the above described method to a well studied case: the halo distribution required to describe the CMASS LRG sample of the BOSS survey (White et al., 2011; Dawson et al., 2013). First, we briefly describe the reference catalog and then present a detailed statistical analysis of the results.

### 4.4.1 Reference catalog

For the reference simulation used in this work we rely on the Bound-Density-Maxima (BMD, Klypin & Holtzman 1997) halo catalogs in the  $z = 0.5618$  snapshot of the BigMultiDark-Planck high resolution  $N$ -body simulation (Klypin et al., 2016). This simulation was carried out using the L-Gadget2 code (Springel, 2005), following the Planck  $\Lambda$ CDM cosmological parameters  $\Omega_m = 0.307$ ,  $\Omega_b = 0.048$ ,  $\Omega_\Lambda = 0.693$ ,  $\sigma_8 = 0.823$ ,  $n_s = 0.96$ ,  $h = 0.678$ . The box size for this  $N$ -body simulation is  $2500 h^{-1}$  Mpc, the number of simulation particles is  $3840^3$ , the mass per simulation particle  $m_p$  is  $2.359 \times 10^{10} h^{-1} M_\odot$ , and the

gravitational softening length  $\epsilon$  is  $30 h^{-1}\text{kpc}$  at high- $z$  and  $10 h^{-1}\text{kpc}$  at low- $z$ .

A minimum mass cut of  $0.5 \times 10^{13} h^{-1}M_\odot$  has been applied to the halo catalog so that it matches with the number density of the SDSS III-BOSS CMASS galaxy catalog (White et al., 2011; Dawson et al., 2013). After applying the mass cut, the number density of the final catalog is  $3.5 \times 10^{-4} (h \text{ Mpc}^{-1})^3$ . The MultiDark-PATCHY galaxy catalogs (Kitaura et al., 2016) are calibrated against BOSS-HAM catalogs which were constructed by populating the halos in different snapshots of the BigMultiDark simulation using halo abundance matching (Rodríguez-Torres et al., 2016).

Evaluation of  $P(k)$  and  $\rho(n)$  for a set of bias parameters requires running the forward model of generating halos from the matter density field. Therefore, in order to speed up the fitting procedure we run the PATCHY code with a smaller box size of  $625 h^{-1} \text{Mpc}$  and grid size of 240 in each dimension. This choice of box and grid size preserves the resolution. Furthermore, running the PATCHY code and computing the statistics of the halo catalogs in a smaller box size significantly reduces the computational time needed for constraining the bias parameters.

#### 4.4.2 Bias parameters

The first step in our pipeline consists of producing the large scale dark matter field on a mesh. We use the down-sampled white noise of the BigMultiDark simulation from  $3840^3$  to  $960^3$  cells to estimate the initial conditions used for both FASTPM and ALPT runs, as shown in Fig. 4.1. The dark matter particles are then assigned to a mesh of  $960^3$  cells with clouds-in-cells (CIC), which we define as the large scale dark matter density field  $\rho_m$  required for Eqs. 4.3, 4.4, 4.5.

After running the MCMC chains with the method described in section §4.3, we find constraints on the bias parameters of such equations. These constraints are summarized

in Fig. 4.2. The threshold bias parameter  $\delta_{\text{th}}$  is found to be 1.07 which is equivalent to sampling halos from the regions of high matter overdensity. This supports our intuition that massive halos are generated from high density regions. Our estimated value of the nonlinear bias parameter  $\alpha$  is  $\sim 0.2$ . These values are qualitatively consistent with ALPT (Kitaura et al., 2014), although the threshold bias is slightly reduced and the power law bias is slightly higher (parameters with ALPT:  $\delta_{\text{th}} \sim 1.2$  and  $\alpha \sim 0.12$ ).

The parameter that governs the deviation from Poissonity  $\beta$  is found to be 0.73. This value is significantly larger than the one found with ALPT (about 0.6), i.e., indicating that the deviation from Poissonity is not so pronounced as previously found. The reason for this, is that Lagrangian perturbation theory does not manage to model the one halo term, as done with FASTPM. Therefore a larger deviation of Poissonity had to be assumed to fit the power spectrum towards small scales, as is demonstrated here. In this sense, a more accurate description of the large scale dark matter field permits us to reduce the stochasticity in the halo distribution.

Furthermore, parameters corresponding to the exponential cutoff term in the deterministic bias relation  $\{\rho_\epsilon, \epsilon\}$  are estimated to be  $\sim \{0.15, -0.24\}$ . While the constraints on both parameters of the exponential cutoff bias are consistent with zero, their presence, albeit being small, is essential in a more accurate modeling of the halo bivariate PDF and the halo bispectrum. By including these extra parameters we demonstrate the flexibility and efficiency of the code to incorporate complex bias models. Furthermore, we believe that the exponential cutoff term will become crucial when considering smaller mass halos, which have a non negligible probability of residing in low density regions (Neyrinck et al., 2014).

### 4.4.3 Statistical comparison

In this section we discuss the statistical comparisons between the BDM halo catalog of the BigMultiDark simulation and the halo catalog generated from our method. In particular, the FASTPM-PATHCY mock is generated using the best-fit bias parameters (see Fig. 4.2). For the ALPT-PATHCY mocks we rely on the parameters found from previous PATCHY studies (Kitaura et al., 2016). The halo statistical summaries presented in this work are the number density, the bivariate halo probability distribution function (PDF), the real-space power spectrum and the real-space bispectrum.

By construction our method reproduces the exact number density of halos in the reference catalog (Eq. 4.4). We observe that the bivariate PDF (or halo counts-in-cells) of the reference catalog can be reproduced with good accuracy (Fig. 4.3).

In terms of the agreement between halo PDF of approximate mock catalog and that of the BigMultiDark simulation, we find that significant improvement can be achieved when halos are sampled from the FASTPM dark matter density field.

Furthermore, we present our comparison in terms of the power spectrum  $P$  and the bispectrum  $B$  which are the two-point function and the three-point function in Fourier space. Given the Fourier transform of the halo density field  $\delta_h(\mathbf{k})$ , the power spectrum and the bispectrum are defined as follows

$$\langle \delta_h(\mathbf{k}_1)\delta_h(\mathbf{k}_2) \rangle = (2\pi)^3 P(k_1)\delta^D(\mathbf{k}_1 + \mathbf{k}_2), \quad (4.7)$$

$$\begin{aligned} \langle \delta_h(\mathbf{k}_1)\delta_h(\mathbf{k}_2)\delta_h(\mathbf{k}_3) \rangle &= (2\pi)^3 B(\mathbf{k}_1, \mathbf{k}_2)\delta^D(\mathbf{k}_1 + \mathbf{k}_2 + \mathbf{k}_3), \\ \end{aligned} \quad (4.8)$$

where  $\delta^D$  is the Dirac delta function. The shot-noise contribution to the power spectrum

and bispectrum is modeled in the following way:

$$P_{\text{sn}}(k) = \frac{1}{\bar{n}}, \quad (4.9)$$

$$B_{\text{sn}}(\mathbf{k}_1, \mathbf{k}_2) = \frac{1}{\bar{n}}[P(k_1) + P(k_2) + P(k_3)] + \frac{1}{\bar{n}^2}, \quad (4.10)$$

where  $\bar{n}$  is the halo number density and  $k_3 = |\mathbf{k}_1 + \mathbf{k}_2|$ .

Our methodology is able to reproduce the halo power spectrum of the reference with percentage level accuracy to  $k \sim 0.4 h \text{Mpc}^{-1}$  (within 5% up to  $k \sim 0.6 h \text{Mpc}^{-1}$ ) which corresponds to nonlinear regimes (Fig. 4.3). We have also run our method ignoring the PDF in the posterior sampling, yielding accurate power spectra up to  $k \sim 1 h \text{Mpc}^{-1}$ . Kitaura et al. (2014) also reported accurate power spectra up to high  $k$ , however, using an arbitrary threshold bias of zero. In a later work additionally fitting the PDF, it was found that the power spectra are accurate within 2% up to  $k \sim 0.3 h \text{Mpc}^{-1}$  (Kitaura et al., 2015), in agreement with what is found here using ALPT. An even higher accuracy will require a more complex bias model and a proper modelling of the clustering on sub-Mpc scales, differentiating between centrals and satellites. The current version of PATCHY randomly assigns dark matter particle positions to halos sampled in a given cell. The bias model could be augmented with nonlocal bias terms following McDonald & Roy (2009). We have neglected in this study the perturbation bias term used in Kitaura et al. (2016) (in an attempt to compensate for the missing power towards small scales), where the limit in the accuracy was found to be around  $k \sim 0.3 h \text{Mpc}^{-1}$ . Omitting the perturbation theory term also allows for a fair comparison with the study presented in Kitaura et al. (2015) and is not necessary when using FASTPM.

Fig. 4.3 showed an improved PDF when relying on FASTPM. This is expected to have an impact in the three point statistics, which in fact yields better fits towards small scales, as

we discuss below. We show our results in terms of bispectrum for six different values of  $|\mathbf{k}_1|$  and  $|\mathbf{k}_2|$  as a function of the angle between the two vectors  $\alpha_{12} = \angle(\mathbf{k}_1, \mathbf{k}_2)$ . The adopted wave numbers are  $k_1 = k_2 = 0.1$ ,  $2k_1 = k_2 = 0.2$ ,  $k_1 = k_2 = 0.15$ ,  $k_1 = k_2 = 0.2$ ,  $2k_1 = k_2 = 0.3$ ,  $2k_1 = k_2 = 0.4$  (all wave numbers are expressed in units of  $h \text{ Mpc}^{-1}$ ).

We find that in general for both ALPT and FASTPM there is good agreement between the bispectrum measured from our approximate mock catalogs and that of the BigMultiDark simulation (Fig. 4.4). Deviations as large as 15-20% are expected, as we are using a down-sampled white noise of the BigMultiDark simulation from  $3840^3$  to  $960^3$  cells and are on the level of what was found in Kitaura et al. (2015).

For configurations corresponding to smaller scales ( $2k_1 = k_2 = 0.3 h \text{ Mpc}^{-1}$ ,  $2k_1 = k_2 = 0.4 h \text{ Mpc}^{-1}$ ), the agreement between the bispectra of our approximate mock halo catalogs and the BigMultiDark halos improves when we sample halos from the FASTPM density field. This improvement is dramatic when compared to EZMOCKS (see real-space lines in the lower panels in Fig. 5 of Chuang et al., 2015a).

## 4.5 Summary and Discussion

This work presents a major step in fast and accurate generation of mock halo/galaxy catalogs, extending in particular, the PATCHY code. We have introduced an efficient MCMC technique to automatically obtain the bias parameters relating the halo/galaxy population to the underlying large scale dark matter field based on a reference catalog.

This technique is flexible and admits incorporation of different bias models, and number of bias parameters. This permits us to robustly assess the degeneracies and confidence regions of the different bias parameters.

Furthermore we have introduced in the PATCHY code a particle mesh structure formation

model (the FASTPM code, see Feng et al., 2016) in addition to the previous LPT based schemes.

As a demonstration of the performance of this method, we used the halo catalog of the BigMultiDark  $N$ -body simulation as a reference catalog. Our calibration method makes use of the halo two-point statistics and the counts-in-cells to estimate the bias parameters.

Based on the dark matter field obtained with FASTPM, which includes an improved description towards small scales, and in particular, the enhanced power caused by the one halo term, we have found that previous studies were overestimating the contribution to the power due to deviation from Poissonity. Though present, this deviation turns out to be less pronounced. Also, we have managed to extend the accuracy of the power spectra from  $k \sim 0.3 \ h \text{Mpc}^{-1}$  to  $k \sim 0.6 \ h \text{Mpc}^{-1}$ , being at the level of percentage accuracy up to  $k \sim 0.4 \ h \text{Mpc}^{-1}$ .

We have demonstrated that the novel implementation of the PATCHY code reaches higher accuracy in terms of the bispectrum towards small scales with respect to LPT based schemes, such as ALPT, and even more so with respect to EZMOCKS, which relies on the Zeldovich approximation.

The assignment of halo masses must be done in a post-processing step taking into account the underlying dark matter density field. Zhao et al. (2015) demonstrated that the mass assignment is more precise when the underlying dark matter field is more accurate (ALPT vs Zeldovich). We therefore expect that using FASTPM contributes to further reduce the scatter. We leave the investigation of mass assignment for a later work.

We have also left the analysis of redshift space distortions for a future work, as it turns out that the two and three point statistics are apparently more easily described in redshift space (see e.g. Kitaura et al., 2014; Chuang et al., 2015a,b). However, a better description of the quadrupole on small scales is not trivial and requires further investigation (see Chuang

et al., 2015b).

As we have now implemented a PM solver into our approach, we expect that certain high mass range of halos are correctly described and could be found with a friends-of-friends algorithm, the halos which are not properly resolved could be augmented with the method presented here (see methods to extend the resolution of  $N$ -body simulations, de la Torre & Peacock, 2013; Angulo et al., 2015; Ahn et al., 2015).

It is important to note that our investigation in this work has been focused on the generation of high mass halo (and subhalo) catalogs. One of the main challenges toward generation of mock galaxy catalogs is sampling of low mass halos. These host fainter galaxies which will dominate the observed galaxy samples in upcoming galaxy survey datasets.

We leave a thorough investigation of production of low mass halo catalogs to a future work. This will presumably require more sophisticated bias models including also nonlocal bias terms. The robust, automatic, and efficient methodology presented in this work should be capable of dealing with this.

In summary, the work presented here contributes to set the basis for a method able to generate galaxy mock catalogs needed to meet the precision requirements of the next generation of galaxy surveys.

## Acknowledgments

We are grateful to David W. Hogg, Uros Seljak, Martin White, Emanuele Castorina, Jeremy L. Tinker, and Michael Blanton for discussions related to this work. MV is particularly thankful to David W. Hogg for his continuous support during the completion of this work. We thank David W. Hogg and Alex I. Malz for reading and commenting on the manuscript. This work was supported by the NSF grant AST-1517237. GY acknowledges

financial support from MINECO/FEDER (Spain) under research grant AYA2015-63810-P. Most of the computations in this work were carried out in the New York University High Performance Computing Mercer facility. We thank Shenglong Wang, the administrator of the NYU HPC center, for his consistent support throughout the completion of this study. The CosmoSim database used in this paper is a service by the Leibniz-Institute for Astrophysics Potsdam (AIP). The MultiDark database was developed in cooperation with the Spanish MultiDark Consolider Project CSD2009-00064. The authors gratefully acknowledge the Gauss Centre for Supercomputing e.V. ([www.gauss-centre.eu](http://www.gauss-centre.eu)) and the Partnership for Advanced Supercomputing in Europe (PRACE, [www.prace-ri.eu](http://www.prace-ri.eu)) for funding the MultiDark simulation project by providing computing time on the GCS Supercomputer SuperMUC at Leibniz Supercomputing Centre (LRZ, [www.lrz.de](http://www.lrz.de)).

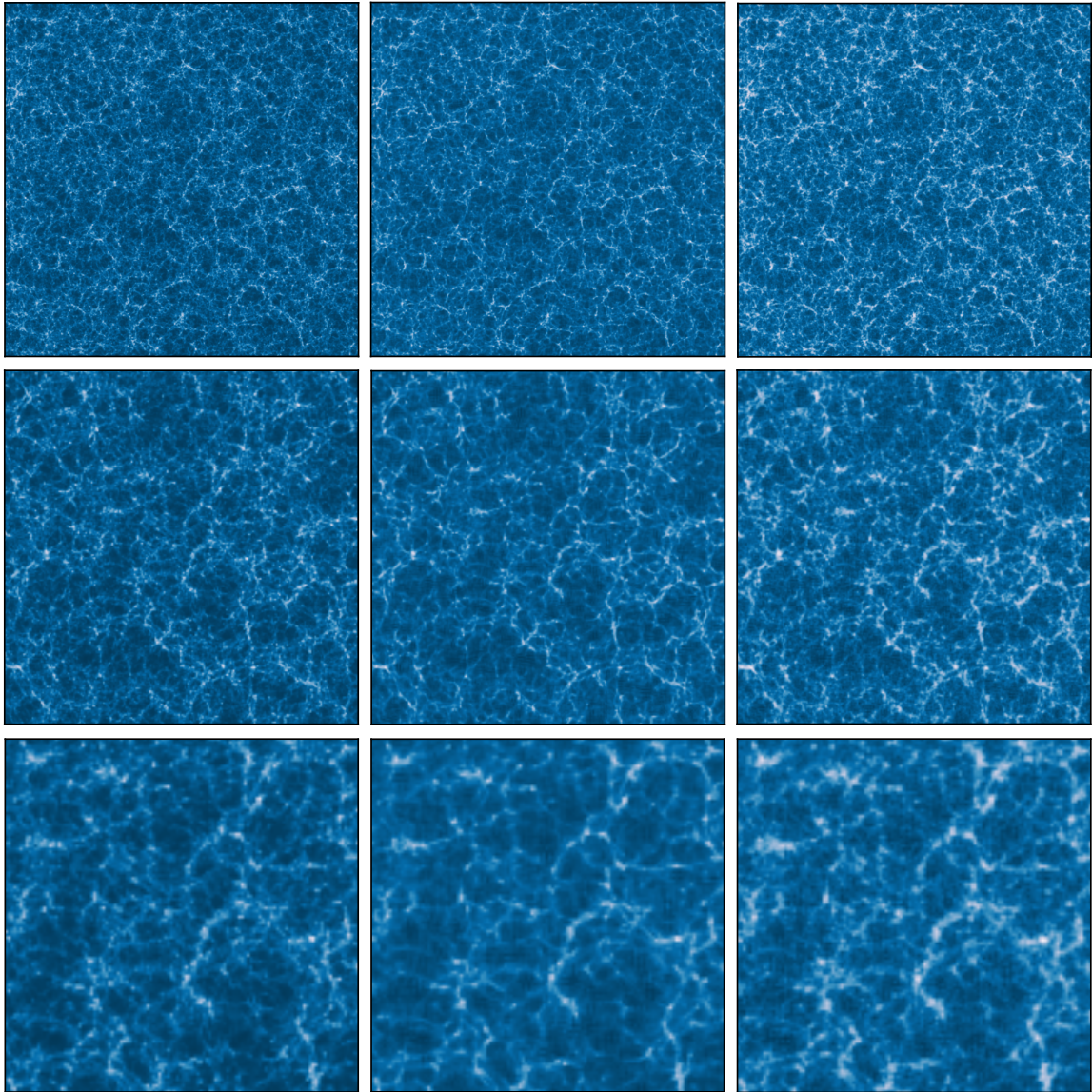


Figure 4.1: Dark matter overdensity  $\delta = \rho_m/\rho - 1$  slices of  $20 h^{-1} \text{Mpc}$  from the high-resolution BigMultiDark simulation (left panels), the low-resolution FASTPM simulation (central panels) and from the ALPT simulation (right panels), taking a subvolume of  $(1250 h^{-1} \text{Mpc})^3$  (top panels),  $(625 h^{-1} \text{Mpc})^3$  (middle panels), and  $(312.5 h^{-1} \text{Mpc})^3$  (bottom panels). The structures in the high-resolution  $N$ -body simulation and the low-resolution FASTPM simulation look very similar inspite of having very different resolutions ( $3840^3$  vs  $960^3$  particles). The low-resolution ALPT simulation looks more diffuse.

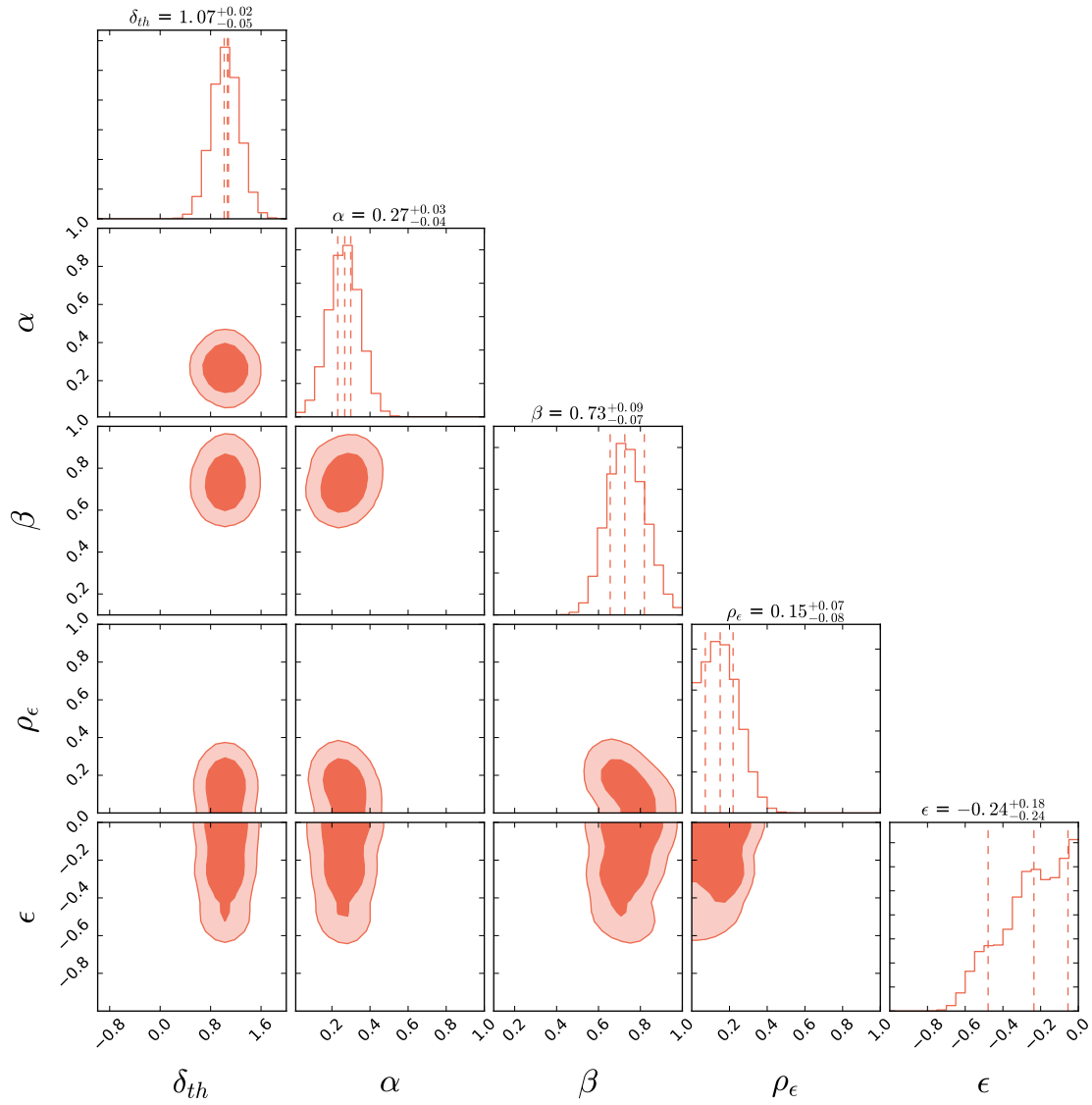


Figure 4.2: Posterior probability distribution of the PATCHY bias parameters  $\{\delta_{th}, \alpha, \beta, \rho_\epsilon, \epsilon\}$ . The contours mark the 68% and the 95% confidence intervals of the posterior probabilities. This plot is made using the open-source software CORNER (Foreman-Mackey 2017).

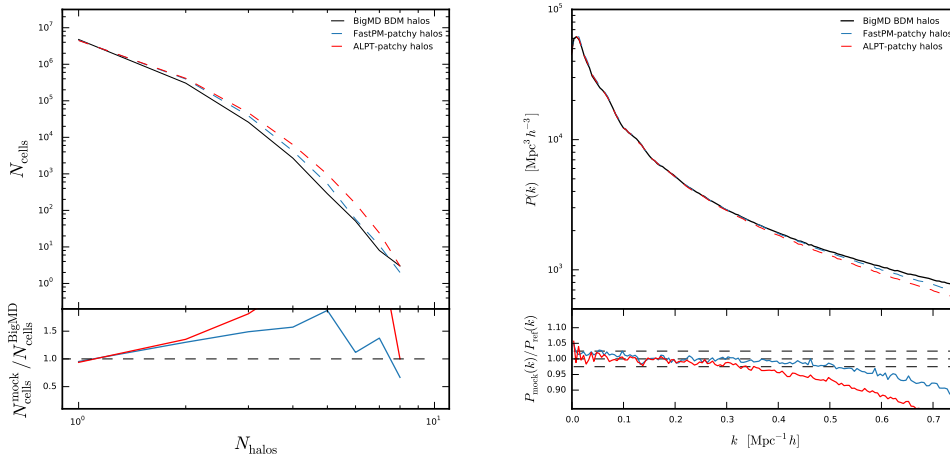


Figure 4.3: Top: Demonstration of the halo bivariate probability distribution function of halos (halo counts-in-cells) in the BigMultiDark simulation (shown in black) and in the FASTPM-PATCHY simulation (shown in blue) and in the ALPT-PATCHY simulation (shown in red) on the left. Comparison between the real-space power spectrum of the BDM halos (shown in black) in the reference BigMultiDark simulation and that of the halos in the FASTPM-PATCHY (ALPT-PATCHY) simulation shown in blue (red) on the right. Bottom: Ratio between the halo PDFs of the approximate mocks and halo PDF of the BigMultiDark simulation on the left. Ratio between the halo power spectra of the approximate mocks and the halo power spectrum of the BigMultiDark simulation on the right.

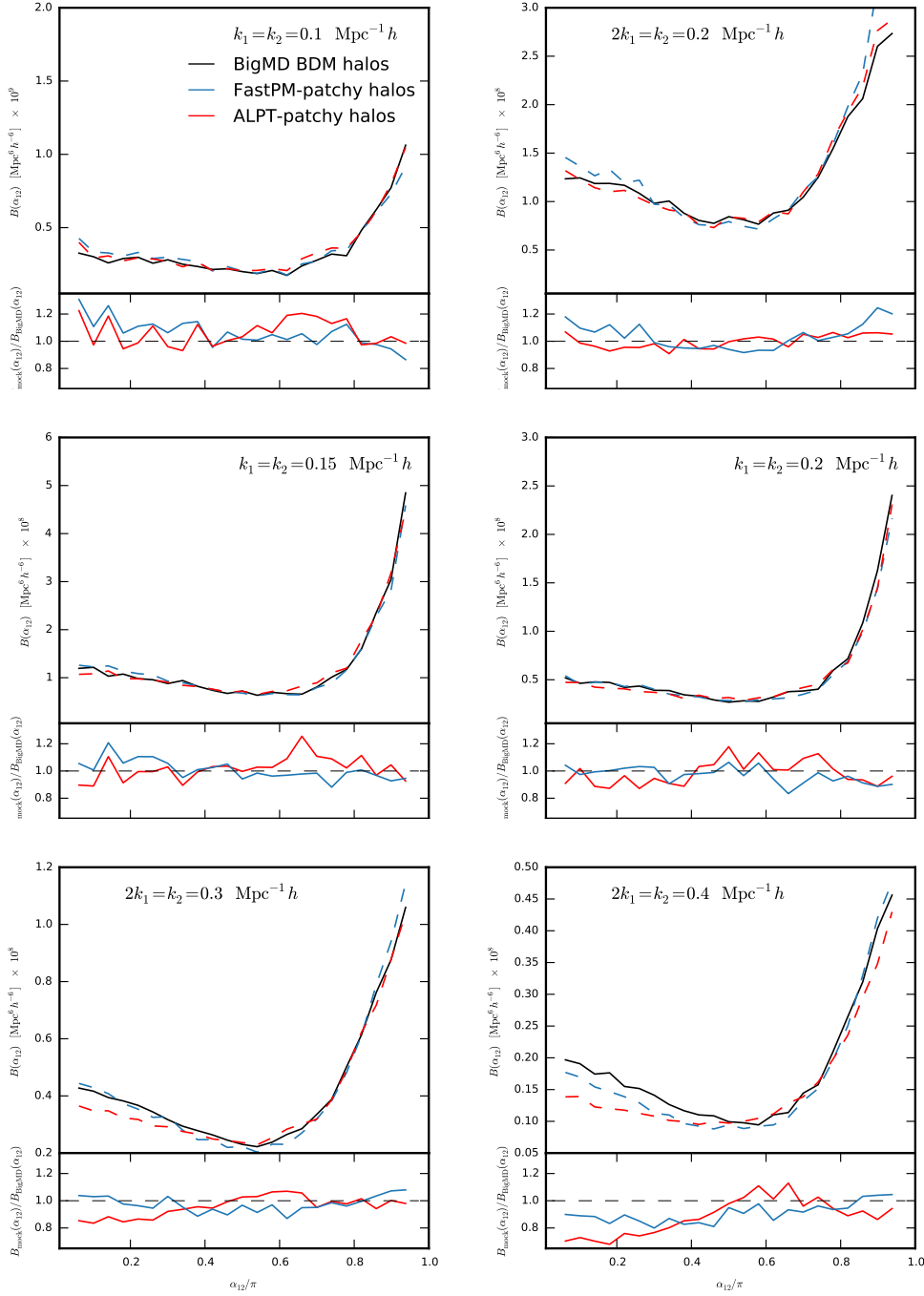


Figure 4.4: Real-space bispectrum of the BigMD BDM halos and that of the approximate mocks as a function of angle  $\alpha_{12}$  between  $\mathbf{k}_1$  and  $\mathbf{k}_2$  for  $k_1 = k_2 = 0.1 \text{ } h \text{Mpc}^{-1}$  (upper left),  $2k_1 = k_2 = 0.2 \text{ } h \text{Mpc}^{-1}$  (upper right),  $k_1 = k_2 = 0.15 \text{ } h \text{Mpc}^{-1}$  (middle left),  $k_1 = k_2 = 0.2 \text{ } h \text{Mpc}^{-1}$  (middle right),  $2k_1 = k_2 = 0.3 \text{ } h \text{Mpc}^{-1}$  (lower left), and  $2k_1 = k_2 = 0.4 \text{ } h \text{Mpc}^{-1}$  (lower right). The BigMD is represented by the solid black line, while ALPT-PATCHY is represented by the dashed red line, and FASTPM-PATCHY is represented by the dashed blue line.

# Chapter 5

## Super-resolution PSF model of HST WFC3-IR

This Chapter is joint work with Ross Fadely (Insight) and David W. Hogg (NYU) and it is being prepared for submission to a refereed journal.

### 5.1 Chapter abstract

Obtaining an accurate model of the Point Spread Function is crucial for reliable point source photometry, astrometry, and weak lensing studies. The PSF model of the *HST* WFC3 IR channel does not meet the accuracy required by these science goals. In addition, the PSF of the *HST* WFC3 IR channel is poorly sampled. Weak lensing studies of poorly resolved images of faint distant galaxies demand excellent knowledge of the PSF sampled at a resolution higher than that of the *HST* WFC3 pixels.

In this Chapter we present a generative forward model of every image taken by the WFC3 IR channel as a set of a number of point sources convolved with the instrument PSF.

We focus on modeling the pixel-convolved PSF, which is the optical PSF convolved with the pixel response function.

In particular, we model the images of point sources observed in the calibration program of the *HST WFC3* IR channel in the *F160W* bandpass. We expect the inference of the super-resolution PSF in other filters of the IR channel to follow a similar procedure. We discuss how the optimal solution of the problem can be found by adopting a variance model that correctly takes into account the model uncertainty, a regularization term that imposes a smoothness condition on the super-resolution PSF, and masking strategy for reducing the impact of overlapping sources on likelihood optimization.

## 5.2 Introduction

The Point Spread Function (hereafter PSF) determines the fraction of photons from a given point source that land at a particular displacement from the center of that point source on a detector. The PSF of the *HST WFC3* camera is under-sampled. That is, if a center of an observed star lies on the center of a pixel, a significant fraction of the brightness of that star will be encapsulated by the single pixel that contains the centroid of the star. In other words, within the full-width half-maximum (FWHM), the PSF is usually not spanned by multiple detector pixels since the pixels are large. This is mainly the result of a compromise made in design of the detectors to cover a wider field of view.

Poor sampling of the PSF by detectors renders many astronomical image processing tasks difficult. Precise astrometry and photometry of individual point sources requires knowledge of the PSF sampled at a higher resolution than that of the detector pixels. In uncalibrated observations, the images of stars are generated by convolution of the point sources with the PSF and multiplication with a non-uniform detector sensitivity called the *flat-field*. Flat-

field corrections are important for photometry and astrometry of individual point sources. In under-sampled images, capturing the sub-pixel variations of the flat-field requires having a high resolution model of the PSF.

Furthermore, cosmic shear studies require accurate measurement of the shapes of individual distant galaxies. The galaxies used for estimation of the cosmic shear signal are faint and often barely resolved by the *HST WFC3* detectors. In order to reliably measure the shapes of these poorly resolved galaxies, we need to convolve the model describing the light distribution of these galaxies with a higher resolution PSF model. Therefore, knowing the high resolution PSF is an essential ingredient in weak lensing studies of galaxies detected by the *HST WFC3* IR channel.

In this investigation, we focus on modeling the *pixel-convolved PSF*, which is the optical (instrumental) PSF convolved with the pixel response function. It is the pixel-convolved PSF that can be directly estimated from observation without making any assumption about the sensitivity of detector pixels. Moreover, it is the pixel-convolved PSF that can be used to perform astrometry and photometry measurements as well as galaxy shape measurement for weak lensing analyses. All of these involve fitting a model to the pixel-convolved PSF.

Another benefit of working with the pixel-convolved PSF is that the centers of pixels simply sample the PSF. That is, no integration of the optical PSF is required to evaluate the model of the images of point sources in observations.

Alternatively, one can deliver a model of the optical (instrumental) PSF based on physical models of the telescope optics. This involves measurement or prediction of the optical wavefront at all locations across the focal plane and the use of physically motivated parameters to model the image produced by the wavefront. Significant progress has been made in exploring the space of physical models that can reasonably describe the optical PSF ([Zernike, 1934; Krist, 1995; Krist et al., 2011; Rowe et al., 2014](#)).

Development of optical models of the PSF are valuable efforts for simulation, validation, and understanding of the systematic uncertainties that can affect astronomical inferences (Mandelbaum et al., 2015; Rowe et al., 2015). In practice, however, using the optical PSF for photometry, astrometry and weak lensing studies requires fitting a star’s model to the wavefront PSF model. The major drawbacks of this approach are the following: (i) This approach does not make use of the available observed data, and (ii) it makes strong assumptions about the sensitivity of detector pixels when it is used for model fitting. Therefore we attempt to build a data-driven or empirical model of the PSF. From now on in this Chapter we refer to the pixel-convolved PSF as the PSF.

This Chapter is structured as follows: In Section 5.3 we discuss the observations and data reduction. In Section 5.4 we discuss the algorithm we have developed for inferring the super-resolution PSF model of the *HST WFC3* IR channel observations. In Section 5.5 we present the preliminary results, and in Section 5.6 we summarize and conclude.

### 5.3 Data

The *WFC3* IR camera takes images through four filters: F105W, F125W, F140W, F160W. In what follows in the rest of this Chapter we focus on modeling the images of point sources in the F160W filter of *HST WFC3* IR channel. In our analysis, we make use of the FLT images that are calibrated with the recent models of charge transfer efficiency, flat-field, etc. We choose not to use drizzled images (Fruchter & Hook, 2002; Avila et al., 2012) because they introduce correlated noise and distortions to the PSF that are not consistent across the image (a new algorithm developed by Rowe et al. 2011 for the WFIRST mission does not suffer from these issues). These distortions pose a challenge for optimal extraction of the PSF information and accurate measurement of shapes of galaxies. Therefore we find

the pixels in the FLT images to be better-suited for PSF modeling.

For each FLT image, we follow the following procedure to select stars with sufficiently high signal-to-noise ratio for PSF modeling. First the Source Extractor software (Bertin & Arnouts, 1996) is run on each image to detect the objects. For each object, the stellarity index and blending/error flags are extracted. An object is called a *star* if no blending/error flag is raised, its stellarity index is greater than 0.8, and if its peak pixel brightness value is 25 times greater than the median pixel brightness value. The Source Extractor configuration file used in our analysis is shown in Table 5.3.

The FLT files obtained from the HST MAST archive <sup>1</sup> are accompanied by Data Quality extension files. While extracting the super-resolution PSF model from the point sources in FLT images, pixels with data quality other than zero are flagged and we do not include them in model fitting. This requirement ensures that the damaged pixels do not contribute to the PSF model. For each point source, we extract a 25 pixels  $\times$  25 pixels patch that is centered on the brightest pixel of the point source. The Neural-Network weights for Source Extractor star-galaxy separation is available in <https://github.com/mjvakili/supermean/blob/master/default.nnw>.

---

<sup>1</sup><https://archive.stsci.edu>

Table 5.1: **Source Extraction:** Source Extractor configuration file for extraction of the point sources from the *HST WFC3 IR*.

Configuration Parameter	Value	Description
DETECT TYPE	CCD	CCD (linear) or PHOTO (with gamma correction)
DETECT MINAREA	5	minimum number of pixels above threshold
DETECT THRESH	5	sigmas in mag.arcsec <sup>-2</sup>
ANALYSIS THRESH	1.5	sigmas in mag.arcsec <sup>-2</sup>
FILTER	N	apply filter for detection?
DEBLEND NTHRESH	32	Number of deblending sub-thresholds
DEBLEND MINCONT	0.005	Minimum contrast parameter for deblending
CLEAN	Y	Clean spurious detections?
CLEAN PARAM	1.0	Cleaning efficiency
MASK TYPE	CORRECT	type of detection MASKing
FLAG IMAGE	flags.fits	
FLAG TYPE	AND	
WEIGHT GAIN	N	
WEIGHT IMAGE	variance.fits	
WEIGHT TYPE	MAP VAR	
PHOT APERTURES	3,5,7	MAG APER aperture diameter(s) in pixels
PHOT AUTOPARAMS	2.5, 3.5	MAG AUTO parameters: Kron fact, min radius
PHOT PETROPARAMS	2.0, 3.5	MAG PETRO parameters: Petrosian fact , min radius
PHOT FLUXFRAC	0.2, 0.5, 0.9	
SATUR LEVEL	50000.0	level (in ADUs) at which arises saturation
MAG ZEROPPOINT	1.0e-19	magnitude zero-point
MAG GAMMA	4.0	gamma of emulsion (for photographic scans)
GAIN	0.0	detector gain in $e^- / ADU$
PIXEL SCALE	0.13	size of pixel in arcsec
SEEING FWHM	0.17	stellar FWHM in arcsec
STARNNW NAME	“./default.nnw”	Neural-Network Weight table filename
BACK SIZE	64	Background mesh: size
BACK FILTERSIZE	3	Background filter: size
BACKPHOTO TYPE	GLOBAL	Background type: can be GLOBAL or LOCAL

## 5.4 Method

### 5.4.1 generative model

We build our empirical model of the PSF by assuming that a given point source at the center of a patch can be described by the following quantities:

- A global solution for the super-resolution PSF  $X$  that is shared between all point sources across the field of view. We assume that  $X$  is normalized to one and it is centered at the center of the central pixel of the patch. This super-resolution PSF is sampled on a grid with a higher resolution than the native pixel grid of *HST WFC3* IR observations.
- Centroid coordinate of a point source at a given patch  $\Delta_n = (\Delta x_n, \Delta y_n)$ . These two parameters dictate the offset between the position of the centroid of the point source  $n$  with respect to the center of the patch. Because we have centered our  $25 \times 25$  patches on the brightest pixel, we expect these offsets to be small.
- Flux quantity  $f_n$  which is related to the brightness of the point source in each patch.
- A background quantity  $b_n$  which sets the brightness level of the background sky in each patch.

Given these ingredients, we write down the generative forward model of the point sources in the center of patches in the following way:

$$\mathbf{d}_n = \mathbf{m}_n + \text{noise}, \quad (5.1)$$

$$m_{n,i} = f_n K_{il}^{(n)}(\Delta_n) X_l + b_n. \quad (5.2)$$

In Eq. 5.1,  $\mathbf{d}_n$  is the observed 625-dimensional vector describing the brightness of the pixels in the 25 pixels  $\times$  25 pixels patch  $n$ .  $\mathbf{m}_n$  is the model that describes the pixel-convolved model of the point source sitting on the center of the patch  $n$  with the same dimensionality. The noise term noise has a variance that we present shortly. In Eq. 5.2, the operator  $K^{(n)}(\Delta_n)$  is a linear operator that maps the super-resolution PSF  $X$  to a downsampled PSF at the native data grid. That is, when this operator acts on  $X$ , it samples  $X$  on a downsampled grid (with the same resolution as the observations) that is shifted with respect to the grid on which  $X$  is defined. The shift between the two grids is given by the vector  $\Delta_n = (\Delta x_n, \Delta y_n)$ .

We want to be able to explicitly construct these matrices so we can analytically compute the likelihood function and its derivative with respect to the super-resolution PSF  $X$ . We implement the linear sampling operator  $K$  with bivariate cubic-spline interpolation. By comparing our implementation of cubic-spline with that of the open source software `scipy` we note that they have consistent performances.

It is worth noting that there exist many possibilities for designing the sampling operator  $K$ . The simplest and fastest approach that one could choose is bilinear interpolation. But after applying this method to simulated PSFs, we find that this method lacks the accuracy we need. Ideally, one could use a sinc interpolation (Bickerton & Lupton, 2013; Rowe et al., 2015), which is an optimal choice for preserving information. But we find sinc interpolation to be computationally demanding. Under same assumptions, we experimented with Gaussian Process interpolation for designing the downsampling matrix  $K$ , but Gaussian Process interpolation requires additional computing time to set hyper parameters.

The factor by which the PSF is undersampled varies from one filter to another. Our strategy for inferring the super-resolution of the PSF model of F160W filter is as follows. We aim to estimate  $X$  on a 75 pixels  $\times$  75 pixels grid, which is a resolution three times that of the native pixel grid of the observations.

### 5.4.2 likelihood optimization

Now that we have explained the quantities needed to describe the generative model of WFC3 IR observations, we present our strategy for estimating the values of the parameters of individual point sources  $\{f_n, b_n, \Delta_n\}_{n=1}^N$  and the global solution of the super-resolution PSF  $X$ .

In order to estimate the PSF, we optimize the following likelihood function with respect to the parameters  $\{f_n, b_n, \Delta_n\}_{n=1}^N$  and the PSF solution  $X$ :

$$-2 \ln L = -2 \sum_{n=1}^{N_{\text{patches}}} \ln L_n, \quad (5.3)$$

$$-2 \ln L_n = \sum_{i=1}^{N_{\text{pix}}} \left( \frac{(d_{n,i} - m_{n,i})^2}{s_{n,i}^2} + \ln(2\pi s_{n,i}^2) \right), \quad (5.4)$$

where  $L_n$  is the likelihood of patch  $n$ ,  $L$  is the likelihood of the entire astronomical scene,  $s_{n,i}$  is the  $i$ th component of the 625 dimensional vector  $\mathbf{s}_n$ , and  $\mathbf{s}_n^2$  is variance of the noise model in patch  $n$ . The variance is composed of two terms, one arising from the Gaussian readout noise and another arising from the Poisson noise. Therefore the total variance is given by a constant per-pixel variance of a Gaussian noise and a gain-like term that is proportional to the model  $\mathbf{m}_n$  defined in Eqs. ??:

$$\mathbf{s}_n^2 = \sigma^2 + g \cdot \mathbf{m}_n, \quad (5.5)$$

where we extract Gaussian variance  $\sigma^2 = 0.01$  and gain  $g = 0.05$  from the *HST* data.

It is important to note that our forward model of the WFC3 IR observations given by Eq. 5.2 suffers from multiple degeneracies. The first degeneracy is between the flux values  $\{f_n\}$  and the super-resolution PSF  $X$ . This degeneracy will prevent us from finding a unique

solution for  $\{f_n\}$  and  $X$ . This degeneracy can be broken by introducing a regularization term to Eq. 5.3 that imposes smoothness condition to  $X$ .

We add the following term to the log-likelihood  $L$

$$C_{\text{reg}} = -2 \ln L + \epsilon \sum_{j,k} \delta_{j,k}^2, \quad (5.6)$$

where the second term is the sum of the squared of the matrix  $\delta$  whose  $j, k$  components are given by the difference between the  $j$ th row and  $k$ th column of the super-resolution PSF and its nearest pixels. The prefactor  $\epsilon$  sets the strength of the regularization term. This enforces our prior belief that the PSF should be a smoothly varying object.

The second type of degeneracy is between the centroid offsets  $\{\Delta_n\}$  and the super-resolution PSF  $X$ . In order to lift this degeneracy, we do not add any regularization term. Instead, throughout the optimization procedure we enforce a set of conditions that break this degeneracy. These conditions enforce the super-resolution PSF to be normalized and centered around the central pixel of the higher resolution grid.

For inference of the PSF, we follow an optimization procedure similar to the method of Expectation Maximization (EM). In the context of astronomy, EM has been employed in extreme deconvolution (Bovy et al., 2011) and heteroscedastic matrix factorization (Tsalmantza & Hogg, 2012). Finding the optimal solution of  $X$  and  $\{f_n, b_n, \Delta_n\}$  proceeds as follows.

First we initialize the parameters  $X$  and  $\{f_n, b_n, \Delta_n\}$ . We initialize the centroid offsets  $\Delta_n$  by the matched-filter polynomial centroiding described in Chapter 1. In particular, we correlate a Gaussian kernel with FWHM of 2.0 pixels with the  $5 \times 5$  central pixels of each patch before applying the polynomial centroiding method. The reason for why we apply the polynomial method to the central pixels of each patch is that many of the stars in our *HST* observations are in crowded fields and therefore applying the matched-filter

centroding method to the entire patch could lead to biases as a result of light contamination from overlapping or nearby sources.

The initial background values  $\{b_n\}$  are estimated by taking the median pixel value in each patch. For initializing the flux values  $\{f_n\}$ , first we subtract the initial estimates of background values from each patch. Afterwards, the  $\{f_n\}$  values are initialized by computing the sum of the pixel values within  $5 \times 5$  apertures centered on the central pixels of the patches. The reason for limiting our initialization of the flux estimates to the  $5 \times 5$  apertures is to prevent contamination of fluxes from overlapping and nearby sources. Besides, since the PSF is poorly sampled, we expect the majority of the flux to be captured by a few pixels around the centers of the patches.

Lastly, the super-resolution PSF  $X$  is initialized in the following way. First we subtract our initial estimates of the sky background levels from the patches. Then we divide the pixel values of the patches by their corresponding initial flux estimates. Then we use the cubic-spline interpolation method to interpolate the rescaled patches to a high resolution  $75 \times 75$  grids that are shifted by  $\{-\Delta_n\}$  with respect to the patch centers. Afterwards, we evaluate the mean of the interpolated rescaled patches to estimate the initial PSF. Furthermore, we normalize the PSF and interpolate it such that it is centered on the central pixel of the  $75 \times 75$  high resolution grid.

Now that we have initialized the parameters of our model, we present the EM algorithm for optimizing them. At every iteration, we follow this iterative scheme. In the  $n$ th patch, we update  $b_n$  by optimizing  $L_n$  while holding  $\{f_n, \Delta_n, X\}$  fixed. Then we update  $f_n$  by optimizing  $L_n$  while holding  $\{b_n, \Delta_n, X\}$  fixed. Then we update  $\Delta_n$  by holding  $\{f_n, b_n, X\}$  fixed. Once  $\Delta_n$  is updated, we update the sampling matrix  $K^{(n)}$  accordingly.

After updating  $\{b_n, f_n, \Delta_n\}$  for all patches, we update  $X$  by optimizing the regularized cost function  $C_{\text{reg}}$  given in Eq. 5.6. At every iteration, we normalize the super-resolution

PSF and interpolate it such that it is centered on the center of the  $75 \times 75$  grid. We repeat these iterations until the value of regularized cost function  $C_{\text{reg}}$  converges.

So far we have not addressed the problem of how our generative forward model of the patches takes into account the contamination arising from overlapping or nearby sources. In order to alleviate this issue, we introduce an additional noise model for identifying and masking out pixels that are in ill-fit portions of the patches.

The variance of this noise model is given by

$$\tilde{s}_n^2 = \sigma^2 + g\mathbf{m}_n + q\mathbf{m}_n^2, \quad (5.7)$$

which is similar to the variance given by Eq. 5.5 but with an additional term is proportional to the squared, downsampled model describing the patch. This accounts for possible discrepancies between the downsampled PSF model of the point source at the center of the patch and the observed pixels. That is, it is an effective model “wrongness term” term.

This variance is used in a  $\chi^2$  clipping technique to mask out ill-fit portions of the patches. This clipping step will prevent the the pixels affected by nearby sources to bias the inferred parameters. In particular, after every model realization we identify the pixels that are not faithfully represented by the model and mask them so they do not contribute to computation of the patch likelihood function (5.4).

At every iteration of optimizing the patch log-likelihood function, we mask out the pixels for which a clipped  $\chi^2$  (denoted by  $\chi_{\text{clip}}^2$  from now on) is larger than 3. For a given patch  $n$ , the clipped  $\chi^2$  is defined in the following way:

$$\chi_{n,\text{clip}}^2 = \frac{(\mathbf{d}_n - \mathbf{m}_n)^2}{\tilde{s}_n^2}, \quad (5.8)$$

where  $\tilde{s}_n^2$  is given by Eq. 5.7. In a given patch  $n$ , the log-likelihood pixels with  $\chi_{n,\text{clip}}^2 > 3$

do not contribute to computation of  $L_n$  and its derivatives with respect to model variables. We set the parameter  $q$  to 1. We note that this choice of does a good job at masking out the pixels that receive light from the nearby or overlapping sources. In principle  $q$  needs to decrease iteratively as our knowledge of the PSF improves. In this work however, we choose to hold the value of  $q$  fixed at one.

## 5.5 Preliminary Results

With the ingredients of our methodology explained in Section 5.4, we now present the results of applying our method to the observations of the point sources in the *HST WFC3* IR channel. We train our PSF model with a number of patches that were selected such that majority of them only contain one point source.

In principle given the methodology explained in Section 5.4, we can train our forward model on patches with arbitrary number of stars. But in order to minimize the training time as much as possible, we select a set of isolated and relatively high signal-to-noise ratio stars as our training sample. It is important to note that selecting patches containing isolated sources does not necessarily guarantee that there is *no* light contamination by the nearby sources.

Therefore it is necessary to follow the procedure explained in the previous section to clip the pixels that may have received light contamination from the nearby sources. The parameter  $q$  will be held at the constant value of  $q = 1$  and any pixel with  $\chi_{\text{clip}}^2 > 3$  will not be permitted to contribute to the likelihood function. This will ensure that the ill-fit portions of the training pixels will not bias the final PSF estimate.

Note that we also need to set the strength of the smoothness regularization term  $\epsilon$ . Here, we can take advantage of the patches that were not used in training the PSF model to

perform cross-validation. Cross-validation can be done in the following way. A set of values  $S_\epsilon$  for the parameter  $\epsilon$  need to be selected. For every  $\epsilon$  in  $S_\epsilon$ , the optimization procedure as described above can be followed to estimate  $X_\epsilon$  which is the estimated  $X$  corresponding to  $\epsilon$ .

Then one can optimize the patch negative log-likelihood  $-2 \ln L_n$  given in Eq. 5.4 to find a solution for  $\{f_n, b_n, \Delta_n\}$  variables for every patch in the cross-validation set. Afterwards, the optimal values of  $-2 \ln L_n$  in cross-validation patches can be summed up to compute the cross-validation score  $C_{cv}$  as a function of the regularization strength  $\epsilon$ . In the end, the PSF solution  $X_\epsilon$  that minimizes this cross-validation cost function will be selected as the optimal solution.

Although it is important to set the value of  $\epsilon$  by minimizing a cross-validation score, in practice one can choose a value for  $\epsilon$  by ensuring that neither the negative log-likelihood nor the regularization term will dominate each other.

Choosing an arbitrarily large value of  $\epsilon$  will drive the optimization procedure to only optimize the smoothness term, while choosing a very small value of  $\epsilon$  will make the smoothness regularization negligible. We found that with  $\epsilon = 1000$ , the contributions received from the two terms of the right hand sides of Eq. (5.6) remain similar. Therefore in what follows in the remainder of this Chapter we set  $\epsilon$  to 1000. Furthermore, we only use the validation set (patches not used in estimating the PSF) for validating our PSF model and verifying our methodology for masking the contribution of nearby stellar sources to patch fitting.

In Figure 5.1 we show our initialization of the super-resolution PSF method and our final estimate of the PSF found by minimizing Eq. (5.6). We note that in comparison to the final estimate of the PSF, our initial estimate based on scaling, shifting, upsampling and averaging is very smooth. Additionally, the initial PSF misses many of the sharp features and structures that exist in the optimized solution, specially along the tails of the PSF.

Performance of the method at modeling the patches in the training sample is demonstrated in Figures 5.2, 5.3, 5.4, 5.5. Note that, we have *intentionally* selected isolated sources with relatively high signal-to-noise ratios for training our algorithm. In addition to the data and the scaled realization of the model at the native pixel grid, we show a  $\chi$  map (a measure for the goodness-of-fit), and a map of various pixels across the patch that have been flagged by the observations or the model. Pixels with  $\text{FLAG} = 0$  are the pixels used in PSF modeling.  $\text{FLAG} = 1$  corresponds to pixels that were flagged in MAST data quality extensions. Finally,  $\text{FLAG} = 2$  corresponds to the group of pixels for which  $\chi_{\text{clip}}^2 > 3$ .

Figures 5.2 and 5.3 show examples of two relatively bright sources. Note that even in our training pixels, there are pixels that are ill-fit and are masked out according to the clipping criteria. Figures 5.4, 5.5 show the performance of our method at modeling the relatively low signal-to-noise ratio point sources in the training sample. We note that overall, the model shows good performance at modeling these sources.

The validation set consists of stellar sources that are mostly present in crowded fields. The majority of the patches in the validation set have either more than one point source, or have light contamination by nearby sources. We have not used these sources in our PSF modeling but we show how our super-resolution PSF estimate can be used in modeling the crowded astronomical scenes in the validation set. In each patch, we optimize the patch negative log-likelihood function given in Eq. (5.4) to estimate the background sky, flux, and the centroid of the point source on the center of the patch.

Furthermore, we use the clipping criterion  $\chi_{\text{clip}}^2 > 3$  to mask out pixels for which the squared model residuals are larger than modified variance given in equation (5.7). Note that the masking procedure needs to be repeated at every realization of the patch model given in equation (5.2). After applying this clipping method to the validation set, we extended it in the following way: after every model realization and identifying the flagged pixels with

$\chi_{\text{clip}}^2 > 3$ , we grow the flagged regions in every direction by one pixel. We found this to be a more conservative choice and also better at capturing the pixels that receive light from the outer tails of the PSF from other stars. In what follows, we show examples for both the original and the extended versions of our masking algorithm.

Examples of the performance of our model with a less conservative masking algorithm are shown in Figs. 5.6, 5.7, 5.8, 5.9. As it can be seen in Figs. 5.6, 5.7, 5.8, the masking algorithm identifies majority of the pixels that are ill-fit with the PSF model (5.2) and prevents them from contributing to the  $\chi$  map. However, there are still pixels that receive a small fraction of their brightness from the nearby point sources and are not masked out of the  $\chi$  map.

Figure 5.9 demonstrates the most extreme case in which a tail of the PSF from a very bright nearby source is present in the patch and it is not completely masked out by the original clipping algorithm. This shows the need to adopt the more conservative choice described above and grow the masked regions in every direction by one pixel. Figures 5.10, 5.11, 5.12 demonstrate patch-fitting examples in which a more conservative masking algorithm is adopted. Note that in these patches most of the light received from the nearby sources or the ill-fit pixels are almost completely removed from the  $\chi$  map.

## 5.6 Summary and Discussion

In this work, we have presented the first generative forward model of the observations of every point source in the rich *HST WFC3 IR* dataset. The point spread functions of WFC3 IR channels are the most undersampled amongst all *HST* channels. The exercise of making highly accurate measurements of the shapes of faint and poorly resolved galaxies, accurate and precise astrometry and photometry of point sources, correction of the variable sub-pixel response function “flat-field” of the telescope, and many other scientific applications require

great knowledge of the PSF at a resolution higher than what is sampled by the WFC3 IR detectors.

Our approach differs from the analysis developed for the *Euclid satellite* presented in Ngol  Mboula et al. (2015, 2016) in that it does not attempt to infer the super-resolution PSF in a wavelet basis and it does not impose any sparsity regularization. It assumes a more general noise model that includes both the Gaussian pixel noise and the Poisson noise arising from the instrument gain.

Our analysis is different than the approach of Anderson & King (2000) as we estimate the PSF by optimizing a well-motivated objective function that is based on a generative forward model of the observations. However, they are similar in that they both require regularization of the PSF model after every iteration so that the degeneracy between the super-resolution PSF and the centroids of stars can be lifted. The method presented in Anderson & King (2000) is based on shifting, averaging and eventually smoothing the PSF but it does not involve optimizing any likelihood function. Furthermore, it is restricted to using only the isolated point sources and it is not prone to patches in which there is light contamination by the nearby sources.

The method presented in this Chapter implements a rigorous treatment of every pixel that is ill-fit by the PSF model as a result of overlapping sources or light contamination by nearby sources. We implemented this by introducing a clipped  $\chi^2_{\text{clip}}$  that takes into account the model uncertainty. At every model realization throughout patch-fitting, pixels with  $\chi^2_{\text{clip}}$  more than a certain level are prevented from contributing to the likelihood function.

PSF estimation and accurate point source photometry on a crowded field has two main challenges. *First*: a large fraction of the pixels may not be usable for modeling purposes. This could lead to significant information loss. *Second*: using pixels that receive photons from multiple sources in modeling the PSF can bias the final PSF estimate. Using a validation

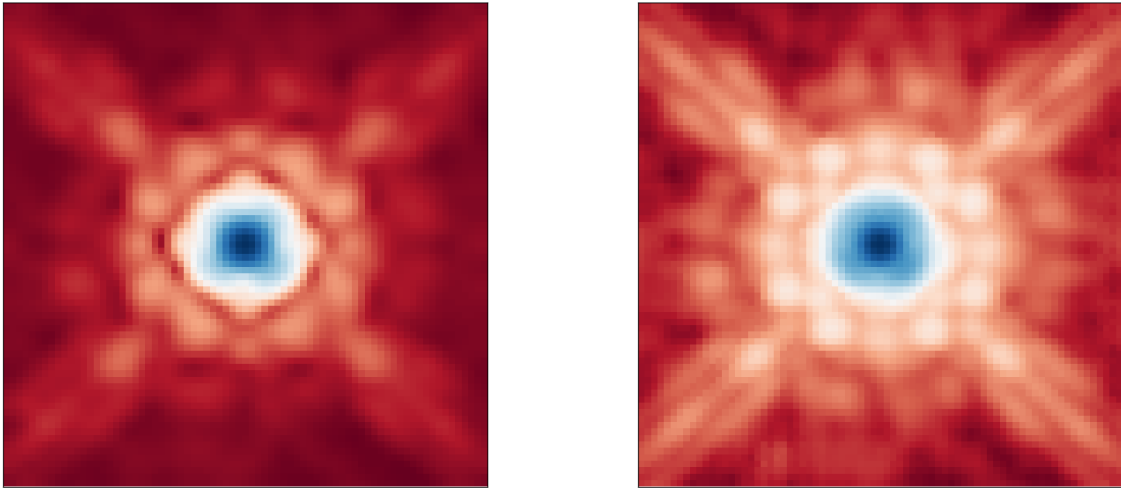


Figure 5.1: Left: Demonstration of the initialization of the super-resolution PSF model. The initial PSF was constructed by scaling (background subtraction and flux normalization), shifting (through matched-filter polynomial centroiding), upsampling (with cubic spline interpolation), and averaging the isolated stars in the observation sample. Right: Super-resolution PSF estimated by optimizing the likelihood function after six iterations. We note that the averaged upsampled initial PSF is smooth and lacks the sharp features visible across the full radian support of the PSF, specially the tails.

set containing many point sources in the crowded fields, we show that we can successfully use our technique to learn the pixel-convolved PSF. This allows us to make optimal use of all the pixels in *WFC3* IR observations of crowded fields.

## Acknowledgments

We are grateful to Jay Anderson, Dan Foreman-Mackey, Michael Blanton, and Alex Malz for discussions related to this work.

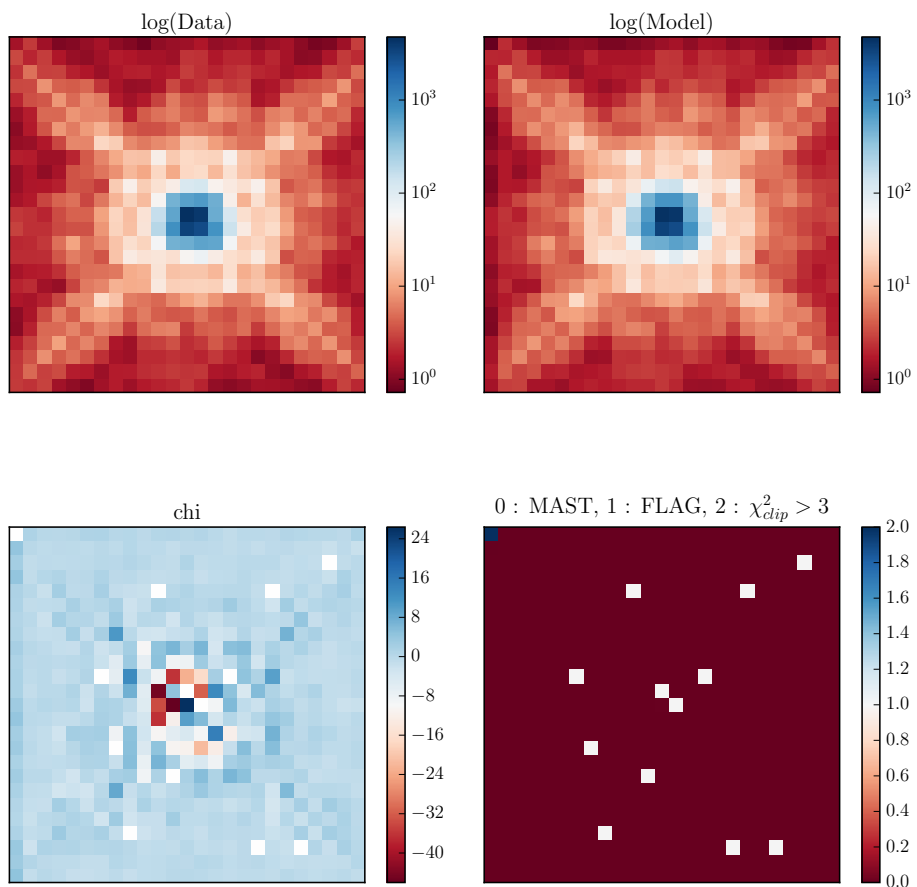


Figure 5.2: An example of a patch containing a high signal-to-noise ratio star in the training set. Upper-left and upper-right panels show the data and the model respectively. The lower left panel shows  $\chi$ . The lower right panel shows the flagged pixels. Pixels with  $\text{FLAG} = 0$  are used in PSF-fitting. Pixels with  $\text{FLAG} = 1$  (provided by the MAST data) are masked out prior to the analysis. Finally, pixels with  $\text{FLAG} = 2$  correspond to the pixels in a given model realization with  $\chi_{\text{clip}}^2 > 3$ .

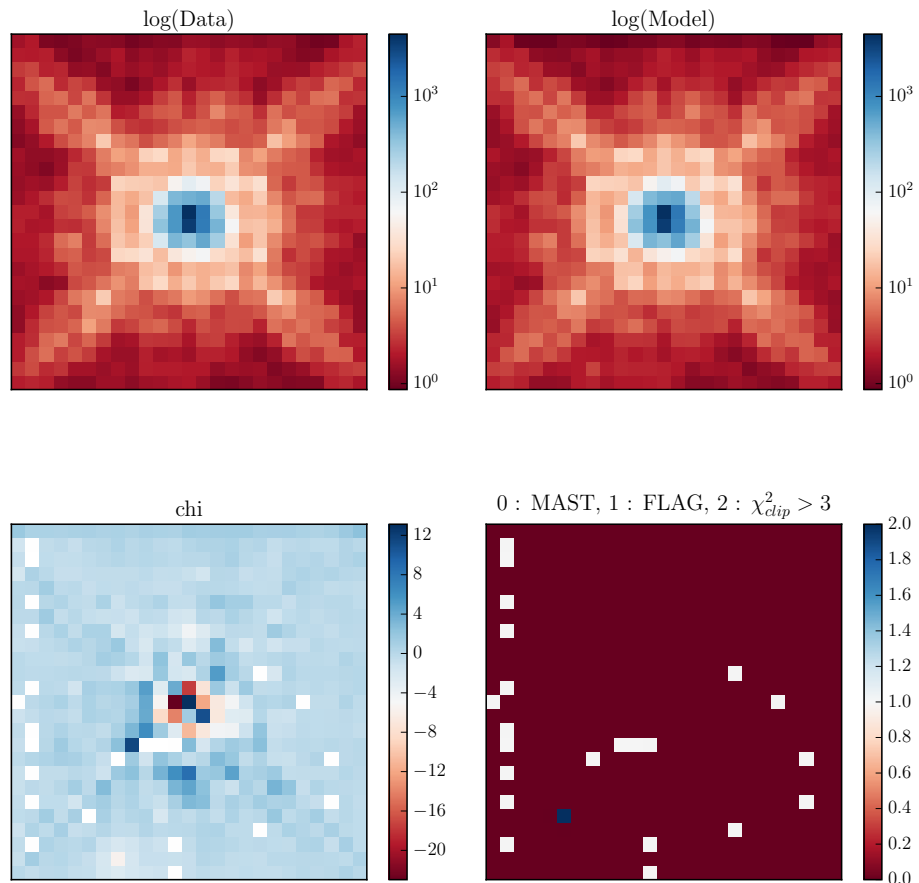


Figure 5.3: Same as Figure 5.2 but showing a different high signal-to-noise ratio star in the training set.

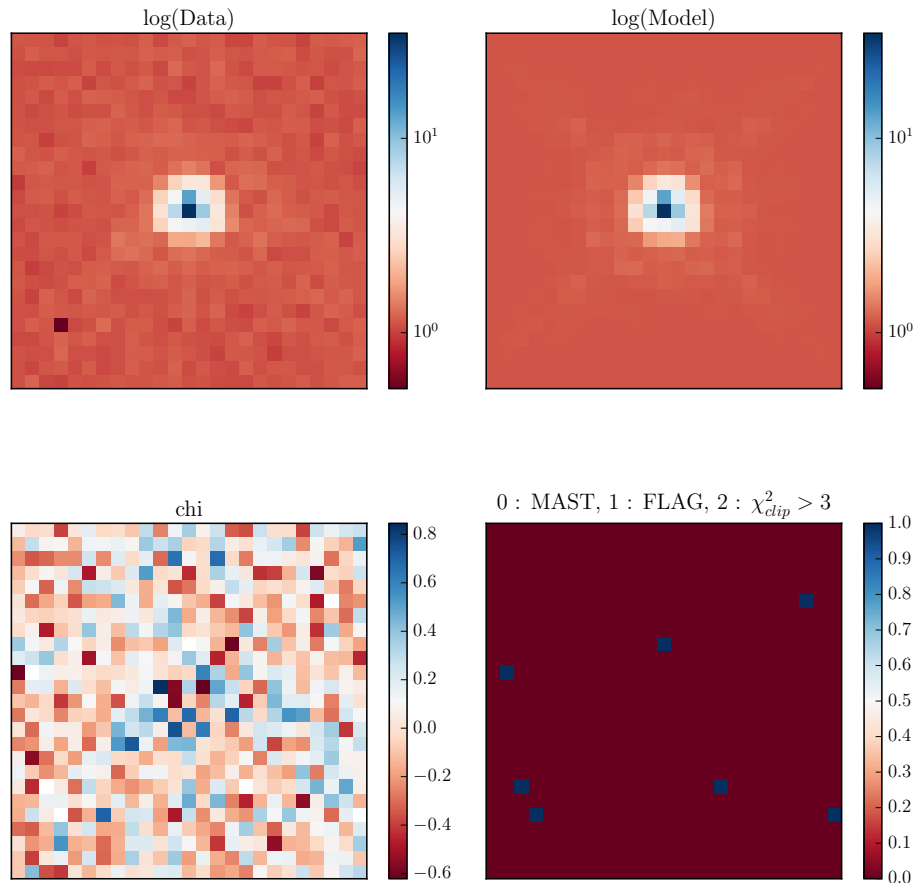


Figure 5.4: Same as Figure 5.2 but showing a low signal-to-noise ratio star in the training set.

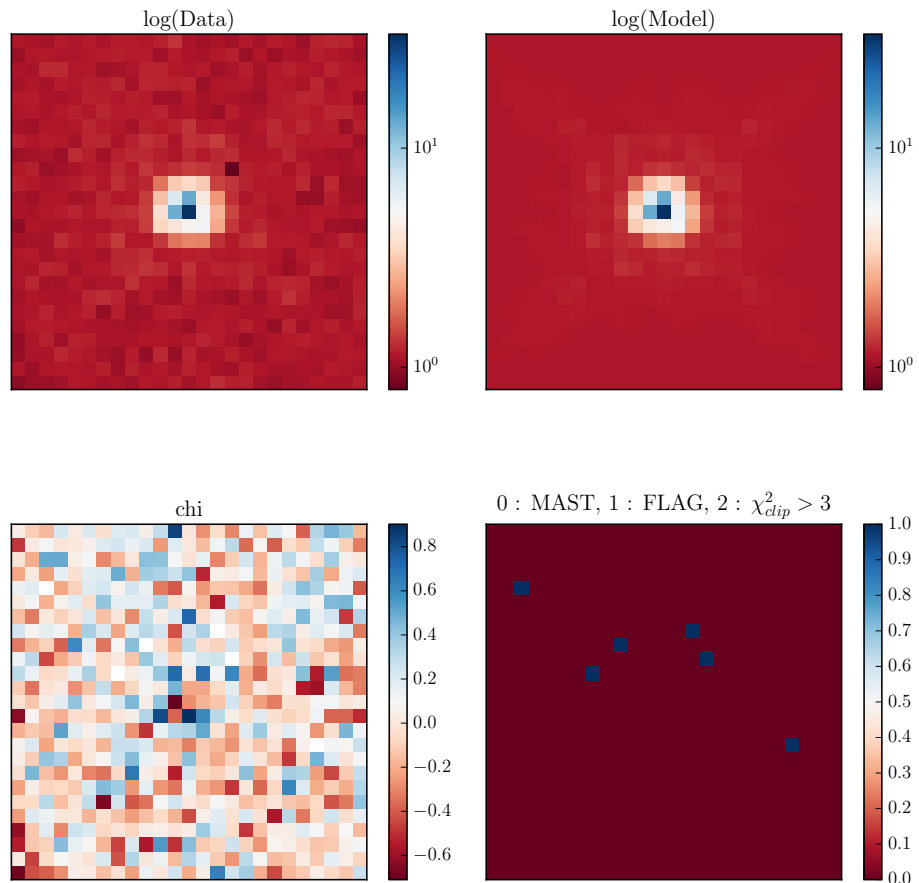


Figure 5.5: Same as Figure 5.2 but showing a different low signal-to-noise ratio star in the training set.

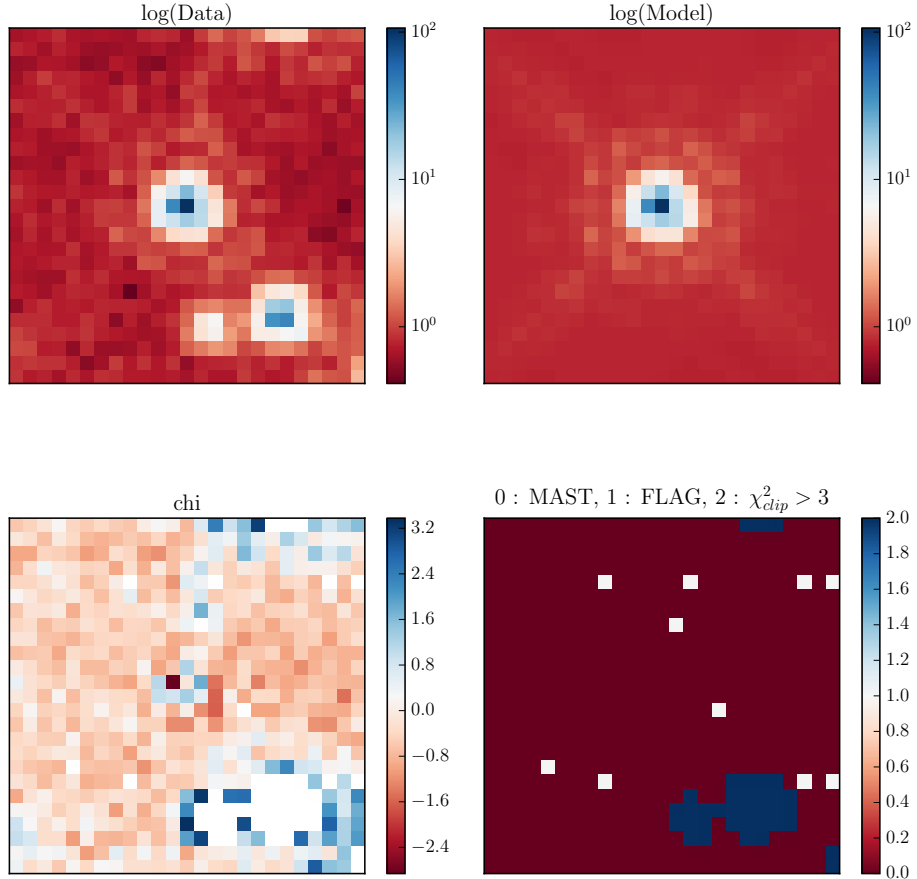


Figure 5.6: An example of a patch in the validation set containing multiple point sources. Upper-left and upper-right panels show the data and the model respectively. The lower left panel shows the  $\chi$  map. The lower right panel shows the flagged pixels. Pixels with **FLAG** = 0 are used in PSF-fitting. Pixels with **FLAG** = 1 (provided by the MAST data) are masked out prior to the analysis. Finally, pixels with **FLAG** = 2 correspond to the pixels in a given model realization with  $\chi^2_{clip} > 3$ . In the lower left panel, pixels with  $\chi^2_{clip} > 3$  are masked out from the  $\chi$  map. Note that the point sources visible in the lower right and upper right corner of the data are masked out in the  $\chi$  map. Here we do not grow the masked regions and therefore a small fraction of the light from the other point sources still contribute to the map.

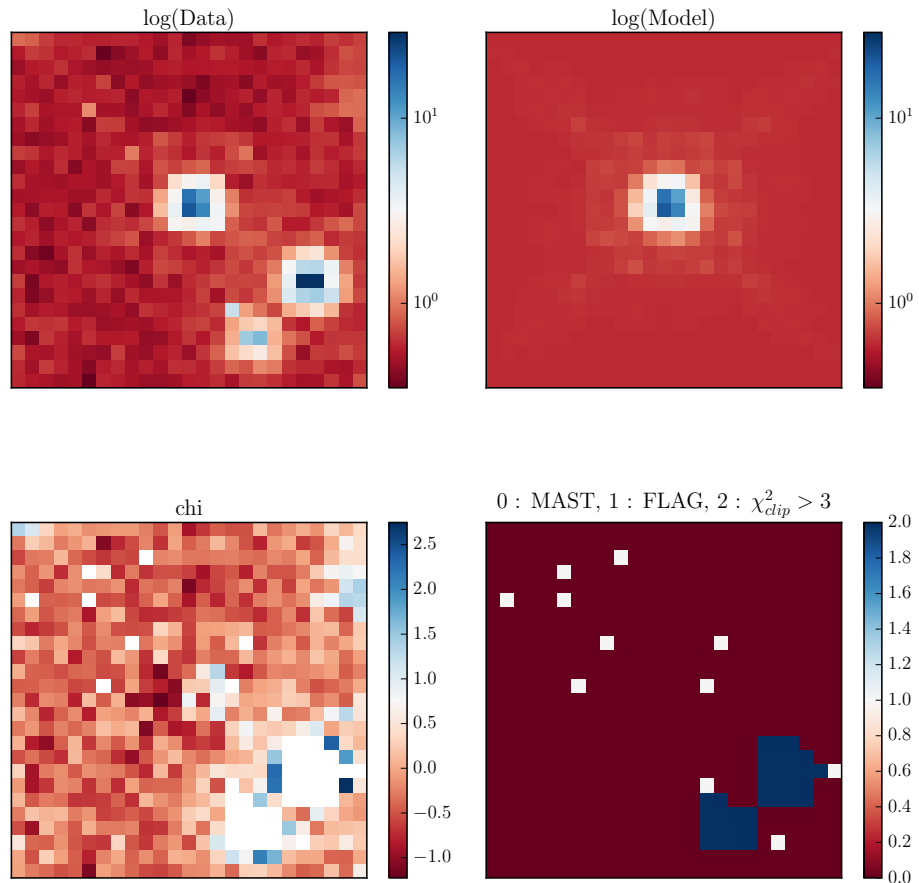


Figure 5.7: Same as Figure 5.6 but showing a different patch of sky.

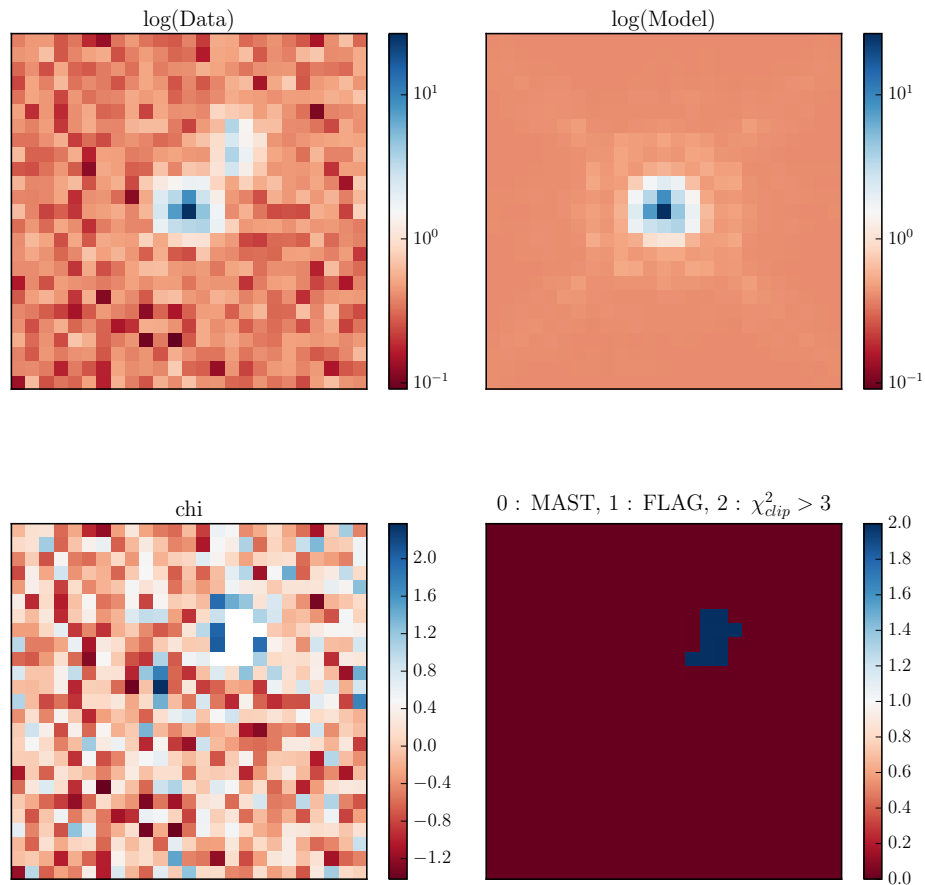


Figure 5.8: Same as Figure 5.6 but showing a different patch of sky. Two nearly overlapping faint point sources are present in this patch. The clipping algorithm masks out the second star. Since we do not grow the masking regions in this example, it is likely that the second faint star could still have slight contribution to the  $\chi$  map.

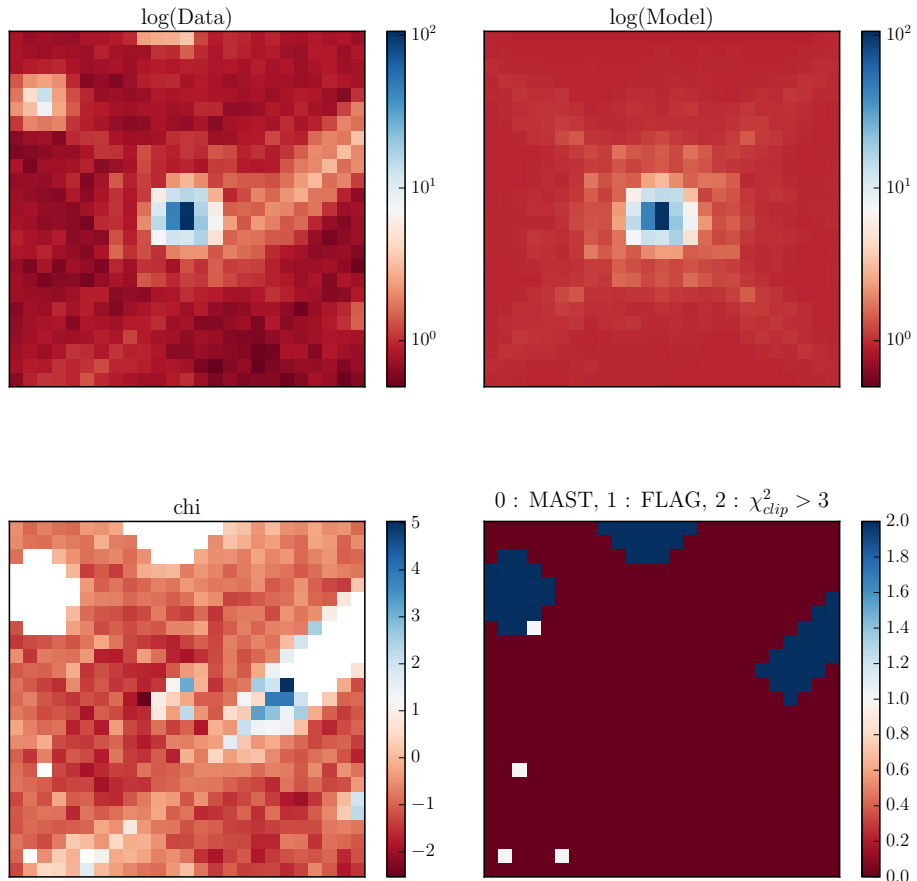


Figure 5.9: Same as Figure 5.6 but showing a different patch of the sky and and a PSF diffraction spike from a nearby source whose centroid is not in the patch. The clipping algorithm masks out most of the pixels that are affected by the PSF tail from an external source. Once again, this demonstrates the need to adopt the more conservative masking algorithm that grows the clipped regions in every direction.

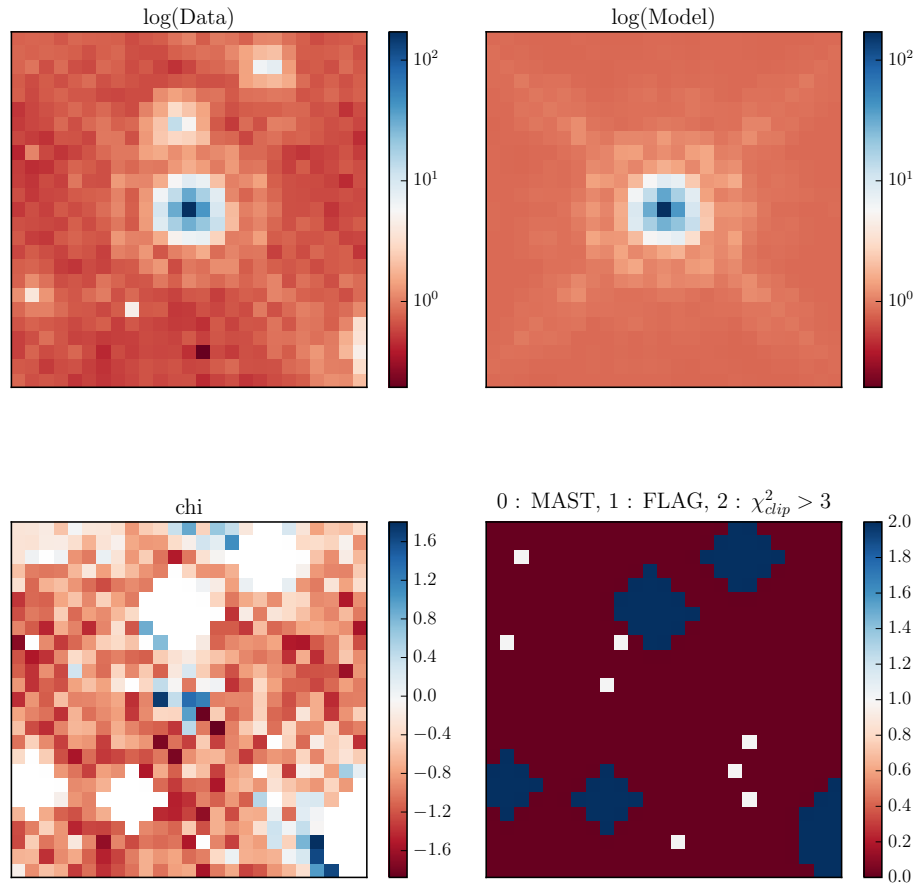


Figure 5.10: Same as Figure 5.6 but showing a different patch of sky and a more *conservative* clipping algorithm. Masked regions containing the pixels with  $\chi_{clip}^2 > 3$  are grown in every direction with one pixel.

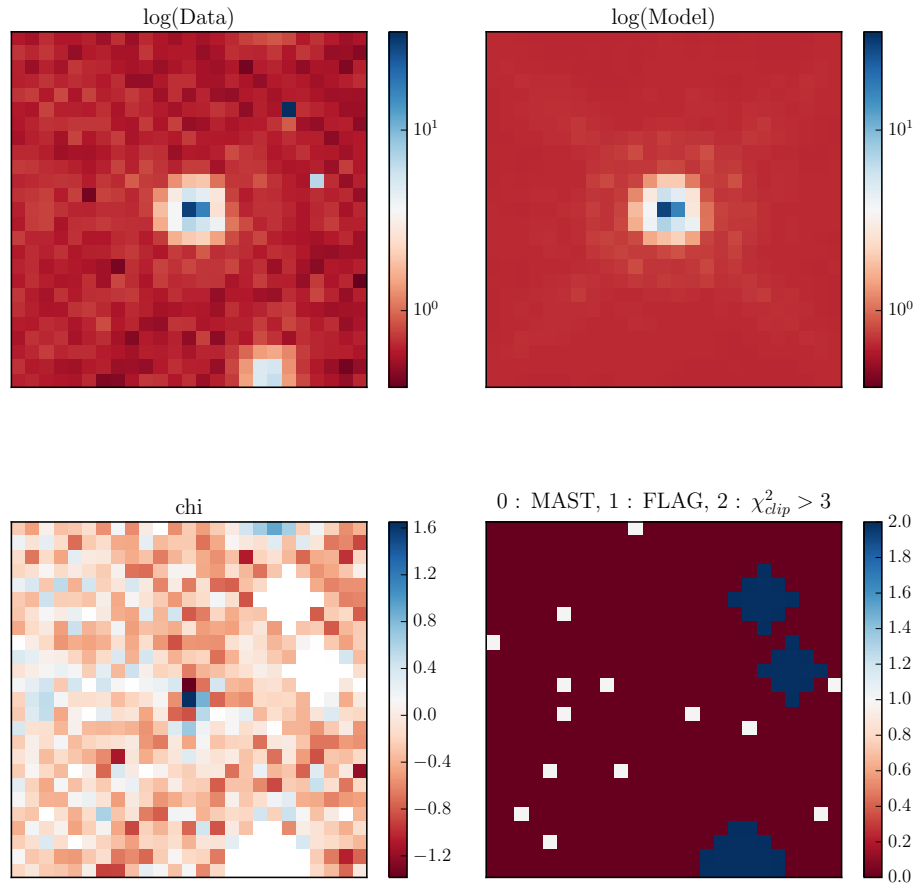


Figure 5.11: Same as Figure 5.10 but showing a different patch of sky. The more *conservative* clipping algorithm masks out pixels that are ill-fit given the downsampled PSF model given by Eq. 5.2.

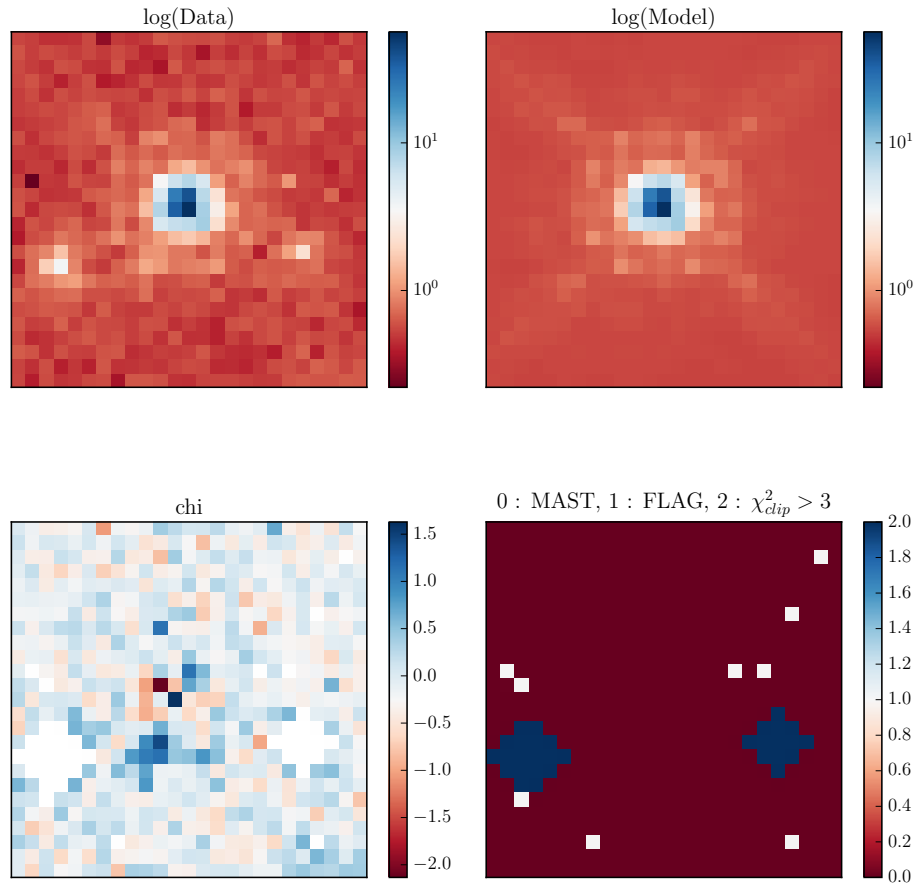


Figure 5.12: Same as Figure 5.10 but showing a different patch of sky. Note that the pixels along the lower tails of the PSF receive light contribution from other point sources and are masked out in the  $\chi$ -map.

# Conclusion

In this dissertation, we try to address some of the longstanding computational problems associated with interpreting the large scale structure and weak lensing datasets. We show that in the presence of noise, approximate stellar centroiding methods capture most of the information available in Fisher information matrix. Our investigation ensures that the PSF bias arising from the use of fast centroiding methods will be minimal.

We show that likelihood free inference methods such as ABC can be used for robust parameter estimation in large scale structure cosmology. We demonstrate that our ABC-PMC method is capable of deliver unbiased parameter estimation by incorporating sample variance in the generative forward model. Furthermore, this method can be used for inference with summary statistics beyond two point correlation functions such as the group multiplicity function.

We constrain the impact of halo assembly bias on galaxy clustering measurements of the local universe. We show that by taking into account the dark matter halo properties beyond mass can lead to slight improvements in accuracy of the galaxy clustering predictions on large scales. But we find that the effect is only marginal and is fully consistent with the galaxy clustering predictions of a simple mass-only HOD prescription.

We present a novel method for estimation of the galaxy clustering uncertainties in the form of covariance matrices. With an accurate N-body simulation, we show that our method

is able to model the nonlinear halo two-point and three-point statistics with a percent level accuracy needed for the next generation of redshift space distortion and Baryonic acoustic oscillation studies with the upcoming galaxy surveys.

Then we present a probabilistic model for estimating the super-resolution PSF of the HST WFC3-IR channel. We show that our generative forward model can accurately model the point sources observed by this telescope. We are able to estimate the PSF at a resolution higher than the native pixel grid. We are also able to robustly model the images of point sources in crowded fields in the HST WFC3-IR observations.

# Bibliography

Abazajian, K., Zheng, Z., Zehavi, I., et al. 2005, ApJ, 625, 613

Abazajian, K. N., Adelman-McCarthy, J. K., Agüeros, M. A., et al. 2009, ApJS, 182, 543-558

Ahn, K., Iliev, I. T., Shapiro, P. R., Srisawat, C. 2015, MNRAS, 450, 1486

Akaike, H. 1974, IEEE Transactions on Automatic Control, 19, 716

Akeret, J., Refregier, A., Amara, A., Seehars, S., & Hasner, C. 2015, J. Cosmology Astropart. Phys., 8, 043

Alam, S., Ata, M., Bailey, S., et al. 2016, arXiv:1607.03155

Anderson, J., & King, I. R. 2000, PASP, 112, 1360

Anderson, J., & King, I. R. 2003, PASP, 115, 113

Anderson, L., Aubourg, E., Bailey, S., et al. 2012, MNRAS, 427, 3435

Angulo, R. E., Baugh, C. M., & Lacey, C. G. 2008, MNRAS, 387, 921

Angulo, R. E., Baugh, C. M., Frenk, C. S., Lacey, C. G. 2014, MNRAS, 442, 3256

Ata, M., Kitaura, F.-S., Müller, V. 2015, MNRAS, 446, 4250

Avila, R. J., Hack, W. J., & STScI AstroDrizzle Team 2012, American Astronomical Society Meeting Abstracts #220, 220, 135.13

Bagla, J. S. 2002, Journal of Astrophysics and Astronomy, 23, 185

Bardeen, J. M., Steinhardt, P. J., & Turner, M. S. 1983, Phys. Rev. D, 28, 679

Bardeen, J. M., Bond, J. R., Kaiser, N., & Szalay, A. S. 1986, ApJ, 304, 15

Beaumont, M. A., Cornuet, J.-M., Marin, J.-M., & Robert, C. P. 2008, arXiv:0805.2256

Behroozi, P. S., Wechsler, R. H., & Conroy, C. 2013, ApJ, 770, 57

Behroozi, P. S., Wechsler, R. H., & Wu, H.-Y. 2013, ApJ, 762, 109

Berlind, A. A., & Weinberg, D. H. 2002, ApJ, 575, 587

Berlind, A. A., Frieman, J., Weinberg, D. H., et al. 2006, ApJS, 167, 1

Bernardeau, F., Colombi, S., Gaztañaga, E., & Scoccimarro, R. 2002, Phys. Rep., 367, 1

Bernstein, G. M., Armstrong, R., Krawiec, C., & March, M. C. 2016, MNRAS, 459, 4467

Bertin, E., & Arnouts, S. 1996, A&AS, 117, 393

Bickerton, S. J., & Lupton, R. H. 2013, MNRAS, 431, 1275

Bishop, C. M., & Nasrabadi, N. M. 2007, Journal of Electronic Imaging, 16, 049901

Blanton, M. R., Hogg, D. W., Bahcall, N. A., et al. 2003, ApJ, 592, 819

Blanton, M. R., Schlegel, D. J., Strauss, M. A., et al. 2005, AJ, 129, 2562

Blanton, M. R., & Berlind, A. A. 2007, ApJ, 664, 791

- Blot, L., Corasaniti, P. S., Amendola, L., & Kitching, T. D. 2016, MNRAS, 458, 4462
- Bond, J. R., Cole, S., Efstathiou, G., & Kaiser, N. 1991, ApJ, 379, 440
- Bonnett, C., Troxel, M. A., Hartley, W., et al. 2016, Phys. Rev. D, 94, 042005
- Bouchet, F. R., Colombi, S., Hivon, E., & Juszkiewicz, R. 1995, A&A, 296, 575
- Bovy Jo, Hogg, D. W., & Roweis, S. T. 2011, Annals of Applied Statistics, 5,
- Buchert, T., & Ehlers, J. 1993, MNRAS, 264,
- Cacciato, M., van den Bosch, F. C., More, S., Mo, H., & Yang, X. 2013, MNRAS, 430, 767
- Cameron, E., & Pettitt, A. N. 2012, MNRAS, 425, 44
- Campbell, D., van den Bosch, F. C., Hearin, A., et al. 2015, MNRAS, 452, 444
- Carlson, J., White, M., & Padmanabhan, N. 2009, Phys. Rev. D, 80, 043531
- Casas-Miranda, R., Mo, H. J., Sheth, R. K., & Boerner, G. 2002, MNRAS, 333, 730
- Catelan, P. 1995, MNRAS, 276, 115
- Cen, R., & Ostriker, J. P. 1993, ApJ, 417, 415
- Chan, K. C., & Blot, L. 2016, arXiv:1610.06585
- Chaves-Montero, J., Angulo, R. E., Schaye, J., et al. 2016, MNRAS, 460, 3100
- Choi, A., Heymans, C., Blake, C., et al. 2016, MNRAS, 463, 3737
- Chuang, C.-H., Kitaura, F.-S., Prada, F., Zhao, C., & Yepes, G. 2015, MNRAS, 446, 2621
- Chuang, C.-H., Zhao, C., Prada, F., et al. 2015, MNRAS, 452, 686

- Codis, S., Gavazzi, R., Dubois, Y., et al. 2015, MNRAS, 448, 3391
- Conroy, C., Wechsler, R. H., & Kravtsov, A. V. 2006, ApJ, 647, 201
- Conroy, C., & Wechsler, R. H. 2009, ApJ, 696, 620
- Conti, I. F., Herbonnet, R., Hoekstra, H., et al. 2017, MNRAS,
- Cooray, A., & Sheth, R. 2002, Phys. Rep., 372, 1
- Coupon, J., Arnouts, S., van Waerbeke, L., et al. 2015, MNRAS, 449, 1352
- Crocce, M., Cabré, A., & Gaztañaga, E. 2011, MNRAS, 414, 329
- Croton, D. J., Gao, L., & White, S. D. M. 2007, MNRAS, 374, 1303
- Dalal, N., White, M., Bond, J. R., & Shirokov, A. 2008, ApJ, 687, 12-21
- Davis, M., Efstathiou, G., Frenk, C. S., & White, S. D. M. 1985, ApJ, 292, 371
- Dawson, K. S., Schlegel, D. J., Ahn, C. P., et al. 2013, AJ, 145, 10
- Dawson, K. S., Kneib, J.-P., Percival, W. J., et al. 2016, AJ, 151, 44
- de la Torre, S., & Peacock, J. A. 2013, MNRAS, 435, 743
- Del Moral, P., Doucet, A., & Jasra, A. 2012, arXiv:1203.0464
- DESI Collaboration, Aghamousa, A., Aguilar, J., et al. 2016, arXiv:1611.00036
- Dodelson, S., & Schneider, M. D. 2013, Phys. Rev. D, 88, 063537
- Doob, J. L. 1946, Science, 104, 450
- Dressler, A. 1980, ApJ, 236, 351

- Driver, S. P., Hill, D. T., Kelvin, L. S., et al. 2011, MNRAS, 413, 971
- Dutton, A. A., & Macciò, A. V. 2014, MNRAS, 441, 3359
- Dvornik, A., Cacciato, M., Kuijken, K., et al. 2017, arXiv:1703.06657
- Eifler, T., Krause, E., Schneider, P., & Honscheid, K. 2014, MNRAS, 440, 1379
- Eifler, T., Krause, E., Dodelson, S., et al. 2015, MNRAS, 454, 2451
- Eriksen, H. K., O'Dwyer, I. J., Jewell, J. B., et al. 2004, ApJS, 155, 227
- Feldman, H. A., Kaiser, N., & Peacock, J. A. 1994, ApJ, 426, 23
- Feng, Y., Chu, M.-Y., Seljak, U., & McDonald, P. 2016, MNRAS, 463, 2273
- Filippi, S., Barnes, C., Cornebise, J., & Stumpf, M. P. H. 2011, arXiv:1106.6280
- Foreman-Mackey, D., Hogg, D. W., Lang, D., & Goodman, J. 2013, PASP, 125, 306
- Foreman-Mackey, D., Montet, B. T., Hogg, D. W., et al. 2015, ApJ, 806, 215
- Foreman-Mackey, D. 2017, Astrophysics Source Code Library, ascl:1702.002
- Friedrich, O., Seitz, S., Eifler, T. F., & Gruen, D. 2016, MNRAS, 456, 2662
- Friedrich, O., & Eifler, T. 2017, arXiv:1703.07786
- Frieman, J., & Dark Energy Survey Collaboration 2013, American Astronomical Society Meeting Abstracts #221, 221, 335.01
- Fruchter, A. S., & Hook, R. N. 2002, PASP, 114, 144
- Fry, J. N., & Gaztanaga, E. 1993, ApJ, 413, 447

Gao, L., Springel, V., & White, S. D. M. 2005, MNRAS, 363, L66

Gao, L., & White, S. D. M. 2007, MNRAS, 377, L5

Gelman, A., Hwang, J., & Vehtari, A. 2013, arXiv:1307.5928

Gelman, A., & Rubin, D. B. 1992, Statistical Science, 457

Gil-Marín, H., Jimenez, R., & Verde, L. 2011, MNRAS, 414, 1207

Gil-Marín, H., Noreña, J., Verde, L., et al. 2015, MNRAS, 451, 539

Gil-Marín, H., Verde, L., Noreña, J., et al. 2015, MNRAS, 452, 1914

Gil-Marín, H., Percival, W. J., Verde, L., et al. 2017, MNRAS, 465, 1757

Goodman, J., & Weare, J. 2010, Communications in applied mathematics and computational science, 5, 65

Grieb, J. N., Sánchez, A. G., Salazar-Albornoz, S., & Dalla Vecchia, C. 2016, MNRAS, 457, 1577

Guth, A. H., & Pi, S.-Y. 1982, Physical Review Letters, 49, 1110

Guo, Q., White, S., Li, C., & Boylan-Kolchin, M. 2010, MNRAS, 404, 1111

Guo, H., Zehavi, I., & Zheng, Z. 2012, ApJ, 756, 127

Guo, H., Zheng, Z., Jing, Y. P., et al. 2015, MNRAS, 449, L95

Guo, H., Zheng, Z., Zehavi, I., et al. 2015, MNRAS, 453, 4368

Guo, H., Zheng, Z., Behroozi, P. S., et al. 2016, MNRAS, 459, 3040

Guo, H., Zheng, Z., Behroozi, P. S., et al. 2016, ApJ, 831, 3

- Hahn, C., Vakili, M., Walsh, K., et al. 2016, arXiv:1607.01782
- Hahn, C., Scoccimarro, R., Blanton, M. R., Tinker, J. L., & Rodríguez-Torres, S. 2017, MNRAS,
- Harker, G., Cole, S., Helly, J., Frenk, C., & Jenkins, A. 2006, MNRAS, 367, 1039
- Harnois-Déraps, J., & van Waerbeke, L. 2015, MNRAS, 450, 2857
- Hartlap, J., Simon, P., & Schneider, P. 2007, A&A, 464, 399
- Hearin, A. P., Zentner, A. R., Berlind, A. A., & Newman, J. A. 2013, MNRAS, 433, 659
- Hearin, A. P., & Watson, D. F. 2013, MNRAS, 435, 1313
- Hearin, A. P., Watson, D. F., Becker, M. R., et al. 2014, MNRAS, 444, 729
- Hearin, A. P., Watson, D. F., & van den Bosch, F. C. 2015, MNRAS, 452, 1958
- Hearin, A., Campbell, D., Tollerud, E., et al. 2016, arXiv:1606.04106
- Hearin, A. P., Zentner, A. R., van den Bosch, F. C., Campbell, D., & Tollerud, E. 2016, MNRAS, 460, 2552
- Heitmann, K., Lukić, Z., Fasel, P., et al. 2008, Computational Science and Discovery, 1, 015003
- Heitmann, K., Higdon, D., White, M., et al. 2009, ApJ, 705, 156
- Heitmann, K., White, M., Wagner, C., Habib, S., & Higdon, D. 2010, ApJ, 715, 104
- Heymans, C., Grocott, E., Heavens, A., et al. 2013, MNRAS, 432, 2433
- Hildebrandt, H., Viola, M., Heymans, C., et al. 2017, MNRAS, 465, 1454

- Hoekstra, H., Viola, M., & Herbonnet, R. 2016, arXiv:1609.03281
- Howlett, C., Manera, M., & Percival, W. J. 2015, *Astronomy and Computing*, 12, 109
- Hudson, M. J., Gillis, B. R., Coupon, J., et al. 2015, *MNRAS*, 447, 298
- Huff, E., & Mandelbaum, R. 2017, arXiv:1702.02600
- Ishida, E. E. O., Vitenti, S. D. P., Penna-Lima, M., et al. 2015, *Astronomy and Computing*, 13, 1
- Izard, A., Crocce, M., & Fosalba, P. 2016, *MNRAS*, 459, 2327
- Jarvis, M., Sheldon, E., Zuntz, J., et al. 2016, *MNRAS*, 460, 2245
- Jayaraman, A., Shapiro, C., Mandelbaum, R., et al. 2016, *American Astronomical Society Meeting Abstracts*, 228, 311.04
- Jee, M. J., Tyson, J. A., Hilbert, S., et al. 2016, *American Astronomical Society Meeting Abstracts*, 227, 307.07
- Jennings, E., & Madigan, M. 2016, arXiv:1608.07606
- Jennings, E., Wolf, R., & Sako, M. 2016, arXiv:1611.03087
- Joachimi, B., Cacciato, M., Kitching, T. D., et al. 2015, *Space Sci. Rev.*, 193, 1
- Joachimi, B. 2016, arXiv:1612.00752
- Joudaki, S., Mead, A., Blake, C., et al. 2016, arXiv:1610.04606
- Kacprzak, T., Bridle, S., Rowe, B., et al. 2014, *MNRAS*, 441, 2528
- Kaiser, N. 1984, *ApJ*, 284, L9

- Kalus, B., Percival, W. J., & Samushia, L. 2016, MNRAS, 455, 2573
- Kannawadi, A., Shapiro, C. A., Mandelbaum, R., et al. 2016, PASP, 128, 095001
- Kauffmann, G., Li, C., Zhang, W., & Weinmann, S. 2013, MNRAS, 430, 1447
- Kirk, D., Brown, M. L., Hoekstra, H., et al. 2015, Space Sci. Rev., 193, 139
- Kitaura, F.-S., & Heß, S. 2013, MNRAS, 435, L78
- Kitaura, F.-S., Yepes, G., & Prada, F. 2014, MNRAS, 439, L21
- Kitaura, F.-S., Gil-Marín, H., Scóccola, C. G., et al. 2015, MNRAS, 450, 1836
- Kitaura, F.-S., Rodríguez-Torres, S., Chuang, C.-H., et al. 2016, MNRAS, 456, 4156
- Kitching, T. D., Verde, L., Heavens, A. F., & Jimenez, R. 2016, MNRAS, 459, 971
- Klypin, A., & Holtzman, J. 1997, arXiv:astro-ph/9712217
- Klypin, A. A., Trujillo-Gomez, S., & Primack, J. 2011, ApJ, 740, 102
- Klypin, A., Yepes, G., Gottlöber, S., Prada, F., & Heß, S. 2016, MNRAS, 457, 4340
- Knebe, A., Knollmann, S. R., Muldrew, S. I., et al. 2011, MNRAS, 415, 2293
- Knox, L. 1995, Phys. Rev. D, 52, 4307
- Koda, J., Blake, C., Beutler, F., Kazin, E., & Marin, F. 2016, MNRAS, 459, 2118
- Krause, E., Eifler, T., & Blazek, J. 2016, MNRAS, 456, 207
- Kravtsov, A. V., Klypin, A. A., & Khokhlov, A. M. 1997, ApJS, 111, 73
- Kravtsov, A. V., Berlind, A. A., Wechsler, R. H., et al. 2004, ApJ, 609, 35

- Kravtsov, A. V. 2013, ApJ, 764, L31
- Krist, J. 1995, Astronomical Data Analysis Software and Systems IV, 77, 349
- Krist, J. E., Hook, R. N., & Stoehr, F. 2011, Proc. SPIE, 8127, 81270J
- Kuijken, K., Heymans, C., Hildebrandt, H., et al. 2015, MNRAS, 454, 3500
- Kwan, J., Sánchez, C., Clampitt, J., et al. 2017, MNRAS, 464, 4045
- Landy, S. D., & Szalay, A. S. 1993, ApJ, 412, 64
- Lanusse, F., Ravanbakhsh, S., Mandelbaum, R., Schneider, J., & Poczos, B. 2017, American Astronomical Society Meeting Abstracts, 229, 342.05
- Laureijs, R., Amiaux, J., Arduini, S., et al. 2011, arXiv:1110.3193
- Lawrence, E., Heitmann, K., White, M., et al. 2010, ApJ, 713, 1322
- Leach, S. M., Cardoso, J.-F., Baccigalupi, C., et al. 2008, A&A, 491, 597
- Le Cam, L. M. 1953, University of California press, 1, 11
- Ledoit, O., & Wolf, M. 2004, Journal of Multivariate Analysis, 88, 365
- Ledoit, O., & Wolf, M. 2012, The Annals of Statistics, 40, 1024
- Lehmann, B. V., Mao, Y.-Y., Becker, M. R., Skillman, S. W., & Wechsler, R. H. 2017, ApJ, 834, 37
- Lemson, G., & Kauffmann, G. 1999, MNRAS, 302, 111
- Leauthaud, A., Tinker, J., Behroozi, P. S., Busha, M. T., & Wechsler, R. H. 2011, ApJ, 738, 45

- Leauthaud, A., Tinker, J., Bundy, K., et al. 2012, ApJ, 744, 159
- Leauthaud, A., Saito, S., Hilbert, S., et al. 2017, MNRAS, 467, 3024
- Leistedt, B., & Hogg, D. W. 2016, arXiv:1612.00847
- Levi, M., Bebek, C., Beers, T., et al. 2013, arXiv:1308.0847
- Li, Y., Mo, H. J., & Gao, L. 2008, MNRAS, 389, 1419
- Lin, C.-A., & Kilbinger, M. 2015, A&A, 583, A70
- Lin, C.-A., Kilbinger, M., & Pires, S. 2016, A&A, 593, A88
- Liu, J., Ortiz-Vazquez, A., & Hill, J. C. 2016, Phys. Rev. D, 93, 103508
- Lobos, R. A., Silva, J. F., Mendez, R. A., & Orchard, M. 2015, PASP, 127, 1166
- LSST Science Collaboration, Abell, P. A., Allison, J., et al. 2009, arXiv:0912.0201
- LSST Dark Energy Science Collaboration 2012, arXiv:1211.0310
- Lupton, R., Gunn, J. E., Ivezić, Z., Knapp, G. R., & Kent, S. 2001, Astronomical Data Analysis Software and Systems X, 238, 269
- Mandelbaum, R., Rowe, B., Armstrong, R., et al. 2015, MNRAS, 450, 2963
- Manera, M., Scoccimarro, R., Percival, W. J., et al. 2013, MNRAS, 428, 1036
- Manera, M., Samushia, L., Tojeiro, R., et al. 2015, MNRAS, 447, 437
- Mao, Y.-Y., Williamson, M., & Wechsler, R. H. 2015, ApJ, 810, 21
- McDonald, P., Roy, A. 2009, J. Cosmology Astropart. Phys., 8, 20

- McEwen, J. E., & Weinberg, D. H. 2016, arXiv:1601.02693
- Mead, A. J., Heymans, C., Lombriser, L., et al. 2016, MNRAS, 459, 1468
- Melchior, P., & Viola, M. 2012, MNRAS, 424, 2757
- Miyatake, H., More, S., Mandelbaum, R., et al. 2015, ApJ, 806, 1
- Miyatake, H., More, S., Takada, M., et al. 2016, Physical Review Letters, 116, 041301
- Mo, H. J., & White, S. D. M. 1996, MNRAS, 282, 347
- Mo, H. J., & White, S. D. M. 2002, MNRAS, 336, 112
- Mohammed, I., & Seljak, U. 2014, MNRAS, 445, 3382
- Mohammed, I., Seljak, U., & Vlah, Z. 2017, MNRAS, 466, 780
- Monaco, P., Theuns, T., Taffoni, G. et al. 2002, ApJ, 564, 8
- Monaco, P., Sefusatti, E., Borgani, S., et al. 2013, MNRAS, 433, 2389
- Monaco, P. 2016, Galaxies, 4, 53
- More, S., van den Bosch, F. C., & Cacciato, M. 2009, MNRAS, 392, 917
- More, S., van den Bosch, F. C., Cacciato, M., et al. 2013, MNRAS, 430, 747
- More, S., Miyatake, H., Mandelbaum, R., et al. 2015, ApJ, 806, 2
- More, S., Miyatake, H., Takada, M., et al. 2016, ApJ, 825, 39
- Morrison, C. B., & Schneider, M. D. 2013, J. Cosmology Astropart. Phys., 11, 009
- Navarro, J. F., Frenk, C. S., & White, S. D. M. 1996, ApJ, 462, 563

- Navarro, J. F., Hayashi, E., Power, C., et al. 2004, MNRAS, 349, 1039
- Neistein, E., Weinmann, S. M., Li, C., & Boylan-Kolchin, M. 2011, MNRAS, 414, 1405
- Neyrinck, M. C., Aragón-Calvo, M. A., Jeong, D., & Wang, X. 2014, MNRAS, 441, 646
- Ngolè Mboula, F. M., Starck, J.-L., Ronayette, S., Okumura, K., & Amiaux, J. 2015, A&A, 575, A86
- Ngolè Mboula, F. M., Starck, J.-L., Okumura, K., Amiaux, J., & Hudelot, P. 2016, arXiv:1608.08104
- Norberg, P., Baugh, C. M., Gaztañaga, E., & Croton, D. J. 2009, MNRAS, 396, 19
- Oh, S. P., Spergel, D. N., & Hinshaw, G. 1999, ApJ, 510, 551
- Padmanabhan, N., White, M., Zhou, H. H., & O'Connell, R. 2016, MNRAS, 460, 1567
- Paranjape, A., & Sheth, R. K. 2012, MNRAS, 423, 1845
- Parejko, J. K., Sunayama, T., Padmanabhan, N., et al. 2013, MNRAS, 429, 98
- Paz, D. J., & Sánchez, A. G. 2015, MNRAS, 454, 4326
- Peebles, P. J. E. 1980, Research supported by the National Science Foundation. Princeton, N.J., Princeton University Press, 1980. 435 p.,
- Peebles, P. J. E. 1980, Research supported by the National Science Foundation. Princeton, N.J., Princeton University Press, 1980. 435 p.,
- Planck Collaboration, Ade, P. A. R., Aghanim, N., et al. 2014, A&A, 571, A16
- Planck Collaboration, Ade, P. A. R., Aghanim, N., et al. 2016, A&A, 594, A13

- Planck Collaboration, Ade, P. A. R., Aghanim, N., et al. 2016, *A&A*, 594, A17
- Planck Collaboration, Ade, P. A. R., Aghanim, N., et al. 2016, *A&A*, 594, A20
- Plazas, A. A., Shapiro, C., Kannawadi, A., et al. 2016, *PASP*, 128, 104001
- Pope, A. C., & Szapudi, I. 2008, *MNRAS*, 389, 766
- Prada, F., Klypin, A. A., Cuesta, A. J., Betancort-Rijo, J. E., & Primack, J. 2012, *MNRAS*, 423, 3018
- Press, W. H., & Schechter, P. 1974, *ApJ*, 187, 425
- Reddick, R. M., Wechsler, R. H., Tinker, J. L., & Behroozi, P. S. 2013, *ApJ*, 771, 30
- Reid, B. A., Seo, H.-J., Leauthaud, A., Tinker, J. L., & White, M. 2014, *MNRAS*, 444, 476
- Riess, A. G., Filippenko, A. V., Challis, P., et al. 1998, *AJ*, 116, 1009
- Rodríguez-Puebla, A., Drory, N., & Avila-Reese, V. 2012, *ApJ*, 756, 2
- Rodríguez-Puebla, A., Behroozi, P., Primack, J., et al. 2016, *MNRAS*, 462, 893
- Rodríguez-Torres, S. A., Chuang, C.-H., Prada, F., et al. 2016, *MNRAS*, 460, 1173
- Ross, A. J., Percival, W. J., Sánchez, A. G., et al. 2012, *MNRAS*, 424, 564
- Rowe, B. 2010, *MNRAS*, 404, 350
- Rowe, B., Hirata, C., & Rhodes, J. 2011, *ApJ*, 741, 46
- Rowe, B., Jarvis, M., & Mandelbaum, R. 2014, Astrophysics Source Code Library, ascl:1402.009

Rowe, B. T. P., Jarvis, M., Mandelbaum, R., et al. 2015, *Astronomy and Computing*, 10, 121

Rykoff, E. S., Rozo, E., Busha, M. T., et al. 2014, *ApJ*, 785, 104

Santiago, B. X., & Strauss, M. A. 1992, *ApJ*, 387, 9

Schaye, J. 2015, *IAU General Assembly*, 22, 2250042

Schaan, E., Krause, E., Eifler, T., et al. 2016, arXiv:1607.01761

Schneider, P., van Waerbeke, L., Kilbinger, M., & Mellier, Y. 2002, *A&A*, 396, 1

Schneider, M. D., Hogg, D. W., Marshall, P. J., et al. 2015, *ApJ*, 807, 87

Schwarz, G. 1978, *Annals of Statistics*, 6, 461

Scoccimarro, R., Sheth, R. K., Hui, L., & Jain, B. 2001, *ApJ*, 546, 20

Scoccimarro, R., Sheth, R. K. 2002, *MNRAS*, 329, 629

Semboloni, E., Hoekstra, H., & Schaye, J. 2013, *MNRAS*, 434, 148

Seljak, U. 2000, *MNRAS*, 318, 203

Sellentin, E., & Heavens, A. F. 2016, *MNRAS*, 456, L132

Sellentin, E., & Heavens, A. F. 2017, *MNRAS*, 464, 4658

Sheth, R. K., Mo, H. J., & Tormen, G. 2001, *MNRAS*, 323, 1

Sheth, R. K., & Tormen, G. 2004, *MNRAS*, 350, 1385

Shirasaki, M., Takada, M., Miyatake, H., et al. 2016, arXiv:1607.08679

- Silk, D., Filippi, S., & Stumpf, M. P. H. 2012, arXiv:1210.3296
- Simpson, F., Blake, C., Peacock, J. A., et al. 2016, Phys. Rev. D, 93, 023525
- Singh, S., Mandelbaum, R., & Brownstein, J. R. 2017, MNRAS, 464, 2120
- Singh, S., Mandelbaum, R., Seljak, U., Slosar, A., & Vazquez Gonzalez, J. 2016, arXiv:1611.00752
- Sinha, M. 2017, 10.5281/zenodo.55161
- Sheldon, E. S., & Huff, E. M. 2017, arXiv:1702.02601
- Slepian, Z., Eisenstein, D. J., Beutler, F., et al. 2015, arXiv:1512.02231
- Slepian, Z., Eisenstein, D. J., Blazek, J. A., et al. 2016, arXiv:1607.06098
- Slepian, Z., Eisenstein, D. J., Brownstein, J. R., et al. 2016, arXiv:1607.06097
- Smith, R. E., Scoccimarro, R., & Sheth, R. K. 2008, Phys. Rev. D, 77, 043525
- Somerville, R. S., Lemson, G., Sigad, Y., et al. 2001, MNRAS, 320, 289
- Somerville, R. S., & Davé, R. 2015, ARA&A, 53, 51
- Spergel, D., Gehrels, N., Baltay, C., et al. 2015, arXiv:1503.03757
- Springel, V. 2005, MNRAS, 364, 1105
- Steidel, C. C., Adelberger, K. L., Dickinson, M., et al. 1998, ApJ, 492, 428
- Sun, L., Wang, Q., & Zhan, H. 2013, ApJ, 777, 75
- Sunayama, T., Hearin, A. P., Padmanabhan, N., & Leauthaud, A. 2016, MNRAS, 458, 1510

- Takada, M., & Spergel, D. N. 2014, MNRAS, 441, 2456
- Takahashi, R., Yoshida, N., Takada, M., et al. 2011, ApJ, 726, 7
- Tasitsiomi, A., Kravtsov, A. V., Wechsler, R. H., & Primack, J. R. 2004, ApJ, 614, 533
- Tassev, S., Zaldarriaga, M., & Eisenstein, D. J. 2013, J. Cosmology Astropart. Phys., 6, 036
- Tassev, S., Eisenstein, D. J., Wandelt, B. D., & Zaldarriaga, M. 2015, arXiv:1502.07751
- Taylor, A., Joachimi, B., & Kitching, T. 2013, MNRAS, 432, 1928
- Taylor, A., & Joachimi, B. 2014, MNRAS, 442, 2728
- Tinker, J. L., Weinberg, D. H., Zheng, Z., & Zehavi, I. 2005, ApJ, 631, 41
- Tinker, J. L., Weinberg, D. H., & Warren, M. S. 2006, ApJ, 647, 737
- Tinker, J. L. 2007, MNRAS, 374, 477
- Tinker, J. L., Conroy, C., Norberg, P., et al. 2008, ApJ, 686, 53-71
- Tinker, J., Kravtsov, A. V., Klypin, A., et al. 2008, ApJ, 688, 709-728
- Tinker, J. L., & Conroy, C. 2009, ApJ, 691, 633
- Tinker, J. L., Robertson, B. E., Kravtsov, A. V., et al. 2010, ApJ, 724, 878
- Tinker, J., Wetzel, A., & Conroy, C. 2011, arXiv:1107.5046
- Tinker, J., Wetzel, A., & Conroy, C. 2011, arXiv:1107.5046
- Tinker, J. L., Sheldon, E. S., Wechsler, R. H., et al. 2012, ApJ, 745, 16
- Tinker, J. L., Leauthaud, A., Bundy, K., et al. 2013, ApJ, 778, 93

- Trujillo, I., Aguerri, J. A. L., Cepa, J., & Gutiérrez, C. M. 2001, MNRAS, 328, 977
- Tsalmantza, P., & Hogg, D. W. 2012, ApJ, 753, 122
- Vale, A., & Ostriker, J. P. 2004, MNRAS, 353, 189
- van den Bosch, F. C., Mo, H. J., & Yang, X. 2003, MNRAS, 345, 923
- van den Bosch, F. C., Yang, X., Mo, H. J., et al. 2007, MNRAS, 376, 841
- van den Bosch, F. C., More, S., Cacciato, M., Mo, H., & Yang, X. 2013, MNRAS, 430, 725
- van den Bosch, F. C., Jiang, F., Hearin, A., et al. 2014, MNRAS, 445, 1713
- Voigt, L. M., & Bridle, S. L. 2010, MNRAS, 404, 458
- Wandelt, B. D., Larson, D. L., & Lakshminarayanan, A. 2004, Phys. Rev. D, 70, 083511
- Wang, H. Y., Mo, H. J., & Jing, Y. P. 2007, MNRAS, 375, 633
- Wang, L., Weinmann, S. M., De Lucia, G., & Yang, X. 2013, MNRAS, 433, 515
- Watson, D. F., Berlind, A. A., & Zentner, A. R. 2012, ApJ, 754, 90
- Watson, W. A., Iliev, I. T., D'Aloisio, A., et al. 2013, MNRAS, 433, 1230
- Wechsler, R. H., Zentner, A. R., Bullock, J. S., Kravtsov, A. V., & Allgood, B. 2006, ApJ, 652, 71
- Weinmann, S. M., van den Bosch, F. C., Yang, X., & Mo, H. J. 2006, MNRAS, 366, 2
- Wetzel, A. R., & White, M. 2010, MNRAS, 403, 1072
- Weyant, A., Schafer, C., & Wood-Vasey, W. M. 2013, ApJ, 764, 116

- White, M., & Scott, D. 1996, *Comments on Astrophysics*, 18,
- White, M., Blanton, M., Bolton, A., et al. 2011, *ApJ*, 728, 126
- White, M., Tinker, J. L., & McBride, C. K. 2014, *MNRAS*, 437, 2594
- York, D. G., Adelman, J., Anderson, J. E., Jr., et al. 2000, *AJ*, 120, 1579
- Zehavi, I., Zheng, Z., Weinberg, D. H., et al. 2011, *ApJ*, 736, 59
- Zentner, A. R., Berlind, A. A., Bullock, J. S., Kravtsov, A. V., & Wechsler, R. H. 2005, *ApJ*, 624, 505
- Zentner, A. R., Hearin, A. P., & van den Bosch, F. C. 2014, *MNRAS*, 443, 3044
- Zentner, A. R., Hearin, A., van den Bosch, F. C., Lange, J. U., & Villarreal, A. 2016, arXiv:1606.07817
- Zernike, F. 1934, *MNRAS*, 94, 377
- Zhao, C., Kitaura, F.-S., Chuang, C.-H., et al. 2015, *MNRAS*, 451, 4266
- Zheng, Z., Berlind, A. A., Weinberg, D. H., et al. 2005, *ApJ*, 633, 791
- Zheng, Z., Coil, A. L., & Zehavi, I. 2007, *ApJ*, 667, 760
- Zheng, Z., & Guo, H. 2016, *MNRAS*, 458, 4015
- Zu, Y., & Mandelbaum, R. 2015, *MNRAS*, 454, 1161
- Zu, Y., & Mandelbaum, R. 2016, *MNRAS*, 457, 4360
- Zu, Y., Mandelbaum, R., Simet, M., Rozo, E., & Rykoff, E. S. 2016, arXiv:1611.00366
- Zuntz, J., Kacprzak, T., Voigt, L., et al. 2013, *MNRAS*, 434, 1604

Zuntz, J., Kacprzak, T., Voigt, L., et al. 2014, Astrophysics Source Code Library,  
ascl:1409.013